



universität
wien

DISSERTATION

Titel der Dissertation

„Geochemical, isotopic, and petrographic investigations
of rocks from the Bosumtwi impact structure“

Verfasserin

Anna Izabela Losiak MSc

angestrebter akademischer Grad

Doktorin der Naturwissenschaften (Dr.rer.nat.)

Wien, 2013

Studienkennzahl lt. Studienblatt:

A 791 426

Dissertationsgebiet lt. Studienblatt:

Erdwissenschaften/Geologie

Betreuer:

Univ.-Prof. Dr. Christian Koeberl

DEDICATION



The very excited author of this thesis sitting on an outcrop with multiple shatter cones at the Gosses Bluff impact structure (Australia 2012, photo by Matthew Huber).

This thesis is dedicated to Jacek Wojciechowski.

PREFACE

This thesis summarizes three years of study at the Department of Lithospheric Research, University of Vienna. The thesis discusses three aspects related to the development of the Bosumtwi impact crater (Ghana, West Africa): 1) characterization of the target rocks, especially granites, from the vicinity of the Bosumtwi crater (chapter three); 2) formation of planar deformation features within shocked rocks on the example of sample from the Bosumtwi impact crater (chapter four); and 3) mixing of the target rocks during the impact cratering process by studying ^{10}Be contents within suevites from Bosumtwi crater (chapter five). Manuscripts discussing results of those projects have been submitted for publication in peer-reviewed journals (Lithos and Meteoritics and Planetary Science).

The thesis also includes a short introduction to impact cratering (chapter one), as well as a brief discussion of the main principles of the methods used in this study (chapter two). In addition, co-authored articles related to the thesis project are attached at the end of the thesis along with the CV of the thesis' author.

ACKNOWLEDGMENTS

I am very grateful to my advisor professor Christian Koeberl for his support during the time that I spent at the Department of Lithospheric Research, especially for teaching me how science and academia works.

I would like to also thank:

- Professor Eva M. Wild (University of Vienna) for all that she has taught me about the ^{10}Be and ^{14}C sample preparation, all her advice and a lot of kind help.
- Professor W. Uwe Reimold (Museum of Natural History, Berlin) for encouragement, a lot of great advice and co-organizing an amazing field trip in South Africa that introduced me to the world of impact cratering.
- Doctor Ludovic Ferrière (Naturhistorisches Museum Wien) for teaching me about the wonders of shocked quartz, all great discussions, and fruitful collaboration.
- (soon) doctor Matthew Huber (University of Vienna) for his friendship, countless discussions, fun time during field trips, and many hours that he has spent proofreading my manuscripts.
- (soon) doctor Mattia Galiazzo (University of Vienna) for his enthusiasm and making astronomers and geologists from our group working together.
- (soon) doctor Akos Bazso (University of Vienna) for many interesting discussions and his serenity.
- Leonard Michlmayr for his help in the laboratory VERA.
- Doctor Lidia Pitarello (Vrije Universiteit Brussel, formerly University of Vienna) for many interesting discussions, and introducing me to fascinating world of Italians and organists.
- Doctor Tamara Goldin (Nature Geoscience, formerly University of Vienna) for teaching me impact modeling and starting the “Crater Caffee”
- Doctor Dieter Mader (University of Vienna) for all his amazing help and every-day assistance and translating the abstract of this thesis to German.
- Doctor Toni Schulz (University of Vienna) for his help with the isotope analysis and fun time in Bonn.

- Professor Rudolf Dvorak (University of Vienna) for an interesting class in astronomy.
- Doctor Gerlinde Habler (University of Vienna) for help with SEM analysis and cutting the FIB section.
- (soon) doctor Maartje Hamers (Universiteit of Utrecht) for TEM analysis.
- Professor Boris A. Ivanov (Russian Academy of Sciences) for introducing me to the basics of numerical modeling and for collaboration.
- Ronald Conze (GFZ, Potsdam, Germany) for helping me during the sampling of the Bosumtwi cores in the Potsdam core repository.
- Doctor Lutz Hecht (Museum of Natural History, Berlin) for help with obtaining some references and taking care of me in during the visit at the Museum of Natural History, Berlin.
- Doctor Joerg Fritz (Museum of Natural History, Berlin) for many interesting discussions and providing me with samples of shocked quartz.
- Doctor Michael Poelchau (University of Freiburg) for interesting discussions during conferences.
- Professor Lech Czechowski (University of Warsaw) for interesting cooperation.
- Professor Andrzej Muszynski (University of Poznan) for his hospitality during the trip to the Morasko impact crater site and inviting me to the 19th Meeting of the Petrology Group of the Mineralogical Society of Poland Obrzycko, Polska.
- Professor Susanne Gier (University of Vienna) for her help with the XRD analysis.
- Professor Eugen Libowitzky (University of Vienna) and professor Lutz Nasdala (University Vienna) for an interesting class in Mineral Spectroscopy.
- Doctor Daniel Boamah (Geological Survey of Ghana) for helping me to obtain some references.
- Doctor David Kring (Lunar and Planetary Institute) for giving me the opportunity to take part in Lunar Summer Intern Project a few years ago and in the Meteor Crater Field Camp at Barringer Meteorite Crater.
- Professor Sylvain Bouley (Paris Observatory), professor David Baratoux (Paul Sabatier University), doctor Lenka Baratoux (Institute de Recherche pour le Développement),

professor Francois Colas (Pic du Midi observatory) and Jean-Luc Dauvergne (Ciel et Espace) for an amazing Tajik adventure.

- Doctor Bob Craddock (Smithsonian), doctor Ben Andrews (Smithsonian) and Rob Dennen (Smithsonian) for a breathtaking escapade to Hawaii and sharing the sausage fried over the lava.
- Doctor Gernot Groemer (University of Innsbruck) and the entire OeWF team for amazing Martian experience.

and

- Jacek Wojciechowski for his support, love and amazing work as an editor of my articles.

I am grateful to the Meteoritical Society for support in the form of travel grants enabling me to attend conferences and to the European Geosciences Union for making it possible for me to attend the EGU meeting for three consecutive years.

The funding for my project was provided by the University of Vienna doctoral school IK-1045 and the Austrian Science Foundation grant P21821-N19.

ABSTRACT

The Bosumtwi structure is a 1.07 million year old, well-preserved, 10.5 km wide complex impact crater. It is associated with one of only four tektite strewn fields known on Earth and it is the source of the Ivory Coast tektites. It was drilled in 2004 by the International Continental Scientific Drilling Program (ICDP), and since then it has been the object of intensive research on various aspects of impact cratering process. This thesis is a continuation of those studies.

Chapter 3 of this thesis presents a full and detailed characterization of the three granitoid intrusions and one mafic dike located in the vicinity of the Bosumtwi crater in terms of petrology, major and trace element geochemistry, geochronology, as well as isotopic composition. This allows us to characterize magmatic evolution of the West African Craton in this area and better understand the geological framework and target rocks of the impact. This study shows that the similar composition (strongly peraluminous muscovite granites and granodiorites) and age (between 2092 ± 6 Ma and 2098 ± 6 Ma) of granitic intrusions in the proximity of the Bosumtwi crater suggest that they are co-genetic. The granitoids were probably formed as a result of anatexis of TTGs (or rocks derived from them) at relatively low pressure and temperature. We propose that the intrusions from the Bosumtwi area are genetically related to the Bansa granite occurring to the east of the crater and can be classified as basin-type, late-stage granitoids. Also a mafic dike located to the NE of the Bosumtwi crater seems to be genetically related to those felsic intrusions. Based on those findings a revised version of the geological map of the Bosumtwi crater area is proposed.

Chapter 4 presents results of the investigation of the spatial relations between a statistically significant number of shocked quartz grains (278) showing PDFs (409) developed within a given area of a single thin section ($\sim 35 \text{ mm}^2$) from the Bosumtwi impact crater. Previous studies of PDFs were either based on single grains or on a randomly chosen quartz grain "population" did not allow to detect possible spatial relationships between quartz grains and PDFs developed within them. The present study shows that some of the PDFs patterns and clusters (consisting of quartz grains with the same PDF

orientation present) that we observed are suggestive of a heterogeneous shock field, very similar to the one recently modeled numerically. Additionally, PDFs developed along different planes within the crystal lattice differ in their physical characteristics, appearance, and location within a grain. The PDFs developed along the $\{10\bar{1}3\}$ orientation are commonly very well visible, thick and usually cover a significant area of the grain. The PDFs developed along the $\{10\bar{1}1\}$ and $\{11\bar{2}2\}$ orientations tend to be very short, faint and hardly visible under the universal-stage microscope. This difference was not noted in the previous studies; it is likely that this indicates that different PDF orientations are formed in a somewhat different way. This work also presents a new web-based program for indexing PDF sets.

Chapter 5 discusses results of the study on ^{10}Be present within the samples from the drill cores LB-07A and LB-08A from the Bosumtwi impact crater, Ghana. A ^{10}Be signal was detected in two samples from the LB-07A core out of 25 samples, and in none of five samples from the LB-08A core. After excluding other possibilities we conclude that the elevated ^{10}Be content within two greywacke clasts is most probably due to pre-impact origin of those clasts from a layer of the target rocks close to the surface (20-25 meters). The results obtained in this study suggest that in-crater breccias were well mixed during the impact cratering process. Additionally, the lack of ^{10}Be signal within the rocks located close to the lake sediments-impactites boundary suggests that infiltration of meteoric water within the crater floor was limited. This may imply that the infiltration of the meteoric water within the crater takes place not aurally, through the pore-space, but rather through a localized system of fractures.

ZUSAMMENFASSUNG

Die Bosumtwi Struktur ist ein gut erhaltener komplexer Impaktkrater mit 10,5 km Durchmesser und einem Alter von etwa 1,07 Ma. Er wird mit der Entstehung eines der vier auf der Erde bekannten Tektitstreufelder, den Elfenbeinküsten-Tektiten, verbunden. Im Jahr 2004 fand ein internationales und multidisziplinäres Bohrprojekt im Rahmen des International Continental Scientific Drilling Program (ICDP) statt und seitdem wurden der Krater und seine Gesteine intensiv untersucht. Diese Dissertation ist eine Fortführung dieser Untersuchungen mit neuen Fragestellungen und Methoden.

Kapitel 3 der Dissertation präsentiert eine detaillierte Charakterisierung der drei Granittypen (und eines mafischen Ganges) in der Nähe des Bosumtwi Kraters bezüglich Petrographie, Haupt- und Spurenelementgeochemie, Geochronologie und der Isotopenzusammensetzung. Dies erlaubt es, die magmatische Entwicklung des Westafrikanischen Kratons in diesem Gebiet zu charakterisieren und die geologischen Rahmenbedingungen und Zielgesteine des Impaktes zu verstehen. Diese Studie legt durch die Ähnlichkeit der Zusammensetzung (stark Al-reiche Muskovitgranite und Granodiorite) und der Alter (zwischen 2092 ± 6 Ma und 2098 ± 6 Ma) aller granitischen Intrusionen nahe des Bosumtwi-Kraters eine kogenetische Entstehung nahe. Die Granitoide wurden vermutlich durch Tonalite-Trondjemite-Granodiorite (TTG)-Anatexis (oder davon abgeleiteter Gesteine) bei relativ niedrigem Druck und Temperatur gebildet. Darauf leitet sich ab, dass die Intrusionen des Bosumtwi-Gebietes genetisch verwandt mit dem Bansa-Granit östlich des Kraters sind und als Becken-Typ Granitoide im Spätstadium klassifiziert werden können. Auch ein mafischer Gang nordöstlich des Bosumtwi-Kraters scheint mit jenen felsischen Intrusionen genetisch verwandt zu sein. Basierend auf diesen Erkenntnissen wird eine Verbesserung der bisherigen geologischen Karte des Bosumtwi-Kraters vorgeschlagen.

Kapitel 4 präsentiert Ergebnisse der Untersuchung der räumlichen Beziehungen zwischen einer statistisch signifikanten Anzahl von Körnern (278) die, innerhalb eines bestimmten Bereiches eines einzelnen Dünnschliffs ($\sim 35 \text{ mm}^2$) des Bosumtwi Impaktkraters, planare Deformationstrukturen (PDFs) (409) zeigen. Vorherige Studien an PDFs basierten

entweder an einzelnen Körnern oder an einer zufällig gewählten Quarzkorn-"Population". Mit diesem Vorgehen war es nicht möglich, etwaige räumliche Beziehungen zwischen Quarzkörnern und ihren zugehörigen PDFs zu erfassen. Die aktuelle Studie zeigt, dass einige der beobachteten PDF-Muster und Anhäufungen (bestehend aus Quarzkörnern mit der gleichen PDF-Orientierung) den Eindruck eines heterogenen Schockfeldes vermitteln - ähnlich den Erkenntnissen einer kürzlich numerisch modellierten Studie. Weiters zeigt sich, dass die PDFs welche sich entlang unterschiedlicher Ebenen innerhalb des Kristallgitters bildeten, in ihren physischen Eigenschaften, Erscheinung und Lage im Korn unterscheiden. Die PDFs welche sich entlang der $\{10\bar{1}3\}$ Orientierung bilden sind sehr gut sichtbar, breit, und bedecken im Allgemeinen signifikante Bereiche des Korns. PDFs die sich entlang $\{10\bar{1}1\}$ and $\{11\bar{2}2\}$ orientieren sind sehr kurz, undeutlich und unter dem Universaldrehtisch kaum sichtbar. Dieser Unterschied wurde in früheren Untersuchungen nicht diskutiert. Möglicherweise deutet dies darauf hin, dass sich unterschiedliche PDF-Orientierungen auf etwas unterschiedliche Weise bilden. Zusätzlich wird ein neues web-basiertes Programm zur Indizierung von PDF-Sets vorgestellt.

Kapitel 5 diskutiert die Ergebnisse der Untersuchung der Bohrkerne LB-07A und LB-08A des Bosumtwi-Kraters, Ghana. In zwei Proben, von insgesamt 25, des Kerns LB-07A und in keiner der fünf Proben des Kerns LB-08A wurde ein ^{10}Be -Signal gefunden. Nach Ausschluss anderer Möglichkeiten scheint es am wahrscheinlichsten, dass der erhöhte ^{10}Be Gehalt in zwei Grauwackenklasten höchstwahrscheinlich darauf zurückzuführen ist, dass die Ausgangsgesteine dieser Klaster vor dem Einschlag in Oberflächennähe (20-25 m Tiefe) waren. Die Ergebnisse dieser Studie deuten auf eine gute Durchmischung der Krater-Brekzien während des terrestrischen Impaktprozesses, während diese Durchmischung bei submarinen Kratern weniger ausgeprägt ist. Weiterhin weist das Fehlen eines ^{10}Be -Signals in den Gesteinen direkt an der Seesediment-Impaktit-Grenze auf eingeschränkte meteorische Wasserinfiltration innerhalb des Kraterbodens hin. Das könnte bedeuten, dass die meteorische Wasserinfiltration innerhalb eines Kraters nicht durch oberirdische Porenraum-Infiltration, sondern eher durch ein lokales Bruchsystem stattfindet.

TABLE OF CONTENTS

DEDICATION.....	III
PREFACE.....	V
ACKNOWLEDGMENTS	VII
ABSTRACT.....	XI
ZUSAMMENFASSUNG:.....	XIII
TABLE OF CONTENTS.....	XV
1. Introduction to impact cratering.....	1
1.1. History of the impact cratering studies	1
1.2. Economical importance of impact craters.....	4
1.3. Impact cratering process	7
1.3.1. Contact and compression stage.....	8
1.3.2. Excavation stage	8
1.3.3. Modification stage	10
1.4. Crater morphology.....	10
1.4.1. Simple craters	11
1.4.2. Complex craters	12
1.4.3. Multiring basins	13
1.5. Terrestrial impact craters.....	15
1.5.1. Spatial distribution of terrestrial impact craters	16
1.5.2. Temporal distribution of terrestrial impact craters	17
1.6. Recognizing impact craters	17
1.6.1. Preserved meteorite fragments	18

1.6.2. Chemical and isotopic signatures from the projectile	19
1.6.3. Presence of shatter cones.....	20
1.6.4. High-pressure (diaplectic) mineral glasses	22
1.6.5. High-pressure mineral phases	23
1.6.6. High-temperature glasses and melts.....	23
1.6.7. Planar deformation features (PDFs) and planar fractures (PFs) in quartz	24
1.7. Bosumtwi impact crater	25
References:	29
2. Theoretical fundamentals of methods used in this study.....	41
2.1. Optical microscope.....	41
2.1.1. Universal stage (U-stage).....	41
2.1.2. Numerical program for automatic indexing of planar deformation features	42
2.2. Scanning Electron Microscopy (SEM).....	43
2.3. X-ray Fluorescence (XRF) spectrometry	45
2.4. Instrumental Neutron Activation Analysis (INAA)	47
2.5. Mass spectrometry (MS)	50
2.5.1. Accelerator Mass Spectrometry (AMS).....	52
References:	55
3. Petrology, major and trace element geochemistry, geochronology, and isotopic composition of granitic intrusions from the vicinity of the Bosumtwi impact crater, Ghana...	59
Abstract	59
3.1. Introduction.....	60
3.2. Geological Background	61
3.2.1. Intrusive bodies: granitoids.....	63

3.2.2. Intrusive bodies: mafic intrusions	69
3.3. Samples and methods.....	71
3.3.1. Samples	71
3.3.2. Methods	71
3.4. Results.....	75
3.4.1. Petrography.....	75
3.4.2. Geochemistry	76
3.4.3. Isotopic data.....	81
3.4.4. Geochronology.....	83
3.5. Discussion	85
3.5.1. Classification of the intrusions in the proximity of the Bosumtwi crater	85
3.5.2. Tectonic setting and petrogenesis of the granites in the proximity of the Bosumtwi crater.....	86
3.5.3. TTG affinity of Bosumtwi intrusions.....	89
3.5.4. Emplacement of the granitoids and interaction with older rocks ..	91
3.5.5. Proposed changes to the map of the Bosumtwi crater area	91
3.6. Conclusions.....	92
Acknowledgments	92
References	93
Supplementary material.....	103
4. Spatial characterization of planar deformation features in quartz and implications for understanding shock wave propagation at the grain scale	113
Abstract.....	113
4.1. Introduction.....	114
4.2. Methods.....	116

4.2.1. Sample investigated	116
4.2.2. Methods used	117
4.2.3. Development of a web-based program for indexing PDFs.....	118
4.3. Results.....	126
4.4. Discussion	130
4.4.1. Sample characterization and comparison of results with previous data	130
4.4.2. Heterogeneous distribution of PDFs in quartz grains from the studied sample	132
4.4.3. Non-random distribution of different PDF types/orientations.....	139
4.4.4. Determination of the average shock pressure in quartz bearing impactites	142
4.5. Conclusions.....	144
Acknowledgments:	146
References	147
5. ¹⁰ Be content in clasts from fallout suevitic breccia in drill cores from the Bosumtwi impact crater, Ghana: Clues to pre-impact target distribution.....	153
Abstract	153
5.1. Introduction.....	154
5.2. Geologic background.....	156
5.3. Samples.....	158
5.4. Methods.....	161
5.4.1. Accelerator mass spectrometry.....	161
5.5. Results.....	165
5.6. Discussion	169
5.6.1. Possible explanations of the obtained data.....	169

5.6.2. Inferences for crater-forming mechanism.....	174
5.7. Conclusions.....	176
Acknowledgments:	177
References	178
RECAPITULATION.....	185
APPENDIX.....	187
CURRICULUM VITAE	199
PUBLICATIONS AND PRESENTATIONS.....	203

1. Introduction to impact cratering

The impact cratering process is one of the most important geologic processes in the Solar System (French 1998). It played a crucial role in the formation of planetary bodies (e.g., Cohen et al. 2000, Gomes et al. 2005), it modified the biological history of the Earth (e.g., Smit and Hertogen 1980), and is still changing properties of the planetary surfaces: on Mars (Malin et al. 2006), on Moon (e.g., Bouley et al. 2012), on Earth (e.g., Kenkmann et al. 2009), and many other bodies in the Solar System. Because of that, only through understanding the impact cratering process, it is possible to comprehend the evolution and current state of Earth and all other planetary bodies within our solar system and outside of it.

1.1. History of the impact cratering studies

Studies on impact cratering are a young branch of geology. Only at the end of the XVIII century scientists started to accept the idea that rocks can fall from the sky (e.g., Marvin 2007). From this time on, multiple witnessed falls (including similar ones to the recent event in Chelabinsk) along with chemical and petrological descriptions of meteorite properties assured researchers that pieces of extraterrestrial material occasionally strike the Earth's surface. However, for a very long time the scientific community was not concerned with the question of what would happen if a body hitting our planet was larger than few meters in diameter.

Very few people in the past dared to explain existence of some of the craters by an impact of an extraterrestrial body. One of them was Daniel M. Barringer, who after hearing about a crater associated with large quantities of iron meteorites was so sure that this structure was formed by an impact of a large iron body that he bought the mining rights of this entire area (Kring 2007). He planned to locate and mine the iron impactor that he thought was buried below the crater's floor (Figure 1.1). He and his team provided a detailed description of the crater and its surroundings including

the ejecta blanket, made several deep drill cores and provided a quite accurate explanation of the observed phenomena (e.g., Barringer 1910, 1914). However, because of his lack of proper understanding of the true physics of the impact cratering process, Barringer was mistaken about his most important claim about the large iron body being located just below the crater floor. As a result, his theory of the extraterrestrial origin of the crater was ridiculed and his mining company went bankrupt.

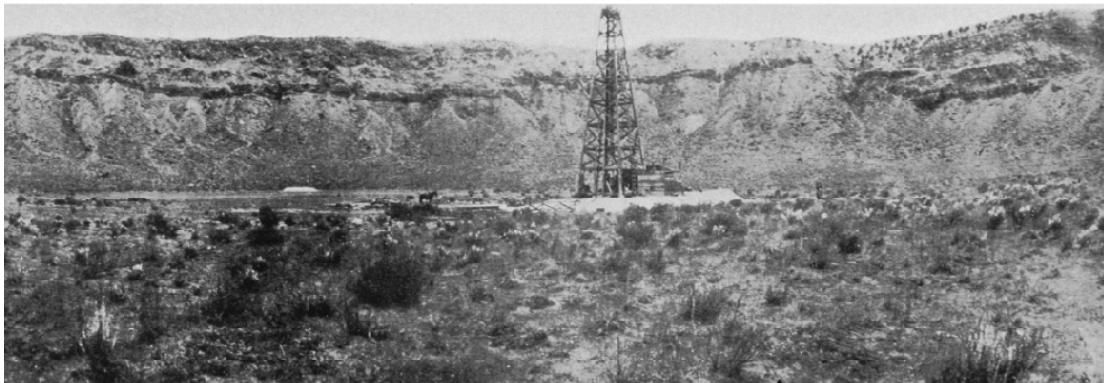


Figure 1.1 Barringer's drilling system at the floor of the crater (source: Figure 1.3 from Kring 2007).

The perception of the scientific community of the idea that some craters had been formed by an impact of an extraterrestrial body started to change in the 1960's because of the work of E.M. Shoemaker (1963). He managed to develop an analytical model of the hypervelocity impacts as a result of his comparative work on craters excavated by nuclear explosions. The discovery of quartz shock-metamorphosed to high-pressure phases such as coesite and stishovite (Chao et al. 1960, 1962) allowed his team to definitively demonstrate the extraterrestrial origin of the Barringer's crater and the Ries crater (Shoemaker and Chao 1961). From this moment the search for impact craters on Earth and other planetary bodies started.

Despite the work of Gene Shoemaker and Edward Chao, for a long time impact cratering has not been widely accepted by the scientific community as a major geological process (e.g., Grieve 1991). Impact cratering studies were slowly getting more recognition as more data about the other planetary bodies became available, but for a long time it was considered relevant only to the extraterrestrial bodies or

deep past of the Earth history. This opinion has been challenged by the discovery that a gigantic impact was responsible for the major biotic turnover at the Cretaceous-Paleogene boundary ~65.5 million years ago, abruptly ending the age of dinosaurs (e.g., Alvarez et al. 1980, Smit and Hertogen 1980, Hildebrand et al. 1991). Studies on this topic clearly showed that formation of impact craters is relevant to understanding our own planet and the development of life on Earth (Schulte et al. 2010).

Finally, impact cratering has been recognized as an important recent planetary process when the Shoemaker-Levy 9 comet collided with the surface of Jupiter in July 1994 (Figure 1.2). This was the first observed collision of two solar system bodies and showed very clearly that the formation of craters is still a geologically active process.

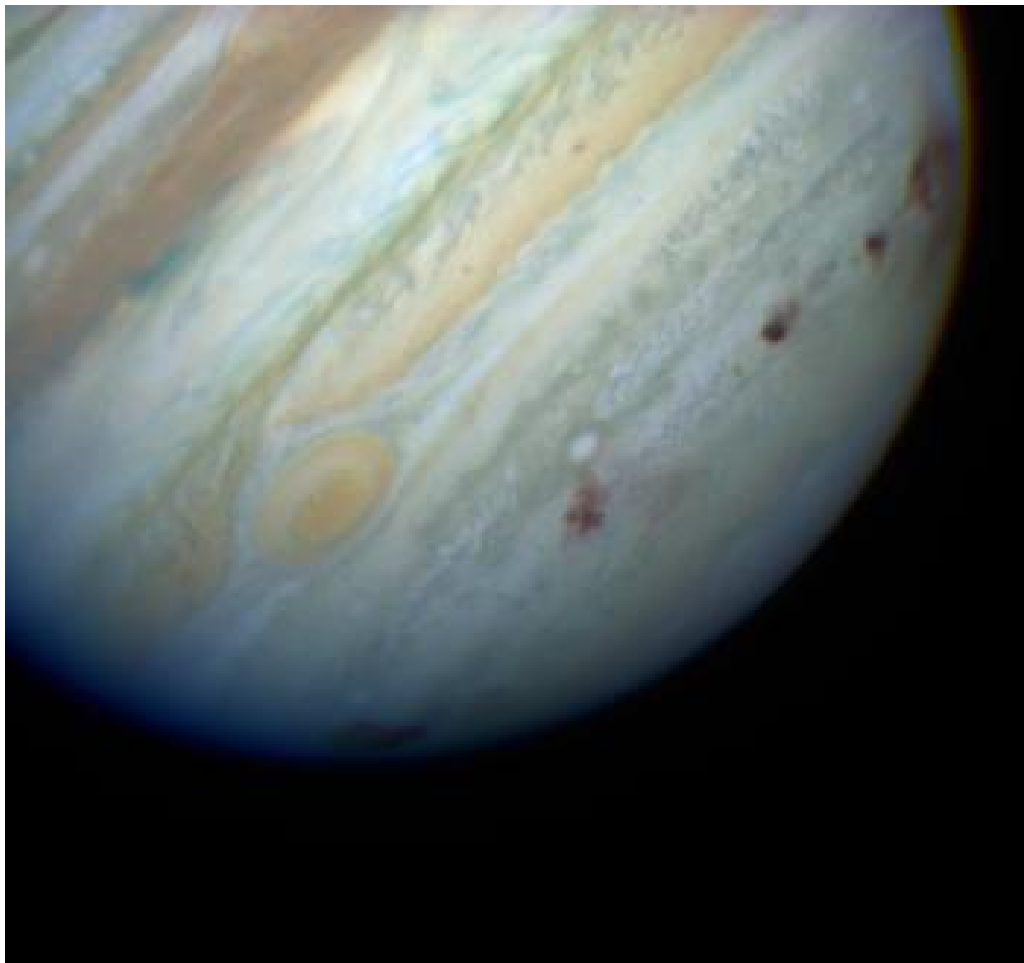


Figure 1.2. Comet Shoemaker-Levy 9 impacting Jupiter (source: NASA).

1.2. Economical importance of impact craters

A large fraction (about 25%) of known terrestrial impact structures are associated with economically relevant natural resources, although only about 12% of them are currently being exploited (e.g., Grieve and Masaitis 1994, Mory et al. 2000, Reimold et al. 2005). Resources can be divided based on their type (e.g., building stones, hydrocarbons, uranium or gold ores) or based on their origin: a) progenetic (deposits that existed within target rocks and were made available for exploitation by the impact), b) syngenetic (deposits formed directly by the impact), and c) epigenetic (deposits formed after the crater formation) (Grieve and Masaitis 1994).

The most common type of resource associated with impact structures is building stones. Impact cratering can be modified the properties of target rocks making them more accessible, useful, or beautiful. The impact origin of the Ries crater in Germany was discovered because the suevite breccia developed during this impact was used as a building stone for the Saint Georg Church's 90 m steeple located in the town of Nördlingen (Shoemaker and Chao 1961). Similarly, the Kentland crater (Figure 1.3) (USA) was discovered thanks to a quarry of industrial limestone exploiting rocks uplifted and deformed during the impact crater formation (e.g., Bjornerud 1998).



Figure 1.3. The quarry of industrial limestone within the central uplift of the Kentland impact structure (USA).

Another type of resource commonly associated with impact structures is gas and petroleum (e.g., Donofrio 1997, Johnson and Campbell 1997). The impact process does not produce hydrocarbons, but it provides a convenient trap for oil and gas within strongly brecciated rocks below the crater floor. Some examples of impact craters associated with gas or petroleum include: Ames (Oklahoma, USA), Red Wing Creek (North Dakota, USA) (French 1998), Avak (USA), Obolon (Ukraine), Steen River (Alberta, USA) (e.g., Reimold et al. 2005). It is also worth noting that multiple other impact structures were discovered during prospecting for oil and gas e.g., Chicxulub (e.g., Hildebrand et al. 1991), BP structure (Koeberl 1994) or Silverpit (probable impact site, e.g., Stewart and Allen 2005).

The impact cratering process can produce diamonds through shock metamorphism of graphite- or coal-bearing target rocks (e.g., Gilmour 1998). In fact, a large number of impact structures and even meteorites include some amount of impact diamonds (e.g., Gilmour 1998, Montanari and Koeberl 2000) but in most cases they are too small and dispersed to be used commercially. However, in the last

year there was news (<http://phys.org/>) about plans to start mining the Popigai crater (Russia) (e.g., Koeberl et al. 1997a, Masaitis 1998) as a source of technical-grade diamonds.

The largest impact crater on Earth, the Vredefort impact structure, is associated with the world's most abundant gold deposit accompanied by uranium ore (Reimold et al. 2005). It is mostly a progenetic deposit: the gold is detrital in origin but it was preserved because it was shielded from erosion due to the impact-induced deformation, although some remobilization of the gold by hydrothermal processes has also taken place (e.g., Reimold et al. 2005).

The most widely known syngenetic ore is the Ni-Cu-PGE deposit of the Sudbury structure (Canada) which was formed from a large differentiating impact melt sheet (e.g., Lightfoot et al. 1997). The metals now present in the ore come from a large volume of terrestrial target rocks melted during the impact, with only a very small addition of the material from the impactor (Reimold et al. 2005).

Lakes are commonly developed within impact craters and because of that they can serve as a convenient source of water or fishing reservoir (e.g., the Bosumtwi impact crater). In recent years impact craters have been also increasingly used in the tourist industry. Several craters have been made available to the public and are popular tourist attractions; e.g., the Barringer Crater (USA), the Ries and the Steinheim impact structures (Germany) and the Tswaing crater (South Africa). Also the Bosumtwi impact crater, a 10-km-diameter crater located near Kumasi, the second-largest city in Ghana, is one of the main attractions for ecotourism in the region (Boamah and Koeberl 2007). Additionally, meteorites, impact glasses, and tektites have been used as jewelry (Reimold et al. 2005). And finally, impact craters have been sometimes considered as sacred places, bearing significant symbolical value to many groups of people (e.g., Hamacher and Norris 2009: Figure 1.4).



Figure 1.4. Central uplift of the Gosses Bluff impact structure in Australia, which is considered a sacred place by Aborigines living in this area.

1.3. Impact cratering process

Impact craters are formed by the collision of cosmic bodies moving with hypervelocity speeds (French 1998). In case of Earth, most objects smaller than a few tens of meters in diameter either disintegrate in the atmosphere or are significantly decelerated during their passage. They hit the ground with relatively low velocities of a few hundred meters per second and form penetration funnels instead of true impact craters (French 1998). However, if the Earth's surface is impacted with a velocity much greater than the speed of sound in the target rock, a shock wave (almost discontinuous change in characteristics of the medium) is generated and an impact crater is formed. The formation of the impact crater can be divided into three stages: 1) contact and compression, 2) excavation and 3) modification (Melosh 1989: Figure 1.5).

1.3.1. Contact and compression stage

The contact and compression stage begins when the projectile touches the target. Almost instantly the projectile is stopped – it can penetrate a distance of not more than 1-2 times its diameter into the target rocks. The kinetic energy of the impacting body is transferred into the target and, as a result, shock waves are generated (Melosh 1989). The shock waves move radially out of the point of contact into the target rock and into the projectile with the initial velocity exceeding 10 km/s. The waves traveling through target rocks lose energy rapidly during their passage and eventually transform into the regular seismic waves. As a result, the further it is from the point of impact, the lower the maximal shock pressure (French 1998).

The shock wave moving through the impactor has a finite distance to cover and when it reaches the end of the projectile the rarefaction (release) wave is produced. The passage of this wave unloads the shock-induced pressures, which leads to almost complete melting and vaporization of the projectile (Melosh 1989).

The end of the contact and compression stage is marked by the entry of the release wave into the target rocks. The duration of the contact and compression stage is determined by the size of the projectile and takes no more than few seconds (French 1998).

1.3.2. Excavation stage

During the excavation stage the release wave is traveling through the target rocks that have been previously compressed by the shock wave (Figure 1.5). Since waves can travel quicker in the more dense media, the release wave eventually takes over the shocks wave. The complex interaction between those two waves leads to excavation of the transient crater (French 1998). The excavation begins when tensional stress exceeds the mechanical strength of the target rocks causing them to be fractured and displaced (Melosh 1989). Some of the rocks are ejected

from the transient cavity; other are dispersed, but do not leave the nearly formed crater.

The transient crater is usually 10-20 times larger than the impactor, and its formation ceases when the expanding shock and release waves are not strong enough to displace the target material (French 1989). The excavation stage in case of a small ~1 km in diameter crater takes ~6 seconds, while formation of the transient cavity for a 200 km crater requires as much as ~90 seconds (Melosh 1989).

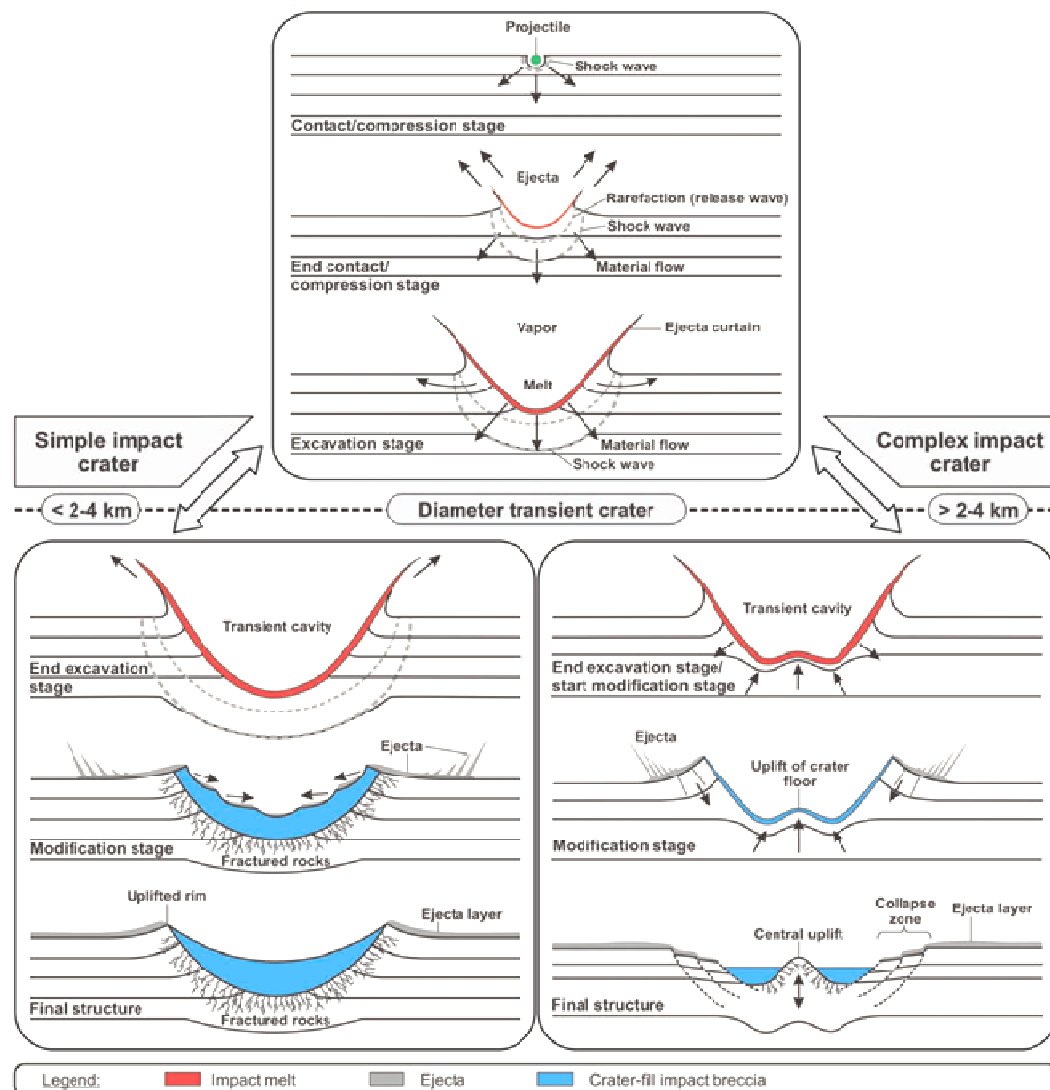


Figure 1.5. A series of diagrams showing development of the simple (left) and the complex (right) impact structure. At first, an impactor contacts target rocks what generates the shock wave (contact/compression stage). Interaction of the shock wave with the target rocks cause the material to move out from the point of impact forming the transient cavity (excavation stage). The final crater form is influenced by extensive mass movements (modification stage). (source: Figure1-4 from Ferriere (2008) based on French (1998)).

1.3.3. Modification stage

The modification stage starts after the transient cavity has reached its final size and shock waves have decayed to normal elastic waves (Figure 1.5). At this stage, conventional geological factors (such as gravity and rock mechanics) influence the final form of the structure (French 1998). As a result, the transient cavity formed by the shock wave interaction with target rocks is modified to form a final crater. Different resulting morphologies of final craters are discussed in the section 1.4.

1.4. Crater morphology

Crater morphology mostly depends on the a) size of the impactor; b) gravitational force of the target body; c) properties of the target rocks; d) angle of the impact (Melosh 1989).

Generally, with increasing size of the impactor, the shape of the crater changes from a simple crater (a bowl-shaped depression with slightly risen rims and overturned rim; Figure 1.6, Figure 1.7) through a complex crater (a relatively flat-floored depression with a hill in the center; Figure 1.8) up to multi ring basins (a set of concentric rings of hills or mountains; Figure 1.9) (French 1998). The transition between morphological types of craters depends strongly on the gravity (Melosh 1989). For example, on Earth the transition between simple and complex crater form takes place at final crater diameters between 2 and 4 km (e.g., Grieve 1987), while on the much smaller Moon, craters as large as 15-20 km can have a simple, bowl-shaped form (e.g., Howard 1974).

The transition between simple and complex craters also depends on the properties of target rocks (Melosh 1989). For Earth's sedimentary rocks this transition occurs around diameter of 2 km, while craters developed in crystalline target rocks start to show properties of complex craters only when they reach a size of about 4 km in diameter (Grieve 1987).

The shape and properties of the crater depend also on the angle of the impact (e.g., Melosh 1989, Collins et al. 2009, Elbeshausen and Wünnemann 2013). Numerical modeling shows that only impacts at $\leq 12^\circ$ form elliptical craters (Bottke et al. 2000). The vast majority of impact craters present on planetary surfaces are circular, and only about 5% of them are elliptical to some extent.

1.4.1. Simple craters

Simple craters are bowl-shaped depressions formed by the collision with an extraterrestrial body (Figure 1.6). Their rims are elevated (about 4% of the crater diameter; Melosh 1989), and debris located on the edge of the crater, form a characteristically overturned sequence of target rocks (Kring 2007). Simple craters are relatively small; their diameter is up to 2-4 km on Earth (e.g., Grieve 1987). For fresh craters the crater depth (measured from the crater rim to the floor) is about 33% of the crater diameter. The crater is filled by “crater-fill breccia” (e.g., French 1998) that usually does not include much melt (e.g., Grieve and Cintala 1992, Barr and Citron 2011).



Figure 1.6. An example of a simple crater: Tswaing crater (1.13 km in diameter, ~220 ka), Republic of South Africa (e.g., Reimold et al. 1992).



Figure 1.7. The overturned rim sequence at the Barringer (aka Meteor) Crater (source: Kring 2007).

1.4.2. Complex craters

Complex craters are shallower (in reference to their diameter) than simple craters and in their center there is a distinct positive morphological feature called the “central uplift” (French 1998). The central uplift is composed of rocks risen from the depth of about one-tenth of the crater diameter (e.g., Melosh 1989, French 1998). The rim of the complex crater is usually flat or slightly inclined towards the center due to extensive faulting and slumping that occurs during the final stage of crater formation (e.g., French 1998). Crater-filling breccias in complex craters have a more significant amount of impact melt present than in the case of simple craters (e.g., Grieve and Cintala 1992, Barr and Citron 2011). The relict of the central uplift is often the only visible structure left after an old and deeply eroded terrestrial impact structure such as Kentland (USA, Bjornerud 1998; Figure 1.3) or Gosses Bluff (Dietz 1967; Figure 1.8).

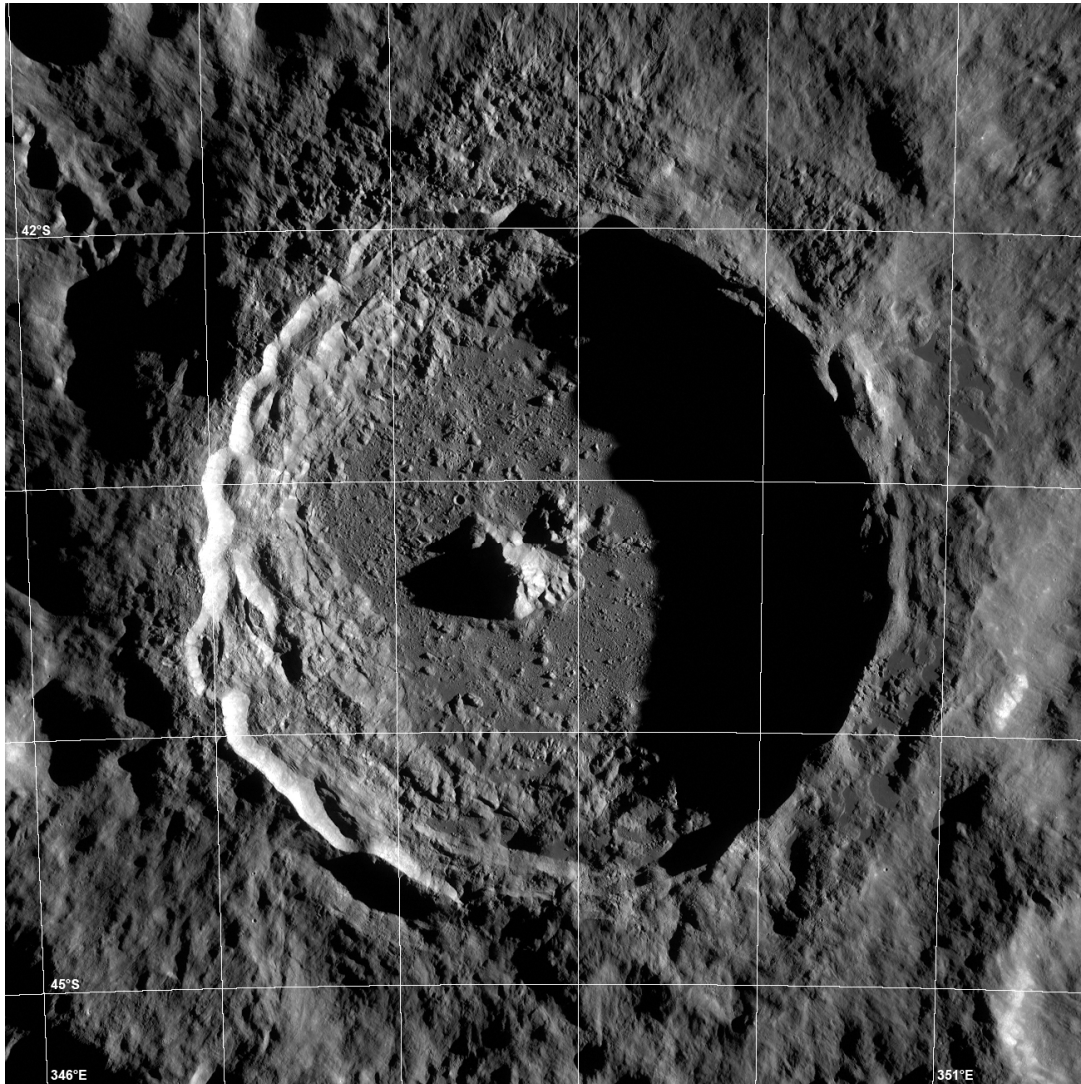


Figure 1.8. An example of a complex impact crater: Tycho crater (86 km in diameter, Moon). Large landslides, formed during the modification stage are visible inside the crater (source: NASA).

1.4.3. Multiring basins

Multiring basins are the largest known type of impact structures (Figure 1.9). They look like a set of concentric rings of hills or mountains and intervening valleys (French 1998). On Earth those features can be produced only by a projectile that is many tens of kilometers in diameter, which are very scarce in the modern Solar System. Many of the known lunar multiring basins were formed before or during the Late Heavy Bombardment period ~ 3.9 Ga (Cohen et al. 2000).

On Earth the transition between complex craters and multiring basins occurs at ~100 km in diameter. Only a few craters of that size are known, and many of those are deeply eroded structures, which limits the possibility of clearly establishing their multiring character (French 1998). However, it is very probable that the following terrestrial structures have some characteristics of multiring basins: Manicouagan (Canada, 100 km), Popigai (Russia, 100 km), Vredefort (South Africa, ca. 300 km), Sudbury (Canada, ca. 250 km), and Chicxulub (Mexico, >180 km) (French 1998).



Figure 1.9. Mare Orientale, a multiring impact basin on the Moon (diameter 930 km). (source: Lunar Orbiter image LO-IV- 4187, LPI).

1.5. Terrestrial impact craters

Up to now, the impact origin of 184 structures has been confirmed (<http://www.passc.net/EarthImpactDatabase/>). The largest three known impact craters are: Vredefort, Chicxulub, and Sudbury and their transient cavities were hundreds of km in diameter (160, 150, and 130 km, respectively). Those largest impact structures are also among the oldest ones, e.g., Vredefort is ~2023 Ma (Kamo et al. 1997). The smallest craters can be only a few tens of meters in diameter, and be as young as only a few years: e.g., the Carancas crater is only 13.5 m in diameter and was formed on 15th September 2007 (Figure 1.10).



Figure 1.10. The Carancas impact crater formed on the 15th of September 2007 is the youngest (formed on the 15th of September 2007) and smallest (13 meters in diameter) known impact structure on Earth (source: <http://www.meteoriteguy.com>).

1.5.1. Spatial distribution of terrestrial impact craters

Identified impact craters are distributed non-randomly on the Earth surface (Figure 1.11), despite the fact that the flux of the impacting bodies was random (Melosh 1989). This is caused by three main factors:



Figure 1.11. Geographic distribution of known terrestrial impact structures. Some of the impact craters mentioned in this chapter are marked on the map. (based on information from <http://www.passc.net/EarthImpactDatabase/index.html>)

1. More impact craters are located on the geologically old areas such as Australian Shield, Scandinavian Shield and Canadian Shield. This is because impact craters located in those areas could be accumulated and preserved over a long period of time (French 1998). Because of that, geologically young areas such as southern Europe tend to have only a few, generally small impact craters present.
2. More craters are being found in areas devoid of dense plant or sediment cover, which is most visible when comparing the distribution of impact craters in Africa. There are multiple known structures of this kind located within desert zones and very few within areas of tropical forest. This factor is especially important with reference to small (only tens of meters in diameter) impact craters.

3. The number of craters per unit area directly correlates with the number of qualified researchers looking for them per unit of this area. There are numerous impact craters known from Canada or Australia where scientists such as Beals et al. (1963) and Shoemaker and Shoemaker (1996) were actively searching for them. In the same time, countries that were not opened to research by the international community (e.g., China), or were dangerous enough to limit scientific exploration (e.g., numerous African countries) have had a very low number of impact craters discovered.

1.5.2. Temporal distribution of terrestrial impact craters

The temporal distribution has been biased by post-impact geological processes (e.g., French 1998). The temporal distribution of terrestrial impact craters is strongly biased towards younger craters, because of the influence of erosion, plate tectonics and other exogenic and endogenic processes removing impact features from the Earth surface. Further bias in cratering statistics is introduced by the fact that smaller craters tend to be removed from the surface of the Earth much more quickly than larger ones. As a result, old features (<200 Ma) and small structures (<5 km) are strongly under-represented in the database of known impact craters (French 1998).

1.6. Recognizing impact craters

Impact cratering studies crucially depend on the ability to unambiguously identify meteorite impact craters and distinguish them from other geological structures (e.g., French and Koeberl 2010). It is important because many other geological processes can produce features that are morphologically similar to meteorite impact structures such as: circular form, brecciation, or gravity and

magnetic anomalies (French 1998). The only factors that can unequivocally identify an impact crater is: 1) the existence of clear indications of the passage of the shock wave generated by the impact of the projectile; 2) preserved meteorite fragments; 3) or chemical and isotopic projectile signatures (French 1998, Langenhorst 2002, French and Koeberl 2010).

1.6.1. Preserved meteorite fragments.

Preserved meteorite fragments associated with a crater have been used to confirm the impact origin especially in the case of relatively small and young impact craters, such as Whitecourt (Alberta Canada: Herd et al. 2008), Morasko (Poland: Stankowski 2001, Figure 1.12) or Barringer (Arizona, USA).. However, usually the impactor almost fully disintegrates as a result of the collision, especially in the case of impact craters larger than a few km in diameter (Melosh 1989). Also, meteorites tend to be extremely susceptible to weathering and usually can be recognized as extraterrestrial objects up to a few tens to hundreds of thousands of years after the impact in the case of iron meteorites, but much shorter for other types of impactors (French and Koeberl 2010). It is also important to remember that in some cases the spatial and even temporal association of a meteorite with a bowl-shaped depression can potentially be only coincidental, e.g., as in case of the Aouelloul crater in Mauritania (Fudali et al. 1978).



Figure 1.12. The largest discovered piece of impactor that formed the Morasko craters.
(source: <http://www.artmet-meteoryty.pl/>)

1.6.2. Chemical and isotopic signatures from the projectile

Finding fragments of preserved meteorites around a crater is very rare; however, identifying a meteorite component within rocks directly affected by the impact is much more common (French and Koeberl 2010). During a meteorite impact most of the bolide is usually almost fully vaporized or melted and mixed with the

target rocks (Melosh 1989). As a result, the meteoritic component even in the most affected rocks is usually below 1 wt. % (Koeberl 2007). The detection of the meteoric component is based on: 1) elements highly enriched in meteorites relative to the terrestrial crustal rocks e.g., Ni, Co, Cr, Au, and the platinum group elements: Ru, Rh, Pd, Os, Ir, and Pt (Alvarez et al. 1980, Palme et al. 1981, Koeberl 1998); 2) isotopic ratios of Os and Cr (Koeberl et al. 2002; Lee et al. 2006, Koeberl et al. 2007). In some cases it was possible to identify the type of impactor using chemical and isotopic characteristics of the detected meteoritic component (see review by Koeberl 2007). When using this kind of tracers, it is important to always perform the analysis with reference to the local target rocks to precisely establish background levels (French and Koeberl 2010).

1.6.3. Presence of shatter cones

Shatter cones are sets of striated conical fractures (full or partial cones) penetrating rocks in which they form. Shatter cones develop at relatively low shock pressures of 2-10 GPa, rarely up to 30 GPa (Dietz 1967, Milton 1977, French 1998, Baratoux and Melosh 2003, Figure 1.3-1.15). They are thought to form in a very early stage of the shock wave passage because in some cases, small pieces of shatter cones can be observed within allochthonous breccias (French and Koeberl 2010). The exact process of shatter cone formation is still not clear, although several different mechanisms have been proposed (e.g., Johnson and Talbot 1964, Gash 1971, Baratoux and Melosh 2003).



Figure 1.13. Shatter cones in the Vredefort impact structure (Republic of South Africa), developed in a fine-grained sedimentary rock.



Figure 1.14. A shatter cone at the Vredefort impact crater (Republic of South Africa), developed in a coarse-grained granitic rock.



Figure 1.15. Shatter cones in the Gooses Bluff impact structure (Australia).

Shatter cones are the only diagnostic criterion allowing for unequivocal identification of impact craters that is visible with the naked eye. However, these features can sometimes be misidentified (French and Koeberl 2010) as 1) slickensides (but those tend to be parallel instead of divergent), 2) some sedimentary features, such as cone-in-cone structures (but those are restricted to one lithology and have less well-developed striations), 3) wind abrasion surfaces (but those are not penetrative).

1.6.4. High-pressure (diaplectic) mineral glasses

Diaplectic glass is an amorphous phase formed from tectosilicate minerals (most commonly quartz or feldspar) without melting, due to the influence of shock pressure above 30-50 GPa (Stöffler 1972; Stöffler and Langenhorst, 1994; French 1998; French and Koeberl 2010). The characteristic feature of diaplectic glass is that despite being fully amorphous, grain's pre-shock morphology and texture are preserved, and flow structures or vesicles are absent. Diaplectic glass may appear

similar to normal types of glasses. The proper identification of diaplectic glass is a complex task (French and Koeberl 2010).

1.6.5. High-pressure mineral phases

High shock pressure caused by a meteorite impact can convert one mineral into others that are normally stable only under very high static pressures (French and Koeberl 2010). The most typical high-pressure mineral used to identify terrestrial impact craters are: coesite and stishovite converted from quartz (e.g., Chao et al. 1960, Shoemaker and Chao 1961, Chao et al. 1962), diamonds derived from graphite (Hough et al. 1995, Masaitis 1998, Gilmour et al. 2003), reidite converted from zircon (Glass et al. 2002, Wittmann et al. 2006), and TiO₂ high pressure polymorph derived from rutile or anatase (Jackson et al. 2006).

Some of these high pressure minerals (coesite and nanodiamonds) can also be found in rocks not affected by the shock metamorphism, but only at great depths within Earth. Because of that, when using high pressure polymorphs as an impact indicator it is necessary to consider the geological context and use a large variety of techniques (such as X-ray diffraction, TEM, Raman spectroscopy, or nuclear magnetic resonance) to unequivocally confirm the identity of those minerals (French and Koeberl 2010).

1.6.6. High-temperature glasses and melts

High temperature glasses are produced during the impact cratering process in regions that experienced high shock levels (>50 GPa) where the temperature after shock reloading can exceed 1500°C (French and Koeberl 2010). The high-temperature melts can be differentiated from other melts by: 1) occurrence of lechatelierite indicative of temperatures $\geq 1750^{\circ}\text{C}$ (Engelhardt and Stöffler 1968, Stöffler 1984); 2) decomposition of zircon to baddeleyite occurring at 1850°C (Wittmann et al. 2006), as well as 3) melting of titanite at 1450°C (French 1968).

Similar high temperature glasses can also be produced by the lightning strikes; however, fulgurites are easily distinguishable in a hand sample (Essene and Fisher 1986).

1.6.7. Planar deformation features (PDFs) and planar fractures (PFs) in quartz

Planar deformation features (PDFs) are commonly used as one of the most important diagnostic features that allow for the unambiguous identification of a meteorite impact structure (e.g., Engelhardt and Stöffler 1968, Chao 1967, Stöffler and Langenhorst 1994, Ferrière et al. 2010). PDFs are straight, parallel sets of planes of (amorphous) material that form along specific crystallographic planes in minerals and that are less than 2 μm wide and spaced 2-10 μm apart (e.g., Stöffler and Langenhorst 1994, Grieve et al. 1996, Figure 1.16). Planar fractures (PFs) are straight, parallel sets that are thin (3-10 μm), spaced >20 μm from apart, open cracks developed in different minerals due to shock wave passage (e.g., French 1998). PDFs and PFs are present in minerals (e.g., zircon: Wittmann et al. 2006), but quartz is the most commonly used mineral to confirm an impact origin of a studied structure (e.g., French 1998, French and Koeberl 2010). PDFs and PFs were reproduced during laboratory experiments, but the details of the process of their formation is still not fully understood (e.g., Langenhorst and Deutsch 1994, Meyer et al. 2011).

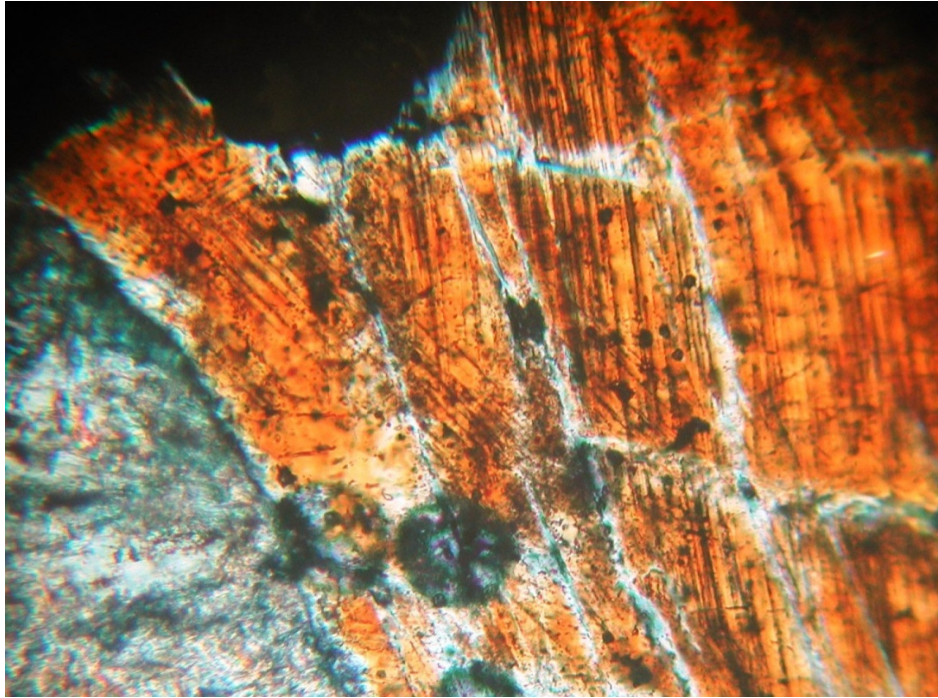


Figure 1.16. Photomicrograph of the planar deformation features in quartz grains from the Manson impact crater (USA). Two cross-cutting sets of PDFs are visible. The image (cross polarized light) is about 1 mm across.

Specific (combinations of) PDF orientations provide information on the peak shock pressure that is recorded by the rocks, within the range of ~5 to 35 GPa, depending on the lithologies (e.g., Hörz 1968, Grieve and Robertson 1976, Stöffler and Langenhorst 1994, Dressler et al. 1998, Ferrière et al. 2008, Holm et al. 2011). PFs are thought to form at lower pressures than PDFs, namely at <10 GPa (Stöffler and Langenhorst 1994) or even <5 GPa (Kieffer 1971).

1.7. Bosumtwi impact crater

All projects presented in this thesis are related to the Bosumtwi impact crater (centered at 06°30'N, 01°25'W). The Bosumtwi impact structure, located in Ghana, West Africa (Figure 1.17), is a well-preserved, 10.5 km wide crater and it is about 1.07 Ma old (e.g., Koeberl et al. 1997b, Koeberl et al. 2007). It is a complex crater; however, its central uplift is currently buried under the thick layer of lake deposits (Koeberl et al. 2007). Lake Bosumtwi is ~8 km in diameter and up to 80 m deep. This

relatively young impact structure is associated with one of only four tektite strewn fields known on Earth (e.g., Koeberl et al. 1997b). It was drilled in 2004 by the International Continental Scientific Drilling Program (ICDP) (Koeberl et al. 2007), and since then it has been an object of intensive research on various aspects of impact cratering process (e.g., Dai et al. 2005, Boamah et al. 2006, Karikari et al. 2007, Coney et al. 2007, 2010, Ferriere et al. 2007, 2008).

The Bosumtwi impact crater was excavated in rocks of the Early Proterozoic Birimian Supergroup of the West African craton (e.g., Jones et al. 1981) formed during the Paleoproterozoic (e.g., Boher et al. 1992, Taylor et al. 1992, Doumbia et al. 1998, de Kock et al. 2011). Its deposition started around 2200 Ma ago, in an arc-back-arc environment (Attoh et al. 2006, Dampare et al. 2008, de Kock et al. 2011), with or without involvement of subduction of the intra-oceanic plateau (Abouchami et al. 1990). The Birimian rocks were metamorphosed during the Eburnean tectono-thermal event at ~2092 Ma to greenschist and (locally) amphibolite facies. Average peak temperatures reached around 500 – 650°C and peak pressures of 500 – 600 MPa (Leube et al. 1990, Hirdes et al. 1992, Taylor et al. 1992, John et al. 1999, Debat et al. 2003, Galipp et al. 2003, Feybesse et al. 2006, Karikari et al. 2007).

The Birimian Supergroup can be divided into two contemporary units: 1) volcanic belts and 2) sedimentary basins aligned in multiple parallel structural features together with numerous, extensive granitoid intrusions (Figure 1.17). The sedimentary unit of the Birimian Supergroup consists of volcanoclastic rocks, argillites, and turbidites that are now metamorphosed to meta-greywackes, phyllites, schists and shales (Leube et al. 1990). The volcanic unit has a predominantly tholeiitic chemical composition and consists of metamorphosed basalts and andesites that at present occur as different types of schists, including hornblende-actinolite-, calcite-chlorite-, mica-schists, and in some cases amphibolites. The Birimian units are occasionally overlain by the Tarkwaian detrital shallow water sediments (Leube et al. 1990, Oberthür et al. 1998, Koeberl and Reimold 2005, Feybesse et al. 2006). Some areas of the Birimian Supergroup, including multiple regions within the Ashanti belt (e.g., Feybesse et al. 2006) have undergone

hydrothermal mineralization of gold between ~2063 Ma and ~2025 Ma (Oberthür et al. 1998, Pigois et al. 2003).

The meta-volcanic and meta-sedimentary rocks are intruded by larger granitic and smaller mafic bodies. The overall granitoid component in the proximity of the Bosumtwi crater is estimated to be about 2% (Reimold et al. 1998, Figure 1.18). Although generally unfoliated, some granites occasionally exhibit N-E foliation and are penetrated by aplite and quartz veins (Boamah and Koeberl 2003). Additionally, numerous, small dikes (<1 m wide) of biotite-bearing granites, with granophyric textures are frequently observed in the crater rim (Moon and Manson 1967, Jones 1985, Reimold et al. 1998). These dikes are intruded conformably into the foliations of bedding planes of the Birimian rocks (Boamah and Koeberl 2003). Small dikes were also found to have been emplaced below the crater (Coney et al. 2007, Ferriere et al. 2007). Some of the dikes near the Bosumtwi crater show strong alteration (Boamah and Koeberl 2003).

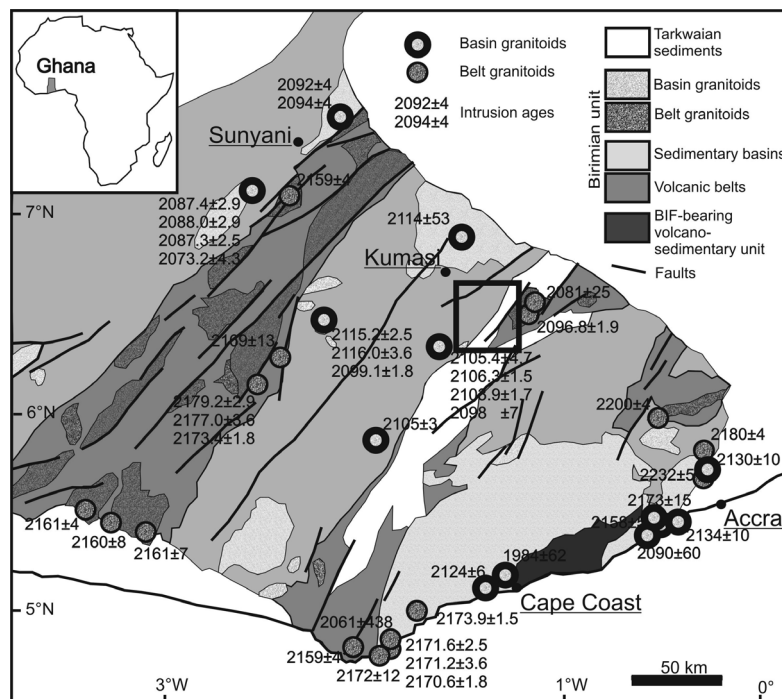


Figure 1.17. Geologic map of the fragment of the Birimian Supergroup with ages of the dated granitic intrusions (Oberthür et al. 1998, Hirdes et al. 1992, Leube et al. 1990, Grenholm et al. 2011, Attoh et al. 2006, Feybesse et al. 2006). The map is based on Feybesse et al. (2006); the division between belt- and basin-type granitoids is based on Hirdes et al. (1992). The location of the Bosumtwi impact structure area is indicated by a black rectangle.

Most of the mafic intrusions in the proximity of Bosumtwi crater are dikes of gabbroic or doleritic composition (Woodfield 1966, Moon and Mason 1967, Jones 1985). There is one small amphibolite body located north of the lake (e.g., Koeberl and Reimold 2005). The dikes are arranged in two directions: NNE-SSW (following the orientation of the Ashanti belt) and NWN-SES. The dikes from the second family are much longer than those from the first, and because they crosscut the Bansa granite, they have to be younger than the proposed date for Bansa granites of 2097 ± 2 Ma (Oberthür et al. 1998). The age of the first family of dikes is unknown.

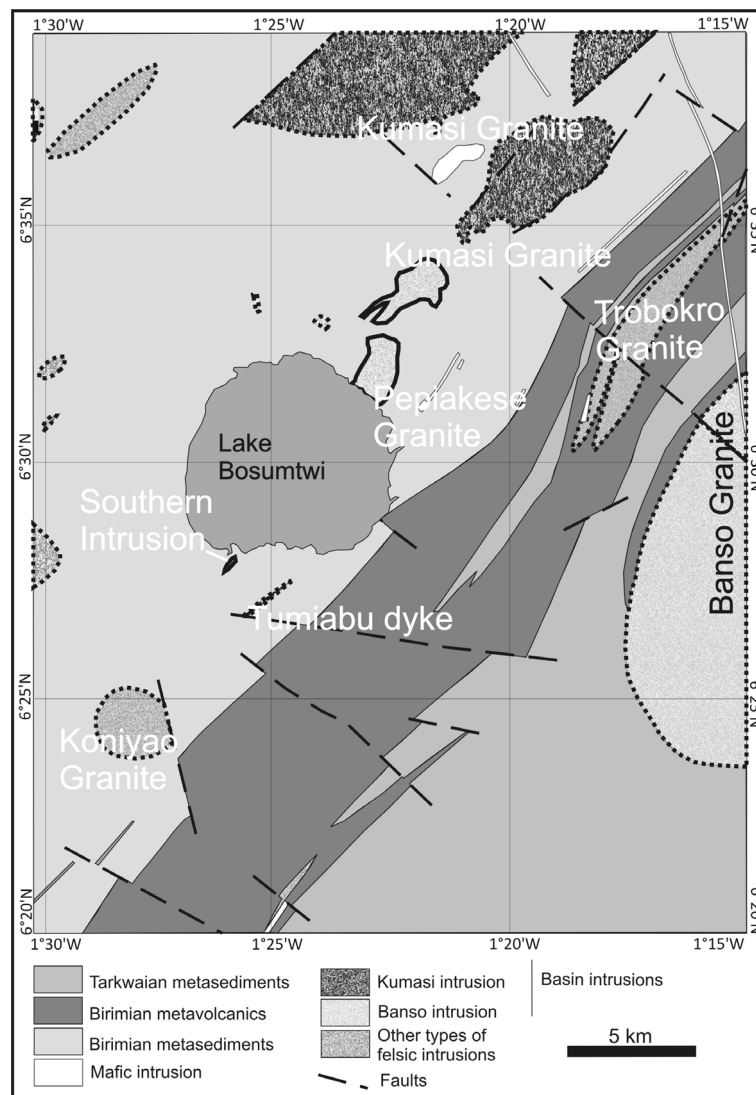


Figure 1.18. Geological map of the vicinity of the Bosumtwi crater (source: this study, modified after Koeberl and Reimold 2005).

References:

- Abouchami W., Boher M., Michard A., and Albarede F. 1990. A major 2.1 Ga event of mafic magmatism in West Africa: an early stage of crustal accretion. *Journal of Geophysical Research* 97: 17605–17629.
- Alvarez L. W., Alvarez W., Asaro F., and Michel H. V. 1980. Extraterrestrial cause for the Cretaceous-Tertiary extinction. *Science* 208: 1095–1108.
- Attoh K., Evans M. J., and Bickford M. E. 2006. Geochemistry of an ultramafic-rodingite rock association in the Paleoproterozoic Dixcove greenstone belt, southwestern Ghana. *Journal of African Earth Sciences* 45: 333–346.
- Baratoux D., and Melosh H. J. 2003. The formation of shatter cones by shock wave interference during impacting. *Earth and Planetary Science Letters* 216: 43–54.
- Barr A. C., and Citron R. I. 2011. Scaling of melt production in hypervelocity impacts from high-resolution numerical simulations. *Icarus* 211: 913–916.
- Barringer D.M. 1910. Meteor Crater (formerly called Coon Mountain or Coon Butte) in northerncentral Arizona. Paper presented at the National Academy of Sciences, Princeton University, Nov. 16, 1909. 24 p. (plus 18 plates, and 3 maps).
- Barringer D. M. 1914. Further notes on Meteor Crater, Arizona. *American Journal of Science* 39: 482-483.
- Beals C. S., Innes M. J. S., and Rottenberg J. A. 1963. Fossil meteorite craters. In *The Moon, Meteorites, and Comets*, edited by Middlehurst B. M. and Kuiper G. P. Chicago: University of Chicago. pp. 235–284.
- Bjornerud M. G. 1998. Superimposed deformation in seconds: Breccias from the impact structure at Kentland, Indiana (USA), *Tectonophysics* 290: 259-269.
- Boamah D., and Koeberl C. 2003. Geology and geochemistry of shallow drill cores from the Bosumtwi impact structure, Ghana. *Meteoritics and Planetary Science* 38: 1137–1159.

- Boamah D., and Koeberl C. 2006. Petrographic studies of “fallout” suevite from outside the Bosumtwi impact structure, Ghana: *Meteoritics and Planetary Science* 41: 1761–1774.
- Boamah D., and Koeberl C. 2007. The Lake Bosumtwi impact structure in Ghana: A brief environmental assessment and discussion of ecotourism potential. *Meteoritics and Planetary Science* 42: 561–567.
- Boher M., Abouchami W., Michard A., Albarede F., and Arndt N. T. 1992. Crustal growth in West Africa at 2.1 Ga. *Journal of Geophysical Research* 97: 345–369.
- Bouley S., Baratoux D., Vaubaillon J., Mocquet A., Le Feuvre M., Colas F., Benkhaldoun Z., Daassou A., Sabil M., and Lognonné P. 2012. Power and duration of impact flashes on the Moon: Implication for the cause of radiation. *Icarus* 218: 115–124.
- Bottke W. F., Love S. G., Tytell D., and Glotch T. 2000. Interpreting the elliptical crater populations on Mars, Venus, and the Moon. *Icarus* 145: 108–121.
- Chao E. C. T. 1967. Impact metamorphism. In *Researches in Geochemistry*, edited by Abelson P. H. New York: John Wiley and Sons. pp. 204–233.
- Chao E. C. T., Shoemaker E. M., and Madsen B. M. 1960. First natural occurrence of coesite. *Science* 132: 220–222.
- Chao E. C. T., Fahey J. J., Littler J., and Milton D. J. 1962. Stishovite, SiO₂, a very high pressure new mineral from Meteor Crater, Arizona. *Journal of Geophysical Research* 67: 419–421.
- Cohen B. A., Swindle T. D., and Kring D. A. 2000. "Support for the Lunar Cataclysm Hypothesis from Lunar Meteorite Impact Melt Ages". *Science* 290: 1754–1755.
- Collins G. S., Davison T., Elbeshausen D., and Wünnemann K. 2009. Numerical simulations of oblique impacts: the effect of impact angle and target strength on crater shape (abstract #1620). *40th Lunar and Planetary Science Conference*. CD-ROM.
- Coney L., Gibson R. L., Reimold W. U., and Koeberl C. 2007. Lithostratigraphic and petrographic analysis of ICDP drill core LB-07A, Bosumtwi impact structure, Ghana. *Meteoritics and Planetary Science* 42: 569–589.

- Coney L., Reimold W. U., Gibson R. L., Koeberl C., and Ogilvie P. 2010. Melt particle characteristics of the within- and out-of- crater suevites from the Bosumtwi impact structure, Ghana: Implications for crater formation. In *Large Meteorite Impacts and Planetary Evolution IV*, edited by Gibson R. L., and Reimold W. U. *Geological Society of America Special Paper* 465: 411–442.
- Dai X., Boamah D., Koeberl C., Reimold W. U., Irvine G., and McDonald I. 2005. Bosumtwi impact structure, Ghana: Geochemistry of impactites and target rocks, and search for a meteoritic component. *Meteoritics and Planetary Science* 40: 1493–1511.
- Dampare S. B., Shibata T., Asiedu D. K., Osae S., and Banoeng-Yakubo B. 2008. Geochemistry of Paleoproterozoic metavolcanic rocks from the southern Ashanti volcanic belt, Ghana: Petrogenetic and tectonic setting implications. *Precambrian Research* 162: 403–423.
- Debat P., Nikiema S., Mercier A., Lompo M., Béziat D., Bourges F., Roddaz M., Salvi S., Tollon F., and Wenmenga U. 2003. A new metamorphic constraint for the Eburnean orogeny from Paleoproterozoic formations of the Man Shield (Aribinda and Tampelga countries, Burkina Faso). *Precambrian Research* 123: 47–65.
- de Kock G. S., Armstrong R. A., Siegfried H. P., and Thomas E. 2011. Geochronology of the Birim Supergroup of the West African craton in the Wa-Bolé region of west-central Ghana: Implications for the stratigraphic framework. *Journal of African Earth Sciences* 59: 1–40.
- Dietz R. S. 1967. Shatter cone orientation at Gosses Bluff astrobleme. *Nature* 216: 1082–1084.
- Donofrio R. R. 1997. Survey of hydrocarbon-producing impact structures in North America: Exploration results to date and potential for discovery in Precambrian basement rock. *Oklahoma Geological Survey, Circular* 100: 17–29.
- Doumbia S., Pouclet A., Kouamelan A., Peucat J. J., Vidal M., and Delor C. 1998. Petrogenesis of juvenile-type Birimian (Paleoproterozoic) granitoids in Central Côte d'Ivoire, West Africa: geochemistry and geochronology. *Precambrian Research* 87: 33–63.

- Dressler B. O., Sharpton V. L., and Schuraytz B. C. 1998. Shock metamorphism and shock barometry at a complex impact structure: Slate Islands, Canada. *Contributions to Mineralogy and Petrology* 130: 275–287.
- Elbeshausen D., and Wünnemann K. 2013. Crater formation in the transition from circular to elliptical impact structures (abstract 1916). *44th Lunar and Planetary Science Conference*.
- Engelhardt W. V., and Stöffler D. 1968. Stages of shock metamorphism in crystalline rocks of the Ries Basin, Germany. In *Shock Metamorphism of Natural Materials*, edited by French B. M., and Short N. M. Baltimore: Mono Book Corporation. pp. 159–168.
- Essene E. J., and Fisher D. C. 1986. Lightning strike fusion: extreme reduction and metal-silicate liquid immiscibility. *Science* 234: 189–193.
- Ferrière L. 2008. Shock metamorphism and geochemistry of impactites from the Bosumtwi impact structure: A case study of shock-induced deformations and transformations in quartz and associated methodology. Ph.D. thesis, University of Vienna, Vienna, Austria.
- Ferrière L., Koeberl C., and Reimold W. U. 2007. Drill core LB-08A, Bosumtwi impact structure, Ghana: petrographic and shock metamorphic studies of material from the central uplift. *Meteoritics and Planetary Science* 42: 611–633.
- Ferrière L., Koeberl C., Ivanov B. A., and Reimold W. U. 2008. Shock metamorphism of Bosumtwi impact crater rocks, shock attenuation, and uplift formation. *Science* 322: 1678–1681.
- Ferrière L., Raiskila S., Osinski G. R., Pesonen L. J., and Lehtinen M. 2010. The Keurusselkä impact structure, Finland – Impact origin confirmed by characterization of planar deformation features in quartz grains. *Meteoritics and Planetary Science* 45: 434–446.
- Feybesse J., Billa M., Guerrot C., Duguey E., Lescuyer J., Milesi J., and Bouchot V. 2006. The paleoproterozoic Ghanaian province: Geodynamic model and ore controls, including regional stress modeling. *Precambrian Research* 149: 149–196.

- French B. M. 1968. Shock metamorphism as a geological process. In *Shock Metamorphism of Natural Materials*, edited by French B. M. and Short N. M. Baltimore: Mono Book Corporation. pp. 1–17.
- French B. M. 1998. *Traces of Catastrophe: A Handbook of Shock-Metamorphic Effects in Terrestrial Meteorite Impact Structures*. Houston: Lunar and Planetary Institute, *LPI Contribution* No. 954. 120 p.
- French B. M., and Koeberl C. 2010. The convincing identification of terrestrial meteorite impact structures: What works, what doesn't, and why. *Earth-Science Reviews* 98: 123–170.
- Fudali R., and Cressy P. J. 1978. Investigation of a new stony meteorite from Mauritania with some additional data on its find site: Aouelloul crater. *Earth and Planetary Science Letters* 30: 262–268.
- Galipp K., Klemd R., and Hirdes W. 2003. Metamorphism and geochemistry of the Paleoproterozoic Birimian Sefwi volcanic belt (Ghana, West Africa). *Geologisches Jahrbuch D* 111: 151–191.
- Gash P. J. S. 1971. Dynamic mechanism of the formation of shatter cones. *Nature Physical Sciences* 230: 32–35.
- Gilmour I. 1998. Geochemistry of carbon in terrestrial impact processes. In *Meteorites: Flux with Time and Impact Effects* edited by Grady M. M., Hutchison R., McCall G. J. H., Rothery D. A. *Geological Society of London Special Publication* 140: 205–216.
- Gilmour I., French B. M., Franchi I. A., Abbott J. I., Hough, R. M., Newton J., and Koeberl C. 2003. Geochemistry of carbonaceous impactites from the Gardnos impact structure, Norway. *Geochimica et Cosmochimica Acta* 67: 3889–3903.
- Glass B. P., Lu S., and Leavens P. B. 2002. Reidite: an impact-produced high-pressure polymorph of zircon found in marine sediments. *American Mineralogist* 87: 562–565.
- Gomes R., Levison H. F., Tsiganis K., and Morbidelli A. 2005. Origin of the cataclysmic Late Heavy Bombardment period of the terrestrial planets. *Nature* 435: 466–469.

- Grieve R. A. F. 1987. Terrestrial impact structures. *Annual Review of Earth and Planetary Sciences* 15: 245–270.
- Grieve R. A. F. 1991. Terrestrial impact: the record in the rocks. *Meteoritics* 26: 175–194.
- Grieve R. A. F., and Cintala M. J. 1992. An analysis of differential impact melt-crater scaling and implications for the terrestrial impact record. *Meteoritics* 27: 526–538.
- Grieve R. A. F., and Masaitis V. L. 1994. The economic potential of terrestrial impact craters. *International Geology Review* 36: 105–151.
- Grieve R. A. F. and Robertson P. B. 1976. Variations in shock deformation at the Slate Islands impact structure, Lake Superior, Canada. *Contributions to Mineralogy and Petrology* 58: 37–49.
- Grieve R. A. F., Langenhorst F., and Stöffler D. 1996. Shock metamorphism of quartz in nature and experiment: II. Significance in geoscience. *Meteoritics and Planetary Science* 31: 6–35.
- Hamacher D. W., and Noris R. P. 2009. Australian Aboriginal Geomythology: Eyewitness accounts of cosmic impacts? *Archaeoastronomy: The Journal of Astronomy in Culture* XXII: 1-51.
- Herd C. D. K., Froese D. G., Walton E. L., Kofman R. S., Herd E. P. K., and Duke M. J. M. 2008. Anatomy of a young impact event in central Alberta, Canada: Prospects for the missing Holocene impact record. *Geology* 36: 955–958.
- Hildebrand A. R., Penfield G. T., Kring D. A., Pilkington M., Camargo A. Z., Jacobsen S. B., and Boynton W. V. 1991. Chicxulub Crater: A possible Cretaceous/Tertiary boundary impact crater on the Yucatán Peninsula, Mexico. *Geology* 19: 867–871.
- Hirde W., Davis D. W., and Eisenlohr B. N. 1992. Reassessment of Proterozoic granitoid ages in Ghana on the basis U/Pb zircon and monazite dating. *Precambrian Research* 56: 89–96.
- Holm S., Alwmark C., Alvarez W., and Schmitz B. 2011. Shock barometry of the Siljan impact structure, Sweden. *Meteoritics and Planetary Science* 46: 1888–1909.

- Hörz F. 1968. Statistical measurements of deformation structures and refractive indices in experimentally shock loaded quartz. In *Shock Metamorphism of Natural Materials*, edited by French B. M. and Short N. M. Baltimore: Mono Book Corporation. pp. 243–253.
- Hough R. M., Gilmour I., Pillinger C. T., Arden J.W., Gilkes K. W. R., Yuan J., and Milledge H. L. 1995. Diamond and silicon carbide in impact melt rock from the Ries impact crater. *Nature* 378: 41–44.
- Howard K. A. 1974. Fresh lunar impact craters: Review of variations with size. *Proceedings, 5th Lunar Science Conference*, pp. 61–69.
- Jackson J.C., Horton Jr. J. W., Chou I. -M., and Belkin H. E. 2006. A shock-induced polymorph of anatase and rutile from the Chesapeake Bay impact structure, Virginia, U.S.A. *American Mineralogist* 91: 604–608.
- John T., Klemd R., Hirdes W., and Loh G. 1999. The metamorphic evolution of the Paleoproterozoic (Birimian) volcanic Ashanti belt (Ghana, West Africa). *Precambrian Research* 98: 11–30.
- Johnson G. P., and Talbot R. J. 1964. A theoretical study of the shock-wave origin of shatter cones. M.S. Thesis, Air Force Institute of Technology, Wright–Patterson Air Force Base, Ohio, USA.
- Johnson K. S. and Campbell J. A., eds. 1997. Ames structure in northwest Oklahoma and similar features: Origin and petroleum production (1995 symposium). Oklahoma Geological Survey Circular 100, 396 p.
- Jones W. B. 1985. Chemical analyses of Bosumtwi crater target rocks compared with the Ivory Coast tektites. *Geochimica et Cosmochimica Acta* 48: 2569–2576.
- Jones W. B., Bacon M., and Hastings D. A. 1981. The Lake Bosumtwi impact crater, Ghana. *Geological Society of America Bulletin* 92: 342–349.
- Kamo S. L., Reimold W.U., Krogh T.E., and Colliston W.P. 1997. A 2.023 Ga age for the Vredefort impact event and a first report of shock metamorphosed zircons in

- pseudotachylitic breccias and Granophyre. *Earth and Planetary Science Letters* 144: 369-387.
- Karikari F., Ferriere L., Koeberl C., Reimold W. U., and Mader D. 2007. Petrography, geochemistry, and alteration of country rocks from the Bosumtwi impact structure. *Meteoritics and Planetary Science* 42: 513–540.
- Kenkmann T., Artemieva N. A., Wünnemann K., Poelchau M. H., Elbeshausen D., and Nunez del Prado H. 2009. The Carancas meteorite impact crater, Peru: Geologic surveying and modeling of crater formation and atmospheric passage. *Meteoritics and Planetary Science* 44: 985–1000.
- Kieffer S. W. 1971. Shock metamorphism of the Coconino Sandstone at Meteor Crater, Arizona. *Journal of Geophysical Research* 76: 5449–5473.
- Koeberl C. 1994. African meteorite impact craters: Characteristics and geological importance. *Journal of African Sciences* 18: 263-295.
- Koeberl C. 1998. Identification of meteoritic component in impactites. In *Meteorites: Flux with Time and Impact Effects* edited by Grady M. M., Hutchison R., McCall G.J.H., and Rothery D.; London: Geological Society. pp. 133–153.
- Koeberl C. 2007. The geochemistry and cosmochemistry of impacts. In *Treatise of Geochemistry* edited by Davis A. New York: Elsevier. pp. 1.28.1–1.28.52.
- Koeberl C., and Reimold W. U. 2005. Bosumtwi impact crater, Ghana (West Africa): An updated and revised geological map, with explanations. *Jahrbuch der Geologischen Bundesanstalt, Wien (Yearbook of the Austrian Geological Survey)* 145: 31–70 (+1 map, 1:50,000).
- Koeberl C., Masatitish V. L., Shafranovsky G. I., Gilmour I., Langenhorst F., and Schrauder M. 1997a. Diamonds from the Popigai Impact Structure, Russia. *Geology* 25: 967–970.
- Koeberl C., Bottomley R., Glass B., and Storzer D. 1997b. Geochemistry and age of Ivory Coast tektites and microtektites. *Geochimica et Cosmochimica Acta* 61: 1745–1772.
- Koeberl C., Peucker-Ehrenbrink B., Reimold W.U., Shukolyukov A., and Lugmair G.W. 2002. A comparison of the osmium and chromium isotopic methods for the detection of

- meteoritic components in impactites: Examples from the Morokweng and Vredefort impact structures, South Africa. In: *Catastrophic Events and Mass Extinctions: Impacts and Beyond*, edited by C. Koeberl and K.G. MacLeod). *Geological Society of America Special Paper* 356: 607-617.
- Koeberl C., Milkereit B., Overpeck J. T., Scholz C. A., Amoako P. Y. O., Boamah D., Danuor S. K., Karp T., Kueck J., Hecky, R. E., King J., and Peck J. A. 2007. An international and multidisciplinary drilling project into a young complex impact structure: The 2004 ICDP Bosumtwi impact crater, Ghana, drilling project—An overview: *Meteoritics and Planetary Science* 42: 483–511.
- Kring D. A. 2007. Guidebook to the Geology of Barringer Meteorite Crater, Arizona (a.k.a. Meteor Crater). LPI Contribution No. 1355. 150 p.
- Langenhorst F. 2002. Shock metamorphism of some minerals: basic introduction and microstructural observations. *Bulletin of the Czech Geological Survey* 77: 265–282.
- Langenhorst F., and Deutsch A. 1994. Shock experiments on pre-heated α - and β -quartz: I. Optical and density data. *Earth and Planetary Science Letters* 125: 407–420.
- Lee S. R., Horton Jr. J. W., and Walker R. J. 2006. Confirmation of a meteorite component in impact-melt rocks of the Chesapeake Bay impact structure, Virginia, USA — evidence from osmium isotopic and PGE systematics. *Meteoritics and Planetary Science* 41: 819–833.
- Leube A., Hirdes W., Maur R., and Kesse G. O. 1990. The early Proterozoic Birimian Supergroup of Ghana and some aspects of its associated gold mineralization. *Precambrian Research* 46: 139–165.
- Lightfoot P. C., Keays R. R., Morrison G. G., Bite A., and Farrell K. P. 1997. Geochemical relationships in the Sudbury Igneous Complex: origin of the main mass and offset dikes. *Economic Geology* 92: 289–307.
- Malin M. C., Edgett K. S., Posiolova L. V., McColley S. M., and Dobrea E. Z. N. 2006. Present-day impact cratering rate and contemporary gully activity on Mars. *Science* 314: 1573–1577.

- Masaitis V. L. 1998. Popigai crater: Origin and distribution of diamond-bearing impactites. *Meteoritics and Planetary Science* 33: 349–359.
- Marvin U. B. 2007. Ernst Florens Friedrich Chladni (1756-1827) and the origins of the modern meteorite research. *Meteoritics and Planetary Science* 42: B3–B68.
- Melosh H. J. 1989. Impact Cratering. A Geologic Process. New York, Oxford University Press. ix + 245 pp.
- Meyer C., Fritz J., Misgaiski M., Stöffler D. Artemieva N. A., Hornemann U., Moeller R. de Vera J- P., Cockell C., Horneck G., Ott S., and Rabbow E. 2011. Shock experiments in support of the Lithopanspermia theory: The influence of host rock composition, temperature, and shock pressure on the survival rate of endolithic and epilithic microorganisms. *Meteoritics and Planetary Science* 46: 701–718.
- Milton D. J. 1977. Shatter cones—an outstanding problem in shock mechanics. In Impact and Explosion Cratering: Planetary and Terrestrial Applications, edited by Roddy D. J., Pepin R. O., Merrill R. P. New York: Pergamon Press. pp. 703–714.
- Montanari A., and Koeberl C. 2000. Impact Stratigraphy. Lecture Notes in Earth Sciences 93, Berlin-Heidelberg: Springer. 364 p.
- Moon P. A., and Mason D. 1967. The geology of 1/4° field sheets nos. 129 and 131, Bompata S.W. and N.W. *Ghana Geological Survey Bulletin* 31: 1–51.
- Mory A. J., Iasky R. P., Glikson A. Y., and Pirajno F. 2000. Woodleigh, Carnarvon Basin, Western Australia: a new 120 km diameter impact structure. *Earth and Planetary Science Letters* 177: 119–128.
- Oberthür T., Vetter U., Davis D. W., and Amanor J. A. 1998. Age constraints on gold mineralization and Paleoproterozoic crustal evolution in the Ashanti belt of southern Ghana. *Precambrian Research* 89: 129–143.
- Palme H., Grieve R. A. F., and Wolf R. 1981. Identification of the projectile at the Brent crater, and further considerations of projectile types at terrestrial craters. *Geochimica et Cosmochimica Acta* 45: 2417–2424.

- Pigois J. P., Grove D. I., Fletcher I. R., McNaughton N. J., and Snee L. W. 2003. Age constraints on Tarkwaian paleoplacer and lode-gold formation in the Tarkwa–Damang district, SW Ghana. *Mineralium Deposita* 38: 695–714.
- Reimold W. U., Koeberl C., Partridge T. C., and Kerr S. J. 1992. Pretoria Saltpan crater: Impact origin confirmed. *Geology* 20: 1079–1082.
- Reimold W. U., Brandt D., and Koeberl C. 1998. Detailed structural analysis of the rim of a large, complex impact crater: Bosumtwi crater, Ghana. *Geology* 26: 543–546.
- Reimold W. U., Koeberl C., Gibson R. L., and B. O., and Dressler B. O. 2005. Economic Mineral Deposits in Impact Structures: A Review. In *Impact Tectonics Impact Studies*, edited by Koeberl C. and Henkel H. Berlin, Heidelberg: Springer. pp. 479–552.
- Schulte P., Alegret L., Arenillas I., Arz J. A., Barton P. J., Bown P. R., Bralower T. J., Christeson G. L., Claeys P., Cockell C. S., Collins G. S., Deutsch A., Goldin T. J., Goto K., Grajales-Nishimura J. M., Grieve R. A. F., Gulick S. P. S., Johnson K. R., Kiessling W., Koeberl C., Kring D. A., MacLeod K. G., Matsui T., Melosh J., Montanari A., Morgan J. V., Neal C. R., Nichols D. J., Norris R. D., Pierazzo E., Ravizza G., Rebolledo-Vieyra M., Reimold W. U., Robin E., Salge T., Speijer R. P., Sweet A. R., Urrutia-Fucugauchi J., Vajda V., Whalen M. T., and Willumsen P. S. 2010. The Chicxulub asteroid impact and mass extinction at the Cretaceous–Paleogene boundary. *Science* 327: 1214–1218.
- Shoemaker E. M. 1963. Impact mechanics at Meteor Crater, Arizona. In *The Moon, Meteorites, and Comets*, edited by Middlehurst B. M. and Kuiper G. P. Chicago: University of Chicago. pp. 301–336.
- Shoemaker E. M., and Chao E. C. T. 1961. New evidence for the impact origin of the Ries Basin, Bavaria, Germany. *Journal of Geophysical Research* 66: 3371–3378.
- Shoemaker E. M., and Shoemaker C. S. 1996. The Proterozoic impact record of Australia. *AGSO Journal of Australian Geology and Geophysics* 16: 379–398.

- Smit J., and Hertogen J. 1980. An extraterrestrial event at the Cretaceous–Tertiary boundary. *Nature* 285: 198–200.
- Stankowski W. T. J. 2001. The geology and morphology of the natural reserve "Meteoryt Morasko". *Planetary and Space Science* 49: 749–753.
- Stewart S. A., and Allen P. J. 2005. 3D seismic reflection mapping of the Silverpit multi-ringed crater, North Sea. *Bulletin of the Geological Society of America* 117: 354–368.
- Stöffler D. 1972. Deformation and transformation of rock-forming minerals by natural and experimental shock processes: I. Behavior of minerals under shock compression. *Fortschritte der Mineralogie* 49: 50–113.
- Stöffler D. 1984. Glasses formed by hypervelocity impact. *Journal of Non-Crystalline Solids* 67: 465–502.
- Stöffler D., and Langenhorst F. 1994. Shock metamorphism of quartz in nature and experiment: I. Basic observation and theory. *Meteoritics* 29: 155–181.
- Taylor P. N., Moorbath S., Leube A., and Hirdes W. 1992. Early Proterozoic crustal evolution in the Birimian of Ghana: Constraints from geochronology and isotope geochemistry. *Precambrian Research* 56: 97–111.
- Wittmann A., Kenkmann T., Schmitt T., and Stöffler D. 2006. Shock-metamorphosed zircon in terrestrial impact craters. *Meteoritics and Planetary Science* 41: 433–454.
- Woodfield P. D. 1966. The geology of the 1/4° field sheet 91, Fumso, N.W. Ghana. *Ghana Geological Survey Bulletin* 30: 1–66.
- <http://phys.org/news/2012-09-popigai-russia-vast-untouched-diamond.html> (Sep 19, 2012 by Marina Lapenkova, retrieved 23.04.2013)
- <http://www.passc.net/EarthImpactDatabase/index.html> (retrieved 31.03.2013)
- <http://www.meteoriteguy.com/adventures/carancas/carancasfallexpedition.htm> (retrieved 31.03.2013)
- <http://www.artmet-meteoryty.pl/pl/wydarzenia/szczeguly.php?pokaz=17> (retrieved 31.03.2013)

2. Theoretical fundamentals of methods used in this study

This chapter discusses the main principles and theoretical foundations of the most important methods used in this thesis. The details of the application of those techniques are given in the respective chapters.

2.1. Optical microscope

Thin sections were studied within all projects of this study. They were examined with an optical transmitted light microscope. Because polarizing light optical microscopy is one of the most common techniques used in geology, no detailed description will be provided here.

2.1.1. Universal stage (U-stage)

The thin section selected for the study of spatial characterization of planar deformation features in quartz (chapter four) was analyzed with the universal stage (U-stage, Figure 2.1). U-stage is a device that is mounted on an optical microscope that enables a thin section to be viewed and measured in three dimensions. For example, it allows the grain boundaries and planar deformation features to be measured.

Sample preparation required for the U-stage measurement is the same as the one necessary to produce a standard thin section. However, it may be advantageous if thin sections measured with the U-stage are slightly thicker than normal thin sections (e.g., ~40 μm).

The analysis performed in this study followed instructions described by Ludovic Ferrière in his thesis (Ferrière 2008) based on work by Reinhard (1931), Emmons (1943) and French (written communication). More information on the U-stage application can be found in: Engelhardt and Bertsch (1969), Stöffler and Langenhorst (1994), French (1998), as well as Ferrière et al. (2009).

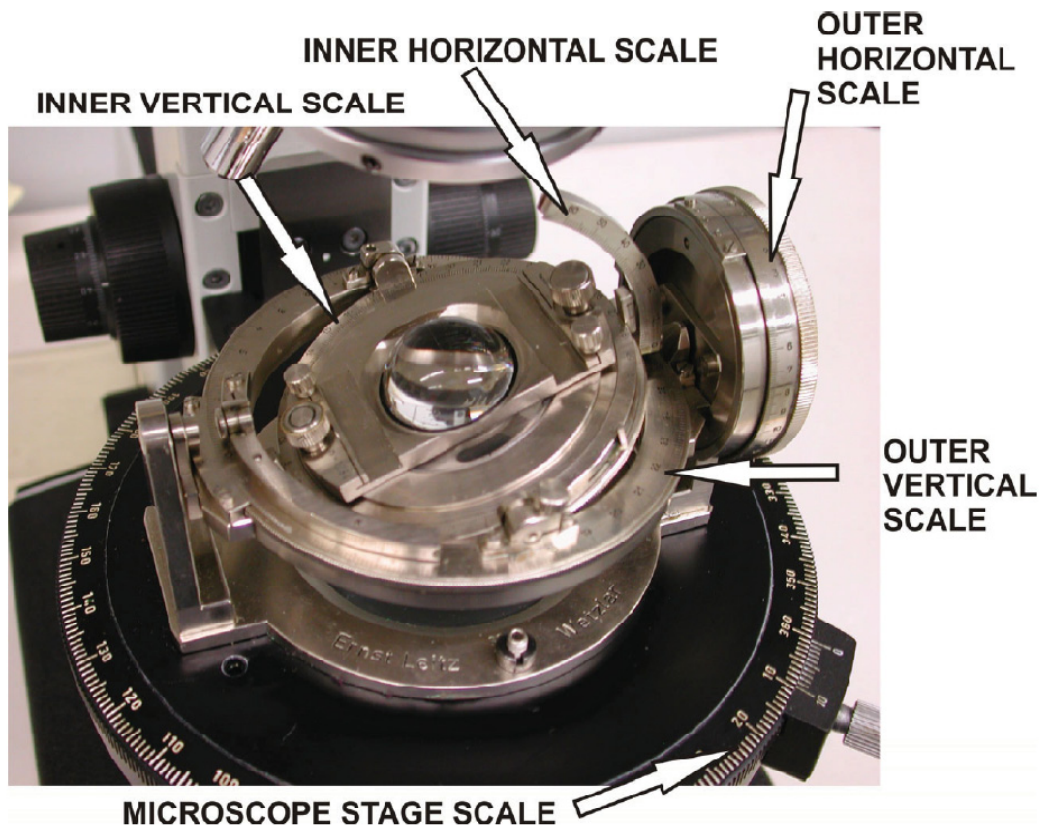


Figure 2.1 Universal stage mounted on an optical microscope with arrows indicating axes of the device. Figure from Bartosova (2010).

2.1.2. Numerical program for automatic indexing of planar deformation features

A computer program was designed to evaluate data from U-stage measurements (Figure 2.2). It works by assessing the relationships between the c-axis and the measured planar features within a given quartz grain and comparing them to angles of known, PDF orientations (as defined in Ferrière et al. 2009, and references therein). The presented approach simplifies the mathematical calculations required for indexing and allows minimizing errors related to distortions that may be induced when representing information derived from a three-dimensional (3D) crystal on a 2D Wulff stereonet.

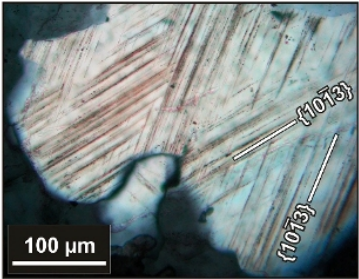
PDF indexing program

Create a new project

Input file

Browse...

Upload




Planar deformation features (PDFs) in quartz grains are the most commonly used diagnostic features of hypervelocity impact structures. PDFs are straight, parallel sets of planes of amorphous material that are less than 2 μm wide and spaced 2-10 μm apart. Specific combinations of PDF orientations provide information on the peak shock pressure recorded by samples, within the range of ~5 to 35 GPa.

The determination of PDF orientations is usually done using a universal-stage (U-stage)-equipped petrographic microscope, followed by indexing measurements to crystallographic orientations in relation to the c-axis. Currently, indexing of PDFs is done manually using a Wulff net and a stereonet and following a strict procedure, which is both time consuming and error-prone. Because of limitations of the manual indexing method, only information about polar angles and Miller-Bravais indices of PDFs were recorded and used in previous studies. The angular relationships between PDF sets were in most cases ignored. Here, we present a web-based program for indexing PDFs that also allows for analysis of azimuthal angles between PDFs in a given quartz grain. The study of combinations of PDF orientations can be useful for a better understanding of impact processes. Our program is available from: <http://lithosphere.univie.ac.at/impactresearch/>. The source code (i.e., implementation in Java programming language) will be made available. [Read more...](#)

[Description of the program](#)

Download [a sample input file](#) and use it to test the program.

PDF indexing program
version 1.0, 02.05.2013



universität
wien

Contact person: Anna Losiak, anna.losiak@univie.ac.at

Figure 2.2. The first page of the PDF indexing program developed during work on this thesis.

2.2. Scanning Electron Microscopy (SEM)

Selected samples were also analyzed with a scanning electron microscope (SEM). This is a type of electron microscope that produces an image by scanning a focused electron beam on the surface of the sample (Figure 2.3). The primary beam used in the SEM commonly has an acceleration voltage between 15 and 30 keV (although lower values can also be used) and works under the conditions of high vacuum.

The spatial resolution of SEM depends on multiple factors: 1) wavelength of the electrons in the primary beam (dependent on the energy), 2) the optical system used in the microscope (the type of electron gun and quality of the electron lenses), 3) the interaction volume of the electrons with sample (dependent on the electron energy and type of material analyzed). The resolution of a SEM is up to few nm.

SEM images can be obtained by measuring electrons generated through two processes: secondary electrons (SE) and back-scattered electrons (BSE). Secondary electrons are low-energy (<50 eV usually ~2-5 eV) electrons ejected from the K-orbitals of excited atoms by inelastic scattering of the beam electrons. They originate from the surface-most layer of the sample and because of this they provide information about topography of the sample. Back-scattered electrons are produced by elastic scattering of high-energy electrons from the beam by interaction with elements of the sample (of energies comparable to those of the primary electron beam). Elements with high atomic number tend to scatter more efficiently than those with lower atomic number (thus generating higher signal), and because of that they appear brighter in the resulting image. The BSE imaging mode allows graphical detection of areas of differing chemical composition.

An SEM equipped with an appropriate detector can be used to analyze X-rays produced due to interactions of the sample with a primary electron beam. Those X-rays can be used to obtain information about the chemical composition of the sample due to the fact that they are characteristic to particular elements and their intensity is proportional to the element concentration in the sample. However, to quantify the measurement it is necessary to reference the wavelengths to the appropriate standards. Two properties of the characteristic X-rays can be measured: photon energy (energy dispersive X-ray spectrometer, EDS) or photon wavelengths (wavelength dispersive spectrometer, WDS); in SEM instruments EDS is used, whereas electron microprobes usually use the WDS method.

Samples used for SEM analysis can include whole sample fragments, but they must be small enough to fit into the sample chamber, or thin sections prepared in the same way as for optical microscopy. Polishing a thin section before analysis makes the dispersal of X-rays more predictable, as under those conditions it depends only on the compositional variation. Samples analyzed under SEM usually have to be coated with a conductive layer (most often carbon, gold or platinum) to avoid accumulation of charging on the surface of the sample (although working with uncoated samples is also possible, but no high-resolution images or analytical data can then be obtained).

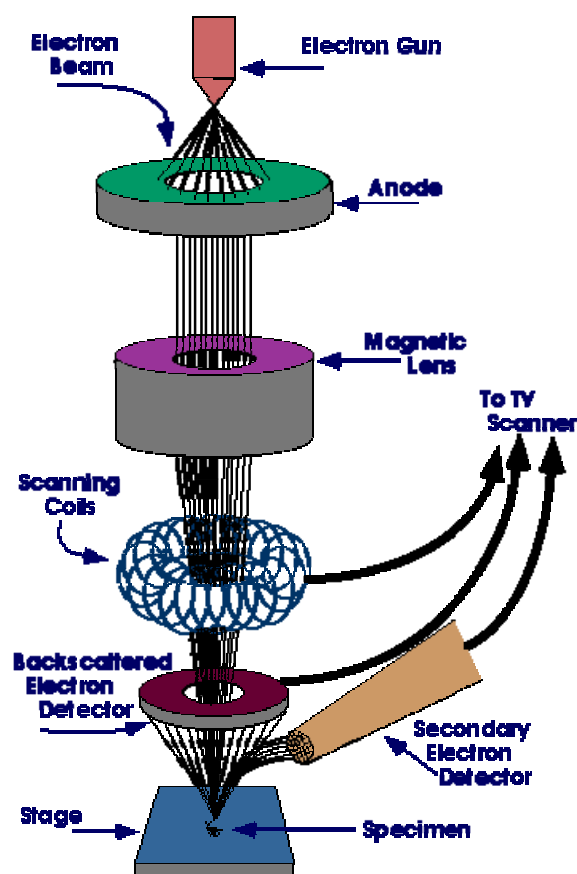


Figure 2.3. A diagram explaining how SEM works. (source: Iowa State University)

More information on SEM is given by Potts (1987), Lee (1993), Reimer (1998), Severin (2004), and Goldstein et al. (2007).

2.3. X-ray Fluorescence (XRF) spectrometry

The bulk chemical analysis of granites from the proximity of the Bosumtwi crater (chapter three) was performed with X-ray fluorescence (XRF) spectrometry. This is a method for determining the concentrations of major oxides (SiO_2 , TiO_2 , Al_2O_3 , Fe_2O_3 , MnO , MgO , CaO , Na_2O , K_2O , P_2O_5 , and SO_3) and many trace elements (Ba, Ce, Co, Cr, Cu, Ga, Mo, Nb, Ni, Pb, Rb, Sc, Sr, Th, U, V, Y, Zn, and Zr).

The XRF method measures the energy and intensity of fluorescent (secondary) X-rays emitted from material that has been excited by irradiation with X-rays. When a sample is irradiated with high-energy X-rays some of the electrons located close to the nucleus (low

energy) can be ejected from their position around the nucleus (Figure 2.4). As this electron configuration is unstable, one of the electrons from the outer orbital fills the newly free position. During this process, energy equal to the difference in energetic level between the “void” orbital and orbital from which the electron filling the void originates is released, forming secondary X-rays. Because each element is characterized by a set of specific allowed energies of fluorescent X-rays, it can be unequivocally identified. The contents of a certain element within the sample can be measured because the intensity of the specific X-ray wavelengths is proportional to the concentration of the certain element in the sample. However, in order to quantify the results, the obtained information about wavelength and intensity of measured X-rays needs to be compared with data obtained for samples of known composition.

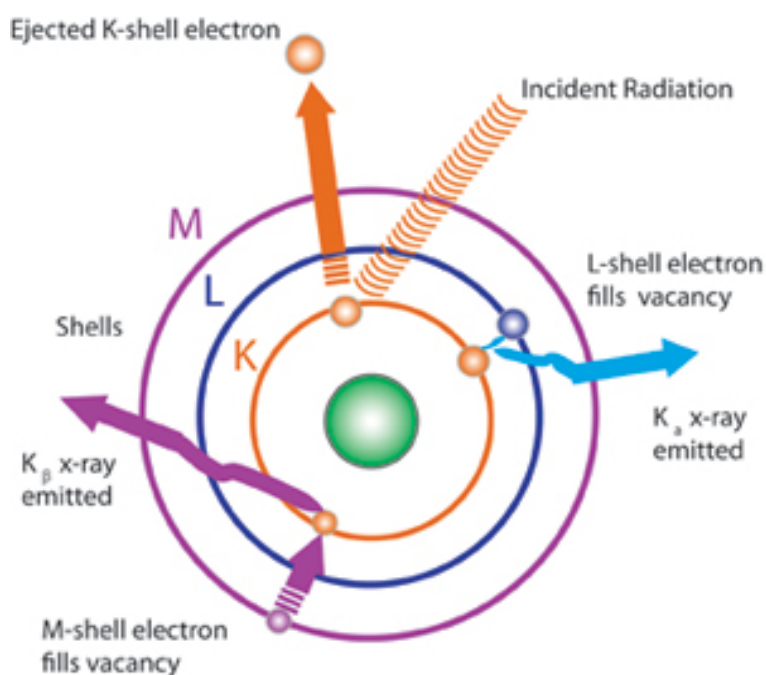


Figure 2.4. Schematic diagram showing the physical principle of the XRF method (source: U.S. Environmental Protection Agency).

Samples to be measured by XRF have to be prepared for analysis. Rock powder can be analyzed in the form of a pressed pellet (after mixing it with polyvinyl alcohol as a binding agent) or a fused pellet (after mixing with lithium tetraborate and heating it). This first technique tends to be used for the minor elements analysis, while fused pellets are used to obtain composition of the major elements within studied samples.

More information about the XRF method is available in Pots (1987), Reimold et al. (1994), and Gill (1997).

2.4. Instrumental Neutron Activation Analysis (INAA)

Instrumental Neutron Activation Analysis (INAA) is a method used to determine content of minor and trace elements, such as Sc, Cr, Co, Ni, Zn, As, Se, Br, Rb, Sr, Zr, Sb, Cs, Ba, Hf, Ta, W, Ir, Au, Th, U, including rare earth elements La, Ce, Nd, Sm, Eu, Gd, Tb, Tm, Yb, and Lu. Some major elements, such as Na, K, and Fe, can be also determined in this way. INAA was performed on the samples used in the study of granites from the proximity of Bosumtwi crater (chapter three). The main principle behind this method is to measure γ -rays emitted by samples that have been artificially irradiated under closely controlled conditions. The energies of emitted γ -rays are characteristic for specific isotopes, while the intensities of the specific energy of radiation can be used to calculate the content of an element in the sample.

At first, samples are prepared of the INAA analysis. This procedure is easy; small pieces of untreated samples or rock powder can be used (e.g., in this thesis between 110 and 160 mg was used). Samples have to be precisely weighed and sealed into small plastic containers.

During the second step of the INAA analysis samples are irradiated with thermal neutrons (characterized by energies <0.5 eV) in a nuclear reactor. Neutrons usually come from the ^{235}U fission but neutrons from accelerators or radioisotopic emitters can also be used. In this study irradiation took place in the 250 kW Triga Mark II reactor at the Atomic Institute of the Austrian Universities for 6–8 h at a thermal neutron flux of $1.7 \times 10^{12} \text{ n cm}^{-2} \text{ s}^{-1}$. About 5-6 days after irradiation, samples can be safely transported to the laboratory and measured.

As a result of the thermal neutron capture reactions some of the atoms present in the sample are converted into short-lived radioactive isotopes of the same element (characterized by the same atomic number but higher mass). Not all elements interact with

the neutrons during irradiation in the same way: the intensity of the interaction is strongly dependent on their “neutron capture cross section”. This means that the same flux of neutrons will convert much higher percentage of gold atoms than beryllium atoms into short-lived radioactive isotopes.

Isotopes formed due to irradiation are usually short-lived and undergo rapid radioactive decay. It is usually a β -decay, which results in emission of an electron or a positron, combined with de-excitation energy transitions in the form of a photon (X-rays or γ -rays). The emitted photons have energies that are characteristic for the decaying isotope, and the intensity of the signal depends on the concentration of the element in the sample. Some of the newly formed isotopes are characterized by short half-lives (e.g., ^{42}K : 12.36 hours) and others half-lives are slightly longer (e.g., ^{152}Eu : 13.542 years). Due to this the measured γ -ray spectrum changes with time and because of that the measurement has to be performed in a few (usually at least three) cycles.

The measurement of the γ -rays is done with a system (Figure 2.5) consisting of a semiconductor detector (high purity germanium HpGe detectors with energy resolutions of 1.76-1.85 keV at 1332 keV), a digital signal processor (processes an amplified voltage signal from the detector), a multichannel-analyzer (where signals are stored in the appropriate channel depending on the energy of the signal) with a computer-based data evaluation unit (that stores acquired data and facilitates its evaluation). The obtained spectra from all cycles of measurements are evaluated with the GenieTM 2000 Spectroscopy Software (Canberra) and the PNNA program. The software finds and measures height peaks from spectra of samples and compares it to the spectra of the standard for which composition is known. Based on this information the elemental concentrations reported in parts per million can be calculated.

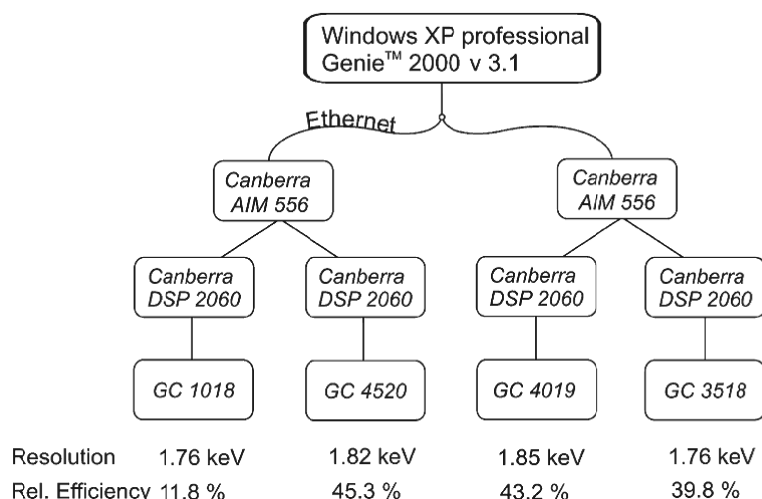


Figure 2.5 Schematic diagram of the system configuration of the INAA laboratory at the Department of Lithospheric Research, University of Vienna. GC stands for Germanium detector, Canberra DSP2060 for the digital signal processor, and Canberra AIM 556 for the acquisition interface module (source: Mader and Koeberl 2009).



Figure 2.6. Part of the gamma spectrometry laboratory for INAA: detector (the green cube is made of lead blocks that provide a radiation shield), digital signal processors and acquisition interface modules (in the cabinet with electronics) at the Department of Lithospheric Research (University of Vienna).

Detailed information about this method along with the description of performance of the INAA laboratory at the Department of Lithospheric Research University of Vienna is given in Koeberl (1993), Koeberl (1995), and Mader and Koeberl (2009).

2.5. Mass spectrometry (MS)

Mass spectrometry (MS) is a technique used to determine the composition of a sample (in terms of its elemental composition or isotopic ratios of specific elements present) by counting particles separated by mass-charge ratio in the magnetic field. Mass spectrometers (of different types) are usually part of more complex systems commonly used in the analysis of geological samples, e.g.,

- Inductively coupled plasma mass spectrometry (ICP-MS),
- Secondary ion mass spectrometry (SIMS),
- Accelerator mass spectrometry (AMS),
- Thermal ionization mass spectrometry (TIMS).

The first step of the analysis is the ionization of molecules or atoms, which enables them to interact with the magnetic field (Figure 2.7). Different types of ionization can be used depending on 1) the type of sample being analyzed (gas, liquid or solid state); 2) molecules or atoms of interest that need to be measured; and 3) expected concentrations of atoms (or molecules) in the sample. Ionization is most commonly performed by electron beam, inductively coupled plasma (ICP-MS), ion beam (SIMS) or heating of the sample (TIMS).

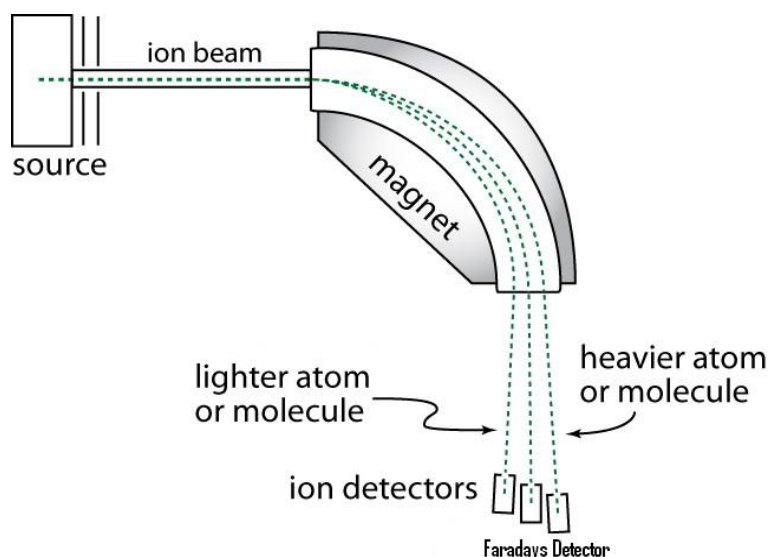


Figure 2.7. The principle of mass spectrometry: if ions are charged in the same way, the path of the lighter one is bent more strongly than the heavier one in the same magnetic field. (source: <http://orgchemguide.blogspot.co.at/>).

Later, the ions are extracted from the ionization system using the magnetic field and sorted according to their mass-to-charge ratio by interaction with the magnetic field. The separation is performed with few different types of devices:

1. "Magnetic sector" (section of a torus shaped magnet), which deflects the path of particles with different mass-to-charge ratios at different rate. If a set of detectors is aligned, the concentration of a few particles can be measured at the same time (Figure 2.7).
2. "Quadrupole" mass analyzer (four cylindrical rods set parallel to each other creating magnetic field between them) allows passage of particles with one, specific mass-to-charge ratio at one moment in time. Only one particle type can be measured at a time.
3. "The time of flight system" works by the accelerating ions in the electric field of known strength and then measuring how long did it take for a particle to travel. It allows all of the ions to be measured at the same time.

Ions sorted by their mass-to-charge ratio are later counted by a detector. Detectors measure the current produced or the charge induced by the ion hitting the detector. Most commonly used detectors are the electron multiplier or the Faraday cups connected to an amplifier. In case of magnetic sector analyzer (the most commonly used for geologic

applications) the mass resolution (ability of a system to distinguish two peaks of slightly different mass-to-charge ratios) depends strongly on the size of the magnet (the larger the magnet, the better mass-to-charge separation), and the physical size of the detectors (the larger the detectors, the worse the mass resolution of a system).

More information about the general MS technique can be found in, e.g., Potts (1987), Vandecasteele and Block (1993), and Gill (1997).

More information about the Chemical Abrasion Thermal Ionization Mass Spectrometry (CA-TIMS) used in this thesis for dating zircons is given in Mattinson (2005), Bowring et al. (2006), Schoene et al. (2006), Thompson et al. (2007), and Peterman et al. (2012).

More information about the Isotope Dilution–Thermal Ionization Mass Spectrometer (ID-TIMS) used in this thesis to determine the whole rock Sm-Nd and Lu-Hf isotopic ratios can be found in Münker et al. (2001), Weyer et al. (2002) and Pin and Zaldegui (1997).

2.5.1. Accelerator Mass Spectrometry (AMS)

If the concentration of atoms of interest is particularly low or if there is an isobar (a nucleus characterized by the same mass (within resolution) as the nucleus of interest) that is interfering with the measurement, it cannot be performed with a regular mass spectrometer. In this case, Accelerator Mass Spectrometry (AMS) is used. AMS is a system that accelerates ions to very high kinetic energies, which allows ions to be separated in a magnetic field (Figure 2.8). The samples that are measured with AMS have to undergo an extensive chemical preparation so that all other chemical compounds (except the element of interest) are suppressed.

The negative ions after formation in the ion source are initially separated by the mass spectrometer and the electrostatic analyzer. This limits the types of particles that are present in the beam injected into the accelerator. The accelerator increases the kinetic energy of the particles and changes their charge from negative to positive by passing through a stripping media (gas or thin foil). This breaks apart all molecules that might have been injected into

the accelerator (e.g., ${}^9\text{Be}^1\text{H}$ in case of ${}^{10}\text{Be}/{}^9\text{Be}$ measurement). However, atomic isobars (e.g., ${}^{10}\text{Be}$ and ${}^{10}\text{B}$) cannot be suppressed by this technique. Depending on the type of particles analyzed, the separation of isobars may be performed by a set of magnetic analyzers, electrostatic analyzers and sometimes also complex detectors commonly consisting of stripping gas or foils that preferentially stop an un-wanted isobar before it reaches the final detector.

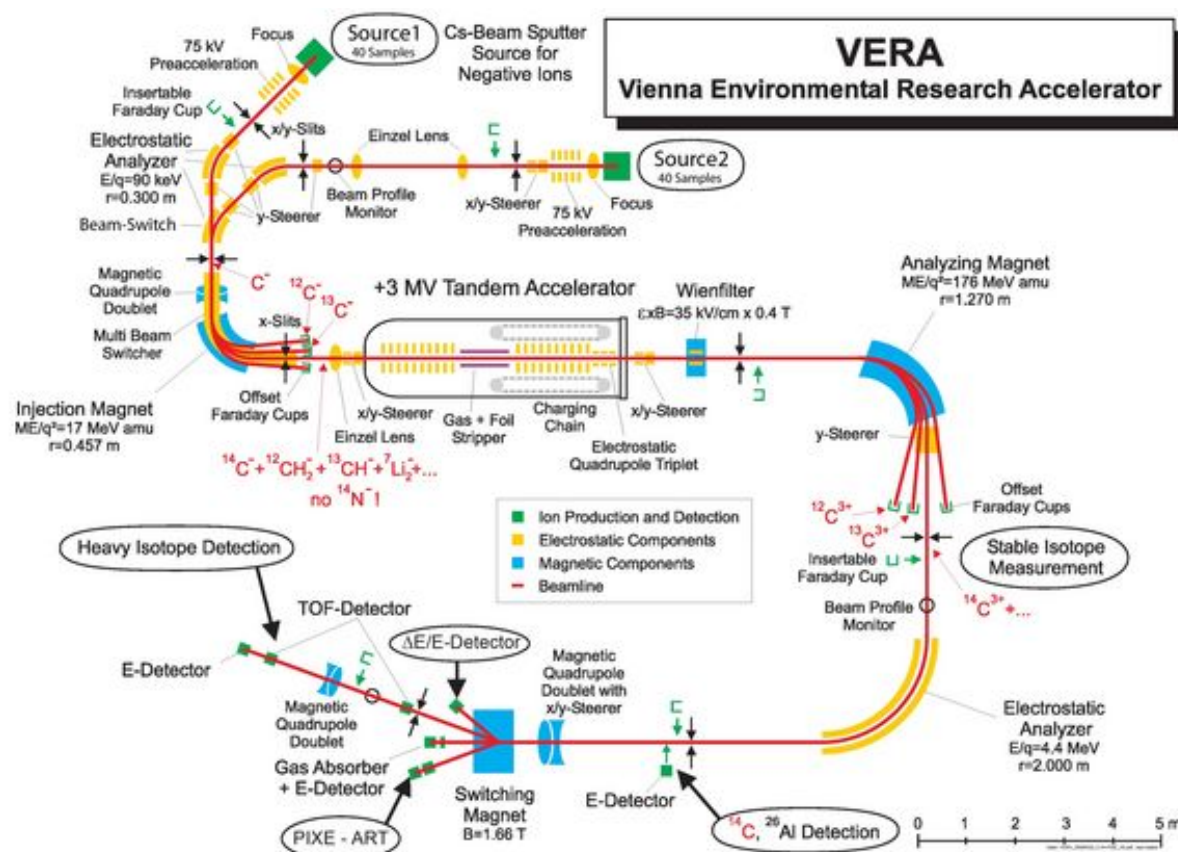


Figure 2.8. The setup of the Vienna Environmental Research Accelerator (VERA) (source: <http://isotopenforschung.univie.ac.at>).

The sample preparation process for the measurement using AMS is extensive and can be divided into three stages: 1) dissolving samples; 2) chemically separating the element of interest; and 3) preparing AMS targets. In case of beryllium measurement, the AMS samples are most commonly prepared with a sequence of ion exchange columns separating beryllium from all other elements, followed by the thermal decomposition of $\text{Be}(\text{OH})_2$ to BeO and mixing it with Cu powder.

More information about AMS is given in, e.g., Kutschera et al. (1997), Priller et al. (2000), Steier et al. (2004), Steier et al. (2005), and Michlmayr (2007). Information about usage of ion-exchange resins is given by Korkisch (1989) and details on the chemical separation of beryllium are given in Auer (2007) and Auer et al. (2007).

References:

- Auer R. M. 2007. Applications of ^{26}Al in atmospheric research. *Ph.D. Thesis*, University of Vienna, Vienna, Austria.
- Auer M., Kutschera W., Priller A., Wagenbach D., Wallner A., and Wild E. M. 2007. Measurement of ^{26}Al for atmospheric and climate research and the potential of $^{26}\text{Al}/^{10}\text{Be}$ ratios. *Nuclear Instruments and Methods in Physics Research Section B: Beam Interactions with Materials and Atoms* 259: 595–599.
- Bartosova K. 2010. Geochemical, mineralogical, and petrographic investigations of the Eyreville drill cores from the Chesapeake Bay impact structure. *Ph.D. thesis*, University of Vienna, Vienna, Austria.
- Bowring J. F., McLean N. M., and Bowring S. A. 2011. Engineering cyber infrastructure for U-Pb geochronology: Tripoli and U-Pb_redux. *Geochemistry, Geophysics, Geosystems* 12 Q0AA19, doi: 10.1029/2010GC003479.
- Emmons R. C. 1943. The universal stage (with five axes of rotation). *Geological Society of America Memoir* 8. 205 p.
- Engelhardt W. v., and Bertsch W. 1969. Shock induced planar deformation structures in quartz from the Ries crater, Germany. *Contributions to Mineralogy and Petrology* 20: 203–234.
- Ferrière L. 2008. Shock metamorphism and geochemistry of impactites from the Bosumtwi impact structure: A case study of shock-induced deformations and transformations in quartz and associated methodology. *Ph.D. thesis*, University of Vienna, Vienna, Austria.
- Ferrière L., Morrow J. R., Amgaa T., and Koeberl C. 2009. Systematic study of universal stage measurements of planar deformation features in shocked quartz: Implications for statistical significance and representation of results. *Meteoritics and Planetary Science* 44: 925–940.

- French B. M. 1998. *Traces of Catastrophe: A Handbook of Shock-Metamorphic Effects in Terrestrial Meteorite Impact Structures*. Houston: Lunar and Planetary Institute, *LPI Contribution No. 954*. 120 p.
- Gill R. 1997. *Modern analytical geochemistry: an introduction to quantitative chemical analysis techniques for earth, environmental and materials scientists*. Harlow, England: Addison Wesley Longman Limited. 329 p.
- Goldstein J., Newbury D., Joy D., Lyman C., Echlin P., Lifshin E., Sawyer L., and Michael J. 2007. *Scanning electron microscopy and X-ray microanalysis*. Third edition. USA: Springer. 690 p.
- Lee R. E. 1993. *Scanning electron microscopy and X-ray microanalysis*. Engelwood Cliffs, New Jersey: PTR Prentice–Hall, Inc. 458 p.
- Koeberl C. 1993. Instrumental neutron activation analysis of geochemical and cosmochemical samples: a fast and reliable method for small sample analysis. *Journal of Radioanalytical and Nuclear Chemistry* 168: 47–60.
- Koeberl C. 1995. Neutron activation analysis. In *Methods and instrumentations: results and recent developments*, Advanced mineralogy, Vol 2, edited by Marfunin A. S. Berlin, Heidelberg, New York: Springer. p. 322–329.
- Korkisch J. 1989. *Handbook of ion exchange resins*. Boca Raton: CRC Press. pp. 352.
- Kutschera W., Collon P., Friedmann H., Golser R., Hille P., Priller A., Rom W., Steier P., Tagesen S., Wallner A., Wild E., and Winkler G. 1997. VERA: A new AMS facility in Vienna. *Nuclear Instruments and Methods in Physics Research B* 123: 47–50.
- Mader D., and Koeberl C. 2009. Using Instrumental Neutron Activation Analysis for geochemical analyses of terrestrial impact structures: Current analytical procedures at the University of Vienna Geochemistry Activation Analysis Laboratory. *Applied Radiation and Isotopes* 67: 2100–2103.
- Mattinson J. M. 2005. Zircon U-Pb chemical abrasion ("CA-TIMS") method: Combined annealing and multi-step partial dissolution analysis for improved precision and accuracy of zircon ages. *Chemical Geology* 220: 47–66.

- Michelmayr L. 2007. Isobar separation with post-stripping for the measurement of cosmogenic ^{10}Be at VERA, *Diploma Thesis*, University Vienna, Vienna, Austria.
- Münker C., Weyer S., Scherer E., and Mezger K. 2001. Separation of high field strength elements (Nb, Ta, Zr, Hf) and Lu from rock samples for MC-ICPMS measurements. *Geochemistry, Geophysics, Geosystems* 2: doi: 10.1029/2001GC000183.
- Peterman E. M., Mattinson J. M., and Hacker B. R. 2012. Multi-step TIMS and CA-TIMS monazite U–Pb geochronology. *Chemical Geology* 312–313: 58–73.
- Pin C., and Zalduegui J.F.S. 1997. Sequential separation of light rare-earth elements, thorium and uranium by miniaturized extraction chromatography: application to isotopic analyzes of silicate rocks. *Analytica Chimica Acta* 339: 79–89.
- Potts P. J. 1987. A handbook of silicate rock analysis. Glasgow: Blackie. 622 p.
- Priller A., Brandl T., Golser R., Kutschera W., Puchegger S., Rom W., Steier P., Vockenhuber C., Wallner A., and Wild E. 2000. Extension of the measuring capabilities at VERA. *Nuclear Instruments and Methods in Physics Research B* 172: 100–106.
- Reimer L. 1998. Scanning electron microscopy, Physics of image formation and microanalysis. Second edition. Heidelberg: Springer. 527 p.
- Reimold W. U., Koeberl C., and Bishop J. 1994. Roter Kamm impact crater, Namibia: Geochemistry of basement rocks and breccias. *Geochimica et Cosmochimica Acta* 58: 2689–2710.
- Reinhard M. 1931. Universaldrehtischmethoden. Basel, Switzerland: Birkhäuser. 118 p.
- Schoene B., Crowley J. L., Condon D. J., Schmitz M. D., and Bowring S. A. 2006. Reassessing the uranium decay constants for geochronology using ID-TIMS U–Pb data. *Geochimica et Cosmochimica Acta* 70: 426–445.
- Severin K. P. 2004. Energy dispersive spectrometry of common rock forming minerals. Dordrecht, Netherlands: Kluwer Academic Publishers. 225 p.

- Steier P., Golser R., Kutschera W., Priller A., Vockenhuber C., and Winkler S. 2004. VERA, an AMS facility for “all” isotopes. *Nuclear Instruments and Methods in Physics Research B* 223–224: 67–71.
- Steier P., Golser R., Liechtenstein V., Kutschera W., Priller A., Vockenhuber C., and Wallner A. 2005. Opportunities and limits of AMS with 3-MV tandem accelerators. *Nuclear Instruments and Methods in Physics Research B* 240: 445–451.
- Stöffler D., and Langenhorst F. 1994. Shock metamorphism of quartz in nature and experiment: I. Basic observation and theory. *Meteoritics and Planetary Science* 29: 155–181.
- Thompson M. D., Grunow A. M., and Ramezani J. 2007. Late Neoproterozoic paleogeography of the Southeastern New England Avalon Zone: Insights from U-Pb geochronology and paleomagnetism. *Geological Society of America Bulletin* 119: 681–696.
- Vandecasteele C., and Block C. B. 1993. Modern methods for trace element determination. Chippenham, Wiltshire, UK: John Wiley & Sons. 330 p.
- Weyer S., Muenker C., Rehkaemper M., and Mezger K. 2002. Determination of ultra-low Nb, Ta, Zr and Hf concentrations and the chondritic Zr/Hf and Nb/Ta ratios by isotope dilution analyses with multiple collector ICP-MS. *Chemical Geology* 187: 295–313.

3. Petrology, major and trace element geochemistry, geochronology, and isotopic composition of granitic intrusions from the vicinity of the Bosumtwi impact crater, Ghana

Anna Losiak¹, Toni Schulz^{1,2}, Robert Buchwaldt³, and Christian Koeberl^{1,4}

¹Department of Lithospheric Research, University of Vienna, Althanstrasse 14, A-1090 Vienna, Austria (anna.losiak@univie.ac.at).

²Steinmann-Institut für Geologie, Mineralogie und Paläontologie, University of Bonn, Poppelsdorfer Schloss, 53115 Bonn, Germany.

³Department of Earth, Atmospheric and Planetary Sciences, Massachusetts Institute of Technology, 77 Massachusetts Avenue, Cambridge, MA 02139-4307, USA.

⁴Natural History Museum, Burgring 7, A-1010 Vienna, Austria.

Article was submitted to “Lithos”, currently it is under review.

Abstract

The Bosumtwi crater is 10.5 km in diameter, 1.07 Ma old, well preserved impact structure located in Ghana (centered at 06°30'N, 01°25'W). It was excavated in rocks of the Early Proterozoic Birimian Supergroup, part of the West African craton. Here, we present a full and detailed characterization of the three granitoid complexes and one mafic dike in the vicinity of the Bosumtwi crater in terms of petrology, major and trace element geochemistry, geochronology, and isotopic composition. This allows us to characterize magmatic evolution

of the West African Craton in this area and better understand the geological framework and target rocks of the impact.

This study shows that the similar composition (strongly peraluminous muscovite granites and granodiorites) and age (between 2092 ± 6 Ma and 2098 ± 6 Ma) of all granitic intrusions in the proximity of the Bosumtwi crater suggest that they are co-genetic. Granitoids were probably formed as a result of anatexis of TTGs (or rocks derived from them) at relatively low pressure and temperature. We propose that the intrusions from the Bosumtwi area are genetically related to the Bansa granite occurring to the east of the crater and can be classified as basin-type, late-stage granitoids. Also a mafic dike located to the NE of the Bosumtwi crater seems to be genetically related to those felsic intrusions. Based on those findings a revised version of the geological map of the Bosumtwi crater area is proposed.

3.1. Introduction

The Bosumtwi structure, located in Ghana, West Africa, is a well preserved, 10.5 km wide impact crater dated at 1.07 Ma old (e.g., Koeberl et al. 1997, Koeberl et al. 2007). This relatively young impact structure is associated with one of only four tektite strewn fields known on Earth (e.g., Koeberl et al. 1997). The crater structure was drilled in 2004 by the International Continental Scientific Drilling Program (ICDP) (Koeberl et al. 2007), and since then it has been the object of intensive research on various aspects of impact cratering (e.g., Dai et al. 2005, Boamah et al. 2006, Karikari et al. 2007, Coney et al. 2010, Ferrière et al. 2010).

To obtain a complete picture of the structure it is crucial to have an in-depth knowledge about target rocks affected by the impact. Previous research (e.g., Jones et al. 1981, Jones 1985, Koeberl et al. 1998, Boamah and Koeberl 2003, Dai et al. 2005, Koeberl and Reimold 2005, Karikari et al. 2007, Ferrière et al. 2010) provided information about the characteristics of the metasediments forming a large part of the target material, but granitic intrusions present in the crater area have not yet been studied in detail.

The aim of this project is to provide a full and detailed characterization of the granitoids occurring in the vicinity of the Bosumtwi crater in terms of petrology, major and trace element geochemistry, isotopic composition as well as geochronology. This will help us to better understand target rocks where this impact structure was emplaced and the early evolution of the West African craton.

3.2. Geological Background

The Bosumtwi impact crater was excavated in metasedimentary and metavolcanic rocks of the Early Proterozoic Birimian Supergroup of the West African craton (e.g., Jones et al. 1981, Figure 3.1). The West African craton is a wide growth zone of crust formed during the Paleoproterozoic and shows very limited influence of an older, Archean crustal component (e.g., Boher et al. 1992, Taylor et al. 1992, Doumbia et al. 1998, de Kock et al. 2011). Although some small areas may have components as old as 2300 Ma (e.g., Gasquet et al. 2003), the main deposition of the Birimian Supergroup started around 2200 Ma ago. Most authors agree that Birimian Supergroup was deposited in an arc-back-arc environment (Attoh et al. 2006, Dampare et al. 2008, de Kock et al. 2011) possibly with involvement of subduction of an intra-oceanic plateau (Abouchami et al. 1990). Both, the volcanic and the sedimentary series are intruded by extensive acidic magmatism (e.g., Hirdes et al. 1996, Hirdes and Davis 1998, Oberthür et al. 1998, Naba et al. 2004, Lompo 2010).

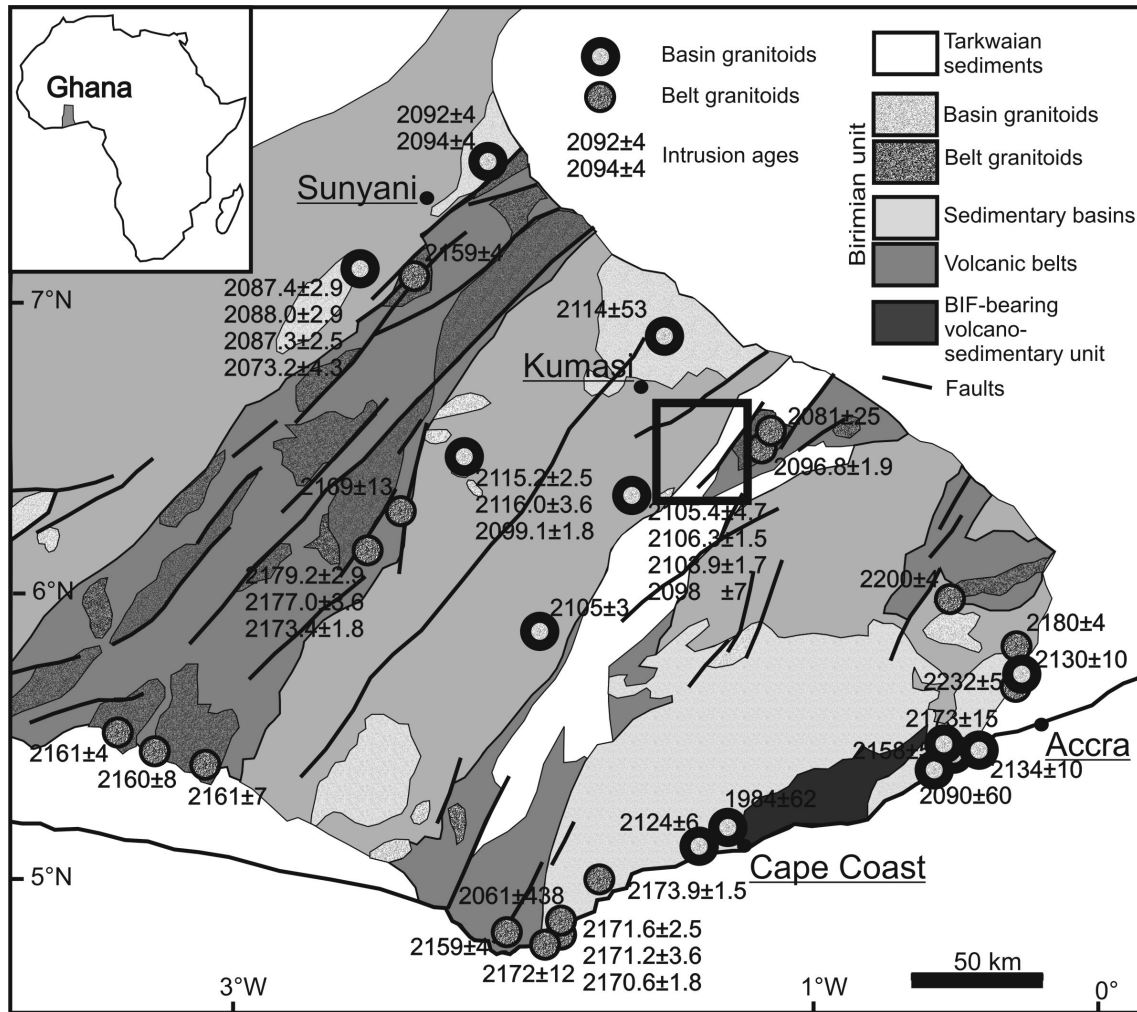


Figure 3.1. Geological map of a southern part of Ghana with ages of some of the dated granitic intrusions (Oberthur et al. 1998, Hirdes et al. 1992, Leube et al. 1990, Grenholm et al. 2011, Attah et al. 2006, Feybesse et al. 2006). The map is based on Feybesse et al. (2006); the division between belt- and basin-type granitoids is based on Hirdes et al. (1992). The black square refers to the location of Figure 3.2.

The Birimian rocks were metamorphosed during the Eburnean tectono-thermal event ~2092 Ma ago at greenschist-facies and (locally) amphibolites-facies conditions. Average peak temperatures reached around 500 – 650 °C and peak pressures of 500 – 600 MPa (Leube et al. 1990, Hirdes et al. 1992, Taylor et al. 1992, John et al. 1999, Debat et al. 2003, Galipp et al. 2003, Feybesse et al. 2006, Karikari et al. 2007). The Birimian Supergroup can be divided into two coeval units: volcanic belts and sedimentary basins aligned in multiple parallel structural features accompanied by numerous, large granitoid intrusions (Figure 3.1).

The sedimentary unit of the Birimian Supergroup consists of volcanoclastic rocks, argillites, and turbidites that are metamorphosed to meta-greywackes, phyllites, schists, and shales (Leube et al. 1990). The volcanic unit has a predominantly tholeiitic chemical

composition and consists of metamorphosed basalts and andesites that occur as different types of schists, including hornblende-actinolite-, calcite-chlorite-, mica-schists, and in some cases amphibolites. The Birimian units are locally overlain by discordant Tarkwaian detrital shallow water sediments (Leube et al. 1990, Oberthür et al. 1998, Koeberl and Reimold 2005, Feybesse et al. 2006). Some areas of the Birimian Supergroup (e.g., Feybesse et al., 2006) have undergone hydrothermal mineralization of gold between ~2063 Ma and ~2025 Ma (Oberthür et al. 1998, Pigois et al. 2003).

The Sm-Nd isotope characteristics of Birimian felsic rocks ($\epsilon_{\text{Nd}} = 1.5\text{-}2.7$; Doumbia et al. 1998) indicate that most of the crust was juvenile and generated between 2.2 and 2.1 Ga (Abouchami et al. 1990, Boher et al. 1992, Doumbia et al. 1998, Gasquet et al. 2003, Pawling et al. 2006). Also the Rb-Sr data (strontium initial ratios $^{87}\text{Sr}/^{86}\text{Sr} = 0.703106$), obtained for the Wakawaka gabbro and Bomburi granodiorite of northern Ghana, suggest that the source material of the magma was quite primitive (de Kock et al. 2011). However, other research suggests that some felsic Birimian rocks are not truly juvenile and were formed from pre-Birimian crustal material differentiated around 2300 Ma (Gasquet et al. 2003, de Kock et al. 2011). So far, such an Archean crustal component was detected in only two areas of Western Africa: 1) in the proximity of the Archean Man nucleus located in the western part of Ivory Coast, Liberia, and Sierra Leone (Kouamelan et al. 1997) and 2) within the Winneba granite located in the southern part of Ghana, west of Accra (Taylor et al. 1992).

3.2.1. Intrusive bodies: granitoids

3.2.1.1. Traditional view

Granitoids constitute about 70% of the rocks of the overall Birimian Supergroup (Naba et al. 2004, Lompo 2010). The granitoids in Ghana are traditionally separated into two main groups based on their respective host rocks location and shared geochemical properties: - the belt (Dixcove) granitoids and the basin (Cape Coast) granitoids (Figure 3.1). However, two additional types (distinguished based on their atypical geochemical and/or isotopic

properties) are locally present: the Winneba (southern Ghana, east of Cape Coast, Figure 3.1) and Bongo (northern Ghana, near Bolgatanga city) granitoids. The following description of Ghanaian granitoids is based on Wright et al. (1985), Leube et al. (1990), and Hirdes et al. (1992); average chemical compositions of basin and belt granitoids from the literature are provided in Table 3.1 (Leube and Hirdes 1986, John et al. 1999, Grenholm et al. 2011).

The belt-type granitoids are present as rather small bodies, located in the proximity of the Birimian volcanic facies (belts). Texturally, they are unfoliated and show a pronounced retrograde mineral alteration; plagioclase is commonly saussuritized or sericitized. Hornblende is the dominant mafic constituent. Geochemically, belt-type granitoids are metaluminous with a dioritic to monzonitic composition (quartz diorite, tonalite and trondhjemite, granodiorite, adamellite, granite). The belt-type granitoids are characterized by higher contents of Na_2O and CaO than the basin granitoids and seem to be geochemically related to tholeiitic basalts forming large parts of the volcanic belts. Belt-type granitoids in eastern Ghana were emplaced from ~2179 Ma to ~2160 Ma (Hirdes et al. 1996, Hirdes and Davis 1998) or, according to other authors, between ~2245 Ma to ~2132 Ma (Davis et al. 1994, Taylor et al. 1992) at approximately the same time as volcanics of the Birimian Supergroup (e.g., Feybesse et al. 2006).

The basin-type granitoids are usually emplaced within the sedimentary basins located between volcanic belts. Texturally, they show strong magmatic foliation, biotite is the dominant mafic constituent and little alteration is present. Geochemically, they are peraluminous and granodioritic in composition (quartz diorites, tonalites and trondhjemites, granodiorites, adamellites, and granites), with higher abundances of Rb and K_2O compared to belt-type intrusions. Based on geochronology, the eastern Ghanaian Basin-type granitoids are younger than belt-type granitoids, and were emplaced between ~2116 and ~2088 Ma (Hirdes et al. 1992, Davis et al. 1994, Hirdes and Davis 1998).

Table 3.1. Whole-rock chemical composition of samples collected from intrusions located in the proximity of Bosumtwi crater analyzed in this study, and average whole rock chemical composition of basin- and belt-type intrusions from Ghana based on the literature (Leube and Hirdes 1986, John et al. 1999, Grenholm et al. 2011).

	BOS 10A	BOS 10B	BOS 11	BOS 12PI	BOS 12Qz	BOS 13	BOS 14A	BOS 14B	BOS 15	BOS 16	BOS 17	BOS 18	BOS 19A	BOS 19B	Basin intrusion			Belt intrusion		
This study															(Leube and Hirdes. 1986), (Grenholm et al. 2011)			(Leube and Hirdes. 1986), (John et al. 1999), (Grenholm et al. 2011)		
Granitic intrusions																				
	Pepiakese					Mafic dyke	Kumasi			Southern					Average	St. dev.	No. of sample	Average	St. dev.	No. of sample
SiO ₂	55.9	77.1	73.9	-	-	49.9	73.6	71.7	75.5	69.1	64.8	63.8	59.8	64.7	69.4	3.33	56	67.1	6.10	60
TiO ₂	0.76	0.15	0.12	-	-	1.06	0.19	0.2	0.12	0.41	0.51	0.5	0.78	0.82	0.38	0.17	56	0.39	0.18	60
Al ₂ O ₃	14.4	14.4	15.0	-	-	10.3	15.9	15.8	14.0	16.6	16.0	16.0	18.4	17.4	15.3	1.51	56	15.0	1.85	60
Fe ₂ O ₃	8.23	1.06	0.99	-	-	12.5	0.84	1.95	1.01	4.16	6.29	5.11	7.65	5.41	2.85	1.18	56	4.07	1.82	60
MnO	0.1	0.01	0.01	-	-	0.18	0.00	0.00	0.01	0.01	0.20	0.05	0.11	0.03	0.04	0.02	56	0.07	0.03	60
MgO	9.31	0.50	0.49	-	-	14.4	0.28	0.48	0.45	1.84	2.50	3.58	2.27	3.11	0.90	0.46	56	1.42	1.24	60
CaO	5.82	0.33	0.84	-	-	9.02	0.42	0.61	0.5	0.25	0.96	2.18	1.55	0.63	2.38	0.72	56	3.42	2.00	60
Na ₂ O	2.99	5.22	4.74	-	-	1.86	5.07	4.42	4.98	4.10	4.32	3.27	3.43	2.3	4.29	0.83	56	4.47	0.61	60
K ₂ O	1.32	1.67	2.09	-	-	0.33	2.11	2.03	1.60	1.93	1.48	1.69	2.04	1.93	3.01	1.16	56	2.11	0.86	60
P ₂ O ₅	0.18	0.02	0.02	-	-	0.11	0.02	0.02	0.02	0.09	0.13	0.14	0.28	0.33	0.11	0.05	56	0.11	0.08	60
SO ₃	-	-	-	-	-	-	-	-	-	-	-	-	-	-	0.02	0.02	56	0.02	0.07	60
LOI	1.47	0.01	0.92	-	-	0.78	1.17	1.77	0.88	2.37	3.06	4.20	3.79	3.33	0.80	0.25	56	1.37	0.82	60
Total	100.41	100.44	99.07	-	-	100.42	99.63	98.96	99.07	100.86	100.25	100.56	100.09	99.94	99.49	0.29	56	99.48	0.30	60
Sc	19.9	3.45	2.76	0.36	0.11	26.6	2.28	2.53	2.67	2.64	13.6	12.6	11.8	14.7	6.52	3.35	56	11.09	5.81	58
V	127	16	7	<1	<1	234	7	7	11	46	84	81	52	111	20	19	55	47	40	60
Cr	623	42	31	18	25	1173	32	35	35	42	157	152	33	108	15	18	42	34	42	53
Co	39	2	2	0	0	69	0	2	2	2	14	9	12	18	33	29	56	22	22	60
Ni	243	13	11	5	1	613	2	7	11	54	58	51	14	49	13	12	46	17	19	53
Cu	22.6	7.2	4.7	4.1	2.4	105.7	8.6	0.9	3.3	10.7	5.5	7.2	4	28.2	11	9	42	19	17	51
Zn	97	16	13	1	1	87	15	47	12	70	76	69	82	124	71	89	42	55	19	51
Ga	60	<19	<10	<20	<0.4	7	<12	8	<21	<11	25	10	23	20	19	3	14	18	3	7
As	24.1	9.47	1.99	0.94	0.22	0.84	2.94	4.19	1.74	2.17	24.0	2.19	15.2	2.56	-	-	-	-	-	-
Se	<2.4	<1.2	<1.2	<0.6	<0.5	2.1	<1.1	<0.8	<0.6	<1.3	<2.1	<1.9	<1.9	<2.0	-	-	-	-	-	-
Br	<0.4	<1.2	<1.2	<1.1	0.1	0.6	<1.1	<0.8	<1.2	<1.4	<1.5	<1.0	<1.2	<1.2	-	-	-	-	-	-
Rb	44.1	37.4	50.7	3.7	0.1	10.8	55.9	64.4	38.3	73.6	54.6	62.9	70	69.3	116	59.2	56	54.8	24.8	60
Sr	520	344	427	409	3	237	453	360	358	326	247	385	462	362	469	210	56	485	325	60
Y	16	5	7	7	1	18	3	3	4	10	14	13	15	24	11	14	56	22	20	60
Zr	87	33	67	27	6	79	75	69	29	105	111	107	117	146	154	71	56	147	75	60
Nb	2	2	2	<1	<1	4	4	4	2	4	4	4	5	6	5.06	3.36	14	5.27	2.45	9
Sb	0.29	0.09	0.19	0.13	0.08	0.14	<0.2	<0.3	<0.3	<0.4	0.26	<0.3	<0.3	<0.3	-	-	-	-	-	-
Cs	1.48	0.79	1.19	0.23	0.06	0.96	1.54	2.10	0.90	0.95	2.87	3.23	3.58	3.56	2.58	2.13	14	3.27	4.19	7
Ba	380	881	1221	112	<5	190	720	742	802	570	387	540	582	606	841	376	56	757	302	60
La	13.7	16.4	24.3	3.57	0.72	8.96	18.0	16.5	14.2	13.7	19.1	18.7	22.8	37.4	29.4	20.1	14	20.2	9.9	9
Ce	33.9	26.4	45.2	6.38	1.50	18.3	35.4	34.9	25.3	23.1	35.5	36.6	43.3	70.9	57.5	37.9	14	41.3	18.5	9
Nd	22.6	11.4	18.6	3.54	0.33	8.52	18.6	15.0	11.6	10.5	17.5	18.5	26.4	33.6	10.56	9.10	56	7.07	6.05	60
Sm	5.36	2.21	2.77	1.01	0.11	2.86	2.63	2.02	1.77	1.71	3.70	3.34	4.78	8.17	3.18	1.67	14	3.05	1.28	9
Eu	1.44	0.72	0.76	0.41	0.03	1.02	0.71	0.64	0.62	0.60	1.15	0.98	1.41	2.39	0.81	0.21	14	0.92	0.28	9
Gd	4.04	1.68	2.05	1.05	<0.5	2.47	1.06	1.15	1.08	1.25	2.63	2.14	2.74	4.96	2.43	1.33	14	2.97	1.02	9
Tb	0.57	0.17	0.24	0.17	0.01	0.39	0.13	0.12	0.16	0.13	0.40	0.32	0.46	0.78	0.31	0.20	14	0.42	0.15	7
Dy	-	-	-	-	-	-	-	-	-	-	-	-	-	-	1.46	1.11	14	2.23	0.85	7
Tm	0.22	0.18	0.18	0.10	0.08	0.25	0.16	0.04	0.15	0.18	0.16	0.23	0.25	0.28	0.10	0.09	14	0.16	0.08	7
Yb	1.38	0.41	0.63	0.79	0.06	1.22	0.15	0.20	0.35	0.36	1.07	1.11	1.03	1.87	0.69	0.62	13	1.05	0.43	9
Lu	0.21	0.07	0.12	0.13	0.01	0.19	0.03	0.03	0.06	0.07	0.19	0.16	0.15	0.29	0.10	0.09	14	0.16	0.08	9
Hf	3.49	1.98	3.22	2.05	0.46	2.09	3.03	2.94	1.89	1.94	3.35	3.37	3.58	4.13	4.09	1.58	14	3.56	0.85	9
Ta	0.16	0.31	0.25	0.03	0.01	0.20	0.24	0.28	0.24	0.26	0.29	0.25	0.37	0.37	0.39	0.30	13	0.36	0.25	9
W	-	-	-	-	-	2.0	-	-	-	-	-	-	-	-	-	-	-	-	-	-
Ir (ppb)	<2.3	<1	<1	<0.5	<0.4	3.6	<0.9	<0.6	<0.5	<1.1	<1.8	<1.7	<1.6	<1.6	-	-	-	-	-	-
Au (ppb)	1.1	<2.6	<3.5	<2.4	0.2	1.4	<2	<2.7	<2.7	<4.1	<3.1	<2.8	<2.7	<2.8	-	-	-	-	-	-
Th	1.21	3.58	6.49	2.49	0.22	0.83	3.15	3.33	3.69	3.01	3.02	2.97	2.95	3.69	17.5	12.8	56	9.34	5.64	60
U	0.46	1.28	1.74	1.66	0.27	0.51	0.83	0.60	1.05	0.94	1.40	1.26	1.02	1.31	3.84	3.00	56	3.52	2.41	60
Pb	6.0	13.5	22.9	17.5	0.1	3.6	9.8	10.5	16.2	9.0	7.7	8.4	11.6	9.2	20.81	10.44	42	14.62	10.87	42

Note: Major element data (in wt%) along with some trace elements (V, Ni, Cu, Zn, Rb, Sr, Y, Zr, Nb, Ba and Pb) as measured by XRF, the other elements as measured by INAA. All Fe as Fe₂O₃. Trace elements data in ppm, except as noted.

3.2.1.2. Difficulties with the traditional granitoid classification

Detailed analysis has revealed that the traditional, host-rock-based classification of the granitoids presented above is an oversimplification. There are examples where intrusions are classified as belt-type (e.g., Koeberl and Reimold 2005), but, based on their age and geochemical and geochronological properties (e.g., Oberthür et al. 1998), they belong to the basin-type (e.g., Feybesse et al. 2006). One example is the Bansa granite, an intrusion that was emplaced within the Ashanti belt in the proximity of the Bosumtwi crater (Figure 3.2). Traditionally, the Bansa granite was considered a belt-type intrusion based on its location and petrologic properties. However, the age of its emplacement (2081 ± 25 Ma: Rb-Sr isochron by Leube et al., 1990; or 2097 ± 2 Ma: a titanite-feldspar Pb-Pb data isochron by Oberthür et al. 1998) falls within the basin-type emplacement period.

Recently, many new Birimian granitoid classifications were proposed (e.g., Doumbia et al. 1998, Egal et al. 2002, Gasquet et al. 2003, Naba et al. 2004, Feybesse et al. 2006, Lompo 2010, Metelka et al. 2011, Perrouty et al. 2012). The most comprehensive one is the categorization by de Kock et al. (2011), which is based on a revision of geochemical, geochronological, tectonic, and isotopic data from the entire West African craton. These authors proposed four emplacement phases of granitic bodies:

1. Intrusions older than 2208 Ma; no rocks from this period were identified and the only surviving evidence is inherited zircon cores in few orthogneisses (e.g., Feybesse et al. 2006, Doumbia et al. 1998).
2. Tonalite-Trondhjemite-Granodiorite (TTG) granitoids, which intruded volcanic belts (and also to some extent the basins) between 2150 and 2126 Ma. This phase corresponds roughly to the belt-type granitoids of the traditional classification.
3. Intrusions between 2116 Ma and 2097 Ma, defined by intrusion of post-deformational S-type granitoids. These granitoids correspond to the basin-type, as they were more commonly (but not exclusively) emplaced within basins.

4. Late-stage granitoids that were emplaced between 2097 and 2074 Ma. These granites can be either undeformed (e.g., in the Ashanti belt) or foliated (Bandama-Katiola region) and are often significantly hydrothermally altered.

The alternative classifications generally agree with the de Kock et al. (2011) scheme, but differ by (i) recognizing an additional main phase of granitoid emplacement between 2180-2150 Ma (e.g., Perrouty et al. 2012), (ii) ignoring the oldest phase, as only very limited evidence of its existence was found (e.g., Doumbia et al. 1998), (iii) combining some of the emplacement phases (e.g., Feybesse et al. 2006), and (iv) providing slightly different ages for the various emplacement periods (e.g., Doumbia et al. 1998, Egal et al. 2002, Gasquet et al. 2003, Naba et al. 2004, Feybesse et al. 2006, Lompo 2010, Metelka et al. 2011, Perrouty et al. 2012).

In this study the new classification by de Kock et al. (2011) will be used, as it provides the most current description of the rocks and processes that formed the Birimian Supergroup, but we refer also to the older basin/belt classification (because most of previous studies used it).

3.2.1.3. The granitoid component in the proximity of the Bosumtwi impact crater

The fraction of granitoids in the rock assemblage into which the Bosumtwi crater was excavated is estimated to be about 2% (Reimold et al. 1998). Intrusions are located within metasediments of the Birimian Supergroup, and are relatively small (the three largest bodies are less than 3 km wide; Koeberl and Reimold 2005; Figure 3.2). Although generally unfoliated, some granitic rocks occasionally exhibit a N-E foliation and are penetrated by aplite and quartz veins (Boamah and Koeberl, 2003). Additionally, numerous small dikes (<1 m wide) of biotite-bearing granites with granophyric textures are frequently observed in the crater rim (Moon and Manson 1967, Jones 1985, Reimold et al. 1998). These dikes are intruded conformably parallel to the foliation of Birimian metasediments (Boamah and Koeberl 2003). Small dikes were also found to have been emplaced below the crater (Coney et al. 2007, Ferrière et al. 2007). Some of the dikes near the Bosumtwi crater show strong alteration (Boamah and Koeberl 2003).

In their map of the Bosumtwi impact crater, Koeberl and Reimold (2005), partly following earlier mappings (Woodfield 1966, Moon and Mason 1967), divided the granitic intrusions into belt- and basin-type bodies based mainly on petrographic observations performed in the field (C. Koeberl, personal communication). Intrusions located on the northern side of the crater were classified as basin-type and were thought to be related to the Kumasi pluton (Figure 3.2). The Kumasi intrusion is located in the NE part of the Kumasi basin and was dated between 2136 ± 9 Ma and 2090 ± 44 Ma (Adadey et al. 2009), with the main emplacement phase at 2116 ± 2 Ma (Hirdes et al. 1992) and 2112 ± 19 Ma (Adadey et al. 2009). Plutons on the southern side were classified as belt-type and they were thought to be related to the Bansa intrusion, which is located about 10 km to the east of the Bosumtwi Lake (Figure 3.2).

The contents of granite found in the within-crater impact breccias is low and varies between zero in the LB-08A core (Deutsch et al. 2007, Ferrière et al. 2007) up to only 0.6 vol% in the LB-07A core (Coney et al. 2007, 2010). Contribution of granitic clasts in breccias and suevites located outside of the crater is higher and commonly varies between 0 and 3 vol% (Boamah and Koeberl 2006), although the contents may be as high as 3.4 vol% (suevites from south of the crater) or even 5.9 vol% (suevites from the north of the crater) and locally may be as high as 18 vol% (Coney et al. 2010). Granitoid clasts found in the northern suevite are ~10 cm (rarely up to 25 cm) in size, while those from the southern suevite are up to 5 cm in size (Coney et al. 2010). However, some older studies reported a much higher contribution of granitic material to target rocks of this impact structure. Based on geochemical modeling of major elements, Jones (1985) concluded that the Ivory Coast tektites (impact glasses formed from the thin surface layer of target material during the impact event) contain about 28 vol% of Papiakese granite. According to Koeberl et al. (1998) Ivory Coast tektites have a ~15 wt% granitic dike (of Southern intrusion composition) component and 14 wt% Papiakese granite, but based on the $\delta^{18}\text{O}$ values, the Papiakese granite component should be lower.

3.2.2. Intrusive bodies: mafic intrusions

3.2.2.1. General description of mafic intrusions

Mafic intrusions, although common across the entire West African craton, are much smaller compared to felsic plutons, and usually form dikes (e.g., Hirdes et al. 1996, Doumbia et al. 1998, Feybesse et al. 2006, Adadey et al. 2009, Perrouty et al. 2012). Mafic intrusions are usually described as gabbro, dolerite, or amphibolite.

Only few age data for emplacement of mafic intrusions are available, but based on tectonic and crosscutting relations, several generations of mafic intrusions in Ghana can be identified (Agyei Duodu et al., 2009). The dates of mafic intrusions include: 2222 ± 32 Ma for a gabbroic sill within metasedimentary rock from the Sewfi belt located to the NNW from Bosumtwi crater (Feybesse et al. 2006), 2102 ± 13 Ma for an unfoliated gabbro from the Kumasi basin (Adadey et al. 2009), 2095 ± 34 Ma for an amphibolite lens intercalated with banded orthogneiss from the Winneba granite area (Feybesse et al. 2006), and 2006 ± 40 Ma for an amphibolite band intercalated with sedimentary rocks of the Sewfi belt with possible metamorphic overprint (Feybesse et al. 2006).

3.2.2.2. Mafic intrusions in the proximity of the Bosumtwi crater

Most of the mafic intrusions in the proximity of the Bosumtwi crater are dikes of gabbroic or doleritic composition (Woodfield 1966, Moon and Mason 1967, Jones 1985). There is one small amphibolite body located north of the lake (e.g., Koeberl and Reimold 2005). Dikes are arranged in two directions: NNE-SSW following the orientation of the Ashanti belt, and NNW-SSE direction. The dikes of the latter orientation are much longer than those of the former. They have to be younger than 2097 ± 2 Ma because they crosscut the Bansa granite (Oberthür et al. 1998). The age of the first family of dikes is unknown.

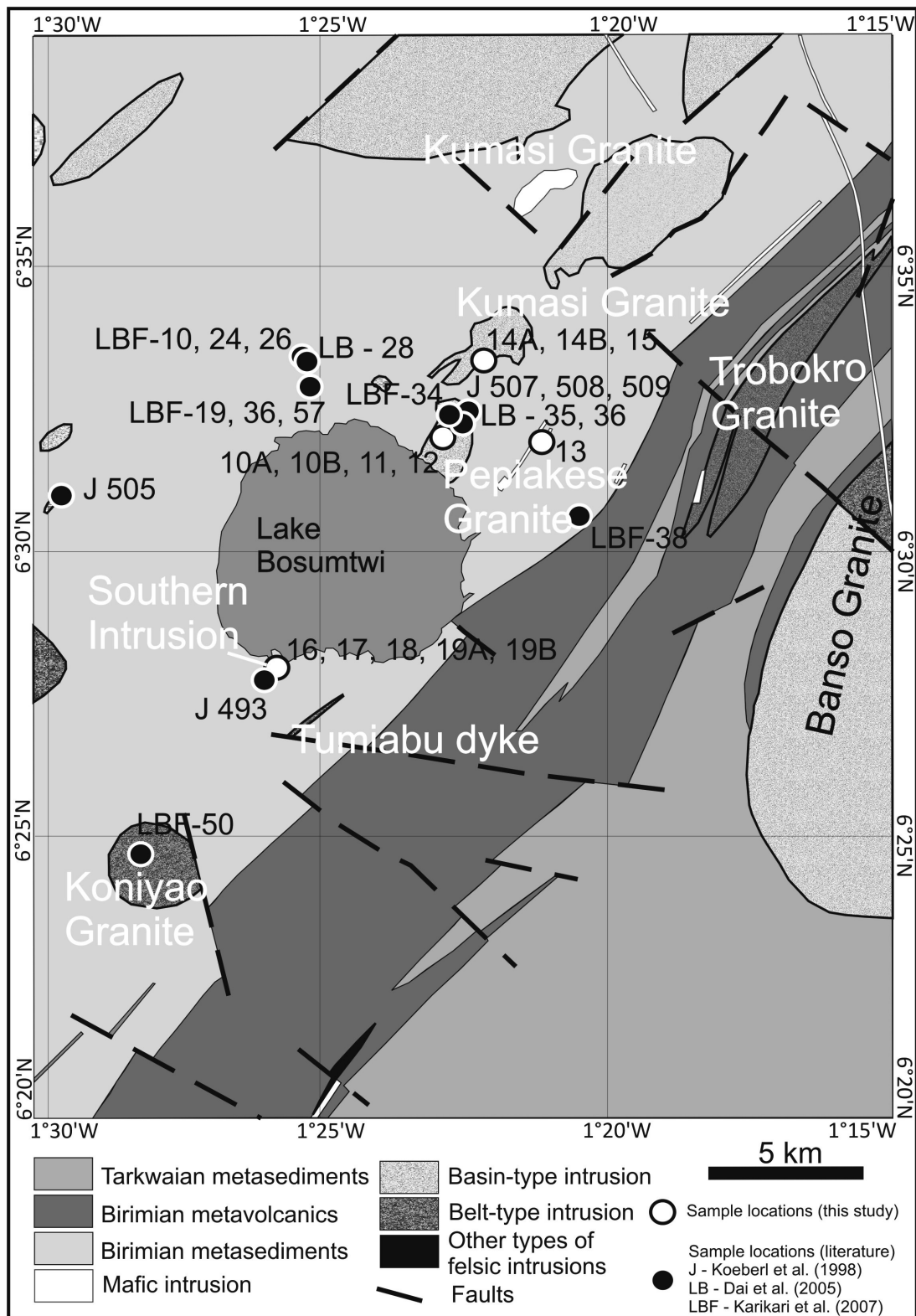


Figure 3.2. Geological map of the vicinity of Bosumtwi crater and sampling locations for this study. Map based on Koeberl and Reimold (2005). Samples used in this study are marked only with a number for the sake of image readability.

3.3. Samples and methods

3.3.1. Samples

As field mapping and sampling in the area of the Bosumtwi crater was seriously impeded by the relative remoteness of the area, dense vegetation, presence of a lateritic cover, and the scarcity of fresh outcrops, sampling was possible in only a few places.

Thirteen samples of intrusive bodies from the vicinity of the Bosumtwi crater were collected by F. Karikari in 2007 (Table 3.1). They represent four different intrusive bodies (Figure 3.2). Twelve samples come from three felsic plutons. Two of those intrusions (referred to as Pepiakese and Kumasi intrusions) located to the NE of the crater were previously described as basin-type granitoids and one intrusion (referred to as the Southern intrusion) was classified as a belt intrusion (Koeberl and Reimold 2005). One sample comes from a small mafic dike located to the north-east of the Bosumtwi structure.

3.3.2. Methods

3.3.2.1. Petrography

Petrographic characteristics of the samples are provided based on optical microscopy (including point counting).

3.3.2.2. Geochemistry

All geochemical analyses were performed at the Department of Lithospheric Research, University of Vienna. Samples were prepared for analysis by powdering them in a mechanical agate mill. Powders were later used to prepare samples for X-ray fluorescence spectrometry (XRF) measurements. About 9 g of the whole-rock powder was used for preparing pressed pellets for minor element XRF analysis and 3 g was used for preparing fused pellets for major element XRF analysis. The contents of major elements (SiO_2 , TiO_2 ,

Al_2O_3 , Fe_2O_3 , MnO , MgO , CaO , Na_2O , K_2O , and P_2O_5) and some trace elements (As, Ba, Ce, Co, Cr, Cu, Ga, La, Mo, Nb, Nd, Ni, Pb, Rb, Sc, Sm, Sr, V, Y, Yb, Zn, and Zr) were determined by XRF (details of the method are given in Reimold et al. 1994). Sample BOS12 was not large enough for a representative analysis of major elements; for this sample only minor element contents were measured.

Between 110 and 160 mg whole-rock sample powder was used for instrumental neutron activation analysis (INAA) to measure the contents of some major elements (Na, K, Fe) and trace elements including the REE (Sc, Cr, Co, Ni, Zn, Ga, As, Se, Br, Rb, Sr, Zr, Sb, Cs, Ba, La, Ce, Nd, Sm, Eu, Gd, Tb, Tm, Yb, Lu, Hf, Ta, W, Ir, Au, Th, and U). Samples were processed and measured according to the method presented in Mader and Koeberl (2009).

The element concentrations measured by both XRF and INAA are generally in good agreement. In this study we report only the measurement obtained by the method with the higher precision for each element. Elements reported as measured by XRF are all major elements along with some trace elements (V, Ni, Cu, Zn, Rb, Sr, Y, Zr, Nb, Ba, Mo, and Pb). Other elements are reported as measured by INAA. Due to the low Tm contents in the INAA standards used, the Tm measurements have large errors.

3.3.2.3. ^{147}Sm - ^{143}Nd and ^{176}Lu - ^{176}Hf isotopic measurements

Seven samples, representing three granitic and one mafic intrusion were selected for the isotopic study (the sample BOS16 was lost during the preparation process for the ^{176}Lu - ^{180}Hf measurement). Hafnium and Nd isotope compositions, as well as Lu, Hf, Sm, and Nd concentrations, were obtained by isotope dilution, employing mixed ^{176}Lu - ^{180}Hf and ^{149}Sm - ^{150}Nd tracers following the protocols of Münker et al. (2001) and Weyer et al. (2002). Lutetium and Hf were separated using Eichrom® Ln spec resin following the protocols described in Münker et al. (2001) and Weyer et al. (2002). From the remaining matrix, Sm and Nd were separated following the method of Pin and Zaldegui (1997). Complete digestion of the samples was achieved by table top digestion, followed by Parr® bomb digestion for three days. Lu, Hf, Sm and Nd were measured using the Finnigan® Neptune multicollector ICP-MS at Bonn. Measured $^{176}\text{Hf}/^{177}\text{Hf}$ were mass bias-corrected to a $^{179}\text{Hf}/^{177}\text{Hf}$ ratio of

0.7325 using the exponential law. The Münster AMES standard, isotopically indistinguishable from the JMC-475 standard, yielded an average $^{176}\text{Hf}/^{177}\text{Hf}$ of 0.282160 with an external reproducibility of ± 40 ppm (2s); all $^{176}\text{Hf}/^{177}\text{Hf}$ data are given relative to a JMC-475 value of 0.282160. The typical external reproducibility of the $^{176}\text{Lu}/^{177}\text{Hf}$ was $\pm 0.2\%$ for ideally spiked samples and also includes effects of error magnification due to non-ideal spike-sample ratios and uncertainties imparted by corrections for Yb interferences (Blichert-Toft et al. 2002, Vervoort et al. 2004, Lagos et al. 2007). The calculated initial Hf isotope compositions include both the propagated external errors from the measured Hf isotope compositions and Lu/Hf ratios. For calculation of the $\epsilon\text{Hf}(t)$ and $\epsilon\text{Nd}(t)$ values, a ^{176}Lu decay constant of 1.867×10^{-11} (Scherer et al. 2001, Söderlund et al. 2004), a ^{147}Sm decay constant of 6.54×10^{-12} (Lugmair and Marti 1978), and the CHUR values of Bouvier et al. (2008) were used. All measured $^{143}\text{Nd}/^{144}\text{Nd}$ data were mass bias-corrected using a value of 0.7219 for $^{146}\text{Nd}/^{144}\text{Nd}$ and the exponential law. During the course of this study the $^{143}\text{Nd}/^{144}\text{Nd}$ measured for a 20 ppb LaJolla standard solution was 0.511809 ± 20 , and all data reported here are given relative to a $^{143}\text{Nd}/^{144}\text{Nd}$ of 0.511859 for LaJolla. The external reproducibility for $^{143}\text{Nd}/^{144}\text{Nd}$ measurements was ± 30 ppm and $\pm 0.2\%$ for $^{147}\text{Sm}/^{144}\text{Nd}$. Total procedural blanks during the course of this study were <15 pg for Lu, <57 pg for Hf, and <50 pg for Sm and Nd.

3.3.2.4. Zircon geochronology

To understand the temporal variation within the samples and area, we extracted zircons from four samples (representing the variety of the intrusive bodies from the Bosumtwi crater) and carried out single zircon CA-TIMS U-Pb geochronology (Mattinson 2005), using standard separation techniques and the laboratory procedures discussed in Ramezani et al. (2007). Data reduction, age calculation, and the generation of Concordia plots utilized the methods of McLean et al. (2011), and the statistical reduction and plotting program REDUX (Bowring et al. 2011).

As a general guiding principle in the age interpretations, we infer closed system behavior of U and Pb in zircon from a tight, approximately concordant cluster of analyses. In this case, the weighted mean $^{207}\text{Pb}/^{206}\text{Pb}$ date provides the most reliable crystallization age

(Bowring et al. 2006, Schoene et al. 2006, Thompson et al. 2007). Details of fractionation and blank corrections are given in Table 3.2.

Table 3.2. Results of the single zircon CA-TIMS U-Pb measurement along with fractionation and blank corrections in relation to selected samples from the intrusions in the proximity of the Bosumtwi impact structure.

Composition			Isotopic Ratios										Dates [Ma]				
Fraction	Th/U ^(a)	Pb ^(b)	Pb/Pbc ^(c)	²⁰⁶ Pb/ ²⁰⁴ Pb ^(d)	²⁰⁶ Pb/ ²⁰⁶ Pb ^(e)	²⁰⁶ Pb/ ²³⁸ U ^(e,f)	$\pm 2\sigma$	²⁰⁷ Pb/ ²³⁵ U ^(g)	$\pm 2\sigma$	²⁰⁷ Pb/ ²⁰⁶ Pb ^(e,f)	$\pm 2\sigma$	²⁰⁶ Pb/ ²³⁸ U ^(f,g)	$\pm 2\sigma$	²⁰⁷ Pb/ ²³⁵ U ^(g)	$\pm 2\sigma$	²⁰⁷ Pb/ ²⁰⁶ Pb ^(f,g)	Corr.
		[pg]			[%]	[%]	[%]	[%]	[%]	[%]	[%]	[abs.]	[abs.]	[abs.]	[abs.]	[abs.]	[abs.]
BOS10A: Zircon																	
z4	0.38	1.1	217.81	12797.9	0.107	0.383206	0.20	6.84139	0.21	0.129540	0.060	2091.2	3.5	2091.1	1.9	2090.9	1.1
z5	0.33	1.3	291.73	17323.8	0.094	0.382922	0.06	6.83766	0.10	0.129566	0.049	2089.9	1.1	2090.6	0.9	2091.3	0.9
z6	0.22	1.7	122.81	7492.1	0.063	0.382896	0.08	6.83567	0.12	0.129537	0.076	2089.8	1.4	2090.4	1.1	2090.9	1.4
z7	0.22	9.4	37.54	2305.0	0.062	0.383001	0.37	6.83885	0.41	0.129524	0.167	2090.3	6.6	2090.5	3.7	2090.7	2.9
BOS14A: Zircon																	
z1	0.29	1.2	889.60	53258.9	0.083	0.381697	0.07	6.82304	0.10	0.129704	0.035	2084.2	1.2	2088.7	0.9	2093.2	0.7
z2	0.16	2.3	564.85	34860.3	0.047	0.382602	0.08	6.84501	0.11	0.129814	0.048	2088.4	1.4	2091.6	1.0	2094.7	0.9
z3	0.09	7.0	365.19	22994.0	0.024	0.381913	0.10	6.83040	0.13	0.129771	0.038	2085.2	1.8	2089.7	1.1	2094.1	0.7
z4	0.17	1.0	1791.32	110411.3	0.048	0.383635	0.08	6.86017	0.11	0.129751	0.045	2093.2	1.4	2093.5	1.0	2093.8	0.8
z5	0.20	1.2	1331.92	81554.6	0.056	0.382857	0.07	6.84432	0.10	0.129714	0.044	2089.6	1.2	2091.5	0.9	2093.3	0.8
z6	0.13	3.0	376.77	23470.2	0.037	0.381110	0.26	6.81340	0.27	0.129720	0.059	2081.5	4.5	2087.5	2.4	2093.4	1.1
BOS15: Zircon																	
z1	0.34	0.5	1223.51	72362.7	0.097	0.384507	0.15	6.88837	0.20	0.129989	0.053	2097.3	2.6	2097.2	1.8	2097.0	1.0
z2	0.36	0.5	1244.33	73212.0	0.104	0.383678	0.08	6.86820	0.11	0.129888	0.049	2093.4	1.4	2094.6	0.9	2095.7	0.9
z3	0.31	0.7	409.10	24382.4	0.089	0.383130	0.51	6.85950	0.52	0.129909	0.077	2090.9	9.1	2093.4	4.6	2095.9	1.4
z4	0.31	0.4	898.27	53528.1	0.088	0.384280	0.08	6.88212	0.11	0.129947	0.041	2096.2	1.5	2096.4	1.0	2096.5	0.8
z5	0.28	0.7	290.28	17433.7	0.080	0.383747	0.20	6.87189	0.23	0.129935	0.074	2093.8	3.6	2095.0	2.0	2096.3	1.3
BOS18: Zircon																	
z1	0.60	0.9	273.35	15255.6	0.171	0.384617	0.08	6.89027	0.13	0.129988	0.081	2097.8	1.5	2097.4	1.2	2097.0	1.4
z2	0.55	1.1	85.63	4840.5	0.158	0.384560	0.13	6.88624	0.18	0.129931	0.097	2097.6	2.3	2096.9	1.6	2096.2	1.7
z3	0.48	1.2	130.75	7508.4	0.137	0.384177	0.15	6.87852	0.19	0.129915	0.091	2095.8	2.7	2095.9	1.7	2096.0	1.6
z4	0.70	1.8	87.36	4777.9	0.201	0.384813	0.06	6.89689	0.13	0.130046	0.098	2098.7	1.1	2098.3	1.1	2097.8	1.7
Pb Blank isotopic composition: ²⁰⁶ Pb/ ²⁰⁴ Pb = 18.42 ± 0.35; ²⁰⁷ Pb/ ²⁰⁴ Pb = 15.36 ± 0.23; ²⁰⁶ Pb/ ²⁰³ Pb = 37.46 ± 0.74																	
(a) Th contents calculated from radiogenic ²⁰⁶ Pb and the ²⁰⁷ Pb/ ²⁰⁶ Pb date of the sample, assuming concordance between U-Th and Pb systems.																	
(b) Total mass of common Pb.																	
(c) Ratio of radiogenic Pb (including ²⁰⁶ Pb) to common Pb.																	
(d) Measured ratio corrected for fractionation and tracer contribution only.																	
(e) Measured ratios corrected for fractionation, tracer, blank, common Pb (lab blank, U blank = 0.1 pg; Mass fractionation correction of 0.25‰/amu ± 0.04‰/amu (atomic mass unit) was applied to single- λ_{238} corrected for initial Th/U disequilibrium using radiogenic ²⁰⁶ Pb and Th/U [magmas] = 2.8																	
(f) Isotopic dates calculated using the decay constants $\lambda_{238} = 1.55125 \times 10^{-10} \text{ yr}^{-1}$, $\lambda_{235} = 9.8485 \times 10^{-10} \text{ yr}^{-1}$ (Jaffey et al. 1971), and for the ²³⁸ U/ ²³⁵ U = 137.818 ± 0.045 (Hess et al. 2012)																	
(h) fraction excluded from age calculation																	
(corr. coef. = correlation coefficient)																	

3.4. Results

3.4.1. Petrography

Detailed petrographic descriptions of the samples, along with microphotographs of some of their characteristic features, are given in Table S1 and in Figure S1. Sampling locations are indicated on Figure 3.2. A generalized petrographic description of the rocks from the four different intrusive bodies is given below. Even though samples were collected in the proximity of the crater, none of the samples shows any signs of shock metamorphism, such as planar deformation features or presence of shock-melted material.

3.4.1.1. Pepiakese intrusion, located NE of the Bosumtwi Lake (BOS10A, BOS10B, BOS11, BOS12)

This granitic body consists mostly of non-foliated, generally unaltered, coarse-grained granite. The dominant mineral phases are quartz and feldspar (k-feldspar being more abundant than plagioclase), additionally muscovite (up to 15 vol%) and rare biotite (~2 vol%) are present. Sample BOS12 is a pegmatite consisting almost exclusively of quartz and k-feldspar with a very small amount of biotite. Sample BOS10A differs from the other samples by a much higher modal abundance of biotite (12 vol% compared to less than 2 vol% in other samples) and amphibole (2 vol%). Previous authors (Jones 1985, Koeberl et al. 1998) have also reported large mineralogical variation within this relatively small intrusive body.

3.4.1.2. Mafic dike, located NE of the Bosumtwi Lake (BOS13)

This body is represented by one sample. It is a fresh diabase and consists of small crystals (<1 mm) of olivine, long but very thin plagioclase laths, and a more fine-grained matrix consisting of clinopyroxene, minor olivine, and oxides. Accessory minerals include hornblende, apatite, and chlorite.

3.4.1.3. Kumasi intrusion, located NE of the Bosumtwi Lake, NE of the Pepiakese intrusion (BOS14A, BOS14B, BOS15)

The samples from this intrusive body are similar to the main group of samples from the Pepiakese granite (i.e., excluding sample BOS10A), however they are slightly more altered (some k-feldspars are sericitized and rare chlorite is present). Rocks from this intrusion are coarse-grained granite with abundant quartz and feldspar, up to 15 vol% of muscovite, and 2-3 vol% of biotite. No amphibole was found.

3.4.1.4. The Southern intrusion, located SE of the Bosumtwi Lake (BOS16, BOS17, BOS18, BOS19A, BOS19B)

Samples from this magmatic body are petrographically diverse. They are more fine-grained compared to samples from the northern bodies. Additionally, all of them are significantly more altered than previously described samples; probably mostly k-feldspars are almost entirely transformed to sericite and a large portion of biotite crystals is replaced by chlorite. Samples BOS16 and BOS18 are non-foliated medium-grained muscovite granite with a small amount of biotite, similar to samples from the northern granitic bodies (e.g., BOS11, BOS14A or BOS15). Samples BOS19A and BOS19B are medium- to fine-grained, foliated with phyllosilicates occurring in a preferred orientation, and have a much higher percentage of opaque minerals compared to samples from other intrusive bodies. Sample BOS17 shows two distinct domains: the first domain shows similarities to samples BOS19A and BOS19B, whilst the second fine-grained domain is comparable to samples BOS16 and BOS18, but has a comparatively finer grain size.

3.4.2. Geochemistry

3.4.2.1. Major elements

The results of major and trace element analyses are given in Table 3.1. For comparison, all previously published samples of granites collected in the proximity of

Bosumtwi crater (Koeberl et al. 1998, Dai et al. 2005, Karikari et al. 2007), along with ranges of compositions of basin- and belt-type granitoids (Leube and Hirdes 1986, John et al. 1999, Grenholm et al. 2011), are given in Table 3.1 and Table 2S.

Based on the point counting and quartz (Q), alkali feldspar (A), plagioclase feldspar (P) (QAP) classification of plutonic rocks (Figure 3.3a), most of the analyzed samples are granodiorites, with one quartz monzodiorite and one gabbro (sample BOS13 from the mafic dike). Based on the total alkali-silica (TAS) plot shown in Figure 3.3b, most of the samples are granodioritic or granitic in composition, but three samples from granitic intrusions (one from this study, and two from Koeberl et al. 1998) are classified as gabbroic diorite and one as a diorite.

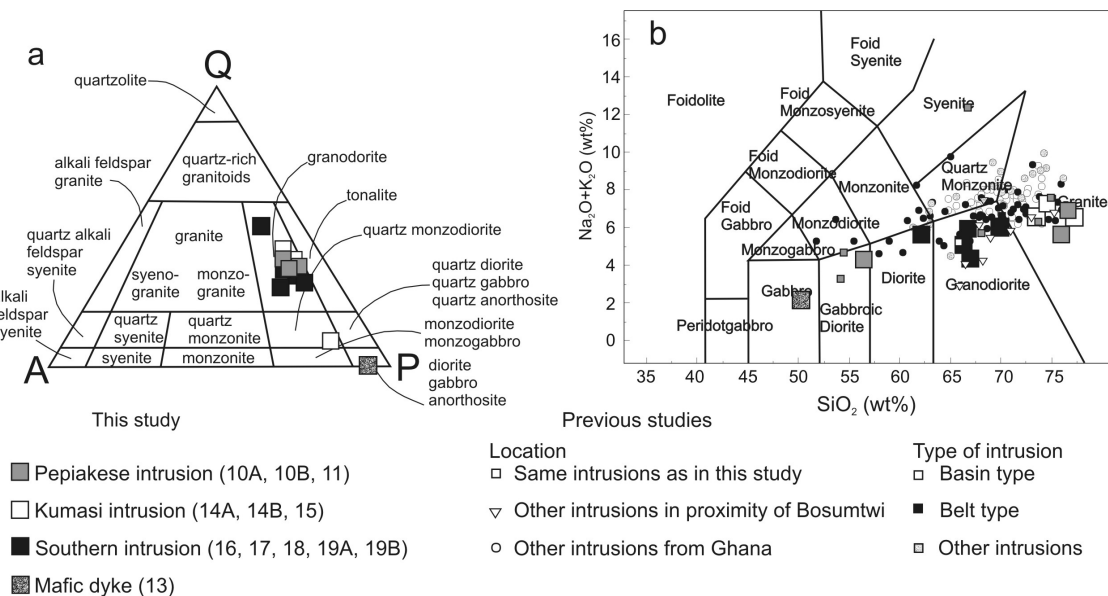


Figure 3.3. Classification of Bosumtwi granites, using a) a quartz (Q), alkali feldspar (A), plagioclase feldspar (P) (QAP) diagram after Streckeisen (1974) and b) a total alkali-silica (TAS) plot after Le Bas et al. (1992). Large squares represent samples analyzed in this study, small squares and triangles show composition of samples analyzed in the literature from locations in the proximity of the Bosumtwi crater (Koeberl et al. 1998, Dai et al. 2005, Karikari et al. 2007). Small circles represent other granites from Ghana (Leube and Hirdes 1986, Leube et al. 1990, John et al. 1999, Grenholm 2011). The same symbols are used in all figures in this paper (unless stated otherwise).

Intrusions from the proximity of the Bosumtwi crater are strongly peraluminous (Figure 3.4) which has been described as being characteristic for basin-type intrusions (e.g., Hirdes et al. 1992). Almost all analyzed samples follow a uniform trend shared also by some of the other basin type intrusions; however, the samples analyzed in this study are characterized by much higher molar Al/(Na + K + Ca) ratios compared to other Ghanaian basin intrusions. Three samples from the Pepiakese intrusion (one analyzed in this study

and two from Koeberl et al. 1998) plot in the array of belt-type intrusions (molar $Al/(Na+K+Ca) < 1.5$ and molar $Al/(Na+K) > 2$), very close to the mafic dike sample analyzed in this study.

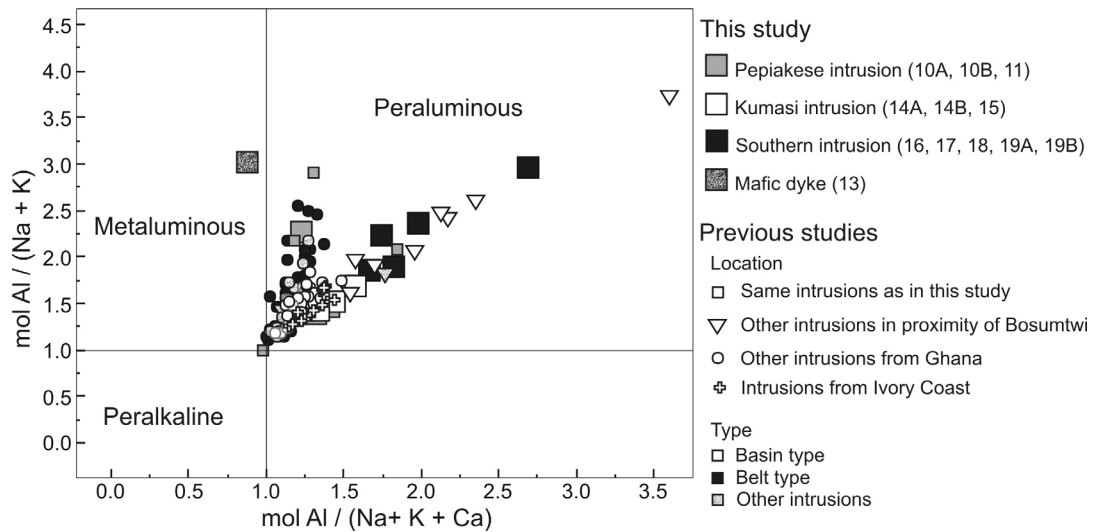


Figure 3.4. A/NK vs. A/CNK plot (after Shand 1943) for granites from Ghana. Most samples fall into the peraluminous field, and two distinct trends are visible: a vertical one characteristic for most of the belt intrusions, and an inclined one that includes basin intrusions (including granitoids from surrounding of Bosumtwi crater). The same symbols and literature are used as in Figure 3.3; additionally, small crosses represent AIG type granitoids from Doumbia et al. (1998).

Granitic rocks collected in the proximity of the Bosumtwi crater display quite a wide range of major element compositions. Based only on samples analyzed in this study, it may appear that the Southern intrusion differs from other granitic bodies around the Bosumtwi crater by having lower average SiO_2 contents and higher Fe_2O_3 , TiO_2 , and MgO contents. However, when taking into account previous studies in this area (mainly Koeberl et al. 1998, Karikari et al. 2007) the range of major element compositions for all three granitic bodies overlap, and the intrusions cannot be differentiated based on their major element compositions.

Figure 3.5 shows Harker variation diagrams using SiO_2 as differentiation index. They represent the scatter in the major element compositions of samples analyzed in this study, along with other samples from the proximity of the Bosumtwi crater and data from other intrusions of basin- and belt-type from Ghana. Apart from CaO , all other elements show a relatively good agreement of the data for samples from this study with those for other Ghanaian granitic intrusions. Granites of this study and typical granites from Birimian Supergroup are characterized by different trends of CaO and K_2O vs. SiO_2 . Samples

analyzed in this study exhibit generally lower CaO contents (average $1.46 \pm 1.8\%$ 1σ) compared to other granitic intrusions in Ghana ($2.86 \pm 1.6\%$ 1σ), and do not follow the typical trend (decrease in CaO with increasing SiO_2), while other major elements behave in a standard way.

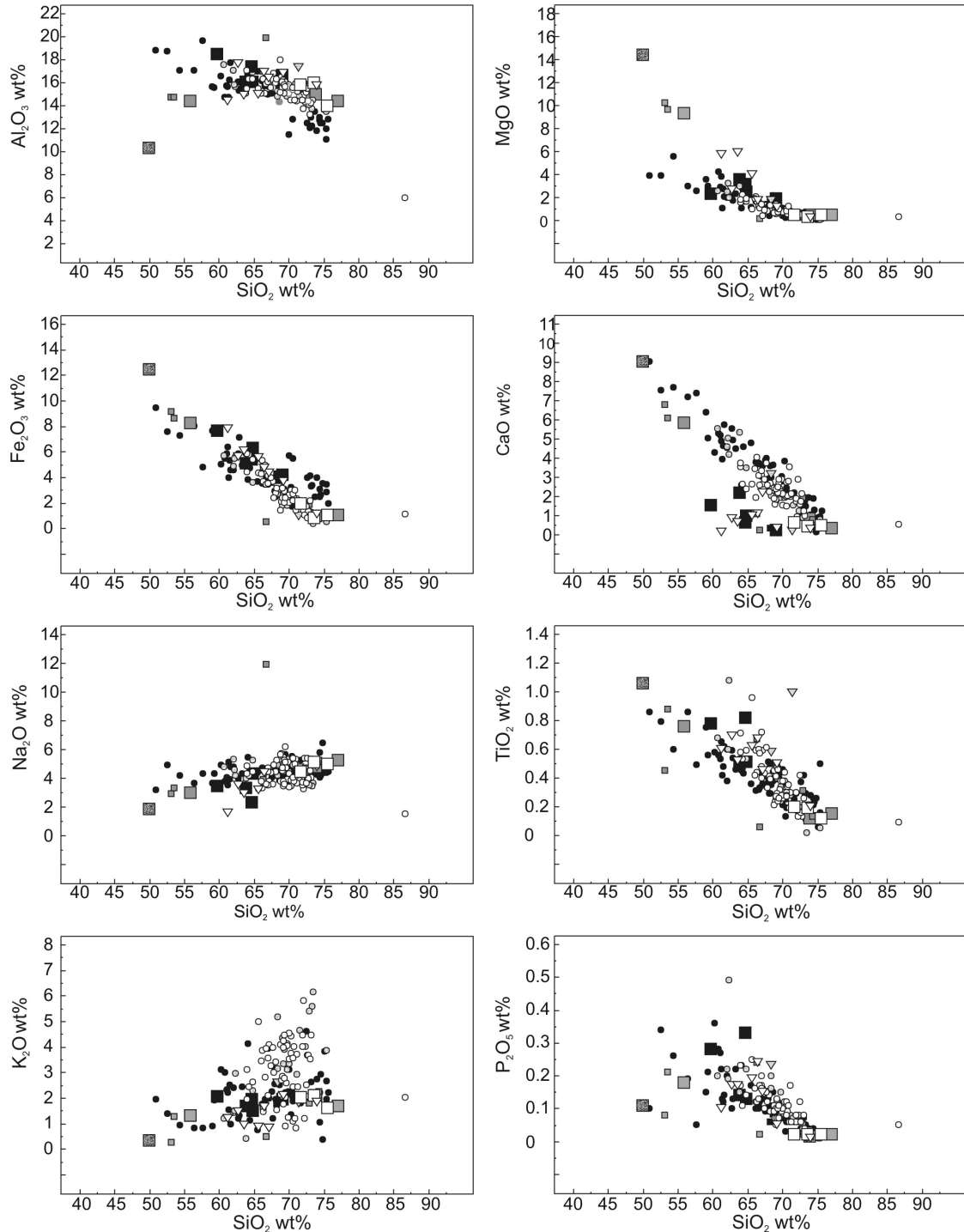


Figure 3.5. Harker variation diagrams for samples from intrusions located in the proximity of Bosumtwi crater analyzed in this study, and for data from the literature (Koeberl et al. 1998, Dai et al. 2005, Karikari et al. 2007, Leube and Hirdes 1986, Leube et al. 1990, John et al. 1999, Grenholm 2011). The same symbols and literature are used as in Figure 3.3.

3.4.2.2. Trace elements

Chondrite-normalized rare earth element (REE) patterns for samples from all intrusive bodies around Bosumtwi are similar (Figure 3.6a) and overlap with the REE patterns of other Ghanaian granites. The samples from intrusions studied here (excluding pegmatite samples) have relatively low total REE contents varying between 52 and 161 ppm. The REE are fractionated (Figure 3.7) with chondrite-normalized La/Yb ratios between 3 (for a plagioclase fraction of a pegmatite vein) and 86, and show relatively low Yb_N contents. On the ocean ridge granite (ORG) normalized multi-element diagram (after Pearce et al. 1984, Figure 3.6b) all the profiles are similar and characterized by enrichment in large-ion lithophile elements (LILE) relative to high field-strength elements (HFSE), with negative Ta-Nb anomalies.

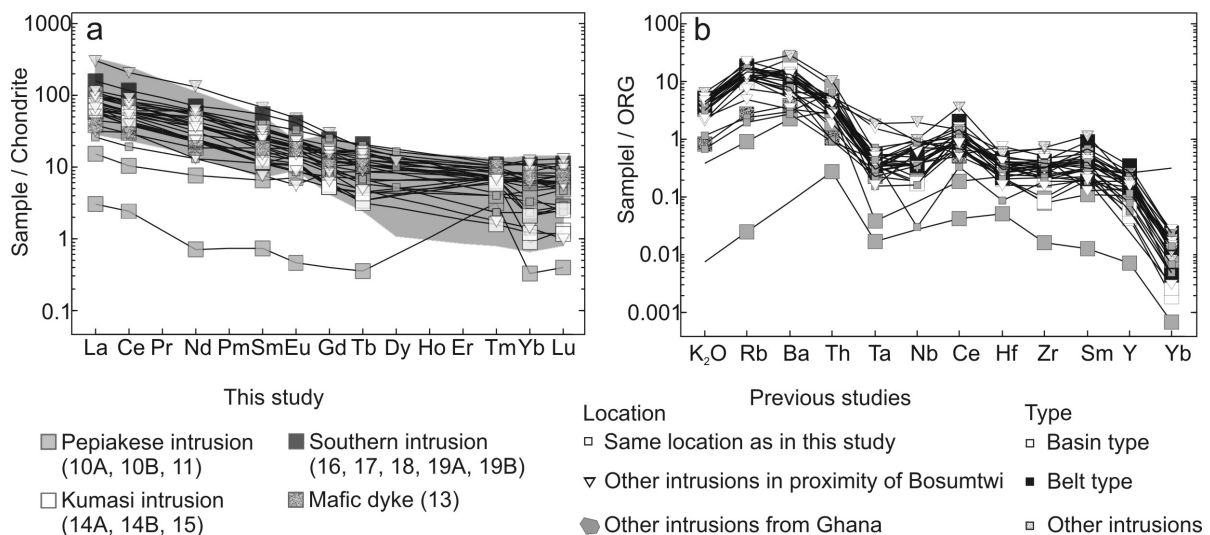


Figure 3.6. Multi element patterns for the intrusions from the Bosumtwi crater and from other granitoids from Ghana, a) Chondrite-normalized (Sun and McDonough 1989) rare-earth element patterns, b) ocean ridge granite (ORG) normalized (Pearce et al. 1984) spider diagram. The same symbols and literature are used as in Figure 3.3; additionally, a grey area shows multi-element patterns for other Ghanaian granitoids (Leube and Hirdes 1986, Leube et al. 1990, John et al. 1999, Grenholm 2011).

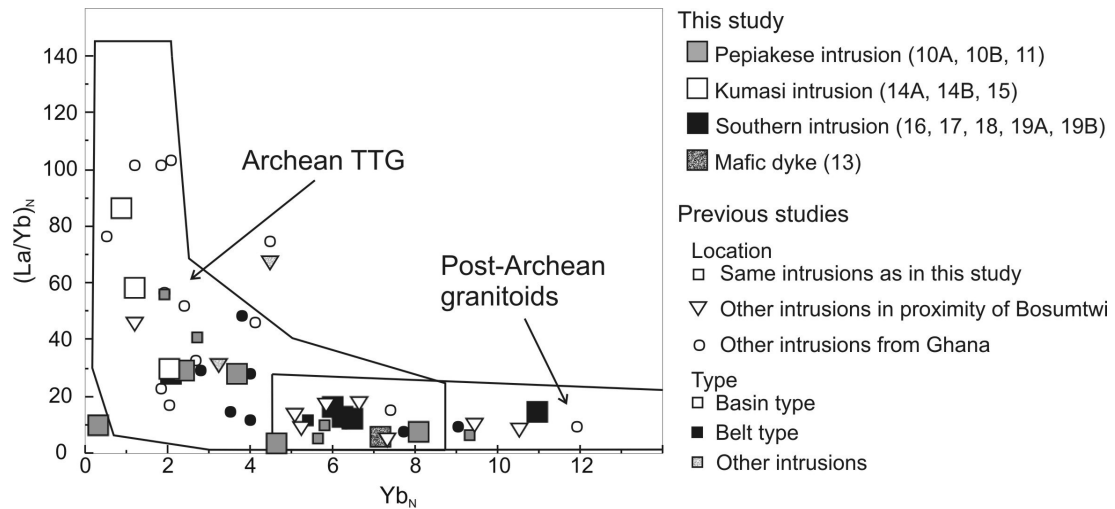


Figure 3.7. $(La/Yb)_N$ vs. Yb_N diagram showing the affinity of the granitoids from the proximity of Bosumtwi crater (along with other granites from Ghana) with the Archean tonalite-trondhjemite-granodiorite (TTG) rocks (CI normalization data from Sun and McDonough 1989) or adakites. Fields for Archean and post-Archean granitoids are from Martin (1993, 1999). Information about other intrusions from Ghana is from: Koeberl et al. (1998), Dai et al. (2005), Karikari et al. (2007) (proximity of Bosumtwi) as well as: Leube and Hirdes (1986), Leube et al. (1990), John et al. (1999), Grenholm (2011) (other Ghanaian granitic intrusions).

3.4.3. Isotopic data

The Sm-Nd isotope data for the samples selected for isotope analysis is summarized in Table 3.3. Ratios of $^{147}\text{Sm}/^{144}\text{Nd}$ for granites range from 0.0905 (sample BOS14A) to 0.1271 (sample BOS10A), whereas the mafic sample BOS13 exhibits a $^{147}\text{Sm}/^{144}\text{Nd}$ value of 0.1512. The initial $\epsilon\text{Nd}(t)$ calculated to an approximate emplacement age of 2100 Ma (Leube et al. 1990, Oberthür et al. 1998, Grenholm et al. 2011), is $+3.1 \pm 0.4$ ϵ -units; only the basaltic sample BOS13 exhibits a slightly lower value ($\sim +2.3$ ϵ -units).

Table 3.3. Sm-Nd isotope data for granite samples from the Bosumtwi crater area.

Sample	Sm (ppm)	Nd (ppm)	Sm/Nd	$^{147}\text{Sm}/^{144}\text{Nd}$	$^{143}\text{Nd}/^{144}\text{Nd}$	$\epsilon\text{Nd}(0)$	$\epsilon\text{Nd}(t)$
BOS10A	4.46	21.21	0.2103	0.1271	0.511818 ± 4	-16	2.8
BOS10B	2.86	17.24	0.1659	0.1001	0.511461 ± 4	-23	3.1
BOS11	2.71	17.35	0.1562	0.0943	0.511362 ± 4	-24.9	2.8
BOS13	2.9	11.54	0.2513	0.1521	0.512139 ± 12	-9.7	2.3
BOS14A	2.54	16.94	0.1499	0.0905	0.511320 ± 4	-25.7	3
BOS15	1.58	9.76	0.1619	0.098	0.511452 ± 5	-23.1	3.5
BOS16	2.92	16.53	0.1766	0.1067	0.511533 ± 4	-21.6	2.7

$\epsilon\text{Nd}(t)$ values were calculated using the CHUR values $^{147}\text{Sm}/^{144}\text{Nd} = 0.1960$, $^{143}\text{Nd}/^{144}\text{Nd} = 0.512630$ (Bouvier et al., 2008), a decay constant for ^{147}Sm of 6.54×10^{-12} (Lugmair and Marti, 1978) and an age of 2.077 Ga.

On the $^{143}\text{Nd}/^{144}\text{Nd}$ versus $^{147}\text{Sm}/^{144}\text{Nd}$ plot, a well-defined correlation line for seven samples (BOS10A, BOS10B, BOS11, BOS13, BOS14A, BOS15 and BOS16) is visible (Figure 3.8). Excluding sample BOS15 (which deviates most from the correlation line) and the mafic sample BOS13, a well-defined isochron can be plotted, yielding an age of 2077 ± 83 Ma (MSWD = 1.7). Including the granitic sample 15 would yield a regression line corresponding to an age of 2011 ± 283 Ma (MSWD = 6.4). The slight scatter in ^{147}Sm - ^{143}Nd potentially indicates some initial isotopic heterogeneity or secondary metamorphic overprint.

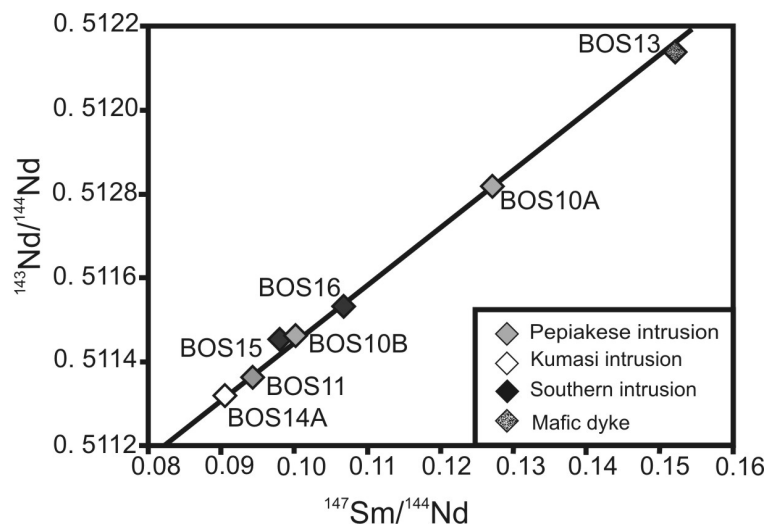


Figure 3.8. Isochron diagram for the Sm-Nd system for samples from Pepiakese intrusion (BOS10A, BOS10B and BOS11), Kumasi intrusion (BOS14A and BOS15), Southern intrusion (BOS16), and from Mafic dike (BOS13). The 2077 ± 83 Ma line probably represents an isochron (this is also supported by zircon ages presented in Table 3.2, and is in agreement with the hypothesis that all studied intrusions from the surroundings of the Bosumtwi crater could be co-genetic). Note: error bars on the ^{147}Sm - ^{144}Nd data are less than or approximately equal to the width of the symbols.

Additionally, $^{176}\text{Lu}/^{177}\text{Hf}$ measurements were performed (Table 3.4 and Figure S2), but because Lu-Hf properties of the samples are so heavily disturbed (and the source of distortion cannot be unequivocally identified). Ratios of $^{176}\text{Lu}/^{177}\text{Hf}$ range for granites from 0.0012 (sample BOS14A) to 0.0098 (sample BOS10A), whereas mafic dike sample BOS13 exhibits a value of 0.0126. Initial $\epsilon\text{Hf}(t)$ values, back calculated to ~ 2100 Ma, are more diverse for the granitic samples (compared to the fairly homogeneous initial $\epsilon\text{Nd}(t)$ values) and range from +3.6 ϵ -units (sample BOS10B) to +5.9 ϵ -units (sample BOS14A). However, the felsic sample BOS15 plots off this trend at +0.7 ϵ , possibly reflecting an analytical artifact (this sample also deviates most from the Sm-Nd isochron). The mafic sample BOS13 is indistinguishable from the granites (+5.8 ϵ -units).

Table 3.4. Lu-Hf isotope data for granite samples from the Bosumtwi crater area.

<i>Sample</i>	<i>Lu (ppm)</i>	<i>Hf (ppm)</i>	<i>Lu/Hf</i>	<i>¹⁷⁶Lu/¹⁷⁷Hf</i>	<i>¹⁷⁶Hf/¹⁷⁷Hf</i>	<i>εHf(0)</i>	<i>εHf(t)</i>
BOS10A	0.1862	2.6885	0.0693	0.0098	0.282003 ± 3	-27.2	5.8
BOS10B	0.0664	1.7755	0.0374	0.0053	0.281761 ± 3	-35.8	3.6
BOS11	0.1212	3.1823	0.0381	0.0054	0.281799 ± 3	-34.4	4.9
BOS13	0.1990	2.2423	0.0887	0.0126	0.282113 ± 3	-23.3	5.8
BOS14A	0.0250	2.9147	0.0086	0.0012	0.281660 ± 3	-39.9	5.9
BOS15	0.0564	1.4344	0.0393	0.0056	0.281690 ± 4	-38.3	0.7

For details about calculations see the “Methods” section and Hoffmann et al. 2011.

3.4.4. Geochronology

Results of the U/Pb dating of our samples are presented in Table 3.5 and Figure 3.9. Zircon ages for samples from three different intrusive bodies in the proximity of the Bosumtwi crater overlap and vary within a narrow range between 2092 Ma and 2098 Ma:

- We analyzed four light brown, elongated, ~150 µm sized zircon grains from sample BOS10A. The analyses show a concordant cluster with a $^{207}\text{Pb}/^{206}\text{Pb}$ weighted mean that indicates a crystallization age of 2092 ± 6 Ma, which is our best estimation for the age of crystallization of the Pepiakese body.
- We selected six clear, pinkish, 150-200 µm sized, idiomorphic zircon grains from BOS14A. Two of the grains are concordant and three are close to concordant. Combining data for these five grains we are able to obtain a statistically reasonable $^{207}\text{Pb}/^{206}\text{Pb}$ weighted mean date of 2095.4 ± 6 Ma. We interpret this date as the time of zircon crystallization in the Kumasi body. One grain is slightly older and has a $^{207}\text{Pb}/^{206}\text{Pb}$ date of 2094.7 Ma, which we interpret as being derived from a small inherited component.
- From BOS15 we analyzed five clear, 200-250 µm prismatic zircon grains with slightly rounded edges. All five analyzed grains cluster on the Concordia and resulted in a $^{207}\text{Pb}/^{206}\text{Pb}$ weighted mean date of 2097 ± 6 Ma, indicating time of crystallization of the Kumasi body
- Lastly, we separated four light brown, 100-150 µm, elongated, idiomorphic, zircon grains from sample BOS18. All isotopic measurements resulted in concordant data with a $^{207}\text{Pb}/^{206}\text{Pb}$ weighted mean date of 2098 ± 6 Ma, which we interpret as well as the time of crystallization and emplacement of the Southern body.

Table 3.5. Results of the zircon U/Pb dating of four granite samples from Bosumtwi.

Sample number	Age [Ma]	\pm [Ma]			MSWD**	Number of analyzed grains
		X*	Y*	Z*		
BOS10A	2091.96	0.56	0.56	6.1	0.16	4
BOS14A	2094.58	0.32	0.32	6.1	2	6
BOS15	2097.19	0.44	0.44	6.1	1.2	5
BOS18	2097.7	0.44	0.72	6.1	1.2	4

* X is the internal error in absence of all systematic errors, Y includes the tracer calibration error, and Z includes both tracer calibration and decay constant errors.

** Mean Square Weighted Deviation

All these dates are in agreement with the emplacement time of one of the youngest Ghanian basin intrusions (Hirdes et al. 1992, Davis et al. 1994, Hirdes and Davis 1998, de Knock et al. 2011).

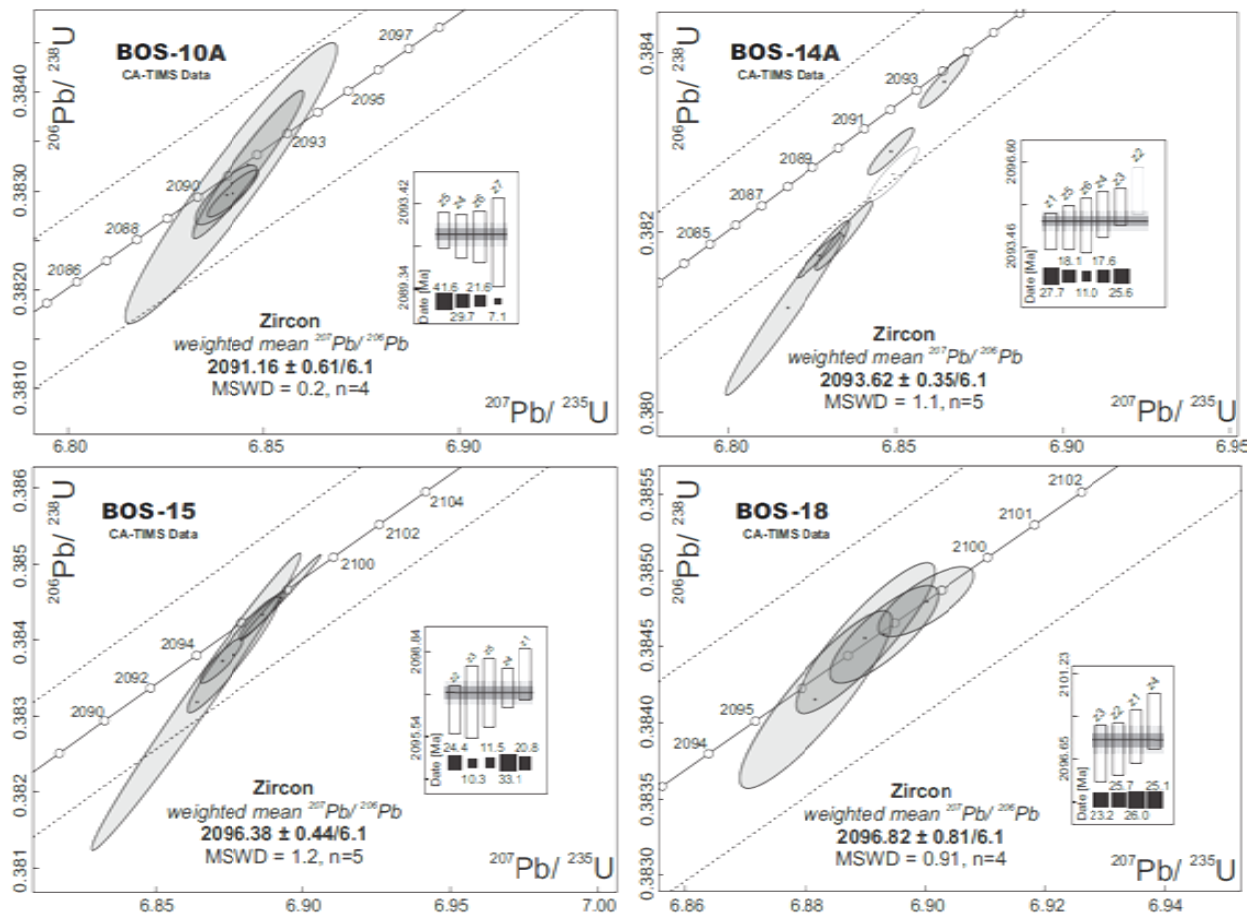


Figure 3.9. U–Pb concordia diagrams for zircons from samples from the proximity of Bosumtwi crater.

3.5. Discussion

3.5.1. Classification of the intrusions in the proximity of the Bosumtwi crater

Koeberl and Reimold (2005) suggested that intrusions in the proximity of the Bosumtwi crater represent two distinct types of Ghanaian granites: the Southern intrusion was considered a belt-type, whereas the Pepiakese and the Kumasi intrusions in the NE were marked as basin-type intrusions (Figure 3.2). However, the current study shows that all intrusions in the proximity of Bosumtwi crater are very similar to each other from the petrographic, geochemical, isotopic, and geochronological point of view and belong to the same genetic type of intrusions (Table 3.1, Table 3.2, Table 3.3, Table 3.5, Table S2). It is possible (based on a slightly different, more fractionated REE pattern) that the pluton located to the SW from the Southern intrusion (sample LB-50) that was studied by Karikari et al. (2007) is different from other intrusions in the proximity of Bosumtwi crater. However, as only a single sample has been described from this body in the literature, it is not possible to fully classify this intrusion here.

Petrographic and chemical properties of the granitoids in the proximity of the Bosumtwi crater are consistent with those granitoids belonging to the basin-type of intrusions. Hirdes et al. (1992) proposed that belt and basin granitoids can be differentiated by their geochemical characteristics; belt granitoids are more metaluminous, while basin granitoids are peraluminous. All typical samples (BOS10B, BOS11, BOS12, BOS14A, BOS14B, BOS15, BOS16, BOS18) from the surroundings of the Bosumtwi crater clearly follow the basin-type trend (Figure 3.4); however, they are characterized by very high ratios of molar $Al/(Na+K+Ca)$ not seen in other Ghanaian granites. This correlates with their generally lower than average CaO and K_2O contents compared to samples from surroundings of Bosumtwi crater (on average 1.46 ± 1.8 wt% and 1.55 ± 0.6 wt%, respectively, in comparison to 2.38 ± 0.7 wt% and 4.38 ± 0.7 wt%, respectively), for other granitic basin intrusions in Ghana.

The formation ages for the granitoids from the vicinity of the Bosumtwi crater are between 2092 and 2098 Ma for the U-Pb zircon chronology, or at 2077 ± 83 Ma for the whole-rock $^{147}\text{Sm}/^{144}\text{Nd}$ systematics (Figure 3.8), which agrees within error with the zircon dates (Table 3.5). Based on their age of formation all studied intrusions can be classified either as basin-type granitoids of the third phase (S-type “Cape Coast” from between 2116 Ma and 2097 Ma) or fourth phase (late-stage granitoids emplaced between 2097 Ma and 2074 Ma) of de Kock et al.’s (2011) classification. The intrusion ages of the Bosumtwi granitoids and the Bansa granite (between 2097 Ma: Oberthür et al. 1998, and 2081 Ma: Leube et al. 1990) are indistinguishable from each other, and different from the age of the main body of the Kumasi intrusion (between 2116.2 Ma: Hirdes et al. 1992; and 2112 Ma: Adadey et al. 2009). Also petrographic and geochemical properties of the Bansa pluton, as described in the literature (e.g., Woodfield 1966, Moon and Mason 1967), generally agree with properties of the intrusions from the Bosumtwi crater area. However, a genetic relation of the intrusions located in the proximity of the Bosumtwi crater to the young fraction of the Kumasi intrusion cannot be excluded without additional research.

3.5.2. Tectonic setting and petrogenesis of the granites in the proximity of the Bosumtwi crater

Emplacement of the late-stage granitoids (2097-2074 Ma) in western Africa was a result of crustal thickening that occurred between 2114 and 2090 Ma, causing a regional metamorphic peak between 2110 and 2090 Ma (de Kock et al. 2011). Feybesse et al. (2006) suggested that those late granitoids were formed in the last stage of the Eburnean orogeny (phase D2-3, 2095-1980 Ma) under conditions of crustal shortening and transcurrent tectonism (e.g., Lompo 2010). Granitic bodies emplaced during this phase are characterized by a spatial association with the strike-slip faults that also controlled their geometry. The same type of association is characteristic to the Bansa intrusion as well as to the bodies located in proximity of the Bosumtwi crater, as they lay in proximity of a strike-slip fault (Feybesse et al. 2006).

The initial $\epsilon\text{Nd}_{(t)}$ calculated to an approximate emplacement age of 2100 Ma for samples of this study is positive and varies between +2.8 and +3.5, indicating short crustal residence times of the rocks before 2100 Ma. This finding is in agreement with previous studies where initial $\epsilon\text{Nd}_{(t)}$ for the late-phase basin granitoids are between +1.5 and +3.5 (e.g., Doumbia et al. 1998, Gasquet et al. 2003). Intrusions from the proximity of the Bosumtwi crater, as well as most other Ghanian granitoids, were derived from a juvenile mantle protolith during the Paleoproterozoic and generally without significant admixture of an Archean crustal component (Abouchami et al. 1990, Boher et al. 1992, Doumbia et al. 1998, Gasquet et al. 2003, Pawling et al. 2006).

Peraluminous granites, such as the Bosumtwi intrusions, can be formed in several different ways (e.g., Barbarin 1997): 1) through closed-system fractional crystallization of amphibole and clinopyroxene in metaluminous magmas; 2) assimilation of aluminous sedimentary rocks; and 3) alkali loss by vapor-phase transfer. However, all these processes produce only relatively small volumes of magma. According to Barbarin (1997), large volumes of peraluminous magmas can be produced only in the case of continental thickening that is causing partial melting of sedimentary and igneous crustal rocks under either dry or wet conditions. Anatexis occurring in an orogenic tectonic zone affected by major crustal shear structures providing a path for fluid migration would lead to formation of two-mica monzogranites and leucogranites (Barbarin 1997). The characteristics of these rocks, along with their general tectonic setting, match some of the properties of granites from the Bosumtwi crater area.

Doumbia et al. (1998) studied young (2094 ± 6 Ma to 2084 ± 29 Ma) peraluminous granitoids called AIG from central Ivory Coast that belong to the Birimian Supergroup that share some characteristics with intrusions from the surroundings of the Bosumtwi crater. AIG intrusions (Ferke and Kowara) are composed of leucogranites rooted in the migmatitic biotite orthogneiss and were emplaced in a sinistral transcurrent shear regime along major fault zones. These intrusions are very similar to intrusions located near the Bosumtwi crater: 1) they have relatively low SiO_2 contents, 2) they follow the same trend on the peraluminosity diagram (but Bosumtwi samples have higher molar $\text{Al}/(\text{Na}+\text{K}+\text{Ca})$ ratios) shown in Figure 3.4; 3) they are characterized by a high amount of primary muscovite; 4) the presence of pegmatites (e.g., sample BOS12 studied here); 5) they have relatively low total

REE contents; 6) a slightly concave shape of the HREE; and 7) they were emplaced at about the same time.

Doumbia et al. (1998) proposed that the Ferke and Kowara intrusions were formed as a result of anatexis at relatively low pressures of about 400-500 MPa (4-5 kbar) (no high-pressure metamorphic minerals were found) and temperatures between 600 and 700 degrees Celsius. The temperature estimate is generally consistent with known conditions during the metamorphic peak in this region between 2110 and 2090 Ma (de Kock et al. 2011). Anatexis could have been triggered by addition of water infiltrating along the transcurrent faults or/and by heat from mantle-derived magmas (Doumbia et al. 1998). Other plutons for which similar emplacement processes were proposed are the Tenkodogo-Yama elongated pluton located in eastern Burkina Faso (Naba et al. 2004) and Kouare in southern Burkina Faso (Vegas et al. 2008). In addition to sharing multiple characteristics with the other late-stage anatectic granitoids, intrusions in the proximity of Bosumtwi crater are located close (less than 10 km to the south) to the main D2 sinistral transcurrent fault, as noted by Feybesse et al. (2006) and de Kock et al. (2011), making this a preferred location for emplacement of this kind of pluton. However, it is important to notice that the Pepiakese or Kumasi intrusions studied here do not have the characteristic elongated shape, and are not located exactly on a currently visible transcurrent fault (Agyei Duodu et al. 2009).

The chondrite-normalized REE patterns of the granitic rocks from the Bosumtwi crater area are very similar to those displayed by other granitoids (Figure 3.6a) from Ghana, with REE fractionation being very similar to the one characterizing the belt-type intrusions. Some of the basin intrusions show stronger HREE fractionation (Figure 3.6a), suggesting garnet being stable in the residue (e.g., Grenholm et al. 2011). Lack of this signal in the case of the Bosumtwi intrusions may point to a relatively shallow depth of melt formation. This is again consistent with the emplacement scenario through crustal anatexis described above.

An anatectic origin of the granites from the Southern intrusion and the Pepiakese intrusion is also supported by $\delta^{18}\text{O}$ values (Koeberl et al. 1998). These authors noted that samples from the Southern intrusion have $\delta^{18}\text{O}$ values between 12.7 and 12.9‰, identical to those for the surrounding sedimentary rocks, whereas values for the Pepiakese granite differ slightly. Koeberl et al. (1998) explained this either by those rocks being derived from mantle magmatic rocks or by being formed by anatexis of hydrothermally altered granites. We

conclude that this second explanation is more consistent with the results of the present study.

3.5.3. TTG affinity of Bosumtwi intrusions

The TTG (tonalite-trondhjemite-granodiorite) suite is one of the defining features of Archean terranes, as TTGs form almost 90% of the Archean continental crust (Martin et al. 2005). TTG were most commonly formed between 4000 Ma and 2500 Ma by partial melting of hydrated mafic material in high temperature and pressure conditions (e.g., Martin et al. 2005). Proposed environments of TTG formation include: a subduction zone (e.g., Martin et al. 2005), overthickened oceanic crust (e.g., Condie 2005), or tectonically thickened mafic island-arc crust (Nagel et al., 2012). Some of the Birimian intrusions (especially the belt-type) were classified as TTG rocks by some authors (e.g., Dia et al. 1997, de Kock et al. 2011, Metelka et al. 2011, Perrouty et al. 2012), whereas others prefer to call these rocks sodic calc-alkaline granitoids similar to TTGs (e.g., Doumbia et al. 1998, Grenholm 2011).

Granitic intrusions in the Bosumtwi region share some characteristics with TTGs (properties as listed by Martin et al. 2005). They are: 1) silica rich – SiO_2 is higher than 64 wt%, but usually more than 70 wt% (Figure 3.5); 2) high Na_2O contents between 3 wt% and 7 wt% correlated with low K_2O contents, with no K-enrichment during magmatic differentiation (Figure 3.5); 3) highly fractionated REE patterns; 4) they plot with TTGs on a $(\text{La/Yb})_N$ vs. Yb_N graph (Figure 3.7) (Martin et al., 1993); 5) $(\text{Fe}_2\text{O}_3 + \text{MgO} + \text{MnO} + \text{TiO}_2)$ contents of TTG and typical intrusions from Bosumtwi is < 5 wt% (Figure 3.5). However, other characteristics of the Bosumtwi intrusions are different from the properties of typical TTGs:

1. TTGs are generally older than 2500 Ma, whereas rocks from the surroundings of Bosumtwi crater are just 2098 ± 6 to 2092 ± 6 Ma old. However, within Birimian Supergroup, the petrogenesis of TTG rocks could have lasted until 2150-2126 Ma (e.g., de Kock et al. 2011);
2. Average Ni and Cr contents in TTGs are 14 and 29 ppm, respectively (Martin et al., 2005), whereas the Bosumtwi intrusions have higher contents of these

elements (Table 3.1, Table S2). However, it was shown that with time, the composition of TTG evolved towards higher MgO, Ni, and Cr contents (Smithies 2000, Martin and Moyen 2002). So the higher MgO, Ni, and Cr contents in the Bosumtwi area rocks may be explained by their younger age (2.09 Ga), or be the result of secondary processes.

3. A ternary Na-K-Ca (molar) diagram is used to distinguish between calc-alkaline and TTG rocks (e.g., Barker and Arth 1976, Martin et al. 1999). As shown in Figure 3.10, samples from Ghanaian intrusions fall within both the calc-alkaline and TTG fields. Intrusions from the proximity of Bosumtwi crater seem to be closer to the trondhjemitic (Td) trend, although they fall outside of the main TTG field.

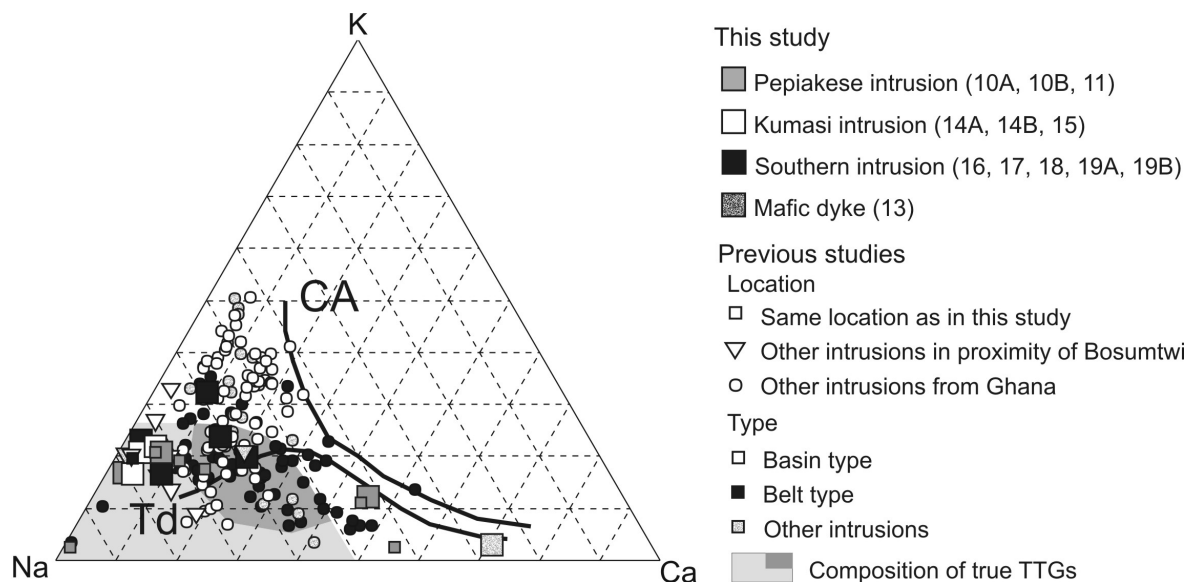


Figure 3.10. Granitoids from Ghana on a Na-K-Ca (molar) diagram used to distinguish between calc-alkaline (CA) rocks from the TTG suite, which generally follow a trondhjemitic (Td) differentiation trend. Grey area shows the composition of true TTGs (with dark grey area showing the most common composition) from Martin et al. (2005). The same symbols and literature are used as in Figure 3.3.

The Bosumtwi intrusions have many similarities to TTG granitoids, which would be expected if they are a result of shallow anatexis of crustal rocks of general TTG composition. Similarly, in the case of the Tenkodogo-Yamba pluton from eastern Burkina Faso (Naba et al. 2004), chemical similarities between TTG and the studied rocks are explained as resulting from partial remelting of slightly older rocks (from second phase of the granitic bodies formation according to de Kock et al. 2011) with more clear TTG affinity, not because

of a shared formation process. In conclusion, the Bosumtwi intrusions should not be termed TTG, even though they are geochemically very similar to them.

3.5.4. Emplacement of the granitoids and interaction with older rocks

Four samples, one from the Pepiakese granite (BOS10A) and three from the Southern intrusion (BOS17, BOS19A and BOS19B), significantly differ petrographically and geochemically from the other samples (Table S1, Figure S1) in terms of their more mafic properties. The atypical composition of the sample BOS10A is probably a result of assimilation of a mafic dike component (not necessarily of the same composition as sample BOS13) by felsic intrusion (see Figure S3). This hypothesis is also supported by Moon and Mason (1967), who hypothesized such assimilation from field evidence.

The second group of samples with more mafic character: BOS17, BOS19A, and BOS19B represents a contact zone between an intruding granitoid (characterized by BOS16 composition) and country rocks (characterized by BOS19A, and BOS19B composition). Lack of the obvious signs of remelting or contact metamorphism within the coarser domain of sample BOS17 and samples BOS19A and BOS19B suggests a generally low temperature during the emplacement at shallow depth.

3.5.5. Proposed changes to the map of the Bosumtwi crater area

Based on our new data, some changes to the geological map of the surroundings of the Bosumtwi impact crater (Koeberl and Reimold 2005) are required (Figure S4 and explanations therein). All studied intrusions have similar petrographic, geochemical, and geochronological properties, and belong to the basin-type granitoids of the fourth (late-stage granitoids emplaced between 2097 ± 3 Ma and 2074 ± 5 Ma) phase of de Kock et al.'s (2011) classification. They are probably related to the Banso granitoid (e.g., Woodfield 1966, Moon and Mason 1967, Feybesse et al. 2006).

3.6. Conclusions

We conclude that all granitic intrusions in the proximity of Bosumtwi crater were derived by a similar process and approximately at the same time and that are genetically related to the Banso granite and can be classified as basin-type, late-stage granitoids (in contrast to the previously published map by Koeberl and Reimold 2005). Their composition (strongly peraluminous muscovite granites and granodiorites) and age (between 2092 ± 6.1 Ma and 2098 ± 6.1 Ma) suggests that they were formed as a result of anatexis of TTGs (or rocks derived from them) at relatively low pressure of about 400-500 MPa and a temperature between 600 and 700 degrees Celsius. The location of their emplacement was governed by proximity to one of the main D2 sinistral transcurrent faults in the area and happened on low depth.

Based on those findings, a revision of the geological map of the Bosumtwi crater area by Koeberl and Reimold (2005) is proposed.

Acknowledgments

This project is funded within the framework of the “IK Planetology – from Asteroids to Impact Craters” (IK-1045) at the University of Vienna. We thank Lutz Hecht for assistance with obtaining some of the literature sources, and Matthew Huber for proofreading the article. We thank Thorsten Nagel and Uwe Reimold for detailed and helpful reviews that significantly improved this paper.

References

- Abouchami W., Boher M., Michard A., and Albarede F. 1990. A major 2.1 Ga event of mafic magmatism in West Africa: an early stage of crustal accretion. *Journal of Geophysical Research* 97: 17605–17629.
- Adadey K., Théveniaut H., Clarke B., Urien P., Delor C., Roig R. J., and Feybesse J. L. 2009. Geological Map Explanation, Map Sheet 0503B (1:100 000). CGS/BRGM/Geoman. Geological Survey Department of Ghana.
- Agyei Duodu J., Loh G. K., Hirdes W., Boamah K. O., Baba M., Anokwa Y. M., Asare C., Brakohiapa E., Mensah R. B., Okla R., Toloczyki M., Davis D. W., and Gluck S. 2009. Geological map of Ghana 1:1 000 000. BGS, GGS, Accra (Ghana), Hannover (Germany).
- Attoh K., Evans M. J., and Bickford M. E. 2006. Geochemistry of an ultramafic-rodingite rock association in the Paleoproterozoic Dixcove greenstone belt, southwestern Ghana. *Journal of African Earth Sciences* 45: 333–346.
- Barbarin B. 1997. Genesis of the two main types of peraluminous granitoids. *Geology* 24: 295–298.
- Barker F., and Arth J. G. 1976. Generation of trondhjemitic- tonalitic liquids and Archean bimodal trondhjemite- basalt suites. *Geology* 4: 596–600.
- Blichert-Toft J., Boyet M., Telouk P., and Albarede F. 2002. Sm-147- Nd-143 and Lu-176-Hf-176 in eucrites and the differentiation of the HED parent body. *Earth and Planetary Science Letters* 204: 167–181.
- Boamah D., and Koeberl C. 2003. Geology and geochemistry of shallow drill cores from the Bosumtwi impact structure, Ghana. *Meteoritics and Planetary Science* 38: 1137–1159.

- Boamah D., and Koeberl C. 2006. Petrographic studies of “fallout” suevite from outside the Bosumtwi impact structure, Ghana. *Meteoritics and Planetary Science* 41: 1761–1774.
- Boher M., Abouchami W., Michard A., Albarede F., and Arndt N.T. 1992. Crustal growth in West Africa at 2.1 Ga. *Journal of Geophysical Research* 97: 345–369.
- Bouvier A., Blichert-Toft J., Vervoort J. D., Gillet P., and Albarède F. 2008. The case for old basaltic shergottites. *Earth and Planetary Science Letters* 266: 105–124.
- Bowring S. A., Schoene B., Crowley J. L., Ramezani J., and Condon D. J. 2006. High-precision U-Pb geochronology and the stratigraphic record: progress and progress, in: Geochronology, Emerging Opportunities, edited by Olszewski T.D. *The Paleontological Society Special Publication* 12. pp. 25-46.
- Bowring J. F., McLean N. M., and Bowring S. A. 2011. Engineering cyber infrastructure for U-Pb geochronology: Tripoli and U-Pb_Redux. *Geochemistry, Geophysics, Geosystems* 12: Q0AA19, doi: 10.1029/2010GC003479.
- Condie K. C. 2005. TTGs and adakites: Are they both slab melts? *Lithos* 80: 33-44.
- Coney L., Gibson R. L., Reimold W. U., and Koeberl C. 2007. Litostratigraphic and petrographic analysis of ICDP drill core LB-07A, Bosumtwi impact structure, Ghana. *Meteoritics and Planetary Science* 42: 569–589.
- Coney L., Reimold W. U., Gibson R. L., Koeberl C., and Ogilvie P. 2010. Melt particle characteristics of the within- and out-of- crater suevites from the Bosumtwi impact structure, Ghana: Implications for crater formation, in: Gibson, R.L., and Reimold, W.U., (Eds.), Large Meteorite Impacts and Planetary Evolution IV: *Geological Society of America Special Paper* 465. pp. 411–442.
- Dai X., Boamah D., Koeberl C., Reimold W. U., Irvine G., and McDonald I. 2005. Bosumtwi impact structure, Ghana: Geochemistry of impactites and target rocks, and search for a meteoritic component. *Meteoritics and Planetary Science* 40: 1493–1511.
- Dampare S. B., Shibata T., Asiedu D. K., Osae S., and Banoeng-Yakubo B. 2008. Geochemistry of Paleoproterozoic metavolcanic rocks from the southern Ashanti

- volcanic belt, Ghana: Petrogenetic and tectonic setting implications. *Precambrian Research* 162: 403–423.
- Davis D. W., Hirdes W., Schaltegger E., and Nunoo E. A. 1994. U/Pb age constraints on deposition and provenance of Birimian and gold-bearing Tarkwaian sediments in Ghana, West Africa. *Precambrian Research* 67: 89–107.
- Debat P., Nikiema S., Mercier A., Lompo M., Béziat D., Bourges F., Roddaz M., Salvi S., Tollon F., and Wenmenga U. 2003. A new metamorphic constraint for the Eburnean orogeny from Paleoproterozoic formations of the Man Shield (Aribinda and Tampelga countries, Burkina Faso). *Precambrian Research* 123: 47–65.
- de Kock G. S., Armstrong R. A., Siegfried H. P., and Thomas E. 2011. Geochronology of the Birim Supergroup of the West African craton in the Wa-Bolé region of west-central Ghana: Implications for the stratigraphic framework. *Journal of African Earth Sciences* 59: 1–40.
- Deutsch A., Luetke S., and Heinich V. 2007. The ICDP Lake Bosumtwi impact crater Scientific Drilling Project (Ghana): Core LB-08A litholog, related ejecta and shock recovery experiments. *Meteoritic and Planetary Science* 42: 635–654.
- Dia A., Van Schmus W. R., and Kröner A. 1997. Isotopic constraints on the age and formation of a Paleoproterozoic volcanic arc complex in the Kédougou Inlier, West Africa. *Journal of African Earth Sciences* 24: 197–213.
- Doumbia S., Pouclet A., Kouamelan A., Peucat J. J., Vidal M., and Delor C. 1998. Petrogenesis of juvenile-type Birimian (Paleoproterozoic) granitoids in Central Côte d'Ivoire, West Africa: geochemistry and geochronology. *Precambrian Research* 87: 33–63.
- Egal E., Thieblemont D., Lahondère D., Guerrot C., Costea C.A., Iliescu D., Delor C., Goujou J. C., Lafon J. M., Tegye M., Diady S., and Kolié P. 2002. Late Eburnean granitization and tectonics along the western and northwestern margin of the Kénéma-Man domain (Guinea, West African Craton). *Precambrian Research* 117: 56–84.

- Ferrière L., Koeberl C., and Reimold W. U. 2007. Drill core LB-08A, Bosumtwi impact structure, Ghana: Petrographic and shock metamorphic studies of material from the central uplift. *Meteoritics and Planetary Science* 42: 611–633.
- Ferrière L., Koeberl C., Thoni M., and Liang C. 2010. Single crystal U-Pb zircon age and Sr-Nd isotopic composition of impactites from the Bosumtwi impact structure, Ghana: Comparison with country rocks and Ivory Coast tektites. *Chemical Geology* 275: 254–261.
- Feybesse J., Billa M., Guerrot C., Duguey E., Lescuyer J., Milesi J., and Bouchot V. 2006. The paleoproterozoic Ghanaian province: Geodynamic model and ore controls, including regional stress modeling. *Precambrian Research* 149: 149–196.
- Galipp K., Klemd R., and Hirdes W. 2003. Metamorphism and geochemistry of the Paleoproterozoic Birimian Sefwi volcanic belt (Ghana, West Africa). *Geologisches Jahrbuch D* 111: 151–191.
- Gasquet D., Barbey P., Adou M., and Paquette J. L. 2003. Structure, Sr-Nd isotope geochemistry and zircon U-Pb geochronology of the granitoids of the Dabakala area (Côte d'Ivoire): evidence for a crustal growth event in the Paleoproterozoic of West Africa? *Precambrian Research* 127: 329–354.
- Grenholm M. 2011. Petrology of Birimian granitoids in southern Ghana – petrography and petrogenesis. Bachelor thesis. Department of Earth and Ecosystem Sciences. Division of Geology, Lund University.
- Hay D. C., and Dempster T. J. 2009. Zircon behaviour during low-temperature metamorphism. *Journal of Petrology* 50: 571–589.
- Hirdes W., Davis D. W., and Eisenlohr B. N. 1992. Reassessment of Proterozoic granitoid ages in Ghana on the basis U/Pb zircon and monazite dating. *Precambrian Research* 56: 89–96.
- Hirdes W., Davis D. W., Luedtke G., and Konan G. 1996. Two generations of Birimian (Paleoproterozoic) volcanic belts in northeastern Cote d'Ivoire (West Africa): consequences for the 'Birimian controversy'. *Precambrian Research* 80: 173–191.

- Hirdes W., and Davis D. W. 1998. First U-Pb zircon age of extrusive volcanism in the Birimian Supergroup of Ghana/West Africa. *Journal of African Earth Sciences* 27: 291–294.
- John T., Klemm R., Hirdes W., and Loh G. 1999. The metamorphic evolution of the paleoproterozoic (Birimian) volcanic Ashanti belt (Ghana, West Africa). *Precambrian Research* 98: 11–30.
- Jones W. B., Bacon M., and Hastings D. A. 1981. The Lake Bosumtwi impact crater, Ghana. *Geological Society of America Bulletin* 92: 342–349.
- Jones W. B. 1985. Chemical analyses of Bosumtwi crater target rocks compared with the Ivory Coast tektites. *Geochimica et Cosmochimica Acta* 48: 2569–2576.
- Karikari F., Ferrière L., Koeberl C., Reimold W. U., and Mader D. 2007. Petrography, geochemistry, and alteration of country rocks from the Bosumtwi impact structure. *Meteoritics and Planetary Science* 42: 513–540.
- Koeberl C., and Reimold W. U. 2005. Bosumtwi impact crater, Ghana (West Africa): An updated and revised geological map, with explanations. *Jahrbuch der Geologischen Bundesanstalt*, Wien (Yearbook of the Austrian Geological Survey) 145: 31–70 (+1 map, 1:50,000).
- Koeberl C., Bottomley R., Glass B., and Storzer D. 1997. Geochemistry and age of Ivory Coast tektites and microtektites. *Geochimica et Cosmochimica Acta* 61: 1745–1772.
- Koeberl C., Reimold W. U., Blum J. D., and Chamberlain C. P. 1998. Petrology and geochemistry of target rocks from the Bosumtwi impact structure, Ghana, and comparison with Ivory Coast tektites. *Geochimica et Cosmochimica Acta* 62: 2179–2196.
- Koeberl C., Milkereit B., Overpeck J. T., Scholz C. A., Amoako P. Y. O., Boamah D., Danuor S. K., Karp T., Kueck J., Hecky R. E., King J., and Peck J. A. 2007. An international and multidisciplinary drilling project into a young complex impact structure: The 2004 ICDP Bosumtwi impact crater, Ghana, drilling project—An overview. *Meteoritics and Planetary Science* 42: 483–511.

- Kouamelan A. N., Delor C., and Peucat J. J. 1997. Geochronological evidence for reworking of Archean terrains during the early Proterozoic (2.1 Ga) in the western Côte d'Ivoire (Man Rise—West African Craton). *Precambrian Research* 86: 177–199.
- Lagos M., Scherer E. E., Tomaschek F., Muenker C., Keiter M., Berndt J., and Ballhaus C. 2007. High precision Lu–Hf geochronology of Eocene eclogite-facies rocks from Syros, Cyclades, Greece. *Chemical Geology* 243: 16–35.
- Le Bas M. J., Le Maitre R. W., and Wooley A. R. 1992. The construction of the Total Alkali-Silica chemical classification of volcanic rocks. *Mineralogy and Petrology* 46: 1–22.
- Leube A., and Hirdes W. 1986. The Birimian Supergroup of Ghana (with a contribution on granitoids by R. Mauer). Technical Cooperation Project No. 80.2040.6, Endbericht, 260 Seiten, BGR ArchivNummer 99529, Hannover.
- Leube A., Hirdes W., Maur R., and Kesse G. O. 1990. The early Proterozoic Birimian Supergroup of Ghana and some aspects of its associated gold mineralization. *Precambrian Research* 46: 139–165.
- Lompo M. 2010. Paleoproterozoic structural evolution of the Man-Leo Shield (West Africa). Key structures for vertical to transcurrent tectonics. *Journal of African Earth Sciences* 58: 19–36.
- Lugmair G. W., and Marti K. 1978. Lunar initial $^{143}\text{Nd}/^{144}\text{Nd}$: differential evolution of the lunar crust and mantle. *Earth Planetary Science Letters* 39: 349–357.
- Mader D., and Koeberl C. 2009. Using Instrumental Neutron Activation Analysis for geochemical analyses of terrestrial impact structures: Current analytical procedures at the University of Vienna Geochemistry Activation Analysis Laboratory. *Applied Radiation and Isotopes* 67: 2100–2103.
- Martin H. 1993. The mechanisms of petrogenesis of the Archean continental crust – comparison with modern processes. *Lithos* 30: 373–388.
- Martin H. 1999. The adakitic magmas: modern analogues of Archaean granitoids. *Lithos* 46: 411–429.

- Martin H., and Moyen J.-F. 2002. Secular changes in TTG composition as markers of the progressive cooling of the Earth. *Geology* 30: 319– 322.
- Martin H., Smithies R. H., Rapp R., Moyen J.-F., and Champion D. 2005. An overview of adakite, tonalite-trondhjemite-granodiorite (TTG), and sanukitoid: Relationships and some implications for crustal evolution. *Lithos* 79: 1–24.
- Mattinson J. M. 2005. Zircon U-Pb chemical abrasion ("CA-TIMS") method: Combined annealing and multi-step partial dissolution analysis for improved precision and accuracy of zircon ages. *Chemical Geology* 220: 47–66
- McLean N. M., Bowring S. A., and Bowring J. F. 2011. An algorithm for U-Pb isotope dilution data reduction and uncertainty propagation. *Geochemistry, Geophysics, Geosystems* 12: Q0AA18 doi:10.1029/2010GC003478.
- Metelka V., Baratoux L., Naba S., and Jessell M. V. 2011. A geophysically constrained litho-structural analysis of the Eburnean greenstone belts and associated granitoid domains, Burkina Faso, West Africa. *Precambrian Research* 190: 48–69.
- Moon P. A., and Mason D. 1967. The geology of 1/4° field sheets nos. 129 and 131, Bompata S.W. and N.W. *Ghana Geological Survey Bulletin* 31: 1–51.
- Münker C., Weyer S., Scherer E., and Mezger K. 2001. Separation of high field strength elements (Nb, Ta, Zr, Hf) and Lu from rock samples for MC-ICPMS measurements. *Geochemistry, Geophysics, Geosystems* 2: doi: 10.1029/2001GC000183.
- Naba S., Lompo M., Debat P., Bouchez J. -L., and Béziat D. 2004. Structure and emplacement model for late-orogenic Paleoproterozoic granitoids: the Tenkodogo–Yamba elongate pluton (Eastern Burkina Faso). *Journal of African Earth Sciences* 38: 41–57.
- Nagel T. J., Hoffmann J. E., and Munker C. 2012. Generation of Eoarchean tonalite-trondhjemite-granodiorite series from thickened mafic arc crust. *Geology* 40: 383–384.

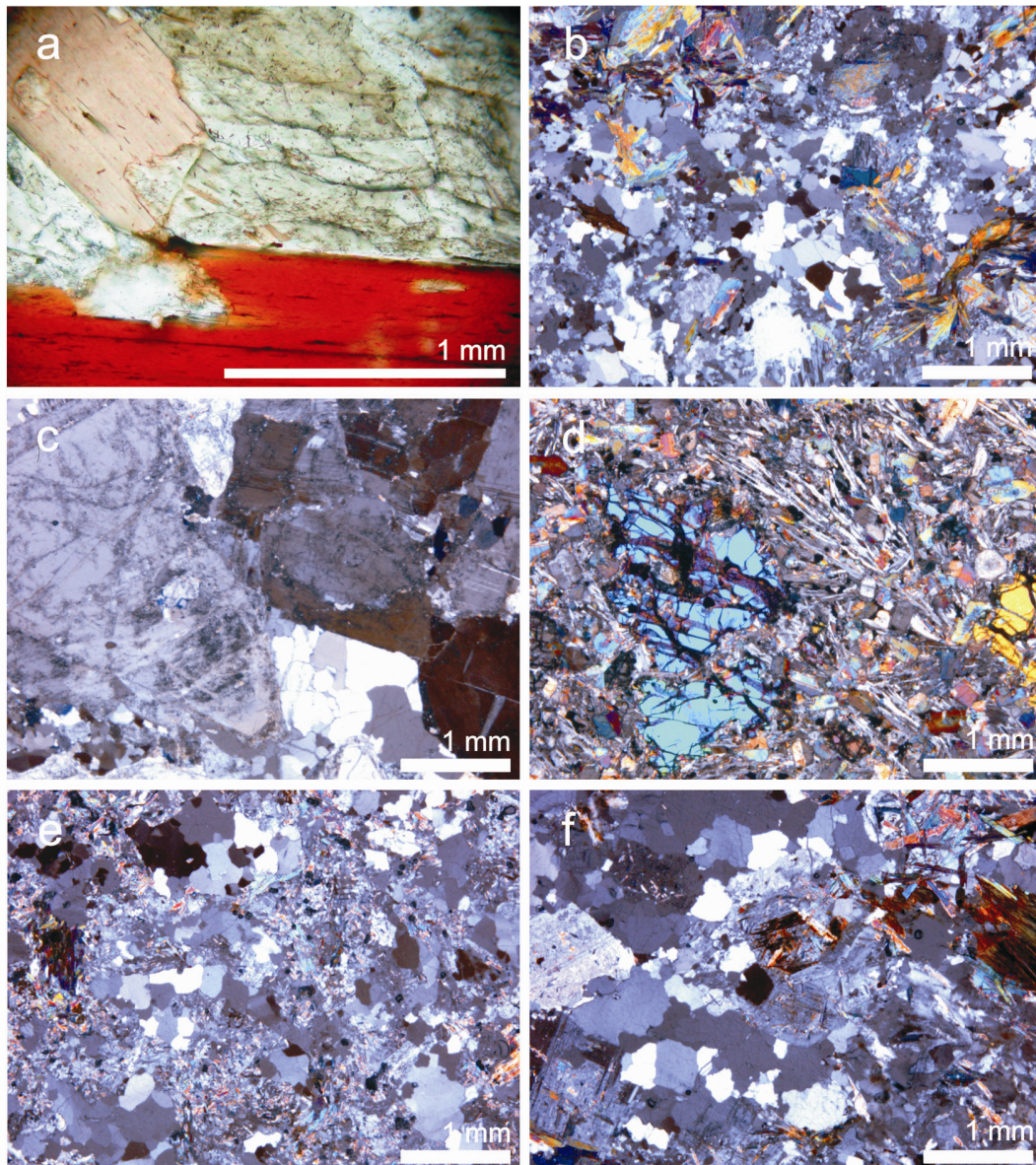
- Oberthür T., Vetter U., Davis D. W., and Amanor J. A. 1998. Age constraints on gold mineralization and Paleoproterozoic crustal evolution in the Ashanti belt of southern Ghana. *Precambrian Research* 89: 129–143.
- Pawlig S., Gueye M., Klischies R., Schwarz S., Wemmer K., and Siegesmund S. 2006. Geochemical and Sr–Nd isotopic data on the Birimian of the Kédougou-Kénieba inlier (eastern Senegal): implications on the Paleoproterozoic evolution of the West African craton. *South African Journal of Geology* 109: 411–427.
- Pearce J. A., Harris N. B. W., and Tindle A. G. 1984. Trace element discrimination diagrams for the tectonic interpretation of granitic rocks. *Journal of Petrology* 25: 956–983.
- Perrouy S., Ailleres L., Jessell M. W., Baratou L., and Bourassa Y. 2012. Revised Eburnean geodynamic evolution of the gold-rich southern Ashanti Belt, Ghana, with new field and geophysical evidence of pre-Tarkwaian deformations. *Precambrian Research* 204–205: 12–29.
- Pigois J. P., Grove D. I., Fletcher I. R., McNaughton N. J., and Snee L. W. 2003. Age constraints on Tarkwaian paleoplacer and lode-gold formation in the Tarkwa–Damang district, SW Ghana. *Mineralium Deposita* 38: 695–714.
- Pin C., and Zalduegui J. F. S. 1997. Sequential separation of light rare-earth elements, thorium and uranium by miniaturized extraction chromatography: application to isotopic analyzes of silicate rocks. *Analytica Chimica Acta* 339: 79–89.
- Ramezani J., Schmitz M. D., Davydov V. I., Bowring S. A., Snyder W. S., and Northrup C. J. 2007. High-precision U–Pb zircon age constraints on the Carboniferous–Permian boundary in the southern Urals stratotype. *Earth and Planetary Science Letters* 256: 244–257.
- Reimold W. U., Koeberl C., and Bishop J. 1994. Roter Kamm impact crater, Namibia: Geochemistry of basement rocks and breccias. *Geochimica et Cosmochimica Acta* 58: 2689–2710.
- Reimold W. U., Brandt D., and Koeberl C. 1998. Detailed structural analysis of the rim of a large, complex impact crater: Bosumtwi crater, Ghana. *Geology* 26: 543–546.

- Scherer E., Muenker C., and Mezger K. 2001. Calibration of the lutetium-hafnium clock. *Science* 293: 683–687.
- Schoene B., Crowley J. L., Condon D. J., Schmitz M. D., and Bowring S. A. 2006. Reassessing the uranium decay constants for geochronology using ID-TIMS U–Pb data. *Geochimica et Cosmochimica Acta* 70: 426–445.
- Shand S. J. 1943. Eruptive Rocks. Their Genesis, Composition, Classification, and Their Relation to Ore-Deposits with a Chapter on Meteorite. New York: John Wiley & Sons.
- Smithies R. H. 2000. The Archaean tonalite–trondhjemite–granodiorite (TTG) series is not an analogue of Cenozoic adakite. *Earth and Planetary Science Letters* 182: 115–125.
- Söderlund U., Patchett P. J., Vervoort J. D., and Isachsen C. E. 2004. The ^{176}Lu decay constant determined by Lu–Hf and U–Pb isotope systematics of Precambrian mafic intrusions. *Earth and Planetary Science Letters* 219: 311–324.
- Sun S. S., and McDonough W. F. 1989. Chemical and isotopic systematics of oceanic basalts: implication for mantle composition and processes, in: Saunders, A.D., Norry, M.J. (Eds.), *Magmatism in Ocean Basins 42. Geological Society of London Special Publication*. pp. 313–345.
- Streckeisen A. L. 1974. Classification and Nomenclature of Plutonic Rocks. Recommendations of the IUGS Subcommittee on the Systematics of Igneous Rocks. *Geologische Rundschau. Internationale Zeitschrift für Geologie* 63: 773–785.
- Taylor P. N., Moorbath S., Leube A., and Hirdes W. 1992. Early Proterozoic crustal evolution in the Birimian of Ghana: Constraints from geochronology and isotope geochemistry. *Precambrian Research* 56: 97–111.
- Thompson M. D., Grunow A. M., and Ramezani J. 2007. Late Neoproterozoic paleogeography of the Southeastern New England Avalon Zone: Insights from U–Pb geochronology and paleomagnetism. *Geological Society of America Bulletin* 119: 681–696.

- Vegas N., Naba S., Bouchez J. L., and Jessell M. 2008. Structure and emplacement of granite plutons in the Paleoproterozoic crust of Eastern Burkina Faso: rheological implications. *International Journal of Earth Sciences* 97: 1165–1180.
- Vervoort J. D., Patchett P. J., Soederlund U., and Baker M. 2004. Isotopic composition of Yb and the determination of Lu concentrations and Lu/Hf ratios by isotope dilution using MCICPMS. *Geochemistry, Geophysics, Geosystems* 5: Q11002 doi: 10.1029/2004GC000721.
- Weyer S., Muenker C., Rehkaemper M., and Mezger K. 2002. Determination of ultra-low Nb, Ta, Zr and Hf concentrations and the chondritic Zr/Hf and Nb/Ta ratios by isotope dilution analyses with multiple collector ICP-MS. *Chemical Geology* 187: 295–313.
- Woodfield P. D. 1966. The geology of the 1/4° field sheet 91, Fumso, N.W. Ghana. *Ghana Geological Survey Bulletin* 30: 1–66.
- Wright J. B., Hastings D. A., Jones W. B., and Williams H. R. 1985. *Geology and Mineral Resources of West Africa*. London: Allen & Unwin.

Supplementary material

Figures



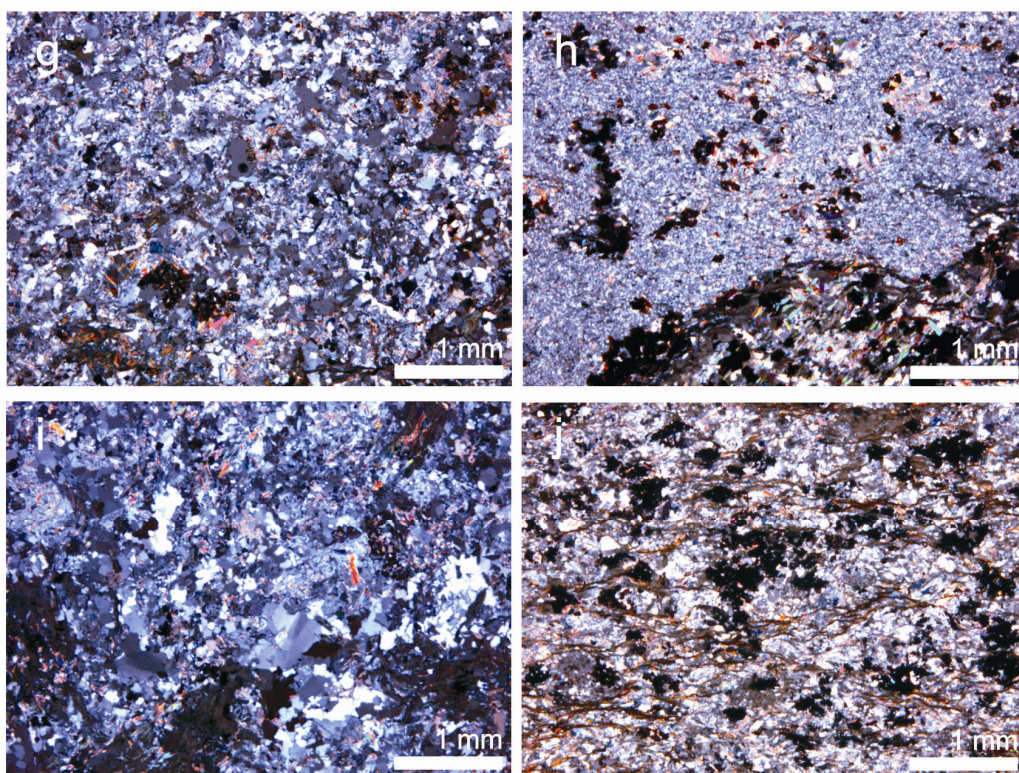


Figure S1. Representative microphotographs (taken with crossed polarizers) of samples from intrusions from the vicinity of Bosumtwi crater: a) sample BOS10A (Pepiakese intrusion), b) sample BOS11 (Pepiakese intrusion), c) sample BOS12 (Pepiakese intrusion), d) sample BOS13 (Mafic dike), e) sample BOS14A (Kumasi intrusion), f) sample BOS15 (Kumasi intrusion), g) sample BOS16 (Southern intrusion), h) sample BOS17 (Southern intrusion), i) sample BOS18 (Southern intrusion), j) sample BOS19B (Southern intrusion).

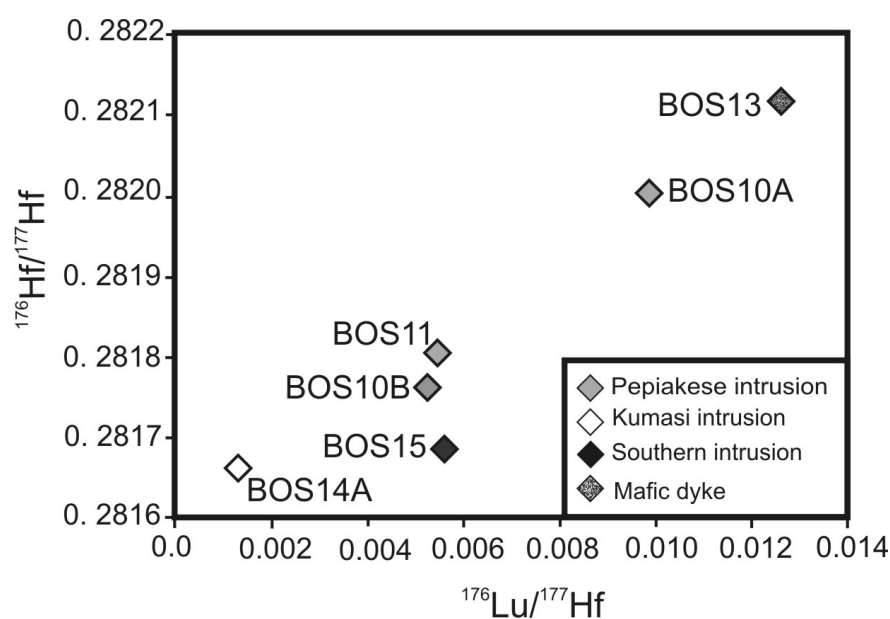


Figure S2. Isochron diagram for the Lu-Hf system for samples from Bosumtwi intrusions Pepiakese intrusion (BOS10A, BOS10B and BOS11) from Kumasi intrusion (BOS14A and BOS15) and from Mafic dike (BOS13). However, there is a large scatter for the six samples (one sample was lost during chemical preparation) analyzed for their Hf isotopes in the $^{176}\text{Hf}/^{177}\text{Hf}$ versus $^{176}\text{Lu}/^{177}\text{Hf}$ space. This most likely is attributable to the existence of zircons inherited from precursor magmas (e.g., Gasquet et al., 2003) or low temperature metamorphic processes (e.g., Hay and Dempster 2009).

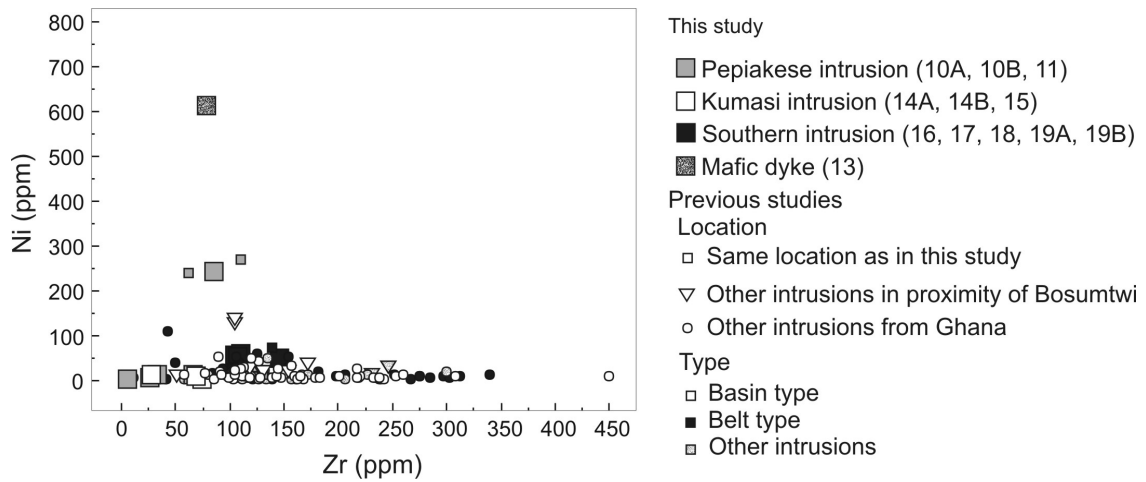


Figure S3. Plot of Zr vs. Ni showing compositional relationships between mafic dike (sample BOS13), three samples from Pepiakese granite and the rest of the samples from the proximity of the Bosumtwi crater and from felsic intrusions in Ghana. The plot shows that one of the samples analyzed in this research (BOS10A) and few samples from previous studies performed in proximity of Bosumtwi crater (J508 and J509 from Koeberl et al. 1998) are much more rich in nickel than the majority of samples from granitic intrusions from Ghana, including proximity of Bosumtwi (BOS10B, BOS11, BOS12, BOS14A, BOS14B, BOS15, BOS16, BOS18). Sample BOS10A also significantly differs petrographically from other samples; samples BOS10A and BOS10B were collected just two meters from each other, but their compositions lie on the two opposite sides of all chemical trends. Additionally, while BOS10B is a muscovite granite with a very small amount of mafic minerals, BOS10A has abundant biotite and some amphiboles. Therefore, we conclude that the atypical composition of samples BOS10A, J508, and J509 could be the result of assimilation of a mafic dike component (not necessarily of the same composition as sample BOS13) by felsic intrusion (see Figure 2S). This hypothesis is also supported by Moon and Mason (1967), who hypothesized such assimilation from field evidence.

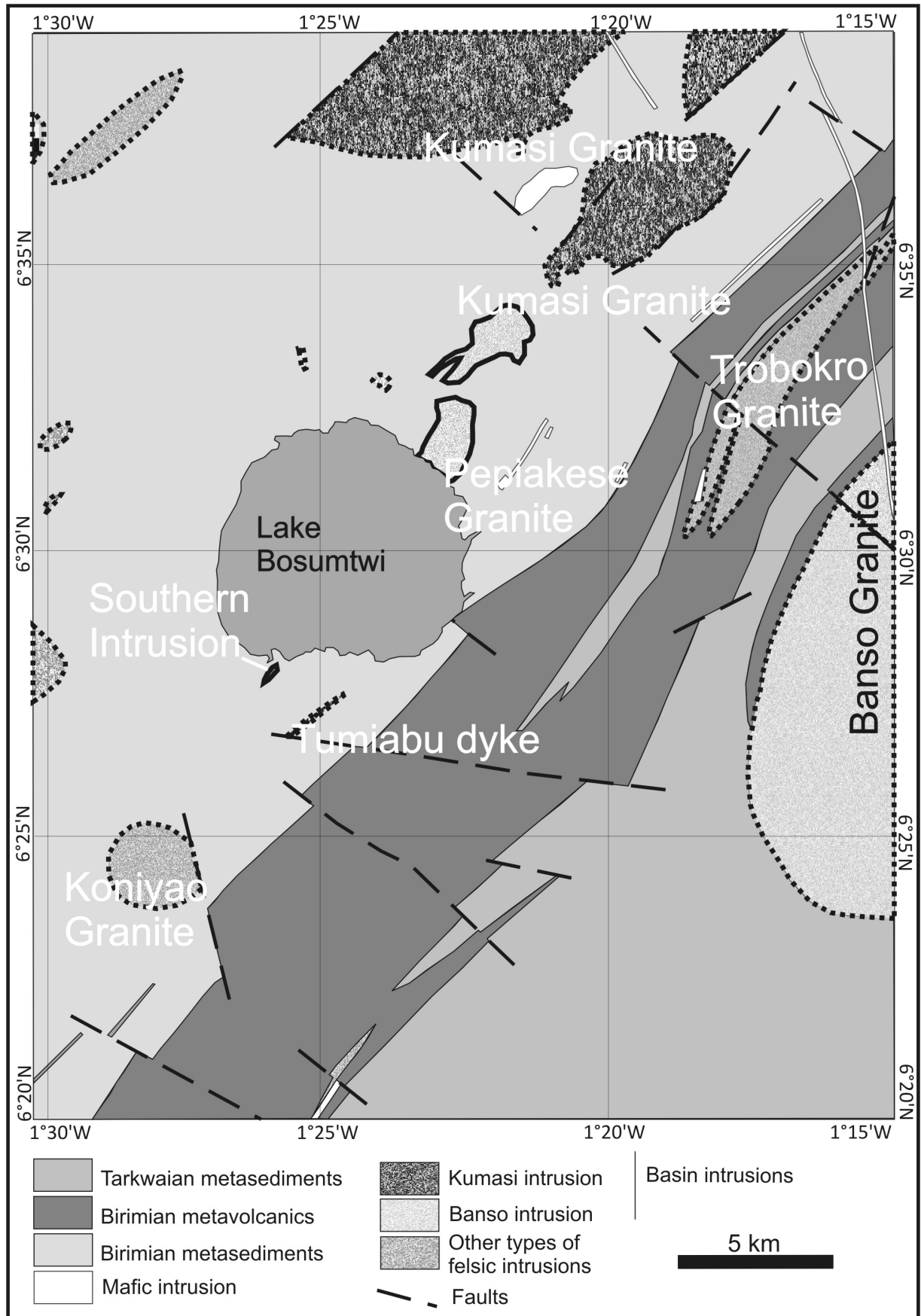


Figure S4. Proposed update of the geologic map by Koeberl and Reimold (2005) of the Bosumtwi impact crater area. We suggest that all studied intrusions belong to the basin-type granitoids of the fourth (late-stage granitoids emplaced between 2097 ± 3 Ma and 2074 ± 5 Ma) phase of de Kock et al.'s (2011) classification and are related to the Banso granitoid (e.g., Woodfield, 1966; Moon and Mason, 1967; Feybesse et al., 2006). Other plutons visible on the map and located between the $6^{\circ}35'N$ and $6^{\circ}30'N$ line are assumed to belong to the same population based on of their geographical proximity. This claim is not supported by any zircon ages, but is a reasonable assumption that can be tested by dating more rocks from the surroundings of Bosumtwi crater. Granitic bodies located to the north of the $6^{\circ}35'N$ line are marked as the Kumasi intrusion based on literature review (e.g., Moon and Mason, 1967; Koeberl and Reimold, 2005; Agyei Duodu et al., 2009). The validity of this classification should be verified in the future by dating more rocks from those intrusions. The Banso intrusion, located in the eastern part of the map, is now marked as a single granitic body of basin-type (late-stage granitoid), not two granitic bodies (northern: belt-type and southern: basin-type) divided by a fault as presented on the map of Koeberl and Reimold (2005). Based on a literature review (Woodfield, 1966; Moon and Mason, 1967) there is no reason to divide this intrusion into two separate areas, especially belonging to two distinct types. The Koni Yao Granite, along with the Trobokro Granite and a granitic body located to the west of the Bosumtwi structure are marked as "other" types on the proposed revised map, as the available data do not allow for their definitive classification.

Tables

Table S1. Petrographic description of samples from the intrusions in the proximity of the Bosumtwi impact structure.

Location	Sample No.	Description
Pepiakese Intrusion	BOS10A	<p>Medium- to coarse-grained muscovite-biotite granite</p> <p>Quartz is relatively rare (up to 14 vol%), and feldspars (34 vol%) consist of an equal amount of plagioclase and K-feldspar. Some of the plagioclases are large and euhedral and some are zoned. The edges of some of the feldspars are wavy, which can suggest recrystallization and equilibration at high temperature. Biotite (12 vol%) is characterized by larger crystals, but muscovite is more abundant (23 vol%). Chlorite (~14 vol%) and few grains of amphibolite (~2 vol%) are present. Accessory minerals are small and rare zircon, tourmaline and possibly apatite grains.</p>
	BOS10B	<p>Medium- to coarse-grained muscovite granite</p> <p>Quartz is abundant, forms almost 45 vol% of the sample and grains show signs of equilibration at high temperature. Feldspar (33 vol%) grains (dominated by K-feldspar), are large and euhedral, partially sericitized. Abundant muscovite (10 vol%) and rare biotite (2 vol%) grains are unaltered. Accessory minerals are: tourmaline, zircon and small opaques. Cracks within quartz and feldspar grains are filled with chlorite or epidote. This along with small patches of brownish material seem to suggest that this sample undergone some low-temperature alteration.</p>
	BOS11	<p>Medium- to coarse-grained muscovite granite</p> <p>Petrographically, this sample is very similar to sample BOS10B. Quartz forms more than 50 vol% of the sample. Quartz grains vary in size, from ones similar in size to feldspar to very small (suggesting reequilibration). Some of the large quartz grains show undulatory extinction. Large euhedral grains of feldspar (~30 vol%) are intergrown by numerous crystals of muscovite and other accessory minerals. In a few places myrmekite is present. Primary sheet silicates are present in groups, commonly consisting of one large biotite grain surrounded by smaller, numerous muscovite grains. Accessory minerals include rutile and tourmaline.</p>
	BOS12	<p>Pegmatite</p> <p>Pegmatite consisting of very large feldspars (75 vol%) (microcline, K-feldspar, and plagioclase) and much smaller quartz grains (21 vol%). Few large biotite grains (1 vol%) on the boundaries between quartz and feldspar crystals are present, as well as a small amount of muscovite within feldspar. Oxides are very rare and aneuhedral.</p>
Mafic dike	BOS13	<p>Porphyritic Diabase</p> <p>This fresh sample consists of large (>1 mm) crystals of olivine (3 vol%), long (up to 2 mm) but very thin plagioclase laths (15 vol%), aneuhedral clinopyroxene crystals (35 vol%) and a more fine-grained matrix (47 vol%) consisting of clinopyroxene, plagioclase, minor olivine and oxides. Accessory minerals include hornblende, apatite, and chlorite.</p>

Kumasi Intrusion	BOS14A	Coarse-grained muscovite granite	The sample consists of large quartz grains (up to 50 vol%), weathered feldspars (35 vol%) and few medium to coarse grained biotites (2 vol%) and primary muscovite crystals. Sample is strongly altered, and a significant portion of the feldspar has fully altered to sericite. Veins within quartz are filled with secondary material (sericite and/or chlorite). Other quartz grains have numerous bubble tracks. Few larger quartz grains display undulatory extinction. Oxides are very rare and anhedral. Accessory minerals: tourmaline and apatite.
	BOS14B	Coarse-grained muscovite granite	Petrographically, this sample is very similar to sample 14A, but includes large (~1 mm) biotite grains, some of which are weathered to chlorite.
	BOS15	Coarse-grained muscovite granite	The sample consists of large euhedral feldspar grains (46 vol%) with inclusions of muscovite, quartz with few bubble tracks (37 vol%), muscovite (11 vol%) and biotite (3 vol%), along with some phases resulting from alteration (3 vol%). At some quartz-feldspar boundaries discrete myrmekite are present. Muscovite and biotite grains always occur together and show very discrete foliation.
Southern Intrusion	BOS16	Medium-grained granite	Quartz grains (45 vol%) are arranged in large aggregates of very small grains. Part of the rare larger quartz grains show undulatory extinction. Feldspars (mostly K-feldspar) form approximately 25 vol% of the sample and some of the grains are almost totally turned into sericite. Biotite (15 vol%) and muscovite are highly altered to chlorite. Various alteration phases (including products of muscovite weathering) take up to 15 vol% of the sample. Few rutile grains are also present.
	BOS17	Contact zone	This sample includes of two domains with very different properties. The first domain is significantly coarser-grained and consists of quartz and feldspar along with chlorite and brownish material with numerous opaque grains. The second domain is much finer-grained and consists of mixture of quartz, feldspar and muscovite. The coarse-grained fraction is foliated and much more altered than fine-grained fraction (biotite and muscovite are altered to chlorite).
	BOS18	Altered granite	Severely altered medium grained granite, similar to sample BOS16. It consists of quartz (40 vol%), feldspars (30 vol%) that are altered to sericite (with few exceptions), muscovite and biotite altered to chlorite, few grains of titanite and very small number of anhedral opaques. Some quartz shows undulatory extinction.
	BOS19A	Gneissified granite	Strongly weathered, foliated fine/medium-grained gneissified granite. It is similar to the coarser-grained part of sample 17. It consists of quartz, feldspars (plagioclase is more common than K-feldspar), and oxides, as well as aligned fine-grained micas (chlorite, biotite, muscovite) and probably hornblende. Also, rare unaltered muscovite grains are present. Few apatite grains are present, as well as a brownish, amorphous phase (likely the result of alteration).
	BOS19B	Gneissified granite	Very similar to sample BOS19A.

Table S2. Whole rock chemical composition of samples collected from intrusions located in the proximity of Bosumtwi crater published previously (Koeberl et al. 1998, Dai et al. 2005, Karikari et al. 2007).

	LBF-10	LBF-18	LBF-24	LBF-26	LBF-36	LBF-57	LBF-34	LBF-38	LBF-50	J493	J505	J507	J508	J509	LB-28	LB-35	LB-36
	Karikari et al. 2007									(Koeberl et al. 1998)					(Dai et al. 2005)		
	Microgranite	Granite	Granite	Granite	Granite	Granite	Granite	Granite	Granite	Granite	Granite	Granite	Granite	Granite	Granite	Granite	Granite
Intrusion	Other (N)					Pepiakese	Other (E)	Other (SW)	Southern	Other (W)	Pepiakese			Other (NW)	Pepiakese		
SiO ₂	62.8	65.6	67.2	61.3	66.4	63.6	74.3	71.4	68.4	68.24	69.24	66.69	53.13	53.6	73.98	72.99	66.36
TiO ₂	0.69	0.62	0.45	0.60	0.67	0.52	0.13	0.99	0.58	0.5	0.5	0.06	0.45	0.88	0.2	0.31	0.67
Al ₂ O ₃	17.6	15.0	16.4	14.4	16.9	14.9	14.9	17.3	15.1	15.7	16.8	19.9	14.7	14.7	15.7	14.9	16.9
Fe ₂ O ₃	5.58	5.51	4.36	7.76	4.72	6.04	1.10	0.98	3.19	4.27	3.66	0.48	9.17	8.61	1.12	1.86	4.81
MnO	0.05	0.08	0.06	0.11	0.05	0.08	0.02	0.01	0.08	0.03	0.00	0.00	0.11	0.09	0.03	0.07	0.05
MgO	2.59	3.98	1.20	5.72	1.74	5.88	0.30	0.34	1.69	1.8	1.09	0.12	10.17	9.6	0.25	0.59	1.74
CaO	0.81	0.97	2.16	0.12	1.09	0.62	0.80	0.16	3.14	0.32	0.31	0.23	6.76	6.1	0.29	1.94	1.09
Na ₂ O	3.51	3.18	4.58	1.57	4.37	2.89	5.21	4.67	4.86	4.62	3.65	11.88	2.92	3.31	4.77	4.46	3.90
K ₂ O	1.46	0.85	0.82	1.20	1.63	0.93	2.25	1.81	2.57	1.77	2.08	0.47	0.27	1.27	1.84	1.78	1.63
P ₂ O ₅	0.17	0.19	0.15	0.10	0.24	0.17	0.03	0.02	0.23	0.06	0.05	0.02	0.08	0.21	0.01	0.05	0.24
SO ₃	-	-	-	-	-	-	-	-	-	-	-	-	-	-	-	-	-
LOI	4.95	4.07	2.34	7.36	3.25	5.28	1.07	2.34	0.53	2.65	3.31	0.51	2.22	1.70	1.97	1.29	3.25
Total	100.10	100.10	99.74	100.30	101.00	100.90	100.00	100.10	100.30	99.99	100.69	100.33	100.01	100.11	100.13	100.24	100.67
Sc	15.0	15.9	8.68	20.7	13.0	16.4	3.58	3.61	6.11	9.78	9.74	1.37	27.9	23.3	1.83	2.29	-
V	113	124	83	139	64	105	14	67	50	92	90	34	145	150	<15	18	64
Cr	57	51	7	550	37	540	9	23	40	157	97	19	753	779	6	10.6	50
Co	13	18	9	24	9	23	1	6	9	13	6	3	43	45	6	2	12
Ni	34	20	19	124	18	135	9	13	27	73	25	11	237	267	8	26	13
Cu	<2	<2	19	<2	<2	<2	15	<2	8	3	18.3	3	34	35.9	<2	<2	<2
Zn	78	70	57	96	59	78	35	25	69	86	77	6	124	139	17	48	53
Ga	-	-	-	-	-	-	-	-	-	46	27	60	70	90	6	12	-
As	13.2	0.93	1.36	3.56	0.95	1.14	2.60	4.86	5.73	27.2	2.56	19.1	3.22	15.9	0.78	1.40	-
Se	1.1	1.5	1.3	2.3	<1.3	<1.8	1.5	0.4	<1.2	0.3	0.2	0.1	0.1	0.1	-	-	-
Br	-	-	-	-	-	-	-	-	-	0.2	0.1	0.2	0.1	0.2	0.6	0.0	-
Rb	46.7	46	29.4	45.7	59.7	19.4	50.5	60.9	79.6	51.2	88.6	9.5	7.9	49.9	51	68	59
Sr	202	390	488	157	361	241	256	566	1205	311	372	335	359	438	392	377	361
Y	10	11	13	13	18	10	13	11	13	10	11	5	9	19	<3	4	18
Zr	173	155	130	105	131	105	78.2	232	247	139	119	73	62	110	52	113	131
Nb	10	8	7	8	9	8	9	20	10	4	3	2	0	4	6	7	9
Sb	0.36	0.25	0.22	0.12	0.31	0.02	0.14	<0.11	0.1	0.21	0.14	0.26	0.64	0.37	-	-	-
Cs	2.05	2.09	1.35	1.98	2.96	0.77	2.1	2.85	4.42	2.73	5.71	0.46	0.63	1.51	1.67	3.19	-
Ba	254	323	297	348	676	168	624	536	1420	496	714	151	136	391	652	583	676
La	7.61	27.5	10.4	21.7	19.4	16.0	13.1	23.8	71.2	14.8	22.8	26.3	6.26	14.1	12.8	25.8	-
Ce	18.5	56.6	24.3	43.2	36.0	32.2	23.3	50.3	127	32.1	46.7	47.2	11.8	37.1	29.2	50.4	-
Nd	6.17	28.9	10.7	20.3	23.0	16.9	11.3	27.6	61.7	13.4	26.1	17.5	6.20	28.7	11.0	24.0	-
Sm	1.15	4.95	2.30	3.94	4.25	3.61	1.70	5.19	10.30	3.49	3.99	2.91	1.69	6.13	1.78	3.61	-
Eu	0.32	1.33	0.87	1.12	1.26	1.12	0.50	1.40	2.77	0.89	1.17	0.83	0.86	1.89	0.51	1.07	-
Gd	1.75	3.40	2.17	3.26	3.55	3.00	1.50	3.40	6.13	3.40	3.40	1.80	2.30	5.10	1.30	1.80	-
Tb	0.32	0.47	0.40	0.52	0.63	0.41	0.25	0.39	0.68	0.61	0.57	0.22	0.45	0.75	0.18	0.25	-
Dy	-	-	-	-	-	-	-	-	-	3.10	3.00	1.30	2.50	4.20	-	-	-
Tm	0.19	0.21	0.17	0.27	0.26	0.18	0.17	0.11	0.17	0.24	0.19	0.10	0.19	0.31	0.05	0.06	-
Yb	1.47	1.33	1.05	1.89	2.11	1.02	1.16	0.65	0.90	1.08	1.17	0.55	1.13	1.87	0.24	0.39	-
Lu	0.27	0.19	0.14	0.24	0.33	0.15	0.15	0.06	0.14	0.16	0.15	0.08	0.12	0.23	0.03	0.06	-
Hf	6.72	2.77	2.36	2.50	3.29	2.36	2.28	5.57	4.91	3.54	3.77	1.84	0.78	3.02	1.44	2.66	-
Ta	1.07	0.29	0.24	0.24	0.29	0.20	0.50	1.30	0.41	0.19	0.36	0.11	0.31	0.16	0.11	0.21	-
W	-	-	-	-	-	-	-	-	-	0.8	0.9	0.3	0.6	0.7	-	-	-
Ir (ppb)	-	-	-	-	-	-	-	-	-	<1.5	<2	<1	<1	<1	<1.1	2.8	-
Au (ppb)	0.5	0.7	1.5	0	<1.4	0.5	1.2	1.9	0.6	25	18	17	10	28	0.8	8.2	-
Th	4.36	5.06	1.48	2.11	2.76	2.21	2.55	3.61	8.37	2.83	3.37	5.17	0.71	0.75	2.13	2.51	-
U	1.60	0.93	0.65	1.02	0.72	0.68	1.38	1.4	2.72	1.86	1.64	1.47	0.23	0.53	0.32	0.7	-
Pb	-	-	-	-	-	-	-	-	-	-	-	-	-	-	-	-	-

Note: Major element data (in wt%) along with some trace elements (V, Ni, Cu, Zn, Rb, Sr, Y, Zr, Nb, Ba, and Pb) as measured by XRF, the other elements as measured by INAA. All Fe as Fe₂O₃. Trace elements data in ppm, except as noted.

4. Spatial characterization of planar deformation features in quartz and implications for understanding shock wave propagation at the grain scale

Anna Losiak¹, Izabela Gołębiowska², Ludovic Ferrière³, Jacek Wojciechowski⁴, Matthew Huber¹ and Christian Koeberl^{1,3}

¹Department of Lithospheric Research, University of Vienna, Althanstrasse 14, A-1090 Vienna, Austria (anna.losiak@univie.ac.at),

²Wydział Geografii i Studiów Regionalnych, University of Warsaw, Poland.

³Natural History Museum, Burgring 7, A-1010 Vienna, Austria.

⁴Smart Information Systems GmbH, Austria.

Article was submitted to “Meteoritics and Planetary Science”, currently it is under review.

Abstact

Planar deformation features (PDFs) in quartz are one of the most important diagnostic features that allow for the unambiguous identification of a meteorite impact structure. Previous studies of PDFs were either based on single grains or on a randomly chosen quartz grain "population". With this approach it was not possible to detect possible spatial relationships between quartz grains and PDFs developed within them. Here we investigate the spatial relations between a statistically significant number of grains (278) with PDFs (409) within a given area of a single thin section ($\sim 35 \text{ mm}^2$) from the Bosumtwi impact crater.

Some of the PDFs patterns and clusters (consisting of quartz grains with the same PDF orientation present) that we observed are suggestive of a heterogeneous shock field, very similar to one recently modeled numerically. Additionally, PDFs developed along different planes within the crystal lattice differ in their physical characteristics, appearance, and location within a grain. The PDFs developed along the $\{10\bar{1}3\}$ orientation are very well visible, thick and commonly cover a significant area of the grain. The PDFs developed along the $\{10\bar{1}1\}$ and $\{11\bar{2}2\}$ orientations are very short, faint and hardly visible under the universal-stage microscope. This difference was not noted in previous studies; it is likely that this indicates that different PDF orientations are formed in a somewhat different way.

We also present a new web-based program for indexing of PDF sets.

4.1. Introduction

There are only few diagnostic features that allow for the unambiguous identification of a meteorite impact structure (for a detailed review, see, e.g., French and Koeberl 2010); including the preservation of meteorite fragments within a crater structure, a specific chemical and/or isotopic signature, the occurrence of shatter cones, shocked minerals, high-pressure minerals/phases, and/or diaplectic glasses. The most commonly used diagnostic feature for the confirmation of an impact structure on Earth is the occurrence of planar deformation features (PDFs) in quartz grains. PDFs are straight, parallel sets of planes of (amorphous) material that form along specific crystallographic planes in minerals and that are less than 2 μm wide and spaced 2-10 μm apart (e.g., Stöffler and Langenhorst 1994, Grieve et al. 1996 and references therein). Additionally, specific (combinations of) PDF orientations provide information on the peak shock pressure that is recorded by the rock, within the range of ~5 to 35 GPa, depending of the lithology (e.g., Hörz 1968, Grieve and Robertson 1976, Gratz et al. 1992, Stöffler and Langenhorst 1994, Huffman and Reimold 1996, Dressler et al. 1998, Ferrière et al. 2008, Holm et al. 2011).

Even though PDFs in quartz typically form along specific crystallographic orientations, their formation mechanism is still not well understood. Many hypotheses have

been proposed, including: 1) PDFs being traces of glide planes that developed within the quartz crystals to release stress (Engelhardt and Bertsch 1969); 2) PDFs being formed by heterogeneous response of the crystal lattice to the shock compression of high strength (Grady 1980), 3) PDFs are the result of the crystal lattice collapse along specific planes with lower (than average) shear resistance in the shock conditions and crystal lattice compensation caused by misfit on both sides of the shock front (Goltrant et al. 1992), 4) a combination of previously proposed models (e.g., Langenhorst 1994, Trepmann 2008).

The determination of the orientation of PDFs is usually done using a universal-stage (U-stage) mounted on a petrographic microscope, followed by the indexation of the measurements to crystallographic orientations in relation to the c-axis of the grains (e.g., Ferrière et al. 2009), or with the use of transmission electron microscopy (TEM; e.g., Goltrant et al. 1991). Currently, U-stage data are usually indexed manually, using a Wulff stereonet and following a strict procedure (e.g., Ferrière et al. 2009 and references therein). This procedure is both time consuming and error-prone, which somewhat also limits the usability and frequency of usage of this method. Additionally, because of the limitations of this method, only information about polar angles and Miller-Bravais indices of PDFs were recorded and used in previous studies (with a few exceptions, e.g., Walzebuck and Engelhardt 1979, Langenhorst and Deutsch 1994, Trepmann and Spray 2005). The angular relationships between PDF sets in a single given quartz grain were in most cases ignored. Recently, a new Excel©-based program for indexing PDFs has been developed by Huber et al. (2011). However, even though this program is much more accurate and faster than the manual (graphical) method, also allowing for the control of the error used in the calculation and the removal of human error from the plotting process, it does not provide information on the full angular relationships between PDF sets and it also cannot easily be used by, e.g., Macintosh users.

Previous studies on the development of PDFs or on the estimation of recorded peak shock pressures were either focused on single grains or on a randomly chosen quartz grain "population" (e.g., Langenhorst and Deutsch 1994, Ferrière et al. 2008). Up to now, no study investigated the spatial relations between a statistically significant number of grains with PDFs within a given thin section area. The aim of the present work is: 1) to investigate the

spatial relations between PDFs developed in all quartz grains that are visible within an area of $\sim 35 \text{ mm}^2$ of a thin section; 2) to introduce a web-based program for PDF indexing that allows the analysis of azimuthal angles between different PDFs in a given quartz grain; and 3) to better understand the shock wave propagation mechanisms at the thin-section scale and the formation mechanism of PDFs.

4.2. Methods

4.2.1. Sample investigated

To evaluate the spatial relationships between PDFs at the thin section scale, one thin section from a highly shocked rock from the Bosumtwi impact crater was used. Bosumtwi is a 10.5 km in diameter, well preserved, 1.07 Ma old impact crater located in Ghana (e.g., Koeberl et al. 2007). Sample KR8-029 was previously studied by Ferrière et al. (2008) and comes from a depth of 271.4 m (LB-08A drill core), from the shocked basement rocks of the crater. This sample is a coarse-grained meta-greywacke with the largest grains, quartz and feldspars, being up to few millimeters in size. It consists of (modal analysis from Ferrière et al. 2008): 46.4 vol.% quartz 23.7 vol.% alkali feldspar, 10.8 vol.% plagioclase, 4.7 vol.% chlorite, 3.6 vol.% calcite, 1.7 vol.% opaques, 1.3 vol.% muscovite, 0.6 vol.% "other minerals" (including e.g., epidote, amphibole, sphene, etc.), and 6.5 vol.% of matrix (i.e., all grains smaller than $50 \text{ }\mu\text{m}$). According to Ferrière et al. (2008), based on counting using a petrographic microscope, 58% of the quartz grains in this thin section show evidence of shock, and 90.8% of these shocked grains display PDFs (the other 9.2% displaying planar fractures, PFs).

This sample was selected for our study because of: 1) the abundance of relatively large quartz grains, 2) most quartz grains occur in aggregates, and 3) the high proportion of shocked quartz grains (mainly with PDFs).

4.2.2. Methods used

At first, all visible PDFs in all the quartz grains within a restricted area were investigated using the U-stage. In total, the properties of 278 grains (directions of their c-axis and if present of the PDFs) were measured along with their position on the thin section. All grains were measured with respect to the same coordinate system, defined by the microscope axis and the orientation of the thin section with respect to the U-stage (Figure 4.1). Repeated measurements of the same grains showed that the error between measurements of planar features is at maximum of 4° . In a second step, PDFs were indexed with the computer program presented here (see below). The generated data for all the grains were then inserted into a database that was linked to a thin section map (prepared with an optical microscopy microphotograph) using a geographic information systems software (GIS). Spatial analysis of the grains and PDFs characteristics was performed using the ArcGIS 10 software produced by ESRI (Kennedy 2001). Additionally, part of the statistical analysis was carried out using the Statistical Package for the Social Sciences (SPSS) 14.0 for Windows developed by IBM.

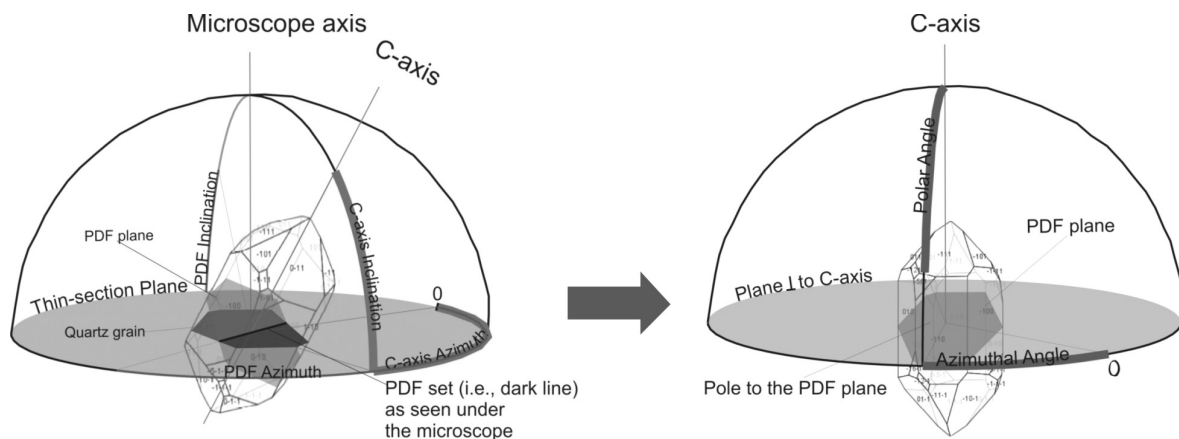


Figure 4.1. Illustration of the process of transformation of the coordinates from "microscope-oriented" (left) to "crystal structure-oriented" (right) coordinates. To avoid confusion, after transformation to the "crystal structure-oriented" coordinates, the PDF (or the c-axis) azimuth becomes an "azimuthal angle", and the inclination angle a "polar angle".

The limitations of the applied methods are as follows: 1) detailed observations using scanning electron microscope (SEM) of some of the grains previously investigated under the optical microscope have revealed that additional PDF sets, not visible and thus not measured with the U-stage, occur. This implies that some of the grains that were described as "unshocked" (i.e., free of PDFs) may contain PDFs; 2) the U-stage do not allow the

determination of the full information on the crystal lattice properties (it is for example not possible to detect Dauphiné twins); 3) the sample size (278 grains from a single thin section) is relatively limited, mainly due to the very time-consuming nature of performing the U-stage measurements; 4) the study is based on one thin section that was prepared from a three-dimensional rock, which may introduce further limitations.

4.2.3. Development of a web-based program for indexing PDFs

4.2.3.1. Description of our program for indexing PDFs

To evaluate the data generated here, and to provide a tool for the community, we developed a web-based program for indexing PDFs. The program is designed to evaluate data from U-stage measurements to quickly assess the relationships between the c-axis and the various PDFs within a given grain. This evaluation is then compared to angles of known, typical, PDFs in quartz (as defined in Ferrière et al. 2009, and references therein). The presented approach simplifies the mathematical calculations required for indexing and allows removing errors related to some distortions that may be induced when representing information derived from a three-dimensional (3D) crystal on a 2D Wulff stereonet.

To properly index PDF sets, two pieces of information are mandatory: 1) the polar angle between the c-axis and the measured feature, and 2) the azimuthal angle between the a-axis and a PDF set. As the exact orientation of the quartz grain a-axis cannot be determined with the U-stage (although this is possible with an Electron Back-Scatter Diffraction-system), an approximation is typically used, namely the angular relationship between two (or more) sets of non-basal PDFs are compared, which can then be used to determine the orientation of the a-axis.

For each quartz grain, U-stage measurements provide angular coordinates (azimuth and inclination) of the c-axis and of all visible PDFs. The program is based on a set of equations that allow the transformation of the coordinates for each grain, from microscope-oriented coordinates to crystal structure-oriented coordinates (Figure 4.1). The program essentially "rotates" a grain to have the c-axis coincide with the central axis of the sphere

used for the indexing (i.e., the c-axis' inclination angle becomes 90°) and corresponding transformations are applied to all planar features determined in the given grain (Figure 4.1), mathematically mimicking the manual process that would be performed with the Wulff stereonet.

The following equations were used to transform the coordinates systems, related to the cosine and sine rules of a spherical triangle:

$$(1) \sin(\delta) = \sin(a) \cdot \sin(\varphi) + \cos(a) \cdot \cos(\varphi) \cdot \cos(A)$$

$$(2) \sin(H) = -\sin(A) \cdot \cos(a) / \cos(\delta)$$

$$(3) \cos(H) = [\sin(a) - \sin(\delta) \cdot \sin(\varphi)] / \cos(\delta) \cdot \cos(\varphi)$$

Where δ is 90° minus the polar angle of the measured planar feature; a is the measured inclination of the planar feature, φ is the measured inclination of the c-axis, A is the azimuthal distance between the c-axis and the planar feature, and H is the azimuthal angle of the planar feature. After performing the transformation described above on the measured PDFs, the relative angular relationships of the PDFs within a grain can be read directly from their coordinates.

The algorithm is designed to find if relative angular relationships between measured features are consistent with the model angular relationships of PDFs as described by Ferrière et al. (2009). This operation consists of four steps (Figure 4.2). First, the measured planar features are indexed using only the polar angle data by comparing calculated values of polar angles with values of polar angles of known PDFs. If no typical orientation corresponds to a known PDF for a calculated polar angle, the measured planar feature is rejected and not used for further computation, and marked as "unindexed" (UNX). For all of the remaining features, one or more known PDF classifications are assigned (this is called here the initial classification). If a single planar feature was measured within a given grain, or also in the case that one other planar feature measured in the grain was indexed as a basal PDF (0001) based on its polar angle, the program will terminate the calculation for this grain at this step. The final display will then indicate that this set of PDF was indexed only based on its polar angle.

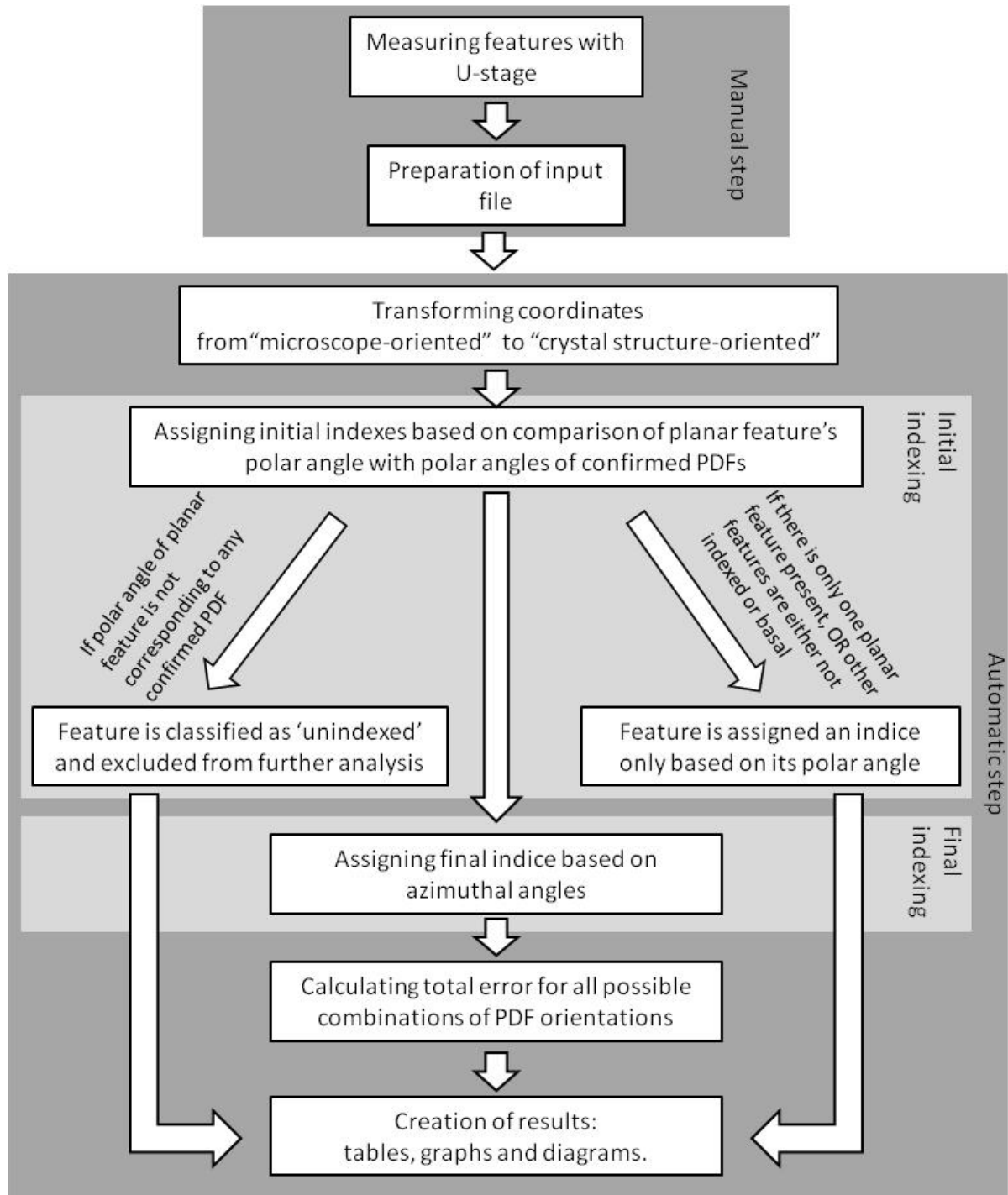


Figure 4.2. Flowchart showing the algorithm of the web-based PDF indexing program presented in this paper.

During the second step, the program compares the angle between measured sets of PDFs in the grain to known typical PDFs. The expected classification of measured PDFs based on the polar angle (step 1) is used to generate the possible and expected azimuthal angles between two sets of PDFs. For example, if two measured features were classified as $\{10\bar{1}3\}$ and $\{10\bar{1}2\}$ orientations in the first step, the only possible azimuthal differences

between them are: 60°, 120°, 180°, 240°, and 300° (\pm error size). If the program finds that the measurements do not fall within these expectations, then, only one set of PDF (i.e., the one with the smaller polar angle error) is indexed, while the other set of PDF is considered to be unindexed. In many cases, more than one combination of indexed PDFs is possible; e.g., some PDFs can be indexed either as $\{10\bar{1}3\}$ & $\{10\bar{1}3\}$ orientations or as $\{10\bar{1}3\}$ & $\{10\bar{1}4\}$ orientations. In this case, the program takes into account all possible combinations of PDF sets.

The third step of the algorithm consists in the calculation of the errors for each of the possible classifications by summing up all angular differences between known PDF orientations and measured orientations of PDFs.

Finally, the combination of PDF sets with the lowest error is chosen as the proper indexed orientation; however, all other possible combinations are also listed in the detailed results table.

4.2.3.2. Input & Output

For the data input, the user has the choice between a .csv file (coma-delimited) or a .txt file. An example of an input file, with detailed instructions, is available online together with our program. Each line of the input file corresponds to a set of numbers describing a single quartz grain. The measured angular data can be entered as a range of values (minimum and maximum measured values; "min-max"). If the c-axis was determined to be vertical during measurements it should be converted manually to the horizontal position (e.g., by "subtracting" 90° from the inclination and by correcting the azimuth by 180°; or the easiest is to change W to E (or E to W) and to "subtract" 90° from the inclination; the corresponding PDFs measurements should not be changed). There are no limitations on the total number of grains in the dataset, or on the number of features/PDFs per grain. If there is an error in the input data (e.g., an inappropriate number of PDFs in relation to the number of input columns), an error message describing the type of problem will be displayed.

Results can be exported as csv and/or jpg files. The results are presented as follows:

1) a main result table with the best possible combination of PDFs orientations for each grain,

2) a detailed results table with input and output data together with all possible combinations of PDFs orientations, 3) aggregated result tables, 4) diagrams for all measured PDFs and also for each grains. The presentation of the results is similar to what is commonly presented in the literature (e.g., Grieve et al. 1996, Ferrière et al. 2009). Additionally, a detailed log of the performed computations is available for each single grain, including detailed information on polar angle, compared azimuthal angles, and all possible combinations of PDF indices.

In addition, two different types of options are available for the calculation, the so-called "error handling" and "error level". "Error handling" specifies how the program interprets data input with a range of values for the c-axis and the sets of PDFs in a given grain (see Figure 4.3). There are two modes of "error handling" for the dataset: 1) "Average": the algorithm calculates the average value of the entire measured interval, and the indexing is performed using this "average value"; 2) "Min-max": values from the entire interval are considered in the subsequent computations. Using this second setting, a PDF will be indexed if any part of the measured interval matches a known, typical, PDF orientation. "Error level" describes the distance from a classified PDF orientation that will still be counted as properly indexed. It is recommended to use a 5° error level, as it is thought to be a level of error inherent to the optical microscopic measurements and have been typically used when plotted manually with the stereographic projection templates (e.g., Engelhardt and Bertsch 1969, Stöffler and Langenhorst 1994, Ferrière et al. 2009).

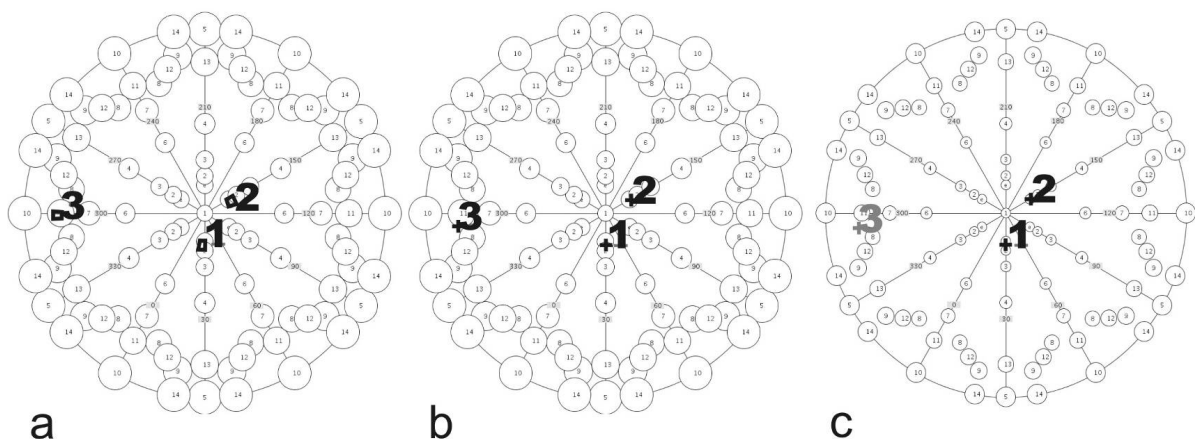


Figure 4.3. Stereographic projection templates (after Ferrière et al. 2009) with the c-axis in the center and the circles representing the positions of the most common poles to PDF planes. These plots show a comparison of the resulting diagrams for a quartz grain with three planar features (marked as 1, 2, and 3, respectively) as produced using different program parameters: a) using the "min-max" method and a 5° error, b) using the "average" method and a 5° error, and c) using the "average" method and a 3° error. Note that in c) feature "3" is unindexed.

The comparison between the produced results using the different "error handling" options is shown in Figure 4.3 and in Table 4.1. Table 4.1 shows that, no matter which method is used, the relative abundance of the different indexed PDF orientations does not change significantly. Additionally, the larger the error level, the more similar are results of the computing using different error handling options. Increasing the "error level" results in a significant decrease of the number of unindexed PDFs. For example, when applying an "average setting" and changing the "error level" from 3°, 5°, to 7°, the number of unindexed PDFs decreases from 43 % through 19 % to only 9 % (see Tab. 1). Furthermore, the proportion of unindexed features/PDFs strongly depends on the error handling method that is used for the calculation; for example, the proportion of unindexed features will increase from 5 % to 19 % just by changing the error handling method used, from the "Min-max" to the "Average" method. Results obtained using the "Min-max" method with a 5° error level and the "Average" method with a 7° error level are usually very similar. This suggests that the average uncertainty on the measurements in this study using the U-stage is at least of 4°.

Table 4.1. Comparison of results for a sample from the Bosumtwi crater (sample BOS-3; data previously published in Ferrière et al. 2009) indexed with our web-based program, using the two available error handling methods; i.e., the "min-max" method (the algorithm uses values from the entire interval) and the "average" method (the algorithm calculates the average value of the entire measured interval, and the indexing is performed using this "average value") and three different error rates (distance from a classified PDF orientation that will still be counted as properly indexed), 3°, 5°, and 7°. Data is given here as number of PDFs.

Method	Error rate	(0001)	$\{10\bar{1}4\}$	$\{10\bar{1}3\}$	$\{10\bar{1}2\}$	$\{11\bar{2}2\}$	$\{10\bar{1}1\}$	$\{11\bar{2}1\}$	$\{21\bar{3}1\}$	$\{22\bar{4}1\}$	$\{31\bar{4}1\}$	$\{40\bar{4}1\}$	$\{51\bar{6}1\}$	$\{10\bar{1}0\}$	$\{11\bar{2}0\}$	$\{51\bar{6}0\}$	Un-indexed
min-max	3°	0	28	51	28	2	6	2	2	6	3	1	3	1	1	0	11
min-max	5°	0	29	53	29	2	8	2	2	7	3	1	2	1	1	0	5
min-max	7°	0	30	54	30	1	9	2	3	7	4	0	1	1	1	0	2
average	3°	0	27	37	20	2	4	0	1	2	4	3	1	1	0	0	43
average	5°	0	30	45	24	2	7	1	4	5	3	2	2	1	0	0	19
average	7°	0	30	50	28	2	7	2	5	6	2	1	1	1	1	0	9

4.2.3.3. Comparison between the "manual" and "automatic" methods for PDF indexing

To test and validate our program we compared the results generated by our program (using the "Min-max" method and 5° error level) with those obtained with the manual

(graphical) method by an experienced researcher (Ludovic Ferrière). For this purpose, we have used data obtained from five samples from different impact structures (see Table 4.2).

The results obtained using the program (“automatic”) and the manual method are almost identical. The differences in absolute frequency percentage are negligible and too insignificant to influence inferences on the shock pressure during impact cratering (e.g., Stöffler and Langenhorst 1994). These minor discrepancies between the manual and automatic methods can have several origins. First, a human operator is more prone to index a feature that is near the boundary (i.e., almost indexed), while the program is very strict. Second, the human operator and the program can choose different Miller-Bravais indices for certain grains, for example, when two PDF sets can be indexed either as $\{10\bar{1}1\}$ & $\{22\bar{4}1\}$ orientations or as $\{11\bar{2}2\}$ & $\{40\bar{4}1\}$ orientations. Due to the lack of a-axis data, it is in fact impossible to differentiate between these two combinations, and the program will choose the option with the smallest cumulative error. Third, it seems that the projection that is used for the manual indexing tends to over-index PDFs with low polar angles. In addition, the manual method does not take into account the full measured interval for the c-axis orientation (Ferrière et al. 2009), while our program does. Finally, even the most accurate and precise human operator will make mistakes due to the wearisome nature of the manual indexing method. The comparison of the PDFs indexed by hand and using the program (Tab. 2) shows that the automatic method of indexing gives very comparable results to the ones obtained by an experienced researcher (Ludovic Ferrière); however, based on the nature of the automated algorithm, the results are more precise and reproducible.

The program that was developed for this study is available online at: www.MeteorImpactOnEarth.com/ustage/program.html. The source code (i.e., implementation in Java programming language) is also available upon request from the authors.

Table 4.2. Comparison between manually (by L. Ferrière) and automatically indexed PDFs (using our web-based program) from five samples from five different impact structures (from: ¹Ferrière et al. 2009, ²Ferrière et al. 2011, ³Ferrière et al. 2010). Data is given here as number of PDFs.

Crater, lithology	Method	(0001)	$\{10\bar{1}4\}$	$\{10\bar{1}3\}$	$\{10\bar{1}2\}$	$\{1\bar{1}22\}$	$\{10\bar{1}1\}$	$\{1\bar{1}2\}$	$\{21\bar{3}1\}$	$\{22\bar{4}1\}$	$\{31\bar{4}1\}$	$\{40\bar{4}1\}$	$\{51\bar{6}1\}$	$\{10\bar{1}0\}$	$\{11\bar{2}0\}$	$\{51\bar{6}0\}$	Un-indexed	Total
Gosses Bluff ¹ , sandstone	program manual	59 59	39 110	70 2	2 5	2 10	13 0	1 0	2 3	2 0	2 3	1 2	2 1	1 1	0 1	1 1	11 10	208 208
Bosumtwi ¹ , meta-greywacke	program manual	0 0	29 81	53 28	29 4	2 4	8 5	2 2	2 3	7 6	3 3	1 2	2 1	1 1	1 0	0 0	5 8	145 145
Manson ¹ , biotite-gneiss	program manual	4 4	46 166	117 2	4 3	2 10	15 0	0 3	5 10	2 2	2 2	1 2	0 1	0 0	0 0	1 1	5 5	212 212
Luizi ² , sandstone	program manual	12 12	45 163	116 5	8 0	0 0	0 0	0 0	0 0	1 0	0 0	0 0	0 0	0 0	0 0	0 0	3 5	185 185
Keurusselkä ³ , ortho-gneiss	program manual	0 0	61 124	66 1	1 0	0 0	0 0	0 0	0 0	0 0	0 0	0 0	0 0	0 0	0 0	0 0	1 4	129 129

4.3. Results

In total, 278 quartz grains from an area of 34 mm² were measured with an U-stage. 219 of these quartz grains display 1 to 5 indexed PDF sets (Figures 4.4, 4.5, 4.7). The mean number of PDF sets per grain is 2.03 (relative to the shocked quartz grains only) and is 1.47 (if all investigated quartz grains are counted; i.e., including also unshocked grains).

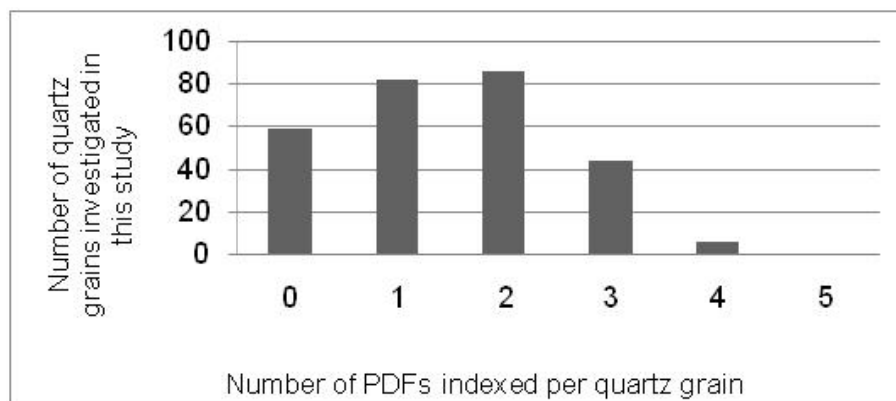


Figure 4.4. Histogram showing the number of indexed PDF sets per quartz grain in the studied thin section of a shocked greywacke (KR8-029; Bosumtwi crater). This plot shows that most of the grains display only one or two indexed PDF sets. Only very few quartz grains include four or five PDF sets. The number of grains that do not display (indexed) PDFs is also represented on this histogram with the value "0".

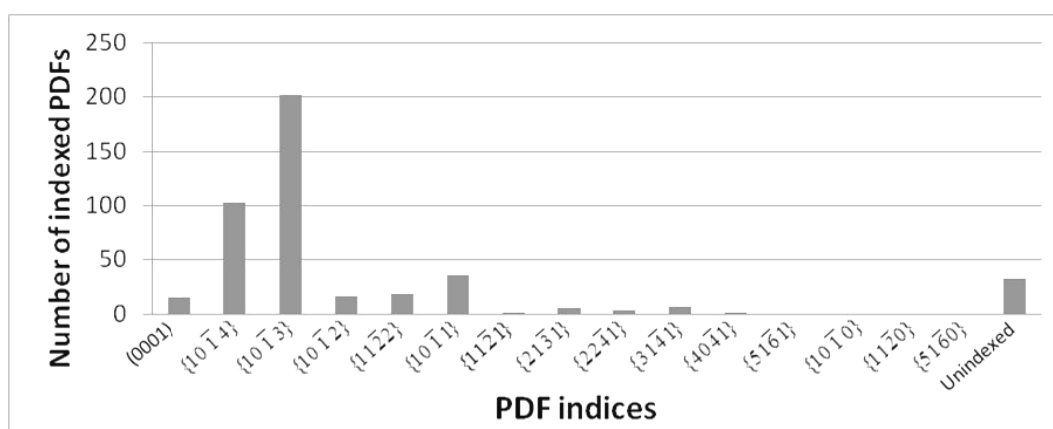


Figure 4.5. Number and type of indexed PDF orientations in quartz grains ("min-max" method, 5° error) measured in the studied sample (KR8-029; Bosumtwi crater). The most common PDF orientations are {10 $\bar{1}$ 3} and {10 $\bar{1}$ 4} (45.8% and 23.4%, respectively), relatively common are also {10 $\bar{1}$ 1} and {11 $\bar{2}$ 2} orientations (8.2% and 4.1%, respectively). Only 7.5% of the measured features are unindexed.

Based on GIS analysis, the measured quartz grains are relatively homogenous in size, with an average area of the grains of $\sim 33 \mu\text{m}^2$. However, the difference between the largest ($295 \mu\text{m}^2$) and the smallest ($2 \mu\text{m}^2$) grains is significant. At the thin section scale, the quartz grains are distributed within twelve unequally sized "clusters" (Figure 4.6, Table 4.4). Cluster #6 is the largest of all; it consists of 52 grains with 75 indexed PDFs. Clusters #4 and #7 are the smallest ones, with 9 and 12 grains and 14 and 12 PDFs, respectively (Figure 4.6). Table 4.4 gives the details concerning the number, mean values, and standard deviations of the number of grains and PDFs in each cluster. Figure 4.7 shows the distribution of clusters and quartz grains (along with information on the number and orientation of PDFs) within the studied area of the thin section.

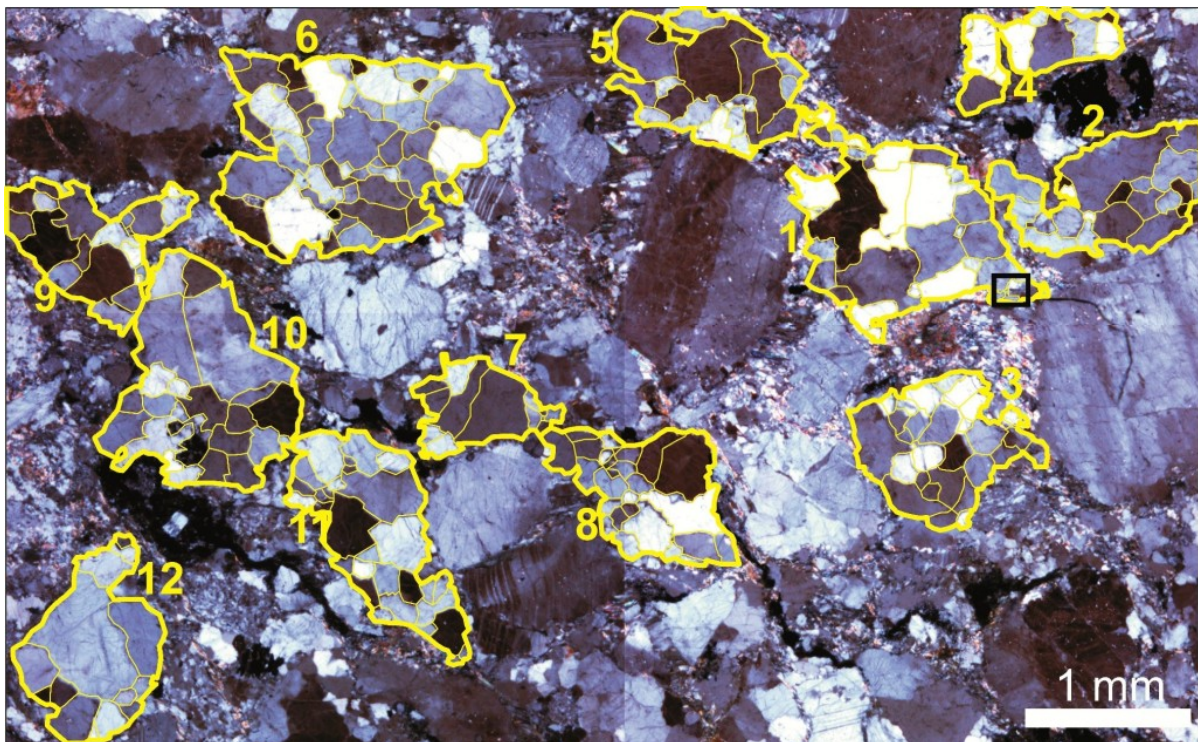


Figure 4.6. Mosaic of microphotographs (in cross-polars) of the investigated thin section of the sample KR8-29 (from the LB-08A drill core; Bosumtwi crater). The exact same area as on the following figures is depicted here with the outline and identification numbers of the different clusters that we have defined. The black rectangle (upper right) shows the location of the Figure 4.9.

The orientation of 441 sets of planar features were measured and subsequently 408 PDFs were indexed using the "min-max" and 5° error level settings of the program described above (Table 4.3). Thirty three (representing 7.5 % of the total) of the measured features were unindexed, using the chosen settings. A detailed analysis of the grains with unindexed

features revealed that, in most cases, these features would be in fact indexed if the error level were to be increased to 6° (instead of 5°). The most common PDF indices are: $\{10\bar{1}3\}$ (45.8 %) and $\{10\bar{1}4\}$ (23.4 %) (Figure 4.5). Less frequent orientations of PDFs are $\{10\bar{1}1\}$ (8.2 %), $\{11\bar{2}2\}$ (4.1 %), and $\{10\bar{1}2\}$ (3.6 %). A total of only 3.4 % of the PDFs were indexed as basal (0001). A few other orientations of PDFs are also present, but represent less than 2 %.

Table 4.3. Crystallographic orientations of PDFs in quartz grains in meta-greywacke sample KR8-029 from the Bosumtwi crater as measured in this study and compared to previous results by Ferrière et al. (2008).

PDF orientation	Un indexed													Total
	(0001)	$\{10\bar{1}4\}$	$\{10\bar{1}3\}$	$\{10\bar{1}2\}$	$\{11\bar{2}2\}$	$\{10\bar{1}1\}$	$\{11\bar{2}1\}$	$\{21\bar{3}1\}$	$\{22\bar{4}1\}$	$\{31\bar{4}1\}$	$\{40\bar{4}1\}$	$\{51\bar{6}0\}$		
This study	Number of PDFs	15	103	202	16	18	36	1	6	3	7	1	0	33
	% of PDF orientations	3.4	23.4	45.8	3.6	4.1	8.2	0.2	1.4	0.7	1.6	0.2	0.0	7.5
Ferrière et al. (2008)	Number of PDFs	1	-	56	2	1	0	0	0	-	-	-	-	1
	% of PDF orientations	1.6	-	91.8	3.3	1.6	0.0	0.0	0.0	-	-	-	-	1.6
														441
														100.0
														61
														100.0

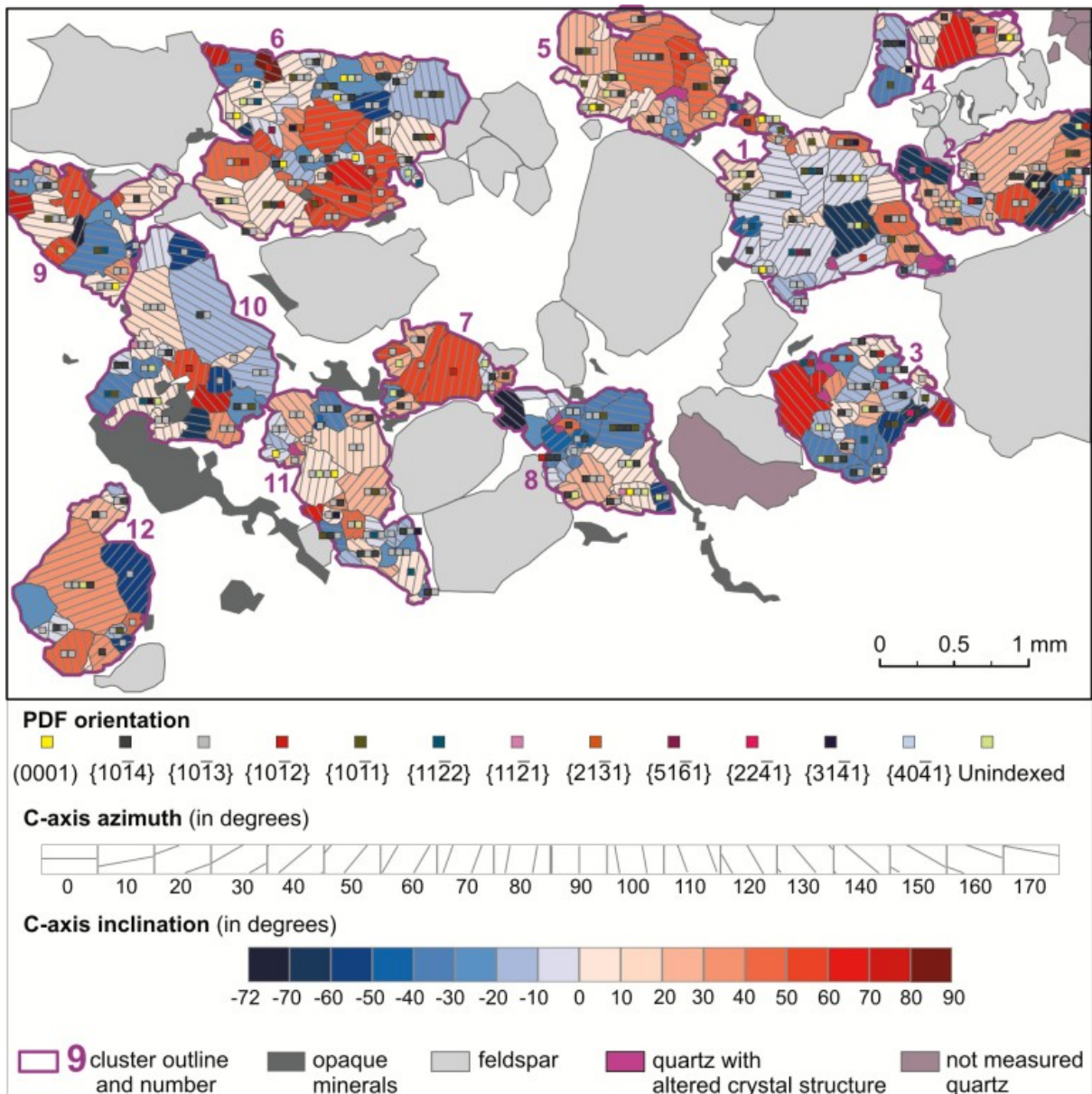


Figure 4.7. Detailed map of the clusters of quartz grains as mapped in sample KR8-29; from the Bosumtwi crater). The orientation of the crystal lattice of the measured quartz grains as well as the number and orientations of the indexed PDFs is shown. In some cases the c-axis of the quartz grains could not be measured because it is too damaged (it is marked as “quartz with altered crystal structure”).

Table 4.4. Basic data on the performed measurements of PDF sets present within quartz grains in sample KR8-29 (Bosumtwi crater). Data are shown for each cluster as number of PDFs, unless indicated otherwise.

	Total	Cluster number no.											
		1	2	3	4	5	6	7	8	9	10	11	12
Entire sample													
Area of cluster [μm²]	34054169	1122954	675038	671447	326923	715248	1632088	329836	621749	555552	1106398	767885	695132
No. of grains	278	33	20	25	9	17	52	12	23	19	21	29	14
Mean area of a grain [μm²]	32651	33299	33378	25231	35330	41268	30418	27448	25793	29145	50536	26286	49657
St. dev. of area of cluster	37999	40341	39699	20488	22302	38060	31113	36084	26207	25528	55796	28768	73438
No. of PDFs	409	54	36	42	14	32	75	12	27	21	31	47	18
Mean no. of PDFs	1.47	1.64	1.80	1.68	1.56	1.88	1.44	1.00	1.17	1.11	1.48	1.62	1.29
St. deviation of no. of PDFs	1.09	1.18	0.75	1.01	1.17	1.02	1.01	0.71	1.31	1.07	1.05	1.22	0.88
Mean no. of PDFs in a grain	1.47	1.64	1.80	1.68	1.56	1.88	1.44	1.00	1.17	1.11	1.48	1.62	1.29
No. of grains without PDFs	61	6	1	4	2	1	11	3	11	7	5	7	3
PDF indices													
(0001)	15	3	0	0	1	2	5	0	1	1	0	2	0
{10 $\bar{1}$ 4}	103	13	9	13	5	10	17	5	10	2	5	9	5
{10 $\bar{1}$ 3}	203	23	16	17	4	15	33	6	12	15	20	30	12
{10 $\bar{1}$ 2}	16	1	3	5	0	0	4	1	1	0	1	0	0
{10 $\bar{1}$ 1}	36	8	2	3	1	5	8	0	3	1	2	2	1
{11 $\bar{2}$ 2}	18	5	3	2	0	0	3	0	0	1	2	2	0
{11 $\bar{2}$ 1}	1	0	1	0	0	0	0	0	0	0	0	0	0
{21 $\bar{3}$ 1}	6	1	1	0	0	0	4	0	0	0	0	0	0
{22 $\bar{4}$ 1}	3	0	0	2	1	0	0	0	0	0	0	0	0
{31 $\bar{4}$ 1}	7	1	0	0	2	0	1	0	0	0	1	2	0
{40 $\bar{4}$ 1}	1	0	1	0	0	0	0	0	0	0	0	0	0
Unindexed	33	3	4	3	0	4	4	3	5	1	3	2	1
Pearson's	0.39	0.60	-0.05	0.02	0.42	0.59	0.51	0.06	0.61	0.48	0.32	0.51	0.54

4.4. Discussion

4.4.1. Sample characterization and comparison of results with previous data

The thin section used in the present study was previously analyzed by Ferrière et al. (2007, 2008) as part of a large study on the Bosumtwi impact crater for which 121 samples

from the drill core LB-08A were analyzed. Comparing the results of the current study with previous work can help to better understand if, and how, our approach affects the results (Table 3). In the present study, using the U-stage and based on a restricted part of the thin section, a total of 78 % of the 278 investigated quartz grains were found to be shocked. This proportion is a much higher percentage than the 58 % (out of 508 grains counted) reported in Ferrière et al. (2008). However, Ferrière et al. (2008) obtained this value of shocked quartz grains using the optical microscope without U-stage; therefore, it is not really surprising that a higher proportion was detected in our study. Ferrière et al. (2008) also discussed the fact that PDF sets not observable under horizontal stage examination are visible when using the U-stage. They noted that the average number of PDF sets per grain is 28 ± 9 rel% higher when determined by U-stage. If we extrapolate this number, our present estimate of the number of shocked quartz grains is in good agreement with the work of Ferrière et al. (2008).

The largest difference between our study and the previous work by Ferrière et al. (2008) is in the percentage of PDFs indexed as $\{10\bar{1}3\}$ orientation; although they dominate (92 %) the sample set in Ferrière et al. (2008), they are much less common, only 46 %, in this study. One of the most likely cause of this apparent discrepancy is in part artificial and due to the different model PDFs matrix used for indexing. PDF indexing by Ferrière et al. (2008) was done using the traditional template with 10 model PDF orientations as given, e.g., in Stöffler and Langenhorst (1994), while in this study, the scheme, with five additional characteristic crystallographic orientations, by Ferrière et al. (2009), was applied. As a result, the PDF orientation $\{10\bar{1}4\}$ was assigned to some features that would have been previously likely classified as $\{10\bar{1}3\}$ orientations (and in a few cases unindexed). Interestingly, Ferrière et al. (2008) did not find any PDF sets with the $\{10\bar{1}1\}$ orientation, while in our study this orientation represents 8 % of the measurements. The re-examination of the grains containing this orientation revealed that the PDFs with the $\{10\bar{1}1\}$ orientation tend to be less easily visible than other PDFs, and thus can in some cases be overlooked. The $\{10\bar{1}1\}$ along with $\{11\bar{2}2\}$ orientations are commonly poorly developed sets, hardly visible under the U-stage, and present on the grain margins as a few microns long planar and parallel features. This difference of physical characteristics, appearance, and location within grain of different

PDFs orientations was not noted in previous research and indicates that different PDFs orientations may have developed under somewhat different conditions.

The average shock pressure is commonly determined based on PDF orientations in a given thin section/sample (see e.g., Hörz 1968, Grieve and Robertson 1976, Huffman and Reimold 1996). The average shock pressure estimates based on the PDF orientations measured in this study and by Ferrière et al. (2008) would be similar (Stöffler and Langenhorst 1994). However, because $\{10\bar{1}1\}$ orientation represents 8 % of PDFs measured in the current study, and is thought to develop at 5 GPa, the range of shock pressures estimated based on current measurements could be slightly lower than based on data from Ferrière et al. (2008).

4.4.2. Heterogeneous distribution of PDFs in quartz grains from the studied sample

There are three different ways in which the PDFs in quartz show a heterogeneous spatial distribution (see Figure 4.8): First, as noted by Walzebuck and Engelhardt (1979) and Kieffer (1971), PDFs are distributed heterogeneously within single quartz grains (e.g., Figure 4.9). One area within a particular grain can be bereft of any indication of shock metamorphism, while another area can be so thickly packed with multiple PDFs belonging to multiple orientations that it is somewhat difficult to clearly identify them, and detect their exact number. Those areas are so damaged by shock that when seen under the cross-polarized light they look almost isotropic. The transition from the apparently "unshocked area" to the shocked area is very abrupt and happens over the scale of a few micrometers. This variability is probably related to pre-shock heterogeneity of the sample, particularly with regard to the collapse of the pore spaces due to shock wave propagation (Kieffer 1971, Kieffer et al. 1976, Güldemeister et al. 2013). Laboratory experiments also show that the local stress can range from half to twice in intensity when compared to the average shock pressure, even though it is clear that such experiments, done on single quartz crystals (Gratz et al. 1992), have some limitations compared to natural processes. Such a local

intensity of stress may be the result of the intrinsic instabilities in the thermo-mechanical deformation process (Grady 1980).

Second, the spatial distribution of grains with a specific number of PDFs per grain-area is heterogeneous; in multiple cases, grains with very different numbers of PDFs per grain-area are located close to each other (Figure 4.7). For example, in our cluster #6, adjacent grains have either a very high or a very low number of PDFs per unit area in the grain. A similar heterogeneity within a single sample was observed by Dressler et al. (1998). This can be related to pre-impact heterogeneity (e.g., small pores or other impurities) in the cluster. The collapse of the pores during the passage of the shock wave could have caused reverberation and/or rarefaction of the shock wave(s), locally amplifying the average shock pressure (see e.g., Kieffer 1971, Bowden et al. 2000, Güldemeister et al. 2013). However, other clusters (e.g., #1, #2, or #12) are relatively consistent, with adjacent grains sharing similar number of PDFs per area. It appears that the stress field in these specific locations in the sample was relatively uniform. The relative homogeneity of these clusters might have been caused by pre-impact grains in these clusters strongly adhering to each other.

Third, heterogeneity is present at the cluster level. Quartz grains in the studied sample are grouped into 12 distinct clusters having between 9 and 52 grains (with an average between 20 and 30 grains). The average number of PDFs per all quartz grains (i.e., including the quartz grains that do not display PDFs) varies between 1.0 (in cluster #7) and 1.9 (in cluster #5) (see Table 4.4). These differences in the shock level recorded by the different clusters are probably caused by the lower level heterogeneities described previously (i.e., at the sub-grain and grain level) and are likely a result of the semi-random distribution of high-pressure areas. This observation suggests that, depending on the location of the analyzed grains, the results (and thus the estimation of the average shock pressure) can vary by as much as a factor of two. This finding supports recommendations given by Ferrière et al. (2009) that in order to assure a proper estimation of the shock level in a given sample, it is important to measure a large number of PDF sets (optimally more than 100) from randomly chosen grains from different locations within a given thin section/sample.

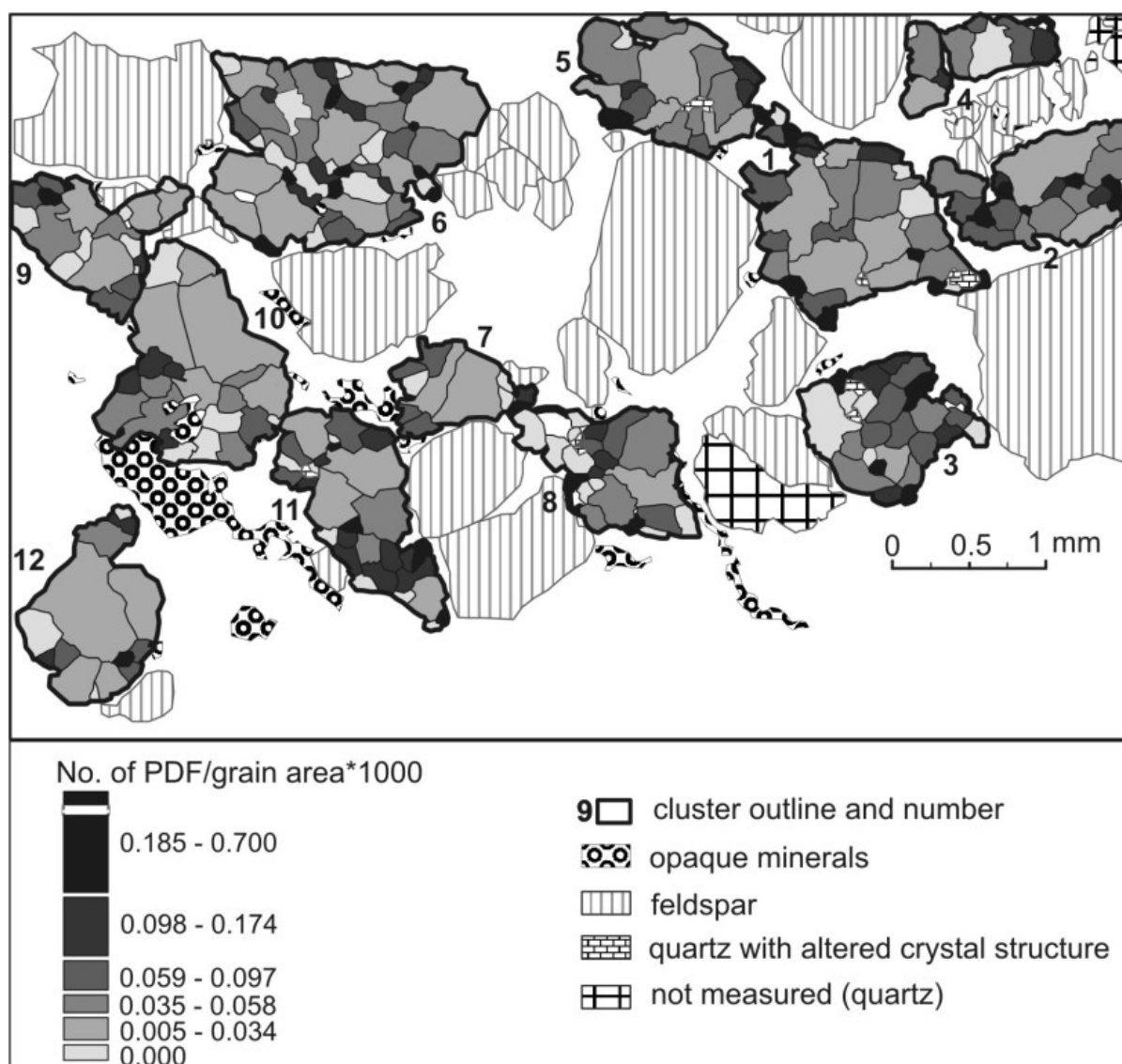


Figure 4.8. Abundance of PDFs per quartz grains (i.e., number of PDFs per grain area) in sample KR8-29 (Bosumtwi crater). The average density of PDF sets per grain-area shows an over-representation of small quartz grains with a very high density of PDF sets per grain-area. This can be explained by either the rotation of part of the crystals previously being part of larger grains, due to extensive shock or a computational artifact (i.e., a single PDF set in one grain gives higher set density than 4 sets within a very large grain). In some cases the c-axis of the quartz grains could not be measured because it is too damaged (it is marked as “quartz with altered crystal structure”).

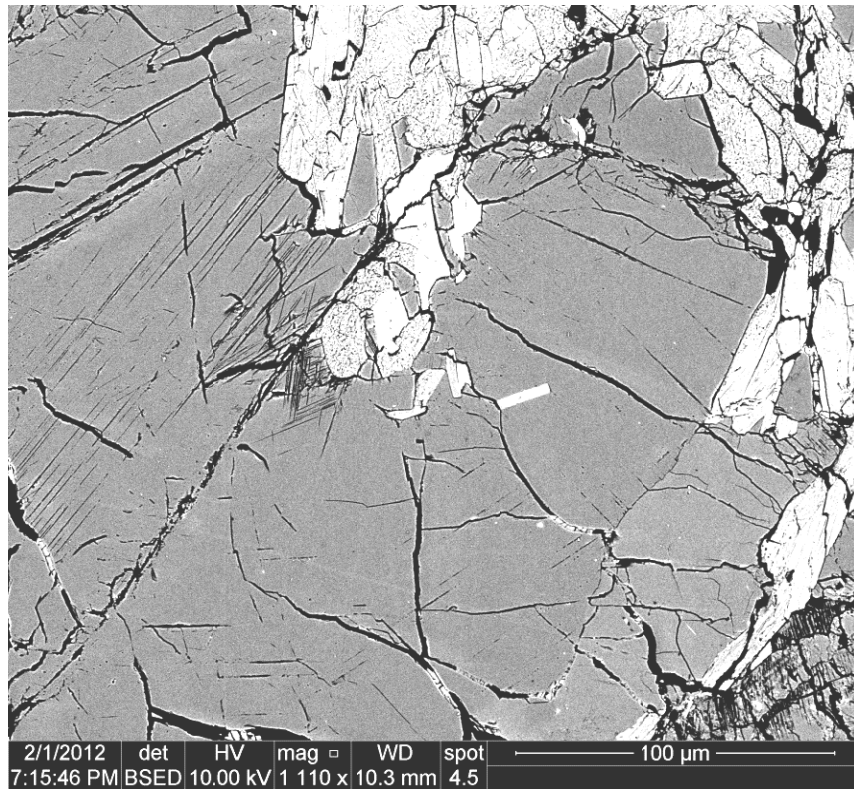


Figure 4.9. Backscattered electron image showing a particular sector of cluster #1 indicated in Figure 4.6. The grey grains in the center and to the left are quartz with planar deformation features. Most of the quartz includes widely spaced PDFs or no planar features at all. The area in the center left includes tightly spaced PDFs (two or more sets in the exact same place). This probably illustrates a local maximum within the heterogeneous stress field produced by shock wave propagation through a heterogeneous sample.

In order to quantify the spatial relationships between the number of PDFs and the spatial relationships of the quartz grains at the scale of the thin section, various statistical tests were performed. The Pearson's product moment (r) statistical test (Rogerson 2001) measuring linear dependence between two variables (Devore and Peck 1997) was used to investigate the correlation between the number of PDFs per grain with two other variables: 1) the total area of a grain, and 2) the location with relation to the edge of a cluster. The Pearson's product moment varies from -1 to 0 to 1 (indicating, respectively: strong anti-correlation, no correlation, or strong correlation) and can be calculated using the following equation:

$$r = \frac{\sum z_x z_y}{n-1}$$

where z_x and z_y are the z-scores (i.e., the distances from the mean expressed as units of standard deviation) associated with x and y variable, respectively, and n the number of observations.

The correlation coefficient calculated for the grain's area and the number of PDF orientations in each grain is 0.34 ($\alpha < 0.01$), indicating a strong positive correlation between the two variables. This correlation indicates that the larger the grain, the more PDF orientations it tends to include; this is in agreement with the findings of Walzebuck and Engelhardt (1979), who noted that with increasing grain size, there is an increasing chance that heterogeneously distributed local stress maxima exceed the threshold pressure necessary for the formation of PDFs within a specific grain. In Figure 4.8, the average density (i.e., relative abundance in a given area) of PDF sets per grain-area is shown; there is an over-representation of the small quartz grains with a very high density of PDF sets per grain-area. These grains are commonly located in the inside part of the clusters, tightly surrounded by other quartz grains. In a few cases, their formation may be explained by the rotation of part of the crystal previously being part of a larger grain, due to extensive shock, as already suggested by Kieffer (1971). Other grains may show a strong correlation due to a calculation artifact (i.e., a single PDF set in one grain gives higher set density than 4 sets within a very large grain).

Kieffer (1971) and Dressler et al. (1997) suggested that quartz grains within a porous rock or embedded in a "soft" matrix are less likely to develop PDFs and/or PFs when compared to quartz grains in an uniformly "hard rock". For this reason we tested the hypothesis that the most heavily shocked grains tend to be located in the inner part of the clusters. However, the result of the Pearson's product moment correlation coefficient seems to indicate that there is no significant correlation between the number of PDFs and the percentage of matching grain borders with the boundary of a cluster (see Tab. 4). Only cluster #1 shows a medium negative correlation close to the 2 sigma level of significance. Therefore, there is no clear evidence that the development of PDFs is directly related to its surroundings (with the notable exception of the collapse of pore spaces). Grains are shocked in a similar way, regardless of whether they are surrounded by other "rigid" quartz grains or by fine-grained "soft" matrix.

In order to test the spatial variability of the shock effects (expressed by the grouping of grains with a similar number of PDFs) on a scale of a few hundreds of micrometers, the Anselin Local Moran's test was applied (Anselin 1999, Rogerson 2001). This test allows detecting local spatial autocorrelation and can be used to identify local clustering (regions where adjacent areas have similar values) or spatial outliers (areas distinct from their neighbors). In this study the Anselin Local Moran's test is used to identify clustering of grains with high number of PDFs (marked as HH on the Figure 4.10), clustering of grains with small number of PDFs (marked as LL), and spatial outliers; e.g. grains with a high number of PDFs surrounded by grains with a small number of PDFs (marked as HL). In this analysis, only grains that share a boundary will influence computations of the central grain (*ArcGIS Help Library* 2010). The Local Moran's statistic of spatial association is given by:

$$I_i = \frac{x_i \bar{X}}{S_i^2} \sum_{j=1, j \neq i}^n w_{i,j} (x_j - \bar{X})$$

where x_i is an attribute for the feature i , \bar{X} is the mean value for this attribute, $w_{i,j}$ is the spatial weight between features i and j , and with:

$$S_i^2 = \frac{\sum_{j=1, j \neq i}^n w_{i,j}}{n-1} - \bar{X}^2$$

where n is the total number of features.

The results of this analysis show that several grains yield statistically significant results (Figure 4.10), thus, indicating that in some cases grains with high, or low, number of PDFs present are spatially clustered. However, it is necessary to take into account that due to the non-continuous space and very irregular shapes of the quartz grains, this analysis is complex and cannot be fully conclusive. Seven of our defined clusters can be categorized as HH, and only one cluster as LL. There are also four LH clusters. All of the LH grains are located on the edge of the clusters whereas the LL grains are located on the border of two clusters. However, because only very few of the measured quartz grains show a relation

between the number of PDF sets present within them and within their neighbors, we conclude that the number of PDF orientations in the grain does not seem to be dependent of the special location of the grain itself.

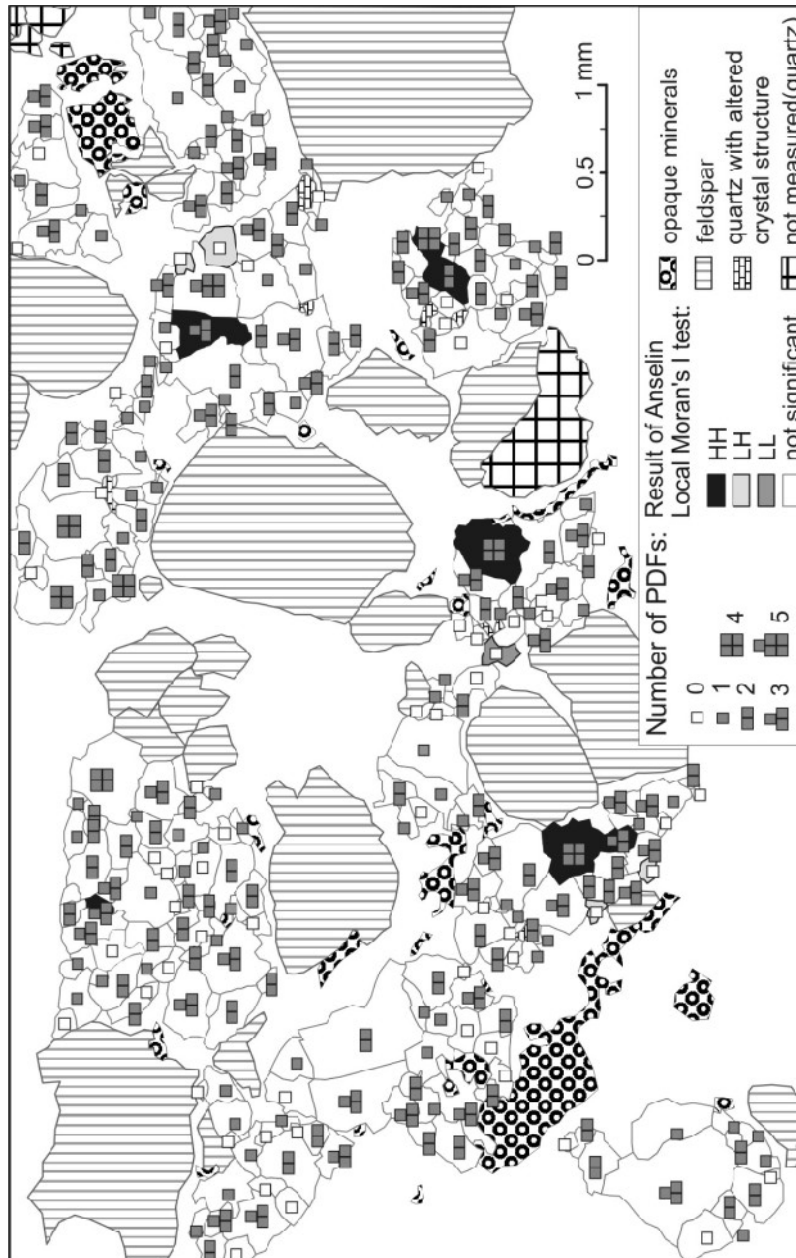


Figure 4.10. Map showing result of Anselin Local Moran's test on quartz grains from sample KR8-29 (Bosumtwi crater). This test allows to identify clusters of grains with high number of PDFs (marked as HH), clustering of grains with small number of PDFs (marked as LL), and spatial outliers; e.g., grains with a high number of PDFs surrounded by grains with a small number of PDFs (marked as HL). The results of this analysis show that several grains yield statistically significant results, thus, indicating that in some cases grains with high, or low, number of PDFs present are spatially clustered. This probably illustrates a local maximum within the heterogeneous stress field produced by shock wave propagation through a heterogeneous sample. In some cases the c-axis of the quartz grains could not be measured because it is too damaged (marked as "quartz with altered crystal structure").

4.4.3. Non-random distribution of different PDF types/orientations

Our statistical analysis revealed that the number of PDF sets within a given quartz grain is likely related to a heterogeneous stress field developed during the impact event. However, the development of specific PDF orientations is potentially more systematic. The Getis-Ord General G statistical analysis is designed to measure the degree of clustering for either high values or low values of the tested variables (Getis 1999). This test was applied here to estimate the degree of clustering of each PDF orientation (Figure 4.11). In this analysis, all grains containing a specific indexed PDF orientation (e.g., $\{10\bar{1}1\}$) are assigned a value of “1”, grains without any PDFs or with PDFs with orientations other than the specific PDF orientation that is investigated are assigned a value of “0”. The General G statistic of overall spatial association is given as:

$$G = \frac{\sum_{i=1}^n \sum_{j=1}^n w_{i,j} x_i x_j}{\sum_{i=1}^n \sum_{j=1}^n x_i x_j}, \forall j \neq i$$

Where x_i and x_j are attribute values for features i and j , and $w_{i,j}$ is the spatial weight between feature i and j . The polygon contiguity conceptualization of spatial relationships is also selected while performing this statistic analysis. The Getis-Ord General G statistic test works best when there is a fairly even distribution of values and only few areas with high values of a variable (in our case a specific PDF set). In addition to the G value, p -value and z -score were also calculated. The p -value is the probability that the observed spatial pattern is created by a random process, and the z -score is the standard deviation. A very high or very low (negative) z -score associated with small p -values (below 0.10 confidence level) indicate that it is unlikely that the observed spatial pattern reflects a random pattern.

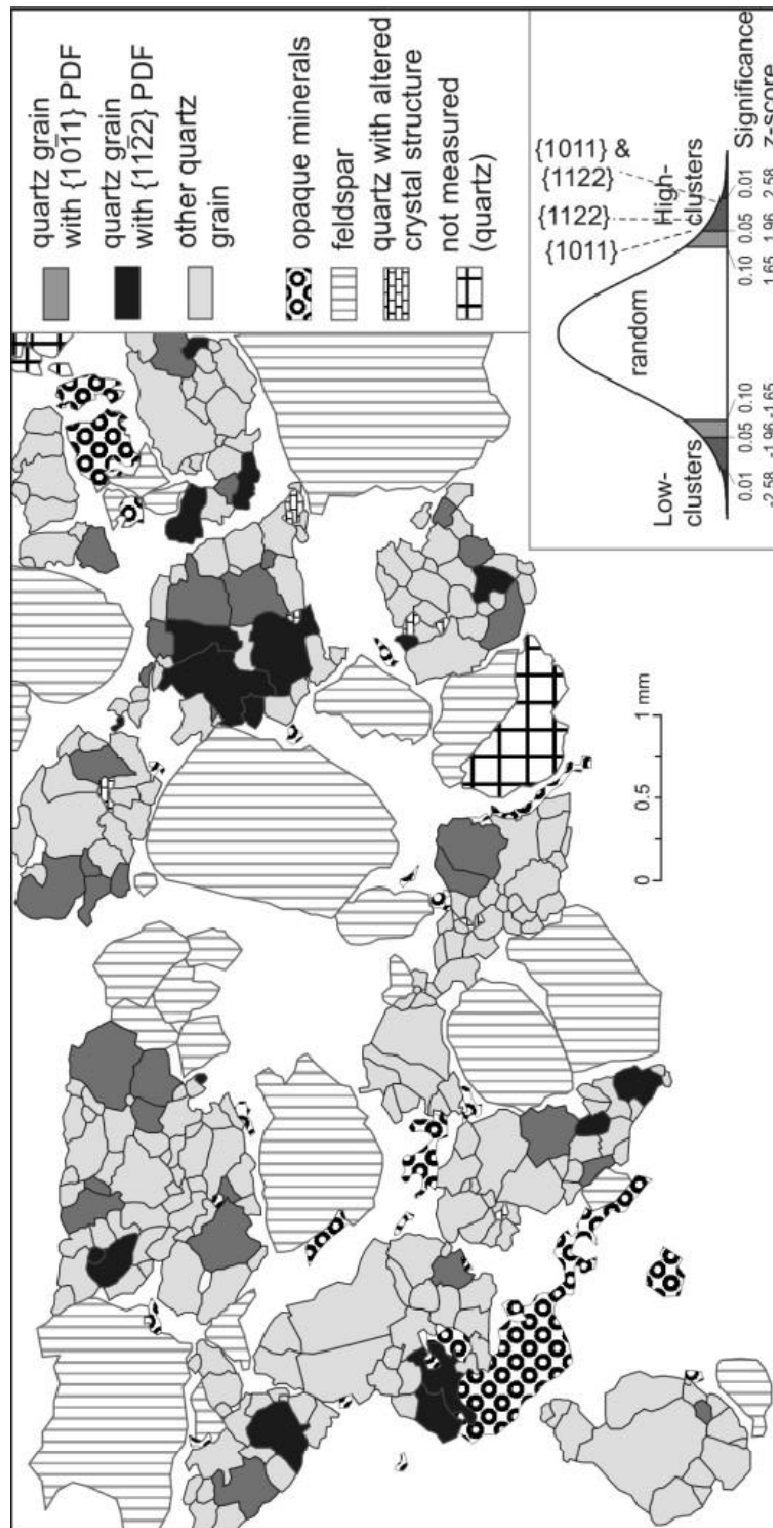


Figure 4.11. Map of location of grains with PDF orientations $\{10\bar{1}1\}$ and $\{11\bar{2}2\}$ in sample KR8-29 (Bosumtwi crater). The results of the Getis-Ord General G statistical analysis is also provided here, showing that quartz grains with these two particular orientations of PDFs tend to occur in clusters that are not random on the 2σ significance level. In some cases the c -axis of the quartz grains could not be measured because it is too damaged (marked as “quartz with altered crystal structure”).

All PDF combinations were tested with the Getis-Ord General G statistic test; however, the results were significant only for $\{10\bar{1}1\}$ and $\{11\bar{2}2\}$ PDFs orientations (see Figure 4.11). The clustering for the other orientations of PDFs cannot be determined because of statistical reasons; Some PDF orientations, such as $\{10\bar{1}3\}$ and $\{10\bar{1}4\}$ orientations are present in most of the grains, and, thus in this analysis they appear as a large single cluster. However, this clustering is only an artifact of their abundance and is not in any case meaningful. On the other hand, other PDF orientations, such as the $\{31\bar{4}1\}$ orientation, are generally not abundant enough to allow a statistically meaningful analysis.

Grains with $\{10\bar{1}1\}$ orientations are characterized by the General G value of 0.023, z-score of 1.96, and p-value of 0.05 (Figure 4.11). Results for the PDF orientation $\{11\bar{2}2\}$ indicates a slightly more clustered pattern, with observed General G value of 0.035, z-score of 2.11, and p-value of 0.04. Moreover, analysis of both of these PDF orientations together yields an even more clustered pattern with a general G value of 0.022, z-score of 2.38, and p-value of 0.0175 (close to the more conservative confidence level). The complete results are presented in Figure 4.11. Based on this analysis, with 95% confidence level, we note that the clustered distribution of the $\{10\bar{1}1\}$ and $\{11\bar{2}2\}$ orientations is not random.

Based on previous research, it was proposed that the development of specific PDF orientations is related to: 1) the orientation of the crystal lattice of the quartz grains with respect to the shock front (as already suggested by, e.g., Walzebuck and Engelhardt 1979, Langenhorst and Deutsch 1994), and 2) the peak shock pressure experienced by the sample (see e.g., Langenhorst and Deutsch 1994, Langenhorst 2002). However, based on analysis in this study, the orientation of the crystal lattice does not seem to explain clustering of grains with specific PDF orientations observed in the studied sample. The $\{10\bar{1}1\}$ and $\{11\bar{2}2\}$ orientations are developed in neighboring grains, even though the crystallographic directions of the quartz grains in the studied sample are very different from each other (Figure 4.7). For example, in cluster #1, grains that include $\{10\bar{1}1\}$ and/or $\{11\bar{2}2\}$ PDF sets have very different orientations of their crystal lattice. However, there are also grains that have a similar orientation of their crystal lattice (with less than 10 degrees of difference) to a grain displaying $\{10\bar{1}1\}$ and/or $\{11\bar{2}2\}$ PDF sets, but that do not show similar PDF orientations. The same observations can be made in other clusters. Therefore, we suggest that the

orientation of the crystal lattice of the grains is likely not correlated with the development of a specific PDF orientation.

It is clear that in a heterogeneous, more or less porous, and multigranular sample from a large impact crater, the shock wave is much more complex than a shock wave produced experimentally in a single crystal sample in a laboratory experiment (e.g., Langenhorst and Deutsch 1994). Thus, heterogeneities of the sample (especially the collapse of pore spaces) can alter the direction and strength of the “initial” shock wave front, producing multiple overlapping/over-imposed shock waves that can travel in different directions (e.g., Kieffer 1971, Baratoux and Melosh 2003, Güldemeister et al. 2013). This implies that the existence of a unique direction of shock propagation influencing development of specific PDF orientations is not a realistic scenario in the case of a natural impact.

The strength of the shock pressure field experienced by a portion of a sample seems to better explain the observed distribution of PDF orientations. Quartz grains that are located within an area experiencing the stress appropriate for the development of $\{10\bar{1}1\}$ and/or $\{11\bar{2}2\}$ orientations will contain them, despite the variable orientation of their crystal lattice. If the shock pressure was, either too high (i.e., above ~25 GPa), or too low (i.e., lower than 5-10 GPa), these PDFs would not have formed (see, e.g., Langenhorst and Deutsch 1994).

4.4.4. Determination of the average shock pressure in quartz bearing impactites

Heterogeneities in the recorded shock effects visible at the outcrop scale, the sample scale and at the thin section scale, draw attention to the question of representativeness of the estimated sample’s “average shock pressure” based on PDFs measurements. The methodological problems in using the orientation of planar microstructures for the estimation of shock-pressures were previously pointed out by several authors, including Grieve et al. (1996) and Ferrière et al. (2008). Even though this method was apparently effective in some cases (e.g., Robertson and Grieve 1977, Grieve et al. 1991, Trepmann and Spray 2005), it did not really work properly with samples that underwent significant amounts of

recrystallization (e.g., Grieve et al. 1990), or in samples that experienced relatively low shock pressure (e.g., Ferrière et al. 2008). Also it was shown that lithological properties of the investigated rock significantly influence the average pressure estimate (e.g., Grieve and Therriault 1995). On the other hand, another significant problem is directly related to the fact that, in most cases, planar microstructures are developed in areas that locally experienced pressures higher than the surroundings grains (which did not develop PDFs), and, thus, using such data may overestimate the “average” shock pressure of the sample.

In some cases the estimation of the relative shock-pressure differences was based on the abundance of shocked quartz grains and/or the average number of PDF sets per grain (e.g., Ferrière et al. 2008). However, because the percentage of shocked quartz grains in a sample also depends on the average grain size (with the larger grains tending to show more PDFs; e.g., Walzebuck and Engelhardt 1979, this study), such an estimate should be done with extreme care and following a very strict procedure. Being aware of all that, it is clear that the comparison of recorded shock levels between lithologically different samples is a very challenging task, unless the obtained values are normalized to the average area of the grains. But even if the percentage of the shocked quartz grains is normalized, it would not be sufficient because different PDF-bearing grains can be shocked to different extent. For example, two grains of similar size – the first with a very limited number of PDFs belonging to a single orientation in a limited portion of the grain, and the second grain fully covered with dense net of PDFs belonging to one orientations – were obviously not shocked to the same level, even if they are treated in this way in most studies.

Somewhat similar limitations also exist for the estimation of recorded shock pressure in a sample based on the average number of PDF sets per grain. Considering that in a given grain, two PDF sets can be either located in different parts of the grain or crosscutting sets, they may not necessarily be classified in the same way. For example, in some cases the development of these two different PDF orientations is clearly the result of Dauphiné twinning that already existed in the quartz grain before it was shocked. Consequently, it might be better to measure the average number of crosscutting PDF sets per grain instead of measuring the average number of PDF sets per grain. However, PDFs in the most highly shocked grains (Figure 4.9) are often not clearly visible under an optical microscope

because of the high density of planar features and the highly distorted crystal lattice, leading to an underestimate of the average shock level.

We have demonstrated in our study that there is a need for an alternative method of estimation of the shock barometry in the case of highly heterogeneous, multigrain, multimineralic, and porous samples. This method should 1) appropriately consider the full spatial variability of the recorded shock pressures, 2) be relatively independent of the lithological differences, and 3) preferably not be more time-consuming than the currently used methods.

4.5. Conclusions

The following conclusions can be drawn from our study:

1. The distribution of PDF-bearing quartz grains is heterogeneous at the scale of a thin section on many different levels:
 - a. Within a single grain (with a uniform orientation of the crystal lattice) some portions of this grain are practically devoid of any sign of shock metamorphism, while other small (up to 20-30 μm in diameter) areas are highly shocked. The higher recorded shock level is due to a very high density of PDFs (expressed as number of planar features per unit area) that cross-cut each other (looking like “nests”). These are usually located either along cracks, or on the boundaries of the grains in contact with other type of minerals/material.
 - b. The heterogeneous distribution of grains bearing a similar number of PDFs is probably in large part derived from the random distribution of these “nests” within the quartz grains as described above.
2. Some zones of homogeneities within areas of the studied sample are also visible:
 - a. Some of the neighboring grains have a statistically significant similar number of PDF sets. This suggests (particularly the planar features

present in most of these grains, not in the “nests”) that they were subjected to a similar stress field intensity.

- b. Grains with PDF orientations along planes $\{10\bar{1}1\}$ and/or $\{11\bar{2}2\}$ tend to occur in groups. This clustering is a result of those grains being subjected to the local shock pressure appropriate for the development of these PDF orientations (probably above 5-10 GPa and below 25 GPa).
3. The orientation of the crystal lattice of the grains does not seem to be an important factor driving the development of PDFs in a specific location (at least not in samples from natural impact craters).
4. The PDFs developed along the $\{10\bar{1}1\}$ and $\{11\bar{2}2\}$ orientations are commonly poorly developed, hardly visible under the U-stage, and present on the grain margins as a few microns long planar and parallel features. This important difference of physical characteristics, appearance, and location within grain of different PDFs orientations, overlooked in previous studies, suggests that these PDFs may formed in a slightly different mode than PDFs of more common orientations (such as the PDFs with $\{10\bar{1}3\}$ orientation).
5. The estimation of the recorded shock pressure from a given sample should be based on a) the average number of PDF sets present per grain, and/or b) the indexed PDF orientations, because these variables do not depend on the thoroughness of the analysis.

The program that was developed for this study allowing to fully automatically index PDFs in quartz grains is available online at: www.MeteorImpactOnEarth.com/ustage/program.html. The source code (i.e., implementation in Java programming language) is also available upon request from the authors.

Acknowledgments:

We acknowledge funding from the University of Vienna doctoral school IK-1045 and the Austrian Science Foundation grant P21821-N19. Authors are also very grateful for multiple interesting conversations about shock metamorphism with: Boris Ivanow, Uwe Reimold, Michael Poelchau, and Bevan French.

References

- Anselin L. 1999. Interactive techniques and exploratory spatial data analysis. In: Geographical Information Systems, edited by Longley P.A., Goodchild M.F., Maguire D.J., and Rhind D.W. New York: John Wiley & Sons. pp. 253–266.
- Baratoux D., and Melosh H. J. 2003. The formation of shatter cones by shock wave interference during impacting. *Earth and Planetary Science Letters* 2016: 43–54.
- Bowden E., Kondo K., Ogura T., Jones A. P., Price G. D., and DeCarli P. S. 2000. Loading path effects on the shock metamorphism of porous quartz (abstract #1582). 31st Lunar and Planetary Science Conference. CD-ROM.
- Devore J., and Peck R. 1997. *Statistics. The Exploration and Analysis of Data*. Duxbury Press: Belmont. 256 p.
- Dressler B. O., Crabtree D., and Schuraytz B. C. 1997. Incipient melt formation and devitrification at the Wanapitei impact structure, Ontario, Canada. *Meteoritics & Planetary Science* 32: 249–258
- Dressler B. O., Sharpton V. L., and Schuraytz B. C. 1998. Shock metamorphism and shock barometry at a complex impact structure: State Islands, Canada. *Contributions to Mineralogy and Petrology* 130: 275–287.
- Engelhardt W. v., and Bertsch W. 1969. Shock induced planar deformation structures in quartz from the Ries crater, Germany. *Contributions to Mineralogy and Petrology* 20: 203–234.
- Ferrière L., Koeberl C., and Reimold W. U. 2007. Drill core LB-08A, Bosumtwi impact structure, Ghana: Petrographic and shock metamorphic studies of material from the central uplift. *Meteoritics and Planetary Science* 42: 611–633.
- Ferrière L., Koeberl C., Ivanov B., and Reimold W. U. 2008. Shock metamorphism of Bosumtwi impact crater rocks, shock attenuation, and uplift formation. *Science* 322: 1678–1681.

- Ferrière L., Morrow J. R., Amgaa T., and Koeberl C. 2009. Systematic study of universal-stage measurements of planar deformation features in shocked quartz: Implications for statistical significance and representation of results. *Meteoritics and Planetary Science* 44: 925–940.
- Ferrière L., Raiskila S., Osinski G. R., Pesonen L. J., and Lehtinen M. 2010. The Keurusselkä impact structure, Finland – Impact origin confirmed by characterization of planar deformation features in quartz grains. *Meteoritics and Planetary Science* 45: 434–446.
- Ferrière L., Lubala F. R. T., Osinski G. R., and Kaseti P. K. 2011. The newly-confirmed Luizi impact structure, Democratic Republic of Congo – Insights into central uplift formation and post-impact erosion. *Geology* 39: 851–854.
- French B.M. and Koeberl C. 2010. The convincing identification of terrestrial meteorite impact structures: What works, what doesn't, and why. *Earth-Science Reviews* 98: 123–170.
- Getis A. 1999. Spatial statistics. In: *Geographical Information Systems*, edited by Longley P. A., Goodchild M. F., Maguire D. J., and Rhind D. W. New York: John Wiley & Sons: pp. 239–251.
- Goltrant O., Doukhan J.-C., Cordier P., and Courtillot V. 1992. An investigation by transmission electron microscopy of planar deformation features in naturally shocked quartz. *Terra Nova* 4: 405–412.
- Goltrant O., Cordier P., and Doukhan J.-C. 1991. Planar deformation features in shocked quartz; a transmission electron microscopy investigation. *Earth and Planetary Science Letters* 106: 103–115.
- Grady D. E. 1980. Shock deformation of brittle solids. *Journal of Geophysical Research* 85: 332–338.
- Gratz A. J., Nellis W. J., Christie J. M., Brocious W., Swegle J., and Cordier P. 1992. Shock metamorphism of quartz with initial temperatures –170 to +1000°C. *Physics and Chemistry of Minerals* 19: 267–288.

- Grieve R. A. F., Langenhorst F., and Stöffler D. 1996. Shock metamorphism of quartz in nature and experiment: II. Significance in geoscience. *Meteoritics and Planetary Science* 31: 6–35.
- Grieve R. A. F. and Theriault A. M. 1995. Planar deformation features in quartz: Target effects. *Proceedings, 26th Lunar and Planetary Science Conference*: 515–516.
- Grieve R. A. F., Stöffler D., and Deutsch A. 1991. The Sudbury Structure: Controversial or misunderstood? *Journal of Geophysical Research* 96: 22753–22764.
- Grieve R. A. F., Coderre J. M., Robertson P. B., and Alexopoulos J. 1990. Microscopic planar deformation features in quartz of the Vredefort structure: Anomalous but still suggestive of an impact origin. *Tectonophysics* 171: 185–200.
- Grieve R. A. F. and Robertson P. B. 1976. Variations in shock deformation at the Slate Islands impact structure, Lake Superior, Canada. *Contributions to Mineralogy and Petrology* 58: 37–49.
- Güldemeister N., Wünnemann K., Duur N., and Hiermaier S. 2013. Propagation of impact-induced shock waves in porous sandstone using mesoscale modeling. *Meteoritics and Planetary Science* 48: 115–133.
- Holm S., Alwmark C., Alvarez W., and Schmitz B. 2011. Shock barometry of the Siljan impact structure, Sweden. *Meteoritics and Planetary Science* 46: 1888–1909.
- Hörz F. 1968. Statistical measurements of deformation structures and refractive indices in experimentally shock loaded quartz. In: *Shock metamorphism of natural materials*, edited by French B. M. and Short N. M. Baltimore: Mono Book Corporation. pp. 243–253.
- Huffman A. R. and Reimold W. U. 1996. Experimental constraints on shock-induced microstructures in naturally deformed silicates. *Tectonophysics* 256: 165–217.
- Huber M. S., Ferrière L., Losiak A., and Koeberl C. 2011. ANIE: A mathematical algorithm for automated indexing of planar deformation features in quartz grains. *Meteoritics and Planetary Science* 46: 1418–1424.
- Kennedy H. 2000. *Dictionary of GIS Terminology*. Redlands: Esri Press. 200 p.

- Kieffer S.W. 1971. Shock metamorphism of the Coconino Sandstone at Meteor Crater, Arizona. *Journal of Geophysical Research* 76: 5449–5473.
- Kieffer S. W., Phakey P. P., and Christie J. M. 1976. Shock processes in porous quartzite: transmission electron microscope observations and theory. *Contributions to Mineralogy and Petrology* 59: 41–93.
- Koeberl C., Milkereit B., Overpeck J.T., Scholz C. A., Amoako P. Y. O., Boamah D., Danuor S. K., Karp T., Kueck J., Hecky R. E., King J., and Peck J. A. 2007. An international and multidisciplinary drilling project into a young complex impact structure: The 2004 ICDP Bosumtwi impact crater, Ghana, drilling project—An overview: *Meteoritics and Planetary Science* 42: 483–511.
- Langenhorst F. 1994. Shock experiments on pre-heated α and β -quartz: II. X-ray and TEM investigations. *Earth and Planetary Science Letters* 128: 683–698
- Langenhorst F., and Deutsch A. 1994. Shock experiments on pre-heated α - and β -quartz: I. Optical and density data. *Earth and Planetary Science Letters* 125: 407–420.
- Langenhorst F. 2002. Shock metamorphism of some minerals: Basic introduction and microstructural observations. *Bulletin of the Czech Geological Survey* 77: 265–282.
- Robertson P. B., and Grieve R. A. F. 1977. Shock attenuation at terrestrial impact structures. In: *Impact and explosion cratering*, edited by Roddy D. J., Pepin P. O., and Merrill R. B. New York: Pergamon Press. pp. 687–702.
- Rogerson P. A. 2001. *Statistical Methods for Geography*. London: SAGE Publications. 248 p.
- Stöffler D., and Langenhorst F. 1994. Shock metamorphism of quartz in nature and experiment: I Basic observation and theory. *Meteoritics* 29: 155–181.
- Treppmann A., and Spray J. 2006. Shock-induced crystal-plastic deformation and post-shock annealing of quartz: microstructural evidence from crystalline target rocks of the Charlevoix impact structure, Canada. *European Journal of Mineralogy* 18: 161–173.

Trepmann C. A. 2008 Shock effects in quartz: Compression versus shear deformation - An example from the Rochechouart impact structure, France. *Earth and Planetary Science Letters* 267: 322–332.

Walzebuck J. P., and Engelhardt W. 1979. Shock deformation of quartz influenced by grain size and shock direction: Observations on quartz-plagioclase rocks from the basement of the Ries crater, Germany. *Contributions to Mineralogy and Petrology* 271: 267–271.

web sites used:

<http://www-01.ibm.com/software/analytics/spss/> [date of collection 02.03.2011]

<http://www.esri.com/> [date of collection 02.03.2011]

ArcGIS Help Library 2010, ESRI

<http://onlinelibrary.wiley.com/doi/10.1111/j.1945-5100.2011.01234.x/supinfo> [date of collection 02.05.2012]

5. ^{10}Be content in clasts from fallout suevitic breccia in drill cores from the Bosumtwi impact crater, Ghana: Clues to pre-impact target distribution

Anna Losiak¹, Eva Maria Wild², Leonard Michlmayr² and Christian Koeberl^{1,3}.

¹Department of Lithospheric Research, University of Vienna, Althanstrasse 14, A-1090 Vienna, Austria (anna.losiak@univie.ac.at).

² VERA Laboratory, Faculty of Physics, Isotope Research, University of Vienna, A-1090 Vienna, Austria.

³Natural History Museum, Burgring 7, A-1010 Vienna, Austria.

Article was submitted to “Meteoritics and Planetary Science”, currently it is under review.

Abstract

Rocks from drill cores LB-07A (crater fill) and LB-08A (central uplift) into the Bosumtwi impact crater, Ghana, were analyzed for the presence of the cosmogenic radionuclide ^{10}Be to determine the extent to which target rocks of various depths were mixed during the formation of the crater-filling breccia, and also to detect meteoric water infiltration within the impactite layer. ^{10}Be abundances above background were found in two (out of 24) samples from the LB-07A core, and in none of five samples from the LB-08A core. After excluding other possible explanations for an elevated ^{10}Be signal, we conclude that it is most probably due to a pre-impact origin of those clasts from target rocks close to the surface (20-30 meters depth).

Our results suggest that in-crater breccias were well mixed during the impact cratering process. Additionally, the lack of a ^{10}Be signal within the rocks located very close to

the lake sediments-impactites boundary suggests that infiltration of meteoric water below the post-impact crater floor was limited. This may suggest that the infiltration of the meteoric water within the crater takes place not aurally (through pore-space), but rather through a localized system of fractures.

5.1. Introduction

During the impact cratering process, a large fraction of the surface layer of the target material is removed from the crater in form of ejecta (mostly distal) or is vaporized/melted (e.g., Melosh 1989). Indeed, the formation of tektites from the uppermost layer of the target rocks has also been well established using the ^{10}Be contents of tektites (e.g., Pal et al. 1982, Ma et al. 2004, Serefiddin et al. 2007), as well as chemical comparison of tektites with their probable source-surface material (e.g., Koeberl 1994, Koeberl et al. 1997, Engelhardt et al. 2005, Son and Koeberl 2005), and reproduced by computer modeling (e.g., Artemieva 2000). However, some research suggests that near-surface target material may be incorporated in crater-filling breccias. This is based on studies of rare impact structures developed within target rocks characterized by easily distinguished, horizontal layers where the approximate depth of origin of clasts present in the resulting crater-filling suevite can be determined by their lithological characterization. Two such craters are Kärddla, a 4 km wide, submarine, 455 Ma crater in Estonia (Puura et al. 2004) and Tswaing, a 1.13 km diameter, subaerial, 0.22 Ma crater in South Africa (Reimold et al. 1992). However, those studies are not sufficient to quantitatively evaluate mixing process within the impact crater's transient cavity. Tswaing is a small crater, such that surface material can be easily incorporated into crater filling breccias during the modification stage by slumping and similar mass-wasting processes (e.g., Melosh 1989). Additionally, the exact percentage and location of the clasts originating near the surface that were incorporated in the crater filling material of the Tswaing crater was not studied (Reimold et al. 1992), and the original drill core is not available for further studies (W.U. Reimold, personal communication). Drawing conclusions about the process of material mixing within the cratering event based on the Kärddla structure is even more problematic (even though an excellent lithostratigraphic profile is available)

because this crater was formed within a shallow <100m deep sea (Puura et al. 2004). Multiple studies suggest that there are significant differences between subaerial and submarine craters with respect to the late stages of crater formation, including the process of mixing of the crater filling material (e.g., Ormö and Lindstrom 2000, Ormö et al. 2010). To better understand the process of material mixing within the transient cavity of subaerial craters more research is necessary.

Unfortunately, with respect to most subaerial craters, the approach used at Tswaing or Kärddla cannot be applied because target rocks are rarely horizontally stratified with layers easily distinguishable from each other. However, if the age of the impact crater is known and less than a few million years, the approximate depth of origin of clasts present within the suevitic breccia can be established using abundances of ^{10}Be within the clast.

^{10}Be is a cosmogenic radionuclide with a newly determined half-life of 1.386 ± 0.016 Ma (Chemeleff et al. 2010) or 1.387 ± 0.012 Ma (Korschinek et al. 2010), but other values are also in use: 1.36 ± 0.07 Ma (Nishiizumi et al. 2007) and 1.51 ± 0.06 Ma (Hofmann et al. 1987). It is produced in the atmosphere and *in situ*, primarily by spallation reactions, negative muon capture or/and thermal neutron capture, due to the interaction of ^{16}O , ^{28}Si and ^9Be with cosmic rays (Dunai 2010). As a result, the ^{10}Be content is enriched in the top few meters of surface materials (Pavich et al. 1985, Serefiddin et al. 2007, Dunai 2010, Graly et al. 2010), and could, therefore, be used to trace the surface origin of clasts displaced during the impact process. Additionally, as ^{10}Be is enriched in meteoric water, this radionuclide can be used to trace water circulation within a drainage basin (e.g., Willenbring and Blanckenburg 2010), such as an impact crater.

The Bosumtwi crater was chosen as an appropriate study site because of its relatively large size (10.5 km in diameter), relatively young age of 1.07 Ma (Koeberl et al. 1997), good preservation, and availability of samples from the drill core (Koeberl et al. 2007a). The size of 10.5 km minimizes the probability of incorporation of surface material by secondary processes (such as slumping) into the core during the modification stage of the crater formation process (e.g., Melosh 1989). The age of the crater of 1.07 Ma is comparable with the radionuclide half-life and thus young enough to allow the usage of the ^{10}Be system, so that it should be possible to recognize surface-derived material within available detection

limits. Samples used in this study were obtained during the 2004 International Continental Scientific Drilling Program (ICDP) Lake Bosumtwi Drilling Project (e.g., Koeberl et al. 2007a). The sampled drill cores have previously been petrographically and geochemically described (e.g., Coney et al. 2007, Ferrière et al. 2007a, 2007b, 2008, 2010).

The aim of this study is to investigate if surface-derived material is present in the suevitic breccia of the Bosumtwi crater so that the extent of mixing of target rocks during crater formation in respect to the fallback breccia can be determined. Additionally, the top-most layer of the impactites were analyzed for elevated ^{10}Be contents, which may result from interaction with meteoric (lake) water after crater formation and could provide information about water circulation within a newly formed crater.

5.2. Geologic background

The Bosumtwi impact crater, located in Ghana, West Africa (Figure 5.1) was formed at 1.07 Ma (e.g., Koeberl et al. 1997). It was excavated in rocks of the Early Proterozoic Birimian Supergroup of the West African craton (e.g., Jones et al. 1981). The Birimian Supergroup can be divided into two contemporary units (volcanic belts and sedimentary basins) aligned in multiple parallel structural features. Additionally, numerous, extensive granitoid intrusions are present. The sedimentary unit of the Birimian Supergroup consists of volcanoclastic rocks, argillites, and turbidites that are now metamorphosed to meta-greywackes, phyllites, schists, and shales (Leube et al. 1990). The volcanic unit has a predominantly tholeiitic chemical composition and consists of metamorphosed basalts and andesites that occur as different types of schists, including hornblende-actinolite-, calcite-chlorite-, mica-schists, and in some cases amphibolites (Leube et al. 1990). The Birimian rocks were metamorphosed during the Eburnean tectono-thermal event at ~2092 Ma to greenschist and (locally) amphibolite facies (Feybesse et al. 2006).

The Bosumtwi impact crater was emplaced within a meta-sedimentary unit (mostly meta-greywackes, phyllites and schists), close to the boundary with meta-volcanics of the Ashanti belt (Figure 5.1). Additionally, in the proximity of the Bosumtwi crater few small

granitic bodies and dikes are present (e.g., Moon and Manson 1967, Jones 1985, Reimold et al. 1998, Koeberl and Reimold 2005, Losiak et al. 2013).

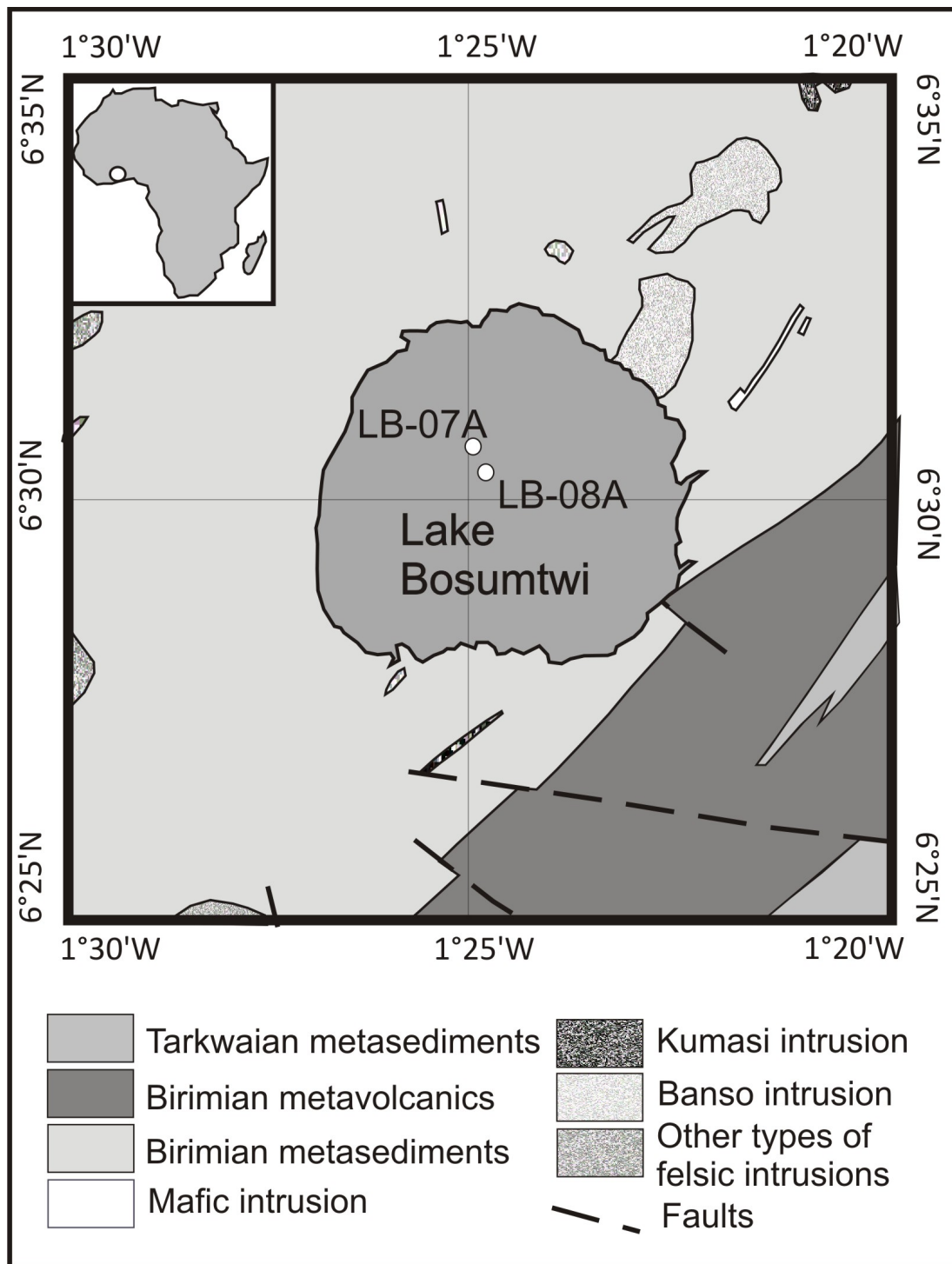


Figure 5.1. Schematic geological map of the Bosumtwi impact crater and location of drill cores LB-07A and LB-08A used in this study (adapted from Koeberl and Reimold 2005 and Losiak et al. 2013).

5.3. Samples

Samples selected for this study come from the impactite layer of the LB-07A and LB-08A cores drilled within the Bosumtwi impact crater (Figure 5.1) (e.g., Koeberl et al. 2007a). The detailed information on the lithostratigraphy, petrography, and geochemistry of those drill cores is available in Coney et al. (2007) and Ferrière et al. (2007a, 2007b) and is presented graphically in Figure 5.2.

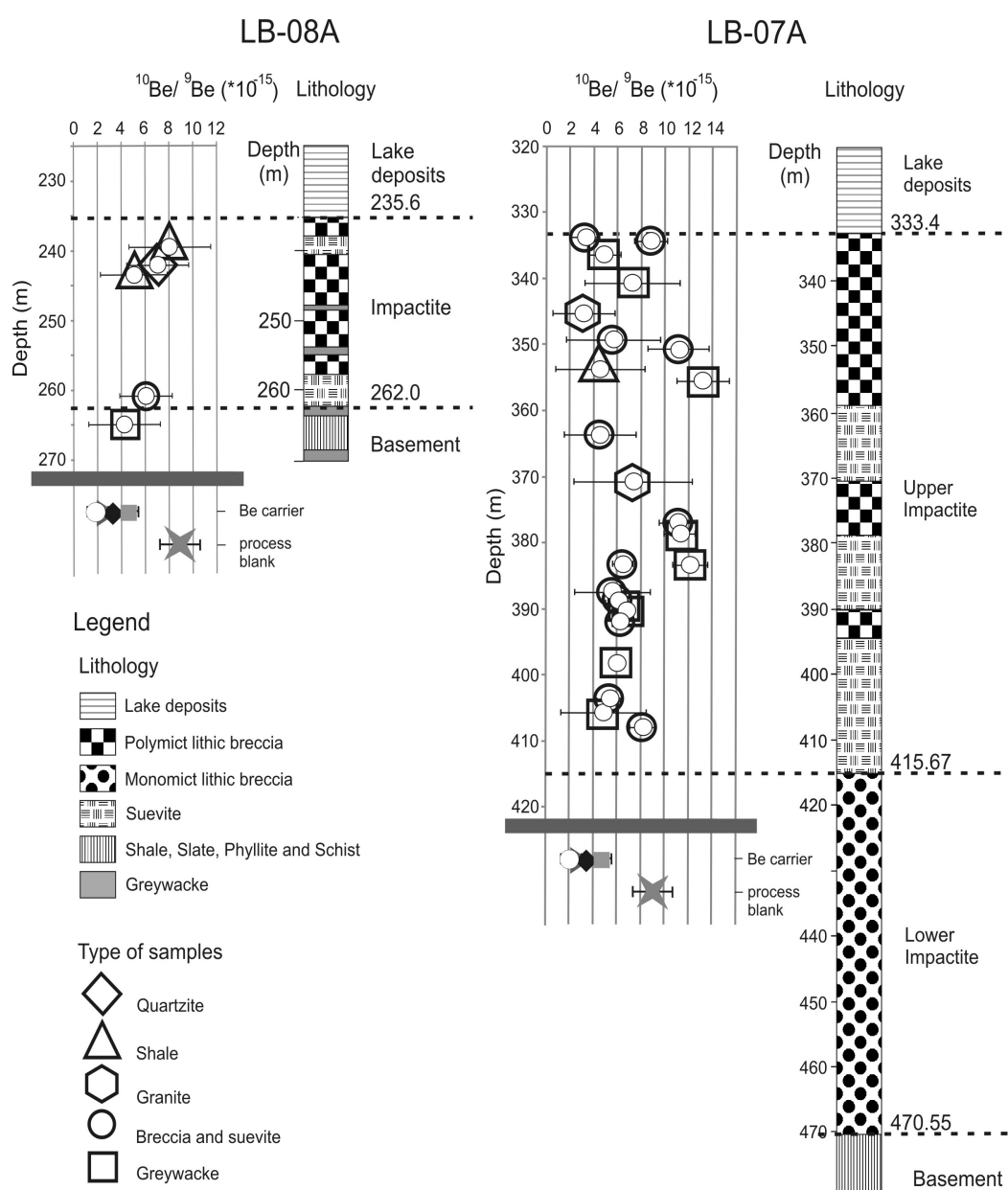


Figure 5.2. $^{10}\text{Be}/^9\text{Be}$ ratios within samples studied in this project showed in a depth profile on a background of the lithological information (data on drill core LB-07A from Coney et al. 2007 and on drill core LB-08A from Ferrière et al. 2007a). The figure shows that there is no clear relationship between the depth of a sample and its ^{10}Be abundance.

Core LB-07A was drilled in the deepest part of the impact crater and impactites come from depths between 333.38 m and 545.08 m (Coney et al. 2007). It consists of three main sequences: 1) the upper impactites (333.38-415.67 m), composed of polymictic lithic breccias and suevite; 2) the lower impactites (415.67-470.55 m), composed of monomictic impact breccia with small suevite injections; and 3) shocked basement (470.55-545.08 m) (Coney et al. 2007).

Core LB-08A was drilled on the outer flank of the central uplift, with impactites having been recovered between 235.6 and 451.33 m depth within the drill core (Ferrière et al. 2007a). The top 25 m impactite sequence consists of polymict, clast-supported lithic breccia intercalated with suevite, while the other part of the core is a highly fractured, shocked metasediment, mostly metagreywacke, phyllite, and slate (Ferrière et al. 2007a, 2007b).

In total, 29 samples were analyzed (Table 5.1): 16 single-clast samples selected from within breccia and 13 breccia samples (without clasts larger than $\sim 1\text{cm}^3$ present). 24 of them came from core LB-07A and represent depths of 333.7 – 407.9 m (“upper impactite layer” Coney et al. 2007) and 5 are from core LB-08A from depths 239.5 – 264.9 m (“fallback breccia” Ferrière et al. 2007a).

The process of single-clast sample selection was guided by the following objectives: 1) relatively uniform coverage of the entire drill core; 2) sampling only clasts larger than $\sim 8\text{cm}^3$; 3) sampling clasts representing different lithologies present in the core. The breccia samples were selected: 1) below the border between impactites and lake deposits to test for the possibility of ^{10}Be contamination by lake water infiltration; 2) if the core section appeared as if it could have been affected by hydrothermal processes (e.g., Karikari et al. 2007); 3) if there was no appropriate clast to be sampled within a significant segment from the core.

Table 5.1. Results of AMS measurements of ^{10}Be contents in the studied samples from the Bosumtwi crater.

Sample Number	Drill core	Depth (m)	Sample type	Mass (g)	^9Be carrier (mg)	$^{10}\text{Be}/^9\text{Be}$ $\cdot 10^{-15}$	\pm (2 σ) $\cdot 10^{-15}$	significance test (*) σ	^{10}Be $\cdot 10^6$ atom/g	\pm (2 σ) $\cdot 10^6$ atom/g
AL1	8A	239.5	shale	0.8045	1	8.1	3.4	-0.4	—	—
AL2	8A	243.4	shale	0.8036	1	5.1	2.6	-2.4	—	—
AL3	8A	242.1	quartzite	0.7118	1	7.1	2.8	-1.0	—	—
AL5	8A	260.9	suevite	0.8061	1	6.1	2.2	-2.0	—	—
AL6	8A	264.9	greywacke	0.8047	1	4.3	3.0	-2.6	—	—
AL7	7A	333.7	breccia	0.8163	0.6	3.3	1.2	-5.4	—	—
AL8	7A	334.3	suevite	0.8167	0.6	8.9	1.4	0.1	—	—
AL9	7A	336.4	greywacke	0.8068	1	4.9	1.4	-3.6	—	—
AL11	7A	340.7	greywacke	0.8075	1	7.3	4.0	-0.7	—	—
AL12	7A	345.2	granite	0.8073	1	3.2	2.6	-3.6	—	—
AL13	7A	349.2	breccia	0.8120	1	5.7	4.0	-1.4	—	—
AL14	7A	350.6	suevite	0.8137	1	11.2	2.6	1.6	—	—
AL15	7A	353.7	shale	0.8118	1	4.6	3.8	-2.0	—	—
AL18	7A	363.6	suevite	0.8092	1	4.6	3.0	-2.5	—	—
AL21	7A	370.7	granite	0.8147	1	7.4	5.0	-0.5	—	—
AL22	7A	377.0	suevite	0.8152	0.6	11.2	1.6	2.1	—	—
AL24	7A	383.2	suevite	0.8156	1	6.5	0.9	-2.5	—	—
AL25	7A	383.4	greywacke	0.8172	1	12.2	1.5	3.1	0.28	0.12
AL26	7A	387.5	breccia	0.8132	1	5.7	3.2	-1.7	—	—
AL28	7A	389.1	greywacke	0.8175	0.6	6.1	1.0	-2.9	—	—
AL29	7A	390.1	greywacke	0.8051	1	6.7	0.7	-2.4	—	—
AL30	7A	392.1	suevite	0.8050	1	6.3	0.6	-2.9	—	—
AL33	7A	403.9	suevite	0.8172	0.6	5.3	1.0	-3.7	—	—
AL37	7A	405.7	greywacke	0.8141	1	4.9	3.6	-2.0	—	—
AL41a	7A	355.5	greywacke	0.8051	1	10.7	0.7	2.1	—	—
AL41b			greywacke	0.8236	0.6	13.3	2.2	3.3	0.33	0.11
AL42	7A	385.2	suevite	0.8207	0.6	8.9	1.1	0.2	—	—
AL43	7A	398.3	greywacke	0.7027	1	6.0	0.5	-3.3	—	—
AL44	7A	407.9	suevite	0.8112	0.6	8.2	1.1	-0.6	—	—
AL45	7A	378.6	greywacke	0.8179	0.6	11.3	1.3	2.4	—	—

Measurements were performed during four independent sessions: A (AL29, AL30, AL41, AL43), B (AL03, AL05, AL06, AL09, AL11), C (AL01, AL02, AL12, AL13, AL15, AL18, AL21, AL26, AL37), D (AL07, AL08, AL14, AL18, AL22, AL24, AL25, AL28, AL33, AL41, AL42, AL44, AL45).

The transmission from the high energy currents to the detector signal is between 30.63% for A session, 25.53% for B session, 5.83% for C session and 27.72% for D session. The precision of the calibration is 0.19% for the A session, 2.5% for the B session, 2.76% for the C session, 1.06% for the D session. This is a correlated uncertainty included in the uncertainties listed in the table. The uncertainty of the standard definition is not considered. The isotope ratios are normalized to the standard. No background correction has been applied.

$^{10}\text{Be}/^9\text{Be}$ ratio of the beryllium carrier was measured four times: A: $(2.78 \pm 0.34) \cdot 10^{-15}$, B: $(2.52 \pm 0.96) \cdot 10^{-15}$, C: $(3.79 \pm 1.9) \cdot 10^{-15}$ and D: $(1.64 \pm 0.52) \cdot 10^{-15}$.

$^{10}\text{Be}/^9\text{Be}$ ratio of the process blank was measured to be $(8.79 \pm 1.62) \cdot 10^{-15}$.

(*) significance test - checks if the sample is significantly different than the process blank by calculating confidence interval for difference between population means. Samples characterized by the calculated values >3 are significantly different from the process blank with a 99.73% probability.

^{10}Be in at/g values are blank corrected, but not decay corrected.

5.4. Methods

5.4.1. Accelerator mass spectrometry

The ^{10}Be concentration in the environment is so low, that the measurement can be performed only by accelerator mass spectrometry (AMS).

5.4.1.1. Sample preparation for AMS

Sample preparation for the ^{10}Be AMS measurement consists of three stages: 1) dissolving samples, 2) separation of beryllium from the sample, and 3) preparing BeO AMS targets. The first stage was performed at the Department of Lithospheric Research, University of Vienna. At least 200 g of each sample was crushed with a hammer. In order to avoid contamination that could have been introduced during drilling, only pieces of sample that were inside the original clasts were selected for further analysis and pulverized in an agate mill. Powders were heated in a muffle furnace to 950°C for 2 hours to remove all organic compounds that could interfere with further steps of the sample preparation procedure (studies of ^{10}Be composition in tektites show that ^{10}Be is not affected by high temperature e.g., Koeberl 1986, 1994, Wasson 2003, Serefiddin et al. 2007). Subsequently, samples were dissolved using an Anton Paar Multiwave 3000 microwave sample preparation system. This system consists of 8 separate Teflon reactors; in each there was ~0.1 g of rock powder added to mixture of 22 mol HF, 15 mol HNO_3 , and H_2O as well as 0.6 mg or 1 mg of ^9Be carrier (see Table 5.1). After full dissolution of the powders (usually after 4 hours in 140°C, but some samples required longer times to fully dissolve), samples were evaporated to dryness using the same sample preparation system. Subsequently, powders were re-dissolved in 7 mol HNO_3 , evaporated to dryness and then re-dissolved again in 6 mol HCl. After evaporating it to dryness for the third time, samples were dissolved in 6 mol HCl and all solutions belonging to the same sample were combined.

The second stage of sample preparation focused on chemical separation of beryllium from the dissolved sample. It was executed at the Vienna Environmental Research

Accelerator Facility (VERA) at the Faculty of Physics, University of Vienna. The beryllium separation from the sample solution was performed by a combination of ion exchange operations (Korkisch 1989) and hydroxide precipitation steps. The chemical method used here is a slightly modified version of the method described by Auer (2007) and Auer et al. (2007).

At first, the samples previously dissolved in 6 mol HCl were passed through the anion exchange column (filled with resin Biorad AG1-X8 100-200 mesh) to remove iron. Then beryllium and aluminum hydroxides were precipitated at pH of 8 with NH_3 (aq) in order to remove Ca and Ni (Merchel and Herpers 1999) as well as to decrease the size of the solution produced afterwards. Hydroxide samples were re-dissolved in few milliliters of 0.5 molar HCl and passed through the cation exchange column (filled with resin Biorad AG50W-X8 100-200) to separate beryllium from aluminum. In this step beryllium is also largely separated from boron. In most cases, due to a very high amount of aluminum present in the samples (from 25 to 113 mg), this step of the chemical separation had to be performed twice (with the precipitation in between).

In order to determine beryllium yields of the sample preparation method, aliquots of the sample solutions were taken after every step of the chemical procedure and the Be and Al contents were measured with atomic absorption spectroscopy. The total beryllium yields of the chemical separation method were determined to be ~80%.

In the third stage the AMS targets were produced by precipitating Be as hydroxide, which was then converted to oxide by heating and afterwards pressed into targets. At first, beryllium hydroxide was precipitated and washed three times with double distilled water to remove boron which interferes with the AMS ^{10}Be measurement. Then the precipitate was transferred into small quartz crucibles, and heated for 4 hours at 850°C to dehydrate the $\text{Be}(\text{OH})_2$ to BeO . BeO was mixed with small amount of Cu powder and pressed into copper AMS targets. As beryllium is highly toxic, all steps of the AMS target preparation were done in a fume hood or in a glove box.

5.4.1.2. Carrier and standards for AMS measurements

The ^9Be carrier that was used in this study was a beryllium standard by Merck for conventional mass spectrometry (MERC 19775 41466612). The amount of the carrier added varied between 0.6 mg and 1 mg of beryllium (Table 5.1). Its $^{10}\text{Be}/^9\text{Be}$ ratios scattered between $1.12 \cdot 10^{-15}$ and $5.69 \cdot 10^{-15}$ (2σ uncertainty) and on average was $2.7 \cdot 10^{-15}$. The measured $^{10}\text{Be}/^9\text{Be}$ ratio of a process blank was $(8.79 \pm 1.6) \cdot 10^{-15}$ (Table 5.1).

The $^{10}\text{Be}/^9\text{Be}$ ratio of the process blank is somewhat higher than the average ratio of the carrier. However, 15 of the measured samples have their $^{10}\text{Be}/^9\text{Be}$ ratios indistinguishable (within 2σ uncertainty) from values characteristic to the highest measured ratio of beryllium carrier used in this study $(3.79 \pm 1.9) \cdot 10^{-15}$, and are significantly lower than in the process blank (Table 5.1). This shows that the real $^{10}\text{Be}/^9\text{Be}$ ratio of the process blank is in most cases lower than $(8.79 \pm 1.62) \cdot 10^{-15}$.

The ^{10}Be standard used in this study is the NIST SRM4325 (NIST National Institute of Standards and Technology) with certified $^{10}\text{Be}/^9\text{Be}$ ratio of $2.68 \cdot 10^{-11}$ ($\pm 5.1\%$); however, according to Nishiizumi et al. (2007) a more precise value of this standard is $(2.79 \pm 0.03) \cdot 10^{-11}$. Our results are referenced to the NIST value.

5.4.1.3. Measurement by AMS

$^{10}\text{Be}/^9\text{Be}$ ratios were measured with the VERA AMS system (see e.g., Kutschera et al. 1997, Steier et al. 2004) – using a post-stripping method for isobar separation (e.g., Michlmayr 2007). The method addresses the discrimination between ^{10}Be and its isobar ^{10}B by using the difference in energy loss of the ion beam in matter, due to the different atomic number of ^{10}Be and ^{10}B (Michlmayr 2007). Detailed information on the set-up and performance of the VERA during the ^{10}Be measurement was described in Martschini (2008).

5.4.1.4. Results of the pilot project

In order to develop an efficient method of sample preparation, as well as assess the accuracy and reproducibility of the measurement and sample preparation method, a pilot

project was performed on soil samples from the Bosumtwi region previously measured by Serefiddin et al. (2007). Our results show a generally good agreement with previously published data (within uncertainty) (Figure 5.3). However, results obtained for sample LB29a are somewhat higher than those measured by Serefiddin et al. (2007). In order to test the precision of our method we have processed samples LB29a and LB29c twice (Figure 5.3). Two sub-samples of the sample LB29a were processed separately throughout the entire procedure to test reproducibility and precision of the sample preparation process. Sample LB29c was divided into two separate targets at the very end of the procedure to test reproducibility and precision of AMS measurement. The results of the pilot project show good accuracy and precision for both sample preparation and the AMS measurement applied in this study.

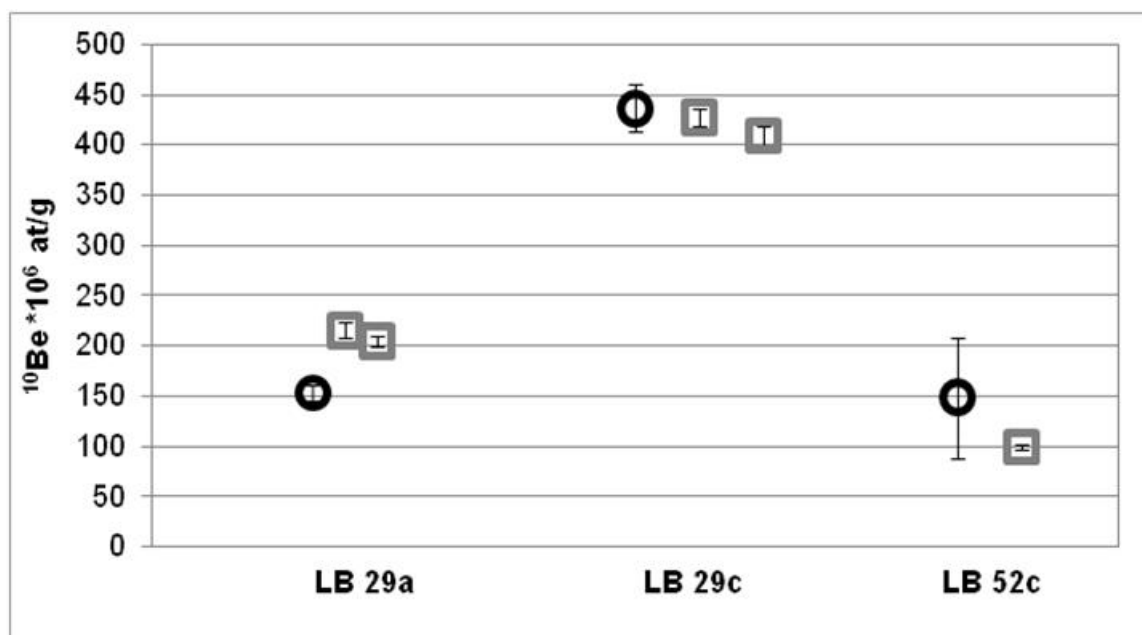


Figure 5.3. Comparison of results obtained by Serefiddin et al. (2007) (black circles) and in this study (grey squares) on soil samples from the Bosumtwi region. The plot shows a generally good agreement with previously published data (within error).

5.5. Results

The detailed petrographic characteristics of the samples are provided in Table 5.2. The studied samples can be divided into a few petrologic groups. Out of a total of 16 clasts, two were identified as granite, ten as greywacke (or metagreywacke), three as shales and one clast as quartzite. Thirteen samples are impact breccias, and ten of them include melt clasts (and were classified as suevite). Most of samples are shocked to some extent; quartz grains have up to three planar deformation feature (PDF) sets, some of them also having a “toasted” appearance (Ferrière et al. 2009).

The results of the AMS measurements are presented in Table 5.1 and Figure 5.4. All measured $^{10}\text{Be}/^9\text{Be}$ ratios are very close to the values characteristic for the ^9Be carrier used in this study.

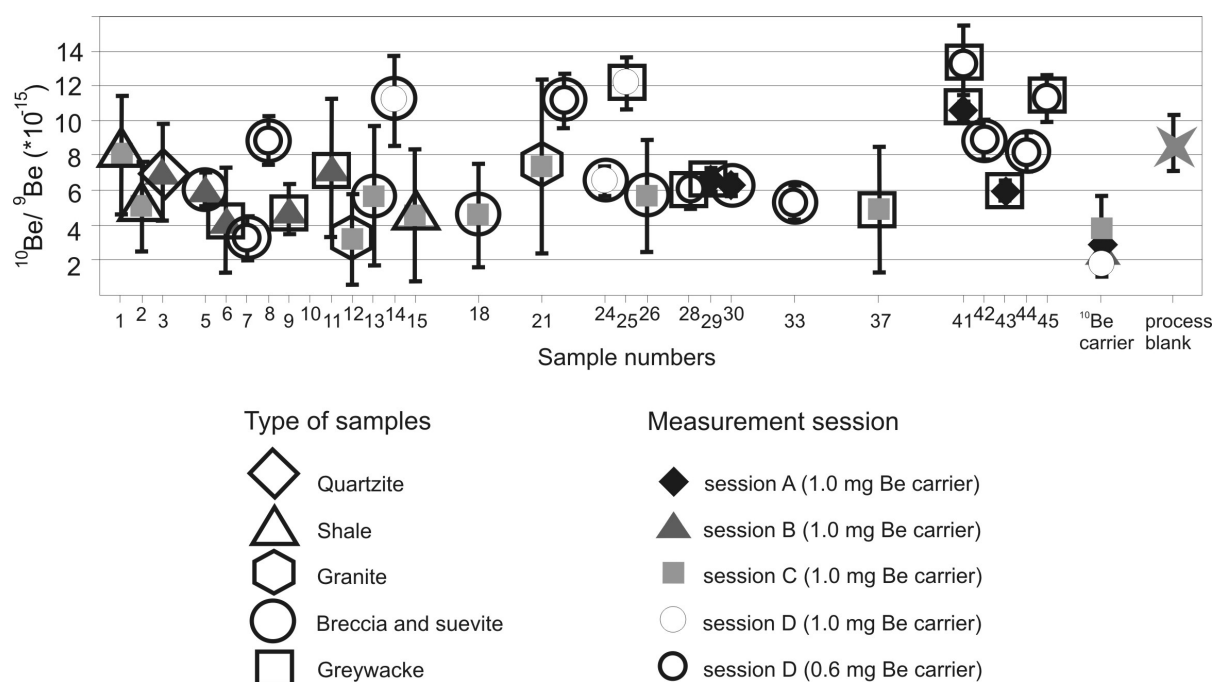


Figure 5.4. $^{10}\text{Be}/^9\text{Be}$ ratios measured in samples from the Bosumtwi crater (error bars plotted as 2σ). Numbers on the horizontal axis correspond to the sample number (see Table 5.1).

The $^{10}\text{Be}/^9\text{Be}$ ratios have been measured during four independent AMS sessions (Table 5.1 and Figure 5.4). The transmission from the high energy currents to the detector signal was about 30% for sessions A, B, and D. For session C the transmission was much

lower and only about 6% due to problems related to terminal voltage instability what resulted in much lower count rates and higher errors.

Two samples (AL25, AL41) have $^{10}\text{Be}/^9\text{Be}$ ratios significantly ($>3\sigma$) above the process blank based on the confidence interval for the difference between population means (e.g., Franklin 2007). Additionally, their 2σ confidence intervals do not overlap with the process blank 2σ confidence interval. Only those two samples are discussed in this study as ones having a true ^{10}Be signal. Because of that, the numbers of ^{10}Be atoms per gram of sample were calculated only for those samples (Table 5.1). The sample AL25 is a greywacke clast collected on the depth of 383.2 m of the core LB-07A, and the sample AL41 is also a greywacke clasts collected from depth of 355.5 m within the same core.

Two additional samples (AL22, AL45) have $^{10}\text{Be}/^9\text{Be}$ ratios higher than the process blank on more than 2σ (but less than 3σ) confidence level. We acknowledge that those samples probably include some internal ^{10}Be . But the experimental setup used in this study was not sufficient to confirm that those samples contain ^{10}Be with a 3σ probability level. 3σ threshold instead of more commonly used 2σ level is used in this study because we are basing our process blank estimate on a single measurement. Samples AL22, AL45 and AL14 will not be discussed in detail in the following section of the manuscript as ones with a detected ^{10}Be signal.

Table 5.2. Petrological description of samples from the Bosumtwi impact crater (cores LB-07A and LB-08A) analyzed in this study.

Sample Number	Drill Hole	Depth [m]	Sample description	Shock properties	metamorphic
AL1	8A	239.5	Highly altered graphitic shale. The fine-grained matrix is composed of quartz, feldspar, micas (sericite and chlorite) graphite, and some accessory minerals including titanite, epidote, and rutile as well as some opaques. Few cross cutting sets of quartz veinlets are present.	PDFs are present in the quartz veinlets (up to 3 cross-cutting sets). Additionally some of the quartz grains display a "toasted appearance".	
AL2	8A	243.4	Well banded graphitic shale (or phyllite), with mylonitic quartz ribbons. Some of the bands consist of large quartz grains. Large subhedral grains of graphite are present.	Rare and faint PDFs are present in some of the quartz grains.	
AL3	8A	242.1	Quartzite consisting mostly of very large quartz grains, with some areas where much smaller grain size is prevailing.	Most of the grains in the sample include some PDFs. Some of the enclaves additionally appear to be "toasted".	
AL5	8A	260.9	Suevite consisting mostly of fine-grained greywacke-derived matrix (quartz, feldspar and micas), and clasts of greywacke and well banded graphitic shale. Melt clasts are scarce.	Some quartz grains are highly shocked and toasted (but most are too small to see indications of shock metamorphism).	
AL6	8A	264.9	Fine-grained, mylonitized greywacke composed of mostly quartz feldspar and various micas (sericite and chlorite). Sample is highly altered, with abundant occurrences of amorphous reddish phase.	Some quartz grains contain PDFs.	
AL7	7A	333.7	Monomictic breccia composed of fine-grained, mylonitized greywacke with large clasts present. The fine-grained matrix is composed of quartz, feldspar and micas (mostly sericite and chlorite).	Rare and faint PDFs are present in some of the quartz grains.	
AL8	7A	334.3	Matrix rich suevite consisting of large variety of lithic and mineral clasts: fine and medium grained metagreywacke, slate, phyllite, quartzite as well as few melt clasts (brown and sub-rounded). Sample similar to sample AL18 and AL41.	Some clasts (or fragments of grains) are isotropized, probably due to heating. No grains bearing PDFs were identified.	
AL9	7A	336.4	Fine-grained, mylonitized greywacke composed of mostly quartz feldspar and various micas (sericite and chlorite) showing a number of rotated and recrystallized quartz porphyroclasts. Sample is highly altered.	Rare and faint PDFs are present in some of the quartz grains.	
AL11	7A	340.7	Medium-grained, partially mylonitized greywacke composed of matrix of quartz, feldspar, various micas (sericite and chlorite), and quartz porphyroclasts. Sample is highly altered (although some not fully sericitized feldspars are present).	Faint PDFs are present in multiple quartz grains.	
AL12	7A	345.2	Medium-grained granite consisting of numerous quartz grains, feldspars (mostly twinned K-feldspar) in large part turned to sericite, and micas (mostly chlorite and sericite) as well as accessory rutile tourmaline and unidentified anhedral opaques. Sample is highly altered.	PDFs are common in the quartz grains present in this sample.	
AL13	7A	349.2	A thin section could not be prepared because sample was not lithified.		
AL14	7A	350.6	Suevite consisting mostly of crushed clasts (that partially conserved previous structure) of fine and medium grained metagreywacke and phyllite. Few melt particles (brown sub-rounded) are also present.	Quartz grains rarely display PDFs.	
AL15	7A	353.7	Very fine-grained, slightly mylonized shale, with few narrow, somewhat darker bands (possibly due to higher contents of graphite).	No shock metamorphic effects were observed.	
AL18	7A	363.6	Similar to sample AL08 and AL41.	Shock metamorphic effects are especially common within grains embedded within matrix.	
AL21	7A	370.7	Medium-grained granite consisting of numerous quartz grains, feldspars (mostly twinned K-feldspar) in large part turned to sericite, and micas (mostly chlorite and sericite), as well as accessory rutile tourmaline and unidentified anhedral opaques. Sample is in the early stage of mylonitization (some of the sericite and chlorite is oriented) and there are elongated opaque-rich pockets present.	Up to two sets of PDFs in a grain were observed.	

AL22	7A	377	Melt-rich suevite without any lithic-clasts. Matrix is composed mostly of melt particles of various sizes (from few tens mm to few um) and of clasts of single grains. Significant amount of calcite is present.	Some grains do not display any signs of shock metamorphism, while others are highly shocked (especially ones being single clasts embedded within matrix).
AL24	7A	383.2	Suevite with a large variety of lithic and mineral clasts including: metagreywacke, slate, phyllite, and quartz and feldspar grain clasts within very fine-grained matrix. Some of the lithic clasts are fully or partially isotropized (probably due to heating during the impact event), and often they have rounded outline.	Up to two sets of PDFs in a grain were observed.
AL25	7A	383.4	Highly shock-heated medium-grained, mylonitized greywacke with locally significant amount of opaques (possibly graphite) present.	Some grains contain very short PDFs.
AL26	7A	387.5	Monomictic breccia composed of fine-grained, mylonitized greywacke with large clasts present. The fine-grained matrix is composed of quartz, feldspar, and micas (mostly sericite and chlorite).	Grains are too small to observe PDFs. Some of the clasts or fragments of clasts are isotropized.
AL28	7A	389.1	Coarse-grained, partially mylonitized greywacke composed of matrix of quartz, feldspar, various micas (sericite and chlorite), as well as quartz and feldspar porphyroclasts. Sample is highly altered (although some not fully sericitized feldspars are present). Highly altered, alteration phases were probably heated during the impact event, and now are in a form of amorphous or microcrystalline material. Very similar to sample AL 30.	Small, short PDFs are observed in some grains.
AL29	7A	390.1	Very fine-grained, not mylonitized greywacke with high amount of graphite present.	No shock effects are observed (possibly due to too small size of the grains).
AL30	7A	392.1	Sample similar to AL 28.	Faint, short PDFs are observed.
AL33	7A	403.9	Fine-grained suevite with small dispersed melt clasts and few small lithic clasts (of banned phyllite), most clasts are minerals (quartz and feldspar).	PDFs were not observed.
AL37	7A	405.7	Slightly mylonitized medium-grained greywacke composed of a matrix of quartz, feldspar, various micas (sericite and chlorite), as well as quartz and feldspar porphyroclasts. Sample is relatively altered and includes significant amount of opaque material (probably graphite).	Some grains have short and relatively faint PDFs present.
AL41	7A	355.5	Medium to coarse-grained slightly mylonitized metagraywacke dominated by large quartz and feldspar clasts in a fine-grained matrix of phyllosilicates, quartz, feldspars, and opaques (possibly graphite). Similar to sample AL 45.	Large fraction of the quartz grains include PDFs.
AL42	7A	385.2	Very similar to sample AL 22.	Rare and faint PDFs are present.
AL43	7A	398.3	Strongly mylonitized medium-grained graphitic greywacke. It is composed of: large recrystallized quartz and feldspar clasts in a fine-grained matrix of mostly phyllosilicates (oriented), but also quartz, feldspars and opaques.	No PDFs (or other signs of shock metamorphism) are observed.
AL44	7A	407.9	Sample similar to AL 08 and AL 18.	Some quartz grains present in the matrix include PDFs.
AL45	7A	378.6	Similar to sample AL 41.	Rare grains include PDFs.

5.6. Discussion

5.6.1. Possible explanations of the obtained data

There are multiple explanations for the measured $^{10}\text{Be}/^9\text{Be}$ ratios of the samples above the blank value: 1) laboratory contamination, 2) contamination introduced during drilling, 3) introduction of the ^{10}Be by meteoric water after crater formation, and 4) surface exposure of the clasts prior to the Bosumtwi crater formation. In the following section of the paper we will discuss and evaluate their validity in explaining our data.

5.6.1.1. Laboratory contamination

If isotopic values measured are as close to the blank value as ones in this study, it is especially easy to introduce contamination during the sample processing in the laboratory. However, explaining the increased $^{10}\text{Be}/^9\text{Be}$ ratios in samples AL25 and AL41 by laboratory contamination seems to be very unlikely. First, the samples with high ratios were processed in different groups, excluding a single source of contamination (e.g., a contaminated reactant or an error during the sample preparation). Additionally, samples with the highest (e.g., AL41) and lowest (e.g., AL07) $^{10}\text{Be}/^9\text{Be}$ ratios were processed and measured together. Second, as no foreign samples with high $^{10}\text{Be}/^9\text{Be}$ ratios were processed together with our samples (except standards that were prepared separately), there is no obvious source of possible contamination. And finally, one of the samples with elevated $^{10}\text{Be}/^9\text{Be}$ ratio (AL41) was processed twice, each time giving the same (within 2σ) result. More importantly, the second measurement (AL41b), with a lower amount of ^9Be carrier, gave a higher ^{10}Be signal than during the first measurement (AL41a) with higher amount of carrier, confirming that the increased ^{10}Be signal comes from the sample, not from the carrier. All of those observations show that sample preparation method failure is an unlikely explanation of the obtained data.

5.6.1.2. Sample contamination during drill cores recovery

As mentioned before, ^{10}Be is mostly produced by the spallation of oxygen and nitrogen in the atmosphere at the rate dependent on the altitude, latitude, variations of the strength of magnetic field with time (Dunai 2010), at present on average amounting to $\sim 1 \cdot 10^6$ at $\text{cm}^{-2} \text{ yr}^{-1}$ (Gosse and Philips 2001). Because of that its concentration is high in rain water and can vary between $1 \cdot 10^3$ at/g up to even $\sim 1 \cdot 10^5$ at/g (Brown et al. 1992, Graham et al. 2003, Heikkilä et al. 2008, Willenbring and Blanckenburg 2010), and in surface waters can be up to 3200 at/g (Brown et al. 1992, Willenbring and Blanckenburg 2010). However, the ^{10}Be concentration in most surface waters is much lower and strongly dependent on many variables such as the chemical properties and history of the water. In most terrestrial surface conditions, beryllium has a tendency to strongly adhere to soil grains: the partition coefficient is $\sim 10^5$ mL/g at $\text{pH} > 6$ (but is much less in acidic conditions) (You et al. 1989). Some ^{10}Be can be also incorporated into clays, organic matter, or oxyhydroxides (e.g., Barg et al. 1997).

As a combined ^{10}Be signal from the *in situ* and meteoric ^{10}Be was measured in this study, contamination of the samples might have also occurred during drilling (from the lake water) or initial sample storage in Ghana (from rain water falling on the samples). If this is true, we could expect that entire sections of the core (or rather entire boxes with samples) should be affected by ^{10}Be contamination in a similar way. However, this is not the case in our dataset. Samples characterized by the highest $^{10}\text{Be}/^9\text{Be}$ ratios are often located very close in the drill core to samples with very low or average $^{10}\text{Be}/^9\text{Be}$ ratio. For example, sample AL41, having the highest ratio measured in this study, is located only 1.8 m from sample AL15 with one of the lowest measured ratios. Both samples were stored in the same sample box. Even more extreme is the example of sample AL25 with $^{10}\text{Be}/^9\text{Be}$ ratio of $(12.2 \pm 1.5) \cdot 10^{-15}$, while sample AL24, located only 0.2 meters from sample AL25, has $^{10}\text{Be}/^9\text{Be}$ ratio of $(6.5 \pm 0.9) \cdot 10^{-15}$. Additionally, the breccias should be much more affected by this process (due to much more surface area allowing beryllium to adhere to the grains) than clasts. However, this is not the case in our dataset (Table 5.1, Figure 5.4).

5.6.1.3. Introducing ^{10}Be by interaction with surface water

^{10}Be present in the measured samples could also come from the meteoric water that might have infiltrated the fallback impactite layer soon after the crater was formed. The Bosumtwi crater is currently located within a humid climate zone, where the average annual rainfall varies from 1380 to 1550 mm yr⁻¹ (Turner et al. 1996). Detailed research of the paleoclimate at this site shows that the Bosumtwi area was most probably relatively wet for most of its history (e.g., Shanahan et al. 2012), suggesting that the crater should have been filled with water soon after its formation. As Bosumtwi is a closed basin with limited amount of the ground-water inflow into the lake, most of the water-balance models suggest that the main source of water within Bosumtwi Lake is rainfall (e.g., Turner et al. 1996).

In order to test the meteoric-derived lake water contamination hypothesis, three samples collected close to the lake sediment-impactite contact within drill core LB-08A were analyzed. They came from depths of 239.5 m, 242.1 m, and 243.4 m blf, respectively, while the lake sediments-impactite contact was at an estimated depth of 235.6 m. It was impossible to collect samples closer to the contact because that part of the core was not available. Results show (Figure 5.2) that, even though there seems to be a slight decrease of the detected ^{10}Be signal with increasing depth below the contact, all obtained results are the same within the 2σ error (and even 1σ error). Additionally, all measured values are within the $^{10}\text{Be}/^9\text{Be}$ ratio of the process blanks used in this study.

Even more importantly, the measurement of sample AL07 from the drill core LB-07A argues against the hypothesis of contamination introduced by interaction with surface waters. This sample is collected from a depth of 333.7 m, just 0.3 m below the lake sediment-impactite contact, so if contamination occurred it should have been heavily affected. Additionally, sample AL07 is a monomictic breccia, characterized by a high surface area, prone to adsorbing ^{10}Be on the surface of grains within this sample (You et al. 1989, Shen et al. 2004, Graly et al. 2010). This suggests that if fluids with elevated ^{10}Be contents reached this depth, it is reasonable to expect that sample AL07 would have an elevated $^{10}\text{Be}/^9\text{Be}$ ratio.

The lack of the ^{10}Be signal only 0.3 m from the lake sediments-impactite contact could be potentially explained by the hypothesis that the top 0.3 m of impactite layer was extremely efficient in adsorption of the ^{10}Be , so that none of this element managed to reach depth of 0.3 meters. However, the measured depth profiles of ^{10}Be within soil and regolith (e.g., Graly et al. 2010 and references within) argue against this explanation. The second possibility is that the impactite layer was separated efficiently from the surface water influence. Initially, the separation could have been provided by the fallback layer: a ~30 cm thick layer consisting of “accretionary lapilli, microtektite-like glass spherules, and shocked quartz grains” retrieved from LB-05 core drilled within the Bosumtwi impact structure (Koeberl et al. 2007b). A similar layer was probably present on the entire crater floor, apparently creating an efficient barrier between lake and impactite deposits. Later on, this separation could have been increased by the thick layer of lake sediments being deposited.

The lack of a significant amount of percolation into the top-most layer of impactites does not mean that there was no contact between surface water and impact-affected rocks. In fact, Karikari et al. (2007) as well as Petersen et al. (2007) found evidence supporting the existence of a hydrothermal system within Bosumtwi crater. Surface water could have penetrated the impactite layer through cracks within the fallback layer: if cracks were large enough to limit the particle-water interaction (and/or chemical properties of water allowed for beryllium to stay in solution), then some amount of ^{10}Be could have been prevented from adhering on the surface of grains located at low depth and transferred down the impactite section. In this case we could expect an increased ^{10}Be signal along the fractures, and that breccias or suevites would be more affected than clasts (due to their higher surface area). However, the $^{10}\text{Be}/^9\text{Be}$ ratio measured in samples AL24 and AL25 located only 0.2 m from each other does not support this hypothesis, because sample AL24 is a suevite (with a high surface area allowing for preferential ^{10}Be adsorption), which is characterized by a low ^{10}Be contents, whereas AL25 is a greywacke clast with a high ^{10}Be contents.

5.6.1.4. Increased ^{10}Be signal as a result of the surface exposure of the clasts prior to the Bosumtwi crater formation

After excluding alternative hypotheses, the most probable explanation of the observed elevated ^{10}Be signal in samples AL25 and AL 41 seems to be their near-surface exposure prior to the Bosumtwi crater formation. However, the exact determination of the clast's depth of origin within the pre-impact target material is not possible because of the following reasons. First, the total ^{10}Be contents generally decrease with depth within weathering profile, although some profiles can have a more complex shape (Graly et al. 2010). No data about deep profiles within soils in the proximity of the Bosumtwi crater are available; the only data are from shallow profiles less than one meter deep (Serefiddin et al. 2007). Potentially comparable, several-meters deep profiles are available from the Ivory Coast and Mali (Barg et al. 1997). However, because all of the available data are based on the studies of the fine fraction of the soils, not clasts within them; the data is not easily transferable. It is reasonable to expect that the average ^{10}Be contents of the clasts within soil profiles (or saprolite) are lower than that within the finer fraction of the soil (Graly et al. 2010), but it is very hard to properly assess the expected ^{10}Be concentration within a clast.

As ^{10}Be is a radionuclide with a half-life of 1.386 ± 0.016 Ma (Chemeleff et al. 2010) and the Bosumtwi impact crater is 1.07 million years old (Koeberl et al. 1997), it was necessary to recalculate concentrations of ^{10}Be in the AL25 and AL41 samples for the time when the impact happened. The decay corrected values are $(0.37 \pm 0.23) \cdot 10^6$ at/g for sample AL41b and $(0.48 \pm 0.28) \cdot 10^6$ at/g for sample AL25. Based on those values, using the analogous tropical oxic soils of the Ivory Coast (Barg et al. 1997) assuming the similar uniformly decreasing ^{10}Be profile within the Bosumtwi crater target rocks sequence, and assuming that values within average soil and clasts is similar, we can estimate the approximate depth of clast origin to be between 20 m and 30 m below the surface for both samples.

5.6.2. Inferences for crater-forming mechanism

The degree of mixing of the target material during the impact cratering process has been studied only to a very limited extent. Within the Kärddla structure, a 4-km-diameter, well-preserved 455 Ma crater formed within a shallow sea, the impactites are very clearly stratified (Puura et al. 2004). The limestone that was forming a top-most 25 meters layer of sedimentary target rocks is present only within the top 40 meters of impactite strata that was interpreted to be a sedimentary slump and resurge breccia (Puura et al. 2004). This suggests that mixing of the target material during the impact cratering process was limited by the interaction with the layer of water (Melosh 1989, Ormö and Lindstrom 2000, Ormö et al. 2010, Wünnemann et al. 2010).

The mechanisms leading to the concentration of the target surface layer in resurge breccia of submarine craters are not present in subaerial craters. The research of the small subaerial impact crater Tswaing (1.13 km in diameter, 0.22 Ma old crater in South Africa) showed that about 2% of the thin layer of diatomite, siltstone, and shale, originally forming a few meters thick layer (<20 m) on the surface of the target rocks, was incorporated into the “sandy” impact breccia present in this crater (Reimold et al. 1992). However, no information about the arrangement of the surface component within the drill core was provided, and because the drill core is no longer available, it is impossible to perform a more detailed study on this topic.

Results of our study suggest that in case of the Bosumtwi crater it is possible to find clasts that were located relatively close to the surface prior to the impact and that they are not concentrated within top layer of impactites (they were found at different depths within the breccia). Samples AL25 and AL41 are characterized by a different ^{10}Be concentration than the other samples located in their proximity. This is consistent with the relatively efficient mixing of the material during the impact cratering process; otherwise we should expect to find other clasts enriched in ^{10}Be close by. Two samples, AL22 (suevite) and AL45 (granite), with ^{10}Be concentration different from the process blank on 2σ level, are located close to each other at depths of 377.0 m and 378.6 m (and close to the AL41). If we assume that those samples truly include some ^{10}Be , then they could represent a poorly mixed layer of

clast-rich suevite formed from material that was originally located close to pre-impact target surface or a material slumped during the modification stage.

In the case of the Bosumtwi crater, if the entire surface layer (about 25 m thickness) was perfectly mixed in the transient crater cavity, it would form up to ~5% of the crater fill material. In reality, this percentage is probably lower due to: 1) the tendency of the surface layer to be removed from the crater in the form of ejecta (Artemieva 2000, including tektites Pal et al. 1982, Serefiddin et al. 2007); 2) being vaporized/melted during the impact process (Melosh 1989), thus decreasing the potential number of clasts that can survive impact and be incorporated within crater-filling breccias; and 3) the surface layer being more weathered and less resistant to mechanical stress. Of course if mixing was not close to perfect, there can be some layers within the drill core characterized by a much higher percentage of the surface material. The particles with ^{10}Be contents suggestive of their origin close to the surface were detected on two different depths within the drill core (AL41: 355.5 m and AL25: 383.4 m). This shows that the surface component within the Bosumtwi crater drill core was not concentrated within the top layer of the fallback breccia, as was the case at Kärddla (Puura et al. 2004).

Both of the clasts (AL25 and AL41) with elevated ^{10}Be contents are greywackes. This is consistent with the predictions based on the characteristics of the geology in the proximity of Bosumtwi crater (e.g., Koeberl and Reimold 2005, Karikari et al. 2007, Losiak et al. 2013). Most of the rocks present at the surface are metagreywacke (Koeberl and Reimold 2005), with only ~2% addition of a granitoid component (Reimold et al. 1998).

5.6.2.1. Implications to formation of the crater-related pitted materials on Mars

Our study has some implications to research of Martian impact craters. Recently, Mougini-Mark et al. (2003) identified a new type of an impact ejecta and crater-fill facies on Mars: a thin layer of ejected materials densely covered with relatively small pits (~10 m to 3 km in diameter) (Tornabene et al. 2012). Boyce et al. (2012) proposed a numerical model of the pits formation by the explosive degassing of water from the water-bearing, impact melt-

rich breccia. However, this model works only if the suevite is composed of very well mixed target material (Boyce et al. 2012). Our research supports this model by demonstrating that material coming from different depths within the target rocks is well mixed within the top-most suevite layer.

5.7. Conclusions

We have conducted a study on the material from the drill cores from the Bosumtwi impact crater to determine the extent of mixing of target rocks during crater formation in respect to the crater-filling breccia. We have detected a ^{10}Be signal in two out of 29 samples. After excluding other possibilities that may explain the elevated ^{10}Be signal, we conclude that the elevated content of ^{10}Be within two greywacke clasts (AL25 and AL41), collected from the impactites from Bosumtwi impact drill core LB-07A, is most probably due to a pre-impact origin of those clasts in a layer of the target rocks close to the surface (20-30 meters).

The location of the samples with ^{10}Be concentrations suggestive of their surface origin within the drill core suggests efficient mixing of material forming in-crater breccia during the impact cratering process. This supports observations from the experimental and numerical modeling studies that in-crater breccia within submarine and subaerial craters form differently (e.g., Ormö et al. 2010).

The lack of a ^{10}Be signal within the rocks located very close to the lake sediments-impactites suggests that infiltration of the meteoric water within the crater floor was very limited. The impactites were separated relatively efficiently from the surface water influence probably by the topmost fallback layer described by Koeberl et al. (2007b). A similar layer was probably present on the entire crater floor, apparently creating a barrier between lake and impactite deposits. Later on, this separation could have been increased by the thick layer of lake sediments being deposited. This may suggest that infiltration of meteoric water within a crater takes place not through the aerial pore-space infiltration, but rather through a localized system of fractures.

Acknowledgments:

We acknowledge funding from the University of Vienna doctoral school IK-1045 and the Austrian Science Foundation grant P21821-N19. We are grateful to Ronald Conze for helping assistance during the sampling of the Bosumtwi cores in Potsdam core repository and to Peter Steier for performing one of the measurements. We thank Matthew Huber for proofreading the manuscript.

References

- Artemieva N.A. 2000. Tektite Origin in Oblique Impacts: Numerical Modeling of the Initial Stage. In: *Impacts in Precambrian Shields*, edited by Plado J. and Pesonen L. J. Heidelberg-Berlin: Springer. pp. 257–276.
- Auer M., Kutschera W., Priller A., Wagenbach D., Wallner A., and Wild E.M. 2007. Measurement of ^{26}Al for atmospheric and climate research and the potential of $^{26}\text{Al}/^{10}\text{Be}$ ratios. *Nuclear Instruments and Methods in Physics Research Section B* 259: 595–599.
- Auer M. 2007. Applications of ^{26}Al in Atmospheric Research. Ph.D. Thesis. University of Vienna, Vienna, Austria.
- Barg E., Lal D., Pavich M.J., Caffee M.W., and Southon J.R. 1997. Beryllium geochemistry in soils; evaluation of $^{10}\text{Be}/^9\text{Be}$ ratios in authigenic minerals as a basis for age models. *Chemical Geology* 140: 237–258.
- Boyce J.M, Wilson L., Mougini-Mark P.J., Hamilton C.W., and Tornabene L.L. 2012. Origin of small pits in martian impact craters. *Icarus* 221: 262–275.
- Brown E.T., Edmond J.M., Raisbeck G.M. Boursin D., Yiou F., and Measures. C. 1992. Beryllium isotope geochemistry in tropical river basins. *Geochimica Cosmochimica Acta* 56: 1607–1624.
- Chemeleff J., von Blanckenburg F., Kossert K., and Jakob D. 2010. Determination of the ^{10}Be half-life by multicollector ICP-MS and liquid scintillation counting. *Nuclear Instruments and Methods in Physics Research Section B* 268: 192–199.
- Coney L., Gibson R.L., Reimold W.U., and Koeberl C. 2007. Lithostratigraphic and petrographic analysis of ICDP drill core LB-07A, Bosumtwi impact structure, Ghana. *Meteoritics & Planetary Science* 42: 569–589.
- Dunai T.J. 2010. *Cosmogenic Nuclides, Principles, Concepts and Applications in the Earth Surface Sciences*. New York, Cambridge: Cambridge University Press: 187 p.

- Engelhardt W.v., Berthold C., Wenzel T., and Dehner T. 2005. Chemistry, small-scale inhomogeneity, and formation of moldavites as condensates from sands vaporized by the Ries impact. *Geochimica et Cosmochimica Acta* 69: 5611–5626.
- Ferrière L., Koeberl C., and Reimold W.U. 2007a. Drill core LB-08A, Bosumtwi impact structure, Ghana: Petrographic and shock metamorphic studies of material from the central uplift. *Meteoritics & Planetary Science* 42: 611–633.
- Ferrière L., Koeberl C., and Reimold W.U. 2007b. Drill core LB-08A, Bosumtwi impact structure, Ghana: Geochemistry of fallback breccia and basement samples from the central uplift. *Meteoritics & Planetary Science* 42: 689–708.
- Ferrière L., Koeberl C., Ivanov B., and Reimold W.U. 2008. Shock metamorphism of Bosumtwi impact crater rocks, shock attenuation, and uplift formation. *Science* 322: 1678–81.
- Ferrière L., Koeberl C., Reimold W.U., Hecht L., and Bartosova K. 2009. The origin of „toasted“ quartz in impactites revisited (abstract #1751). *40th Lunar Planetary Science Conference*.
- Ferrière L., Koeberl C., Brandstätter F., and Mader D. 2010. Geochemistry of basement rocks and impact breccias from the central uplift of the Bosumtwi crater, Ghana - Comparison of proximal and distal impactites. In *Large Meteorite Impacts and Planetary Evolution IV*, edited by Gibson R. L. and Reimold W. U. Boulder: *Geological Society of America, Special Paper* 465: 443–469.
- Feybesse J., Billa, M., Guerrot C., Duguey E., Lescuyer J., Milesi J., and Bouchot V. 2006. The paleoproterozoic Ghanaian province: Geodynamic model and ore controls, including regional stress modeling. *Precambrian Research* 149: 149–196.
- Franklin C. 2007. *Statistics The art and science of learning from data*. Upper Saddle River: Pearson Prentice Hall. 693 p.
- Gosse J. C., and Phillips F.M. 2001. Terrestrial in situ cosmogenic nuclides: theory and application, *Quaternary Science Reviews* 20: 1475–1560.

- Graham I., Ditchburn R., and Barry B. 2003. Atmospheric deposition of ^7Be and ^{10}Be in New Zealand rain (1996–98). *Geochimica Cosmochimica Acta* 67: 361–373.
- Graly J.A., Bierman P.R., Reusser L.J., and Pavich M.J. 2010. Meteoric ^{10}Be in soil profiles – A global meta-analysis. *Geochimica et Cosmochimica Acta* 74: 6814–6829.
- Heikkilä U., Beer J., and Alfimov V. 2008. Beryllium-10 and Beryllium-7 in precipitation in Dübendorf (440 m) and at Jungfraujoch (3580 m), Switzerland (1998-2005). *Journal of Geophysical Research* 113: D11104, doi: 10.1029/2007JD009160.
- Hofmann H.J., Beer, J., Bonani G., von Gunten H.R., Raman S., Suter M., Walker R.L., Walfli W. and Zimmermann D. 1987. ^{10}Be : half life and AMS-standards. *Nuclear Instruments and Methods in Physics Research Section B* 29: 32–36.
- Jones W.B. 1985. Chemical analyses of Bosumtwi crater target rocks compared with the Ivory Coast tektites. *Geochimica et Cosmochimica Acta* 48: 2569–2576.
- Jones W.B., Bacon M., and Hastings D.A. 1981. The Lake Bosumtwi impact crater, Ghana. *Geological Society of America Bulletin* 92: 342–349.
- Karikari F., Ferriere L., Koeberl C., Reimold W.U., and Mader D. 2007. Petrography, geochemistry, and alteration of country rocks from the Bosumtwi impact structure, Ghana. *Meteoritics & Planetary Science* 42: 513–540.
- Koeberl C. 1986. Geochemistry of tektites and impact glasses. *Annual Review of Earth and Planetary Sciences*. 14: 323–350.
- Koeberl C. 1994. Tektite origin by hypervelocity asteroidal or cometary impact: target rocks, source craters, and mechanisms. In *Large Meteorite Impacts and Planetary Evolution* edited by Dressler B. O., Grieve R. A. F., and Sharpton V. L. *Geological Society of America Special Paper* 293: 133–151.
- Koeberl C., Bottomley R., Glass B., and Storzer D. 1997. Geochemistry and age of Ivory Coast tektites and microtektites. *Geochimica et Cosmochimica Acta* 61: 1745–1772.
- Koeberl C., and Reimold W.U. 2005. Bosumtwi impact crater, Ghana (West Africa): An updated and revised geological map, with explanations. *Jahrbuch der Geologischen*

- Bundesanstalt, Wien (Yearbook of the Austrian Geological Survey)* 145: 31–70 (+1 map, 1:50,000).
- Koeberl C., Milkereit B., Overpeck J.T., Scholz C.A., Amoako P.Y.O., Boamah D., Danuor S. K., Karp T., Kueck J., Hecky R.E., King J., and Peck J.A. 2007a. An international and multidisciplinary drilling project into a young complex impact structure: The 2004 ICDP Bosumtwi impact crater, Ghana, drilling project—An overview. *Meteoritics & Planetary Science* 42: 483–511.
- Koeberl C., Brandstaetter F., Glass B.P., Hecht L., Mader D., and Reimold W.U. 2007b. Uppermost impact fallback layer in the Bosumtwi crater (Ghana): Mineralogy, geochemistry, and comparison with Ivory Coast tektites. *Meteoritics & Planetary Science* 42: 709–729.
- Korkisch J. 1989. Handbook of ion exchange resins. Boca Raton: CRC Press. 352 p.
- Korschinek G., Bergmaier A., Faestermann T., Gerstmann U., Knie K., Rugel G., Wallner A., Dillmann I., Dollinger G., von Gostomski C.L., Kossert K., Maiti M., Poutivtsev M., and Remmert A. 2010. A new value for the half-life of ^{10}Be by Heavy-Ion Elastic Recoil Detection and liquid scintillation counting. *Nuclear Instruments and Methods in Physics Research B* 268: 187–191.
- Kutschera W., Collon P., Friedmann H., Golser R., Hille P., Priller A., Rom W., Steier P., Tagesen S., Wallner A., Wild E.M., and Winkler G. 1997. VERA: A new AMS facility in Vienna. *Nuclear Instruments and Methods in Physics Research B* 123: 47–50.
- Leube A., Hirdes W., Maur R., and Kesse G.O. 1990. The early Proterozoic Birimian Supergroup of Ghana and some aspects of its associated gold mineralization. *Precambrian Research* 46: 139–165.
- Losiak A., Schulz T., Buchwaldt R., and Koeberl C. 2013 (in review). Petrology, major and trace element geochemistry, geochronology, and isotopic composition of granitic intrusions from the vicinity of the Bosumtwi impact crater, Ghana. *Lithos*.

- Ma P., Aggrey K.A., Onzola C.T., Chnabel C.S., Icola P.D.E.N., Erzog G.F.H., Asson J.T.W., and Lass B.P.G. 2004. Beryllium-10 in Australasian tektites: constraints on the location of the source crater. *Geochimica et Cosmochimica Acta* 68: 3883–3896.
- Martschini M. 2008. ^{10}Be - ^{10}B isobar separation with a degrader foil: Implementation and testing of an optimized ion-optical setup for AMS of ^{10}Be . Diploma Thesis, University Vienna, Vienna, Austria.
- Melosh H.J. 1989. *Impact Cratering*. New York, Oxford: Oxford University Press, Clarendon Press.
- Merchel S., and Herpers U. 1999. An update on radiochemical separation techniques for the determination of long-lived radionuclides via accelerator mass spectrometry. *Radiochimica Acta* 84: 215–219.
- Michlmayr L. 2007. Isobar separation with post-stripping for the measurement of cosmogenic ^{10}Be at VERA. Diploma Thesis, University Vienna, Vienna, Austria.
- Moon P.A., and Mason D. 1967. The geology of 1/4° field sheets nos. 129 and 131, Bompata S.W. and N.W. *Ghana Geological Survey Bulletin* 31: 1–51.
- Mouginis-Mark P., Boyce J.M., Hamilton V.E., and Anderson F.S. 2003. A very young, large impact crater on Mars (abstract #3004). Sixth International Conference on Mars.
- Nishiizumi K., Imamura M., Caffee M.W., Southon J.R., Finkel R.C., and McAninch J. 2007. Absolute calibration of ^{10}Be AMS standards. *Nuclear Instruments and Method in Physics Research B* 258: 403–413.
- Ormö J., and Lindstrom M. 2000. When a cosmic impact strikes the sea bed. *Geological Magazine* 137: 67–80.
- Ormö J., Lepinette A., Sturkell E., Lindstrom M., Housen K.R., Holsapple K.A. 2010. Water resurge at marine-target impact craters analyzed with a combination of low-velocity impact experiments and numerical simulations. In *Large Meteorite Impacts and Planetary Evolution IV*, edited by Gibson R.L. and Reimold W.U. Boulder: *Geological Society of America Special Paper* 465: 81–101.

- Pal D.K., Tuniz C., Moniot R.K., Kruse T.H., and Herzog G.F. 1982. Beryllium-10 in Australasian tektites: Evidence for a sedimentary precursor. *Science* 218: 787–789.
- Pavich M.J., Brown L., Valette-Silver J.N., Klein J., and Middleton R. 1985. ^{10}Be analysis of a Quaternary weathering profile in the Virginia Piedmont. *Geology* 13: 39–41.
- Petersen M.T., Newsom H.E., Nelson M.J., and Moore D.M. 2007. Hydrothermal alteration in the Bosumtwi impact structure: Evidence from 2M1-muscovite, alteration veins, and fracture fillings. *Meteoritics & Planetary Science* 42: 655–666.
- Puura V., Huber H., Kirs J., Karki A., Suuroja K., Kirsimäe K., Kivisilla J., Kleesment A., Kõnsa M., Preeden U., Suuroja S., and Koeberl C. 2004. Geology, petrography, shock petrography, and geochemistry of impactites and target rocks from the Kärđla crater, Estonia. *Meteoritics & Planetary Science* 39: 425–451.
- Reimold W.U., Koeberl C., Partridge T.C., and Kerr S.J. 1992. Pretoria Saltpan crater: Impact origin confirmed. *Geology* 20: 1079–1082.
- Reimold W.U., Brandt D., and Koeberl C. 1998. Detailed structural analysis of the rim of a large, complex impact crater: Bosumtwi crater, Ghana. *Geology* 26: 543–546.
- Serefiddin F., Herzog G.F., and Koeberl C. 2007. Beryllium-10 concentrations of tektites from the Ivory Coast and from Central Europe: Evidence for near-surface residence of precursor materials. *Geochimica et Cosmochimica Acta* 71: 1574–1582.
- Shanahan T.M., Beck J.W., Overpeck J.T., McKay N.P., Pigati J.S., Peck J.A., Scholz C.A., Heil C.W.Jr., and King J. 2012. Late Quaternary sedimentological and climate changes at Lake Bosumtwi Ghana: New constraints from laminae analysis and radiocarbon age modeling. *Palaeogeography, Palaeoclimatology, Palaeoecology* 361–362: 49–60.
- Shen C.D., Beer J., Kubik P.W., Suter M., Borkovec M., and Liu T.S. 2004. Grain size distribution, ^{10}Be content and magnetic susceptibility of micrometer-nanometer loess materials. *Nuclear Instruments and Methods in Physics Research B* 223–224: 613–617.

- Son T.H., and Koeberl C. 2007. Chemical variation in Lonar impact glasses and impactites. *GFF* 129: 161–176.
- Steier P., Golser R., Kutschera W., Priller A., Vockenhuber C., and Winkle S. 2004. VERA, an AMS facility for “all” isotopes. *Nuclear Instruments and Methods in Physics Research B* 223–224: 67–71.
- Turner B.F., Gardner L.R., and Sharp W.E. 1996. The hydrology of Lake Bosumtwi a climate sensitive lake in Ghana, West Africa. *Journal of Hydrology* 183: 243–261.
- Tornabene L.L., Osinski G. R., McEwen A. S., Boyce J. M., Bray VJ., Caudill C. M., Grant J.A., Hamilton C.W., Mattson S., and Mouginis-Mark P.J. 2012. Widespread crater-related pitted materials on Mars: Further evidence for the role of target volatiles during the impact process. *Icarus* 220: 348–368.
- Wasson J.T. 2003. Large aerial bursts: an important class of terrestrial accretionary events. *Astrobiology* 3: 163–179.
- Willenbring J.K., and von Blanckenburg F. 2010. Meteoric cosmogenic Beryllium-10 adsorbed to river sediment and soil: applications for Earth-surface dynamics. *Earth-Science Reviews* 98: 105–122.
- Wünnemann K., Collins G.S., and Weiss R. 2010. Impact of a cosmic body into Earth's ocean and the generation of large tsunami waves: Insight from numerical modeling. *Reviews of Geophysics* 48: RG4006, doi:10.1029/2009RG000308.
- You C.-F., Lee T. and Li Y.-H. 1989. The partition of Be between soil and water. *Chemical Geology* 77: 105–118.

RECAPITULATION

Three research projects, performed as a part of the PhD studies at the Department of Litospheric Research, University of Vienna, allowed to further improve our understanding of the impact cratering process on the example of the Bosumtwi crater (including better characterization of the geological context of this impact structure):

- **“Petrology, major and trace element geochemistry, geochronology, and isotopic composition of granitic intrusions from the vicinity of the Bosumtwi impact crater, Ghana”:**
 - We provided a detailed characterization of the relatively rare type of granitic intrusions formed within the Birimian Supergroup. This study can be used by the researchers studying the early evolution of the West African Craton.
 - The granitoids from the vicinity of the Bosumtwi crater were formed between 2092 ± 6 Ma and 2098 ± 6 Ma.
 - Despite conclusions of the previous study on this topic, all analyzed intrusions are co-genetic and belong to the basin-type, late-stage granitoids.
 - The intrusions were probably formed as a result of anatexis of tonalites–trondhjemites–granodiorites (or rocks derived from them) at relatively low pressure and temperature.
 - We produced a revised version of the geological map of the Bosumtwi crater area. This map can be used by all researches interested in studying the Bosumtwi structure, as it provides a more accurate description of the geological context of the target rocks into which the Bosumtwi crater was emplaced.
- **“Spatial characterization of planar deformation features in quartz and implications for understanding shock wave propagation at the grain scale”:**
 - We investigated the spatial relations between a statistically significant number of grains (278) and 409 planar deformation features (PDFs) present within a

given area ($\sim 35 \text{ mm}^2$) of a single multi-grain, multi-mineral thin section. This study can be of interest to researchers interested in shock wave propagation within geological materials.

- An innovative method of research (analyzing properties of all quartz grains and PDFs within a given area) and data analysis (geographical information systems methods) allowed to make two new observations:
 - Some orientations of planar deformation features tend to develop in specific locations within a studied sample forming clusters of grains with specific orientation of PDF present.
 - Some orientations of planar deformation features tend to have different physical properties than other ones.
- We also provide a new tool (PDF indexing program) to the community.
- **¹⁰Be content in clasts from fallout suevitic breccia in drill cores from the Bosumtwi impact crater, Ghana: Clues to pre-impact target distribution**:
 - We analyzed rocks from the Bosumtwi crater drill cores for the presence of the cosmogenic radionuclide ¹⁰Be to determine the extent to which target rocks of various depths were mixed during the formation of the crater-filling breccia, and also to detect meteoric water infiltration within the impactite layer. This study may be interesting to scientists working on the details of the late stages of the impact crater formation, as well as those studying post-impact modifications that craters are undergoing (including research of extra-terrestrial craters: e.g., on Mars).
 - Our results suggest that in case of aerial craters, the target material is well mixed before being incorporated into the in-crater breccias.
 - Additionally we have demonstrated that the infiltration of meteoric water within the crater floor was relatively limited in case of the Bosumtwi crater.
 - It is likely that water does not penetrate in-crater breccias in an aerial pore-space infiltration, but rather through a localized system of fractures.

APPENDIX

The appendix includes two papers co-authored by the author of this thesis that were published during the time of PhD studies at the Department of Lithospheric Research, University of Vienna:

- Huber M. S., Ferrière L., Losiak A., and Koeberl C. 2011. ANIE: A mathematical algorithm for automated indexing of planar deformation features in quartz grains. *Meteoritics and Planetary Science* 46: 1418–1424.
- Galiazzo M.A., Bazso A., Huber M.S., Losiak A., Dvorak R., and Koeberl C. 2013. A statistical dynamical study of meteorite impactors: a case study based on parameters derived from the Bosumtwi impact event. *Astronomische Nachrichten / Astronomical Notes* (accepted).



Report

ANIE: A mathematical algorithm for automated indexing of planar deformation features in quartz grains

Matthew S. HUBER^{1*}, Ludovic FERRIÈRE², Anna LOSIAK¹, and Christian KOEBERL^{1,2}

¹Department of Lithospheric Research, University of Vienna, Althanstrasse 14, A-1090 Vienna, Austria

²Natural History Museum, Burgring 7, A-1010 Vienna, Austria

*Corresponding author. E-mail: matthew.huber@univie.ac.at

(Received 12 January 2011; revision accepted 22 June 2011)

Abstract—Planar deformation features (PDFs) in quartz, one of the most commonly used diagnostic indicators of shock metamorphism, are planes of amorphous material that follow crystallographic orientations, and can thus be distinguished from non-shock-induced fractures in quartz. The process of indexing data for PDFs from universal-stage measurements has traditionally been performed using a manual graphical method, a time-consuming process in which errors can easily be introduced. A mathematical method and computer algorithm, which we call the Automated Numerical Index Executor (ANIE) program for indexing PDFs, was produced, and is presented here. The ANIE program is more accurate and faster than the manual graphical determination of Miller–Bravais indices, as it allows control of the exact error used in the calculation and removal of human error from the process.

INTRODUCTION

The presence of planar deformation features (PDFs) in quartz grains has been used as one of the most reliable indicators of shock metamorphism for the confirmation of hypervelocity impact structures (see, e.g., French and Short 1968; Stöffler and Langenhorst 1994; Grieve et al. 1996; French 1998; French and Koeberl 2010 and references therein). PDFs have regularly spaced, thin, planar features generally oriented parallel to rational crystallographic planes (Fig. 1) and formed in quartz grains upon shock compression greater than approximately 5–10 GPa (see Stöffler and Langenhorst 1994 and references therein). As they develop along crystallographic planes, suspected planar features can be investigated (i.e., measured and indexed) to determine if they correspond to known planes that accommodate shock deformation (Engelhardt and Bertsch 1969; Stöffler and Langenhorst 1994; Ferrière et al. 2009). PDFs with specific crystallographic orientations are known to form in quartz at different shock pressures

(e.g., Hörz 1968; Müller and Défourneaux 1968; Huffman and Reimold 1996), so that peak shock pressure can be estimated for a given sample based on PDF orientations measurements (e.g., Robertson and Grieve 1977; Grieve et al. 1990; Dressler et al. 1998; Ferrière et al. 2008). The measurement of the orientations of suspected PDFs is possible using transmission electron microscopy (TEM; e.g., Goltrant et al. 1991; Trepmann and Spray 2006), a spindle stage (e.g., Bohor et al. 1987), or the universal-stage (U-stage) on a petrographic microscope (e.g., Engelhardt and Bertsch 1969; Langenhorst 2002; Ferrière et al. 2009). Nevertheless, a note of caution is necessary: determining if some planar features are true PDFs, especially if they are altered (e.g., in the form of planar fluid inclusion trails), is not possible based on only the determination of the crystallographic orientation of these features, because deformation of quartz crystals will often (but not exclusively) follow the rational crystallographic planes even if shock metamorphism is not involved. Thus, presentation of an orientation diagram alone is not

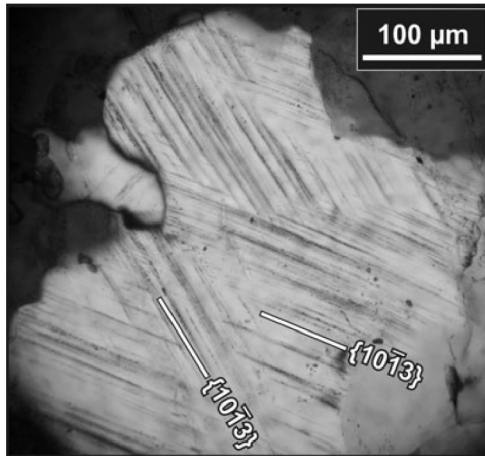


Fig. 1. Photomicrograph (crossed polars) of a quartz grain with two sets of planar deformation features (PDFs); both PDF sets with $\omega\{1013\}$ -equivalent orientations (sample from the Bosumtwi impact crater).

sufficient to confirm the presence of true PDFs. For such questionable features, TEM work remains necessary.

The most common and least expensive method of determining PDF orientations in quartz is the U-stage microscope analysis. According to the recent study by Ferrière et al. (2009), it is also the only technique that allows large, statistically significant data sets to be readily generated. However, the manual process of converting raw measurements from the U-stage to orientations of PDFs has traditionally been done using a graphical method based on a Wulff (equal-angle) stereonet and a stereographic projection template (see, e.g., Engelhardt and Bertsch 1969; Ferrière et al. 2009), and is rather time-consuming. It is also possible that manually determining the Miller-Bravais indices using the graphical method may introduce some additional errors to the data. Herein, for the first time, the mathematical basis for indexing PDFs is presented, along with an algorithm for indexing, named Automated Numerical Index Executor (ANIE), designed for use in Microsoft Excel (version 2007 and later). In addition, mathematically indexed PDFs from three samples, BOS (a meta-graywacke from the Bosumtwi impact crater), M8 (a biotite-gneiss from the Manson impact structure), and AUS (a sandstone from the Gosses Bluff impact structure) (see Ferrière et al. [2009] for more details on these samples) are compared with results obtained by the manual method (i.e., using the stereographic projection template) to demonstrate the veracity of our mathematical method.

MATHEMATICAL METHOD FOR DETERMINING CRYSTALLOGRAPHIC ORIENTATIONS OF PDFs

Previously, indexing PDFs has involved a graphical interface, as described in, e.g., Engelhardt and Bertsch (1969), Stöffler and Langenhorst (1994), and Ferrière et al. (2009). However, this method is, as mentioned above, time-consuming and somewhat imprecise, as it allows a certain “fudge factor” in the plotting of measurements on the stereonet, in the adjustment of the data, and in the actual reading of indices from the projected chart. All these inconveniences provided the motivation for a mathematical method to determine crystallographic orientations of PDFs.

The stereonet (or Wulff net) essentially represents a two-dimensional projection of a three-dimensional sphere. To determine PDF orientations using the stereonet, several steps must be followed. In the first step, the azimuth and inclination of the c -axis and poles perpendicular to planes of all PDFs in a given grain are plotted on a stereonet. Data are then adjusted by rotating the overlay by hand until the c -axis and a given pole lie on the same meridian (N-S great circle on the stereonet) to obtain the polar angle. Next, the c -axis is moved along the equatorial line of the stereonet to the center, and the poles perpendicular to planes of all PDFs are transformed along small circles by the same angle. Finally, the transformed data are compared with the stereographic projection template (STP) of PDFs in quartz, which displays the pole orientations of known PDF planes within a 5° envelope of measurement error. This last step is done by rotating the STP until all poles (or a maximum of them) fall into the circles of the STP (see, e.g., Engelhardt and Bertsch [1969]; Langenhorst [2002]; and/or Ferrière et al. [2009] for the detailed procedure). We describe here how all these graphical steps can be performed using mathematical calculations derived from spherical trigonometry (see Fig. 2).

The first step is to calculate the great circle distance between the c -axis and the pole to PDF plane, which corresponds to the so-called polar angle. This distance is obtained from the Law of Cosines for spherical triangles, and can be calculated using the following equation:

$$\cos(90 - \Psi) = \cos(90 - z) * \cos(90 - \Lambda) + \cos(90 - z) * \cos(90 - \Lambda) * \cos(\alpha - a) \quad (1)$$

where “ z ” is the measured c -axis inclination, “ α ” is the measured c -axis azimuth, “ Λ ” is the measured PDF inclination, “ a ” is the measured PDF azimuth, and “ Ψ ” is the polar angle of the PDF. Note that the center of the sphere would be measured at 90° , so that it is necessary for calculations to be taken as “90 minus measurement” (see Fig. 2). Therefore, the equation can be simplified as follows:

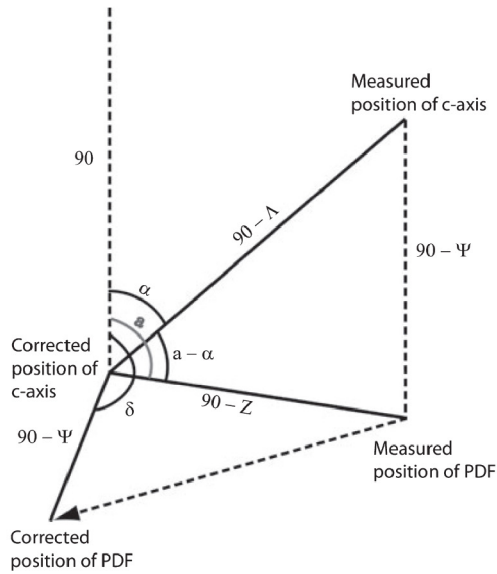


Fig. 2. Simplified representation of the process of indexing planar deformation features (PDFs) in quartz. The c -axis is measured, then moved to the center of a projected sphere; this operation is defined by a distance of “ $90-\Lambda$ ” and an angle of “ α .” The distance between the center of the projected sphere and the measured position of the pole to PDF plane is “ $90-z$,” and the angle is “ a .” There is a distance of “ $90-\Psi$ ” between the c -axis and the pole to PDF plane, which is constant before and after correction to the center. The pole to PDF plane is moved to a new position, which has an angle of “ δ .” The angle between the c -axis and the pole to PDF plane is “ $a-\alpha$.”

$$\sin \Psi = \sin z * \sin \Lambda + \sin z * \sin \Lambda * \cos(\alpha - a) \quad (2)$$

Then, the second step is to calculate the azimuth of the PDF as it would be if the c -axis were in the middle of the sphere. This is calculated from the Law of Sines for spherical triangles using the following equation:

$$\sin \delta / \sin(90 - z) = \sin(\alpha - a) / \sin(90 - \Psi) \quad (3)$$

which simplifies to the following equation:

$$\sin \delta = \sin(\alpha - a) * \cos z / \cos \Psi \quad (4)$$

where “ δ ” is the azimuthal angle of the PDF after correcting the c -axis to the center of the sphere. Importantly, the value of “ δ ” must be corrected to determine the exact azimuth of the PDF, as this equation will only result in an accurate value for half of a circle (owing to the fact that cosine is an even function). To find the exact value of “ δ ,” a determination of the proper quadrant is necessary. The value of “ δ ” does not

need adjustment if Equation 4 is positive and if $\sin(z) > \sin(\Psi) \times \sin(\Lambda)$. The value of “ δ ” should be adjusted by “ $\pi - \delta$ ” if either Equation 4 is negative or $\sin(z) < \sin(\Psi) \times \sin(\Lambda)$. In the case where Equation 4 is negative and $\sin(z) < \sin(\Psi) \times \sin(\Lambda)$, the value of “ δ ” should be adjusted by “ $2\pi + \delta$ ” to ensure that “ δ ” refers to the correct quadrant and can be properly compared with other measured PDF sets in the given grain.

After the inclination “ Ψ ” and azimuth “ δ ” of all PDFs have been calculated for a given grain, the next step is to calculate the great circle distance between the two PDFs being indexed, “ c ”; this can be calculated using the following equation:

$$\cos c = \cos \Psi_1 * \cos \Psi_2 + \cos \Psi_1 * \cos \Psi_2 * \cos(\delta_1 - \delta_2) \quad (5)$$

Once this is calculated, the angle between PDFs (denoted here as “ C ”) can be calculated using the Law of Cosines for spheres with the following equation:

$$\cos C = (\cos c - \cos \Psi_1 * \cos \Psi_2) / (\sin \Psi_1 * \sin \Psi_2) \quad (6)$$

The combination of the polar angle “ Ψ ” and the angle between PDF sets “ C ” allows PDFs to be indexed. Each PDF set has a singular polar angle and occurs at a particular angle to all other PDFs (see Table S1 in the Supporting Information). Two PDF sets can be indexed by first finding the polar angles close to the determined values, then determining if the angle between the measured planes “ C ” is within two times error (i.e., within the 5° envelope of measurement error for each PDF, or 10° error) to the angle between crystallographic planes in the grain.

DESCRIPTION OF THE AUTOMATED NUMERICAL INDEX EXECUTOR PROGRAM

Based on the mathematical method described above, a computer algorithm has been written as a Microsoft Excel 2007 macro. The program, named ANIE (see Supporting Information), allows the automated indexing of up to 10 PDF sets per grain in an unlimited number of quartz grains. Data can be entered directly as obtained from U-stage measurements, including input of the full range of values determined for a particular PDF set, which is input as the low and high measured values for both azimuth and inclination. Data can also be input as both East and West orientations.

From the input screen, the maximum error (corresponding to the “envelope of measurement error”) that is traditionally fixed at 5° (see, e.g., Ferrière et al. 2009) can be defined by the user as any value between 0 and 10°. The user also has options concerning the method of calculation. Grains with a single PDF set can either be included or excluded from the analysis, and the program can either use an average value of the

U-stage measurements or the full range of measured values for indexing. When PDFs fall into the region where $\{10\bar{1}3\}$ and $\{10\bar{1}4\}$ orientations overlap, the program can be set to indicate that both orientations are possible solutions.

The measurements are matched to possible crystallographic indices based on the calculated polar angle (Equation 2) when compared with the ideal angle for each crystallographic index, plus or minus the defined error. Angles between ideal PDF sets (Equation 5) are compared with the list of possible angles between measured planes plus or minus the defined error (Table 1) to narrow the possible orientations for each plane to a single possible Miller–Bravais index. If there are multiple indices that are possible, the Miller–Bravais index with the lowest calculated angular error (i.e., the more likely) is reported.

Such analyses take only a few seconds to complete indexing for each grain; e.g., the analysis of sample AUS, with 208 PDF sets in 71 grains, was completed in approximately 1 minute. After the U-stage measurements are indexed, the program presents the results in two forms. The cumulative data are reported along with graphs presenting the proportion of indexed PDFs and the polar angles of the PDFs. The data are also presented in a grain-by-grain list, with details on the polar angle and Miller–Bravais indices of all PDF sets. Two histograms are presented upon completion of the program (Fig. 3); one with the frequency distribution of polar angle values in bins of 5° , and one with the absolute frequency of indexed PDFs with Miller–Bravais indices (see, e.g., Grieve et al. 1996; Ferrière et al. 2009). The number of PDF sets, the number of quartz grains, as well as the percentage of unindexed planes and the error used for the indexing, are indicated directly on the upper right part of the graph.

Data can also be exported to a comma-separated value spreadsheet, which retains the original input values, the polar angle values, the Miller–Bravais indices of the PDFs, and the angular error of the orientation for each PDF set in all grains. Graphics generated by the ANIE program can be exported directly to a Microsoft Powerpoint presentation, or they can also be copied for export to other programs.

COMPARISON OF MATHEMATICAL METHOD AND GRAPHICAL METHOD FOR INDEXING PDFs

The most recent stereographic projection template (with the pole orientations of known PDF planes; see Ferrière et al. 2009) used for the graphical method is designed to have 5° errors (i.e., “U-stage measurement errors”) associated with all Miller–Bravais indices. However, additional errors can be introduced in this

method from a number of factors, including the width of the line at the border of the circles (i.e., the 5° envelopes), the width of the pencil mark used when comparing the measurements to the STP by rotation, and the high likelihood that the human eye will not be able to properly discern whether measurements that are close to the border of a particular orientation are actually indexed or not. The mathematical method eliminates all of these factors of error and uncertainty. Due to that, a few minor discrepancies appear between the results obtained with graphical method versus mathematical method. Results are summarized in Table 1.

The data for three samples (AUS, BOS, and M8, all containing more than 65 grains with PDFs) have been processed mathematically using the ANIE program under four sets of conditions: (1) with a 5° error and using average values from U-stage data; (2) with a 5° error and using the full range from reported U-stage data; (3) with a 6° error and using average values from U-stage data; and (4) with a 6° error and using the full range from reported U-stage data. The reason for testing the mathematical method with a 6° error was to account for the potential “fudge factor” introduced by the graphical method. Note that all of the PDFs were indexed by hand with the graphical method by an experienced user (see Ferrière et al. 2009, for the exact methodology and procedure). Results using ANIE with average values from U-stage data with both 5° and 6° error have a noticeable difference compared with results obtained with the graphical method. However, very similar results are found between the graphical and mathematical results for 5° error using ranges of values, and near-identical results are found when 6° error is used with ranges of values.

Sample AUS is the largest data set indexed, with 74 grains and 208 measured PDF sets. By hand, it was found to have 10 unindexed planes, whereas when using ANIE and average values from U-stage data, with 5° and 6° error, 49 and 38 unindexed PDF sets were found, respectively. However, using the ranges of values resulted in 21 unindexed PDFs for 5° error, and 10 unindexed PDFs within 6° error. The graphically measured polar angles for AUS were similar to those found using ANIE, though with some minor discrepancies. For example, four PDFs were identified as being basal PDFs when plotted by hand, whereas they were unindexed using the mathematical method as the angular distance between the c -axis and the PDF set was slightly above error. The majority of differences between the graphical and mathematical method are the result of imprecision in the graphical method in the order of less than half a degree. Similar results were found for the samples BOS and M8 (Table 1).

Our comparison of results obtained with both methods allows us to identify three main categories of

Table 1. Comparison of the number of indexed planar deformation feature crystallographic orientations, as obtained using the graphical method and Automated Numerical Index Executor (ANIE) program with different settings, in quartz grains from three samples.

PDF crystallographic orientations	AUS sample (208 PDF sets in 74 grains)				BOS sample (145 PDF sets in 65 grains)				M8 sample (211 PDF sets in 71 grains)			
	Graphical method ^a	5° error averages ^b	6° error ranges ^c	6° error averages	Graphical method	5° error averages	6° error ranges	6° error averages	Graphical method	5° error averages	6° error ranges	6° error averages
<i>c</i> {0001}	59	47	53	58	n.d.	n.d.	n.d.	n.d.	4	4	4	4
{1014} ^d	6	8	22	21	2	12	13	12	10	7	17	4
{1014}//{1013} ^e	44	30	23	35	47	28	21	36	77	64	52	84
ω {1013} ^f	60	48	59	48	32	34	45	35	42	79	61	78
π {1012}	2	2	3	3	28	23	28	27	2	2	6	2
τ , z {1011}	10	11	12	10	5	7	7	6	13	10	15	14
m {1010}	1	1	3	1	1	1	1	1	n.d.	n.d.	n.d.	n.d.
ξ {1122}	5	1	3	1	4	2	3	3	3	3	2	3
s {1121}	n.d.	n.d.	n.d.	1	n.d.	2	4	3	n.d.	n.d.	1	1
p {2131}	3	3	4	2	3	2	2	3	3	3	8	3
x {5161}	1	2	2	2	1	1	n.d.	n.d.	1	1	1	1
a {1120}	1	1	n.d.	1	n.d.	1	1	1	n.d.	n.d.	n.d.	n.d.
{2241}	n.d.	1	n.d.	1	6	5	3	5	10	9	6	12
{3141}	3	3	3	3	3	5	6	4	7	2	2	2
t {4041}	2	1	n.d.	1	n.d.	2	2	2	2	2	2	2
k {5160}	1	n.d.	n.d.	n.d.	n.d.	n.d.	n.d.	n.d.	1	1	n.d.	1
Unindexed	10	49	21	38	8	21	9	12	5	42	16	25

^aPDF planes indexed with the graphical method; Data from Ferrière et al. (2009).

^bPDF planes indexed using ANIE program with a 5° envelope of measurement error and the average value of measurements for indexing.

^cPDF planes indexed using ANIE program with a 5° envelope of measurement error and the ranges of values for indexing.

^d{1014} PDF orientations uniquely indexed.

^e{1014} PDF orientations uniquely indexed.

^f{1013} PDF orientations uniquely indexed.

n.d., none detected.

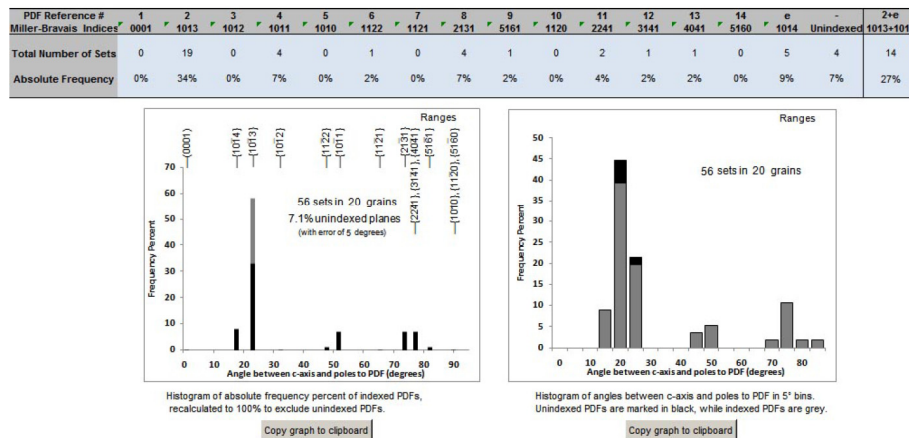


Fig. 3. Indexed planar deformation features (PDFs) data are summarized by the Automated Numerical Index Executor program as a pair of histograms, which show the absolute frequency percent of indexed PDFs and the frequency distribution of polar angle values of PDFs in 5° bins. The error used for analysis is indicated on the graph for indexed PDFs, and each graph also displays whether data are processed based on averages or ranges of values. Unindexed PDFs are marked in black on the histogram of polar angle values of PDFs.

differences between mathematical indexing using ANIE and the graphical indexing of the data. The first one arises when there are multiple possible solutions that allow all measurements to fit within known PDF crystallographic orientations. In the manual version, the user visually estimates the best fit (i.e., using eyes and “intuition”), whereas the mathematical method determines the set of Miller–Bravais indices that has the lowest error and, thus, is the most likely one. This accounts for 48% of the discrepancies. Secondly, PDF sets that are very close to a known PDF crystallographic orientation, but that fall just outside of the defined error (i.e., traditionally of 5° as in the STP presented in Ferrière et al. 2009) may be graphically counted as “indexed sets,” even they are in fact unindexed PDFs. This also accounts for 48% of discrepancies. Finally, all other discrepancies between graphical versus mathematical method that do not correspond to either of these, such as errors in plotting data, account for the remaining 4% of discrepancies. The paucity of such discrepancies indicates that the mathematical method is reliably measuring the exact same features as when using the graphical method, whereas the commonality of the second category of discrepancies indicates that the user, in the case of the graphical method, can easily introduce some errors into the indexing process.

Thus, based on our comparison of results as obtained for the same set of U-stage data with the graphical method and the mathematical method (i.e., using ANIE), very similar results are obtained when

using the range of measured values and an error of 6°. It is recommended that users of the ANIE program, or of the mathematical method described in this article, state specifically which error setting is chosen for the indexing of the PDFs and whether average values or ranges of values are used for the determination of crystallographic indices.

CONCLUSIONS AND RECOMMENDATIONS

The process of indexing PDFs in quartz grains is somewhat tedious, mainly because of the time-consuming and difficult nature of plotting U-stage measurements and properly reading the Miller–Bravais indices after the data have been obtained. The development and presentation of an automated method for the determination of crystallographic orientations of PDFs remove a large part of the tedium for those who are attempting to verify the shock origin of deformation features in quartz grains and/or who are interested in the evaluation of the peak shock pressure recorded by a given sample.

Our comparison of indexing PDF sets using the mathematical method (i.e., the ANIE program) versus the “old” graphical method reveals that the best fit between the two methods is found when using 6° error and the full ranges of values (as opposed to the average value of measurements) in the ANIE program. For the 564 PDFs evaluated in this study, a total of 46 differences were found between indexing with the mathematical method versus the graphical method, which corresponds

to a difference of about 8%. Finally, our study suggests that the graphical method, although designed with a 5° envelope of measurement error, is actually closer to 6° error in reality. However, it is recommended to users to define a 5° error when using ANIE program, because if a 6° error is used, the error envelopes of the PDFs pole traces for {1012} and {1013} orientations partially overlap. Anyone presenting PDF data indexed with the ANIE program or this mathematical method is asked to state clearly the error used in the calculation, as well as whether the average value of measurements or the ranges of values is used for indexing.

Acknowledgments—This work is supported by the University of Vienna doctoral school IK-1045 and the Austrian Science Foundation (FWF), grant P21821-N19 (to C. K.). We express appreciation to Bevan M. French and Sam Watson for discussion and encouragement with this project. Hugues Leroux, John G. Spray, and an anonymous reviewer are thanked for their comments and suggestions to improve the quality of the manuscript. This paper is dedicated to the memory of our late colleague and friend Jared R. Morrow (1959–2010), who was an expert in U-stage measurements of PDFs in quartz grains and who had long hoped for this program to be operating.

Editorial Handling—Dr. John Spray

REFERENCES

- Bohor B. F., Modreski P. J., and Foord E. E. 1987. Shocked quartz in the Cretaceous-Tertiary boundary clays: Evidence for a global distribution. *Science* 236:705–708.
- Dressler B. O., Sharpton V. L., and Schuraytz B. C. 1998. Shock metamorphism and shock barometry at a complex impact structure: State Islands, Canada. *Contributions to Mineralogy and Petrology* 130:275–287.
- Engelhardt W. V. and Bertsch W. 1969. Shock induced planar deformation structures in quartz from the Ries crater, Germany. *Contributions to Mineralogy and Petrology* 20:203–234.
- Ferrière L., Koeberl C., Ivanov B. A., and Reimold W. U. 2008. Shock metamorphism of Bosumtwi impact crater rocks, shock attenuation, and uplift formation. *Science* 322:1678–1681.
- Ferrière L., Morrow J. R., Amgaa T., and Koeberl C. 2009. Systematic study of universal-stage measurements of planar deformation features in shocked quartz: Implications for statistical significance and representation of results. *Meteoritics & Planetary Science* 44:925–940.
- French B. M. 1998. Traces of catastrophe: A handbook of shock-metamorphic effects in terrestrial meteorite impact structures. LPI Contribution 954. Houston, Texas: Lunar and Planetary Institute. 120 p.
- French B. M. and Koeberl C. 2010. The convincing identification of terrestrial meteorite impact structures: What works, what doesn't, and why. *Earth-Science Reviews* 98:123–170.
- French B. M. and Short N. M., eds. 1968. *Shock metamorphism of natural materials*. Baltimore: Mono Book Corporation. 644 p.
- Goltrant O., Cordier P., and Doukhan J.-C. 1991. Planar deformation features in shocked quartz; a transmission electron microscopy investigation. *Earth and Planetary Science Letters* 106:103–115.
- Grieve R. A. F., Coderre J. M., Robertson P. B., and Alexopoulos J. 1990. Microscopic planar deformation features in quartz of the Vredefort structure: Anomalous but still suggestive of an impact origin. *Tectonophysics* 171:185–200.
- Grieve R. A. F., Langenhorst F., and Stöffler D. 1996. Shock metamorphism of quartz in nature and experiment: II. Significance in geoscience. *Meteoritics & Planetary Science* 31:6–35.
- Hörz F. 1968. Statistical measurements of deformation structures and refractive indices in experimentally shock loaded quartz. In *Shock metamorphism of natural materials*, edited by French B. M. and Short N. M. Baltimore: Mono Book Corp. pp. 243–253.
- Huffman A. R. and Reimold W. U. 1996. Experimental constraints on shock-induced microstructures in naturally deformed silicates. *Tectonophysics* 256:165–217.
- Langenhorst F. 2002. Shock metamorphism of some minerals: Basic introduction and microstructural observations. *Bulletin of the Czech Geological Survey* 77:265–282.
- Müller W. F. and Défourneaux M. 1968. Deformationsstrukturen im Quarz als Indikator für Stosswellen: Eine experimentelle Untersuchung an Quarz-Einkristallen. *Zeitschrift für Geophysik* 34:483–504.
- Robertson P. B. and Grieve R. A. F. 1977. Shock attenuation at terrestrial impact structures. In *Impact and explosion cratering*, edited by Roddy D. J., Pepin R. O., and Merrill R. B. New York: Pergamon Press. pp. 687–702.
- Stöffler D. and Langenhorst F. 1994. Shock metamorphism of quartz in nature and experiment: I. Basic observation and theory. *Meteoritics & Planetary Science* 29:155–181.
- Trepmann C. A. and Spray J. G. 2006. Shock-induced crystal-plastic deformation and post-shock annealing of quartz: Microstructural evidence from crystalline target rocks of the Charlevoix impact structure, Canada. *European Journal of Mineralogy* 18:161–173.

SUPPORTING INFORMATION

Additional supporting information may be found in the online version of this article:

Table S1. Angular relationships between pairs of Miller–Bravais indices.

Program. Automated Numerical Index Executor. Requires Microsoft Excel 2007 or later.

Please note: Wiley-Blackwell is not responsible for the content or functionality of any supporting materials supplied by the authors. Any queries (other than missing material) should be directed to the corresponding author for the article.

A statistical dynamical study of meteorite impactors: a case study based on parameters derived from the Bosumtwi impact event

M. A. Galiazzo^{1,*}, Á. Bazsó¹, M. S. Huber², A. Losiak², R. Dvorak¹, and C. Koeberl^{2,3}

¹ Institute for Astrophysics, University of Vienna, Türkenschanzstraße 17, A-1180 Vienna, Austria

² Department of Lithospheric Research, University of Vienna, Althanstraße 14, A-1090 Vienna, Austria

³ Naturhistorisches Museum Wien, Burgring 7, 1010 Vienna, Austria

The dates of receipt and acceptance should be inserted later

Key words impact craters – celestial mechanics – minor planets, asteroids – methods: N-body simulations – methods: statistical

The study of meteorite craters on Earth provides information about the dynamic evolution of bodies within the Solar System. Bosumtwi crater is a well studied, 10.5 km in diameter, ca. 1.07 Ma old impact structure located in Ghana. The impactor was ~ 1 km in diameter, an ordinary chondrite and struck the Earth with an angle between 30° and 45° from the horizontal. We have used a two phase backward integration to constrain the most probable parent region of the impactor. We find that the most likely source region is a high inclination object from the Middle Main Belt.

© 2012 WILEY-VCH Verlag GmbH & Co. KGaA, Weinheim

1 Introduction

When studying impact craters, it is sometimes possible to determine the properties of the impactor that produced the crater, but the source where the impactor originated in the Solar System is more difficult to determine. Recently, the Almahata Sitta fall was observed by astronomers, tracked by satellites as it entered the atmosphere, and collected soon after striking Sudan. In this case, dynamical models were combined with detailed information about the meteorite type to track the impactor back to the Inner Main Belt (Jenniskens et al., 2010). For older impacts, the same precision cannot be achieved because of the lack of detailed information on orbital parameters. However, based on the geological constraints on the dynamic nature of the impactor, a statistical model can be used to suggest the most probable region from which the impactor could have originated. The aim of this study is to statistically constrain the most probable parent region of the impactor that formed the Bosumtwi impact crater.

1.1 Bosumtwi crater: Geological background

The Bosumtwi impact crater was chosen for this study because of its relatively young age and unusually good constraints on the direction of the impactor. The Bosumtwi impact crater is a 10.5 km in diameter complex meteorite impact crater located in the Ashanti Province of southern Ghana. It is 1.07 ± 0.11 Ma old and relatively well preserved (e.g., Koeberl et al., 1997a). The Bosumtwi structure is currently filled by the closed-basin Lake Bosumtwi that is 8 km

in diameter and up to 72.5 m deep. It is considered to be the largest, relatively young, confirmed impact structure on the Earth. Bosumtwi is a unique crater, since it is one of just three craters in the world that are associated with a tektite strewn field (e.g., Koeberl, 1994). Tektites are centimeter-sized pieces of natural glass formed during a hypervelocity impact event by ejection of molten target-surface material and occurring in strewn fields (e.g., Koeberl, 1994). Based on the distribution of tektites around Bosumtwi crater it is possible to constrain the direction of travel of the bolide prior to the impact. Based on the Cr isotope composition of the tektites derived from Bosumtwi, Koeberl et al. (2007b) established that the impactor that formed Bosumtwi crater was most probably an ordinary chondrite (while carbonaceous and enstatite chondrites were excluded). The properties of the impactor that formed the crater have been constrained by numerical modeling. According to Artemieva et al. (2004), the Bosumtwi structure was formed by an impactor 0.75 to 1 km in diameter, moving with a velocity higher than 15 km/s, and most probably 20 km/s. Due to association of the Bosumtwi crater with the Ivory Coast tektite strewn field, the direction of the incoming impactor was estimated to be from N-NE to S-SW and the angle of impact is thought to be between 30° and 45° (Artemieva et al., 2004).

2 Model & Methods

This study uses a statistical approach to constrain the parent region of the Bosumtwi impactor, using $a-i$ space (a and i for semi-major axis and orbital inclination, respectively) and the absolute magnitude (H_v) distribution inside the defined regions of the Solar System. First, we made a back-

* Corresponding author: e-mail: mattia.galiazzo@univie.ac.at

ward integration¹ from the present to the time of impact. The integration used the Radau integrator, included relativity, and all the planets plus Pluto, the Moon, Vesta, Ceres, Pallas and Juno. The integration considered the positions of the Earth between 0.96 and 1.18 Ma (1.07 ± 0.11 Ma) in order to find the possible position of the Earth during the time when the impact occurred, accounting for the error of the impact age measurement. Then, we made another backward integration using the Lie-integrator (Eggl and Dvorak, 2010) without Mercury, Pluto and the 4 asteroids, from the time of the impact to 100 Ma, simulating the orbital evolutions of 924 fictitious Bosumtwi impactors beginning at the calculated location of the Earth. Two cases were considered for this integration:

Fixed case (FC): we started the integration at the location of the Earth (as calculated in the initial integration) exactly at 1.07 Ma. Then, 384 particles, with a gaussian distribution of impact velocities (v_i) around 20 km/s were launched with 32 different velocities. Those velocities correspond to the average value for Earth-impactors, as well as the most likely velocities indicated by numerical modeling for the Bosumtwi impactor (Artemieva et al., 2004). Velocities have a Gaussian distribution in the range of 11.2 to 40 km/s, which are the escape velocity from the Earth and cometary speed, respectively. Then, 4 impact angles were considered using random values among $\Theta = 37.5^\circ \pm 7.5^\circ$ for each velocity and 3 different directions ($\Omega_1 = 67.5 \pm 3.5^\circ$, $\Omega_2 = 78.75 \pm 3.5^\circ$ and $\Omega_3 = 56.25 \pm 3.5^\circ$ from east) for each angle. The launch position is the present latitude and longitude of the Bosumtwi crater site.

General case (GC): 540 particles were integrated using combinations of the following properties to account for the lack of knowledge of the exact position of the Earth at the time of the impact: 3 different orbital positions of the Earth, corresponding to the minimum, average and maximum aphelion (at 3 different times) in the Solar System; 3 different directions of the impactor ($\Omega_1 = 67.5 \pm 3.5^\circ$, $\Omega_2 = 78.75 \pm 3.5^\circ$ and $\Omega_3 = 56.25 \pm 3.5^\circ$ from east); and 60 different sections of the Earth along lines of longitude every 6° for each position of the Earth. For each of the 540 particles, impact angle and latitude² were distributed randomly, and v_i had a gaussian distribution like in the FC.

Once data were generated, analysis was done on two levels. First, regions were defined as in Table 1, where only the semimajor axis was considered. Then, for those particles

¹ Due to the fact that a backward integration could be distorted by chaotic motion in close encounters, we have looked for a measure that is as simple as possible and is expressed in terms of orbital elements, since these are familiar indices of orbit differences. Because there should be preferential orbits in the regions far from the Earth, we can use a statistical approach. We stopped the integration for a particular body whenever the asteroids overcome an eccentricity equal to 0.985 or have had a close encounter with a planet less than $\sim 10^{-5}$ AU.

² varying $\pm 1.3^\circ$ (Neron deSurgy & Laskar, 1995) from the present one, to account for the variance of the obliquity.

which fell into the Main Belt, more specific constraints were necessary because of the much higher population. Assuming the impactor was an ordinary chondrite (Koeberl et al., 2007b) and from the numerical results of Artemieva et al.³ (2004), we can exclude the possibility of a cometary orbit, such as NEOs (Near-Earth objects) with orbits of $Q > 4.5$ AU (Fernández et al., 2002).

REGIONS (Table 1): At the end of the integration, the particles are examined to determine the probability that they fall into a defined region based on the semi-major axis range (called $P(a)$). The orbital properties of the particles were derived from the time intervals between close encounters where they show little variance. The average time between close encounters with planets was determined to be 284 ky.

MAIN BELT GROUPS (Table 2): Asteroids in the Main Belt were subdivided into 3 regions and with these 3 constraints: (1) $1.5264 < a < 5.05$ AU, $Q < 5.46$ AU (aphelion of Hilda family from Broz and Vokrouhlicky, 2008), (2) $q > 1.0017$ AU (the average semi-major axis of the Earth after 100 Myr of integration) and (3) the NEAs with $Q < 4.35$ and $q > 1.0302$.

Then, each of these 3 groups was divided into 2 subgroups: the low inclination group (*LIG*) and the high inclination group (*HIG*), the border between the two regions being $i = 17.16$ (Novaković et al., 2011). The regions with the highest densities of particles were then determined. For these the Tisserand parameter with respect to Jupiter⁴ was calculated to test whether or not the properties correspond to known families in the Main Belt.

2.1 Absolute magnitude and spectroscopy

Ordinary chondrites, thought to be responsible for the Bosumtwi impact, are associated with the taxonomical S-group: S, L, A, K, R, Q and intermediate types SI, Sa, Sk, Sr, Sq (Bus & Binzel, 2002). Surveys have also revealed that the NEA population is dominated by objects belonging to the taxonomic classes *S* and *Q* (25% as Q-type and 40 % as S-type, Bus et al., 2004). When corrected for observational biases, about 40% of the NEA population belong to one of these two taxonomic classes. In the case of Mars crossers, 65% belong to the S class (de Léon et al., 2010). To compute the absolute magnitude of our impactor, we used the equation of Fowler and Chillemi (1992): $H_v = -5 \log(\frac{D_p^{1/2}}{1329})$. Using the average albedo for the S-group asteroids, 0.197 (Pravec et al. 2012), and considering the likely size range of the Bosumtwi impactor, its absolute magnitude ranged from 17.4 to 18.0 mag. The absolute

³ see also their Table 2 where the fit between the diameter of the crater and the impact velocity is in agreement with impact velocities typical of asteroids.

⁴ $T_j = \frac{a_j}{a} + 2\sqrt{\frac{a}{a_j}(1-e^2)} \cos i$, where a_j is the semi-major axis of Jupiter, a , e and i are the actions of the osculatory elements of the asteroid.

magnitude of the impactor can be used to calculate the probability (called $P(H_V)$) that the impactor originated from a particular region based on the likelihood of objects of similar absolute magnitude originating in a particular region, i.e., from the IMB, $11.21 < H_{VIMB} < 27.60$. The spectral properties of ordinary chondrites exclude the possibility that this object come from a family such as Vesta or Hungaria, but it favours the Flora, Ariadne, Nysa, Maria, Eunomia, Mersia, Walsonia, Coelestina, Hellona, Agnia, Gefion and Koronis groups (Cellino et al., 2002) for the *LIG*; Barcelona and Hansa for the *HIG* (Novaković, et al., 2011).

3 Results and discussion

The final backward integration of 100 My shows that particles which survived the integration tend to converge on the Main Belt (Figure 1), and that only a negligible number of them is found in cometary orbits with an initial aphelion greater than Jupiter's one, with a $v_i > 27$ km/s; then a very negligible part in hyperbolic orbits with a $v_i > 33$ km/s. This suggests that the impactor most likely originated in the Main Belt.

REGIONS: The results are listed in Table 1, where $P(H_v)$ shows that on the basis of the absolute magnitude, the object most likely originated from the Main Belt, with a 37% probability of originating from the IMB and a 29% probability of originating in the MMB. The integration performed in this work shows that the majority of backwards integrated particles fall into the IMB and MMB, with $\sim 10\%$ of objects in the FC falling into each of these. The GC, however, resulted in the majority of objects originating from the MMB, again with $\sim 10\%$ of objects, and only $\sim 4\%$ of objects originating from the IMB.

MAIN BELT: Results are given in Table 2, subdivided in 2 rows. In the upper row we have the *LIG* and the lower one, the *HIG*: $P(a, i)$ is the probability to find the asteroid at high or low inclinations in the regions defined via semi-major axis, *G* and *F* stands respectively for GC and FC.

FC: The most probable source region of the Bosumtwi impactor based on the fixed case integration falls within the Main Belt at high inclination, with the most likely group being the MMB at high inclination, with 2% of the population falling into this group. The objects have highly inclined orbits (up to $\sim 75^\circ$), and the most populated zone at $2.42 \pm 0.03 < T_j < 2.84 \pm 0.25$.

GC: The most probable source region of the Bosumtwi impactor based on the general case is from the MMB with high inclination: $i > 36.9$ (Fig. 2) and $2.42 \pm 0.05 < T_j < 2.79 \pm 0.09$. However, low inclination MMB is also possible, together with high inclination IMB.

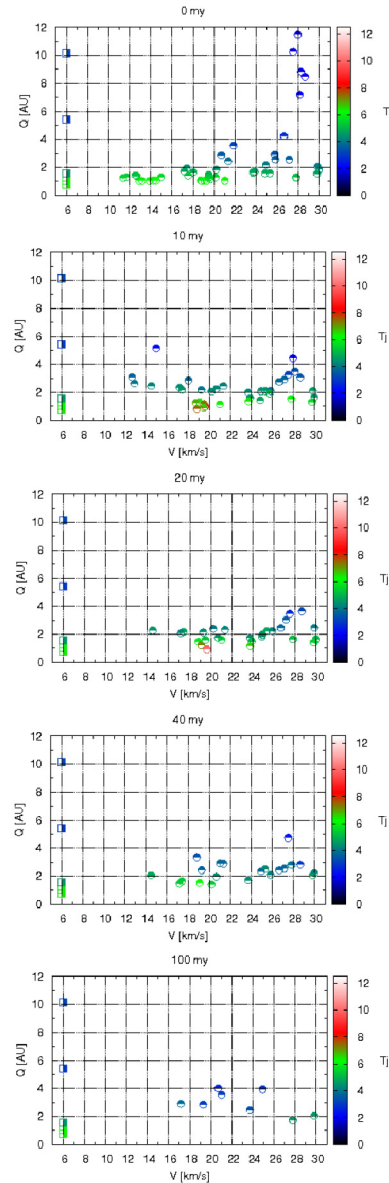


Fig. 1 Evolution of a sample, through the different ranges of admitted velocities, of fictitious asteroids (impactors) over the total integration time. In colours the Tisserand Parameter, on the x-axis, the impact velocity in km/s and on the y-axis the aphelion in AU. On the left, at a fictitious and non-real velocity of 6 km/s we have the planets as reference, from top to the bottom: Saturn, Jupiter, Mars, Earth, and Venus. The T_j shows that the particles tend to achieve the values of the MBAs (see the plot at 100 my).

Reg.	Orb.	$P(H_v)$	$P_{FC}(a)$	$P_{GC}(a)$
IMB	$1.78^* \leq a \leq 2.06$	0.3737	0.0924	0.0404
MMB	$2.06 < a < 3.28$	0.2870	0.1036	0.1030
OMB	$3.28 < a < 5.05$	0.0232	0.0112	0.0121
TRO	$5.05 < a < 5.35$	▲	0.0056	0.0000
CEN	$5.35 < a < 30.00$	▲	0.056	0.0646
TNO	$a > 30.00$	▲	0.0112	0.0020

Table 1 Regions are defined by the a that corresponds to strong perturbative Mean Motion Resonance (2.06 AU for $J_4 : 1$ and 3.28 for $J_2 : 1$), apart for the inner border of the (IMB) equal to the aphelion of Mars. The borders of the Jupiter Trojans (TRO) as in Tsiganis et al. (2005) and for the TNOs, the standard definition is used. MMB, OMB, CEN stand respectively for Middle Main Belt, Outer Main Belt and Centaurs. Orb. stands for semi-major axis borders of the region. For the lower border of the IMB (*), we take the minimum a for the innermost group of asteroids (see Galiazzo et al. 2012). The “▲” means that H_v are biased for the absence of a small bodies survey, so no significative computation is possible. $P_{FC}(a)$ and $P_{GC}(a)$ stands respectively for probability to find the origin in the region through the a in the FC and in the GC.

Reg. Low	$P_F(H_v)$	$P_F(a, i)$	$P_G(a, i)$
Reg. High	$P_F(H_v)$	$P_F(a, i)$	$P_G(a, i)$
IMB Low	0.234	0.006	0.000
IMB High	0.420	0.006	0.018
MMB Low	0.307	0.000	0.010
MMB High	0.113	0.020	0.022
OMB Low	0.023	0.003	0.000
OMB High	0.019	0.000	0.004

Table 2 MBAs group have the same subdivision per semi-major axis, as in Table 1, apart for the IMB: $1.53 < a < 2.06$ where the lower limit is the average aphelion of Mars in 100 Myr from the impact time. “Low”= Low inclined orbit ($i < 17.16$) and “High”= High inclined orbit. $P_F(a, i)$ and $P_G(a, i)$ stands respectively for probability to find the origin in the region defined by semi-major axis, and inclination too, in the FC and in the GC.

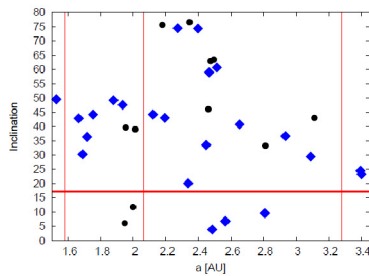


Fig. 2 $a - i$ space. Vertical lines define the border of the regions in semi-major axis, as in Table 1, and the horizontal line discriminate HIG and LIG. Diamonds for GC and circles for FC.

4 Conclusions

The Bosumtwi impactor probably originated in the MMB at orbital inclinations greater than 35° with a possible initial T_j equal to 2.63 ± 0.25 . These values are based only on our numerical integrations (the highest values⁵ in $P_G(a, i)$ and $P_G(a)$ found in the GC, see Table 1 and 2 and Figure 2.) and not considering the spectroscopical type too, because we do not have yet any significant number of measure in this zone of the Main Belt (Cellino et al. 2002). Also this zone is still not well studied and so we could not identify a particular family as the most likely source. Asteroids with similar orbital parameters to the modeled Bosumtwi impactor are: 2002 MO₃, 2009 XF₈, 2002 SU and 2010 RR₃₀. There could be a cluster of asteroids at very high inclined orbits as shown by these results, something that we are planning to study after this work. This method should be improved to find more consistent probabilities (i.e. with more fictitious particles and larger integration times) and it can potentially be applied to other old impact craters with well constrained impactor properties, and even to impacts on other planets.

References

- Artemieva, N., Karp, T., Milkereit, B.: 2004, GGG 5, 11016
- Broz, M.; Vokrouhlicky, D.: 2008, MNRS 390, 715
- Bus, S. J., Binzel, R. P., Volquardsen, E. L., Berghuis, J. L.: 2004, BAAS 36, 1140
- Bus, S. J., Binzel, R. P.: 2002, Icarus 158, 146
- Cellino, A. and Bus, S. J. and Doressoundiram, A. and de León, J., Licandro, J. and 3 coauthors: 2010, A&A 517, A23
- Dvorak, R., Pilat-Lohinger, E., Schwarz, R., Freistetter, F.: 2004, A&A 426, L37
- Eggl, S., Dvorak, R.: 2010, LNP 790, 431
- Fernández, J. A., Gallardo, T., Brunini, A.: 2002, Icarus 159, 358
- Fowler, B., Chillemi, B.: 1992, MNRAS 423, 3074
- Galiazzo M. A., Bazsó, A., Dvorak R.: 2012, PSS
- Koeberl, C.: 1994, GSA Special Paper 293, 133
- Koeberl, C., Bottomley, R., Glass, B. P., Storzer, D.: 1997a, GCA 61, 1745
- Koeberl, C.; Milkereit, B., Overpeck, J. T., and 9 coauthors: 2007a, MPS 42, 483
- Koeberl, C., Shukolyukov, A., Lugmair, G. W., Guenter W.: 2007b, EPSL 256, 534
- Jenniskens, P., Vaubaillon, J., Binzel, R. P. and 13 coauthors: 2010, Met. Plan. Sc. 45, 1590
- Neron de Surgy, O., Laskar, J.: 1995, BAAS 27, 1172
- Novaković, B., Cellino, A., Knežević, Z.: 2011, Icar. 216, 69
- Pravec, P., Harris, A. W., Kusnirák, P., Galád, A. and Hornoch, K.: 2012, Icarus 221, 365
- Tsiganis, K., Varvoglis, H. and Dvorak, R.: 2005, CeMDA 71

⁵ Because of close encounters, some integrations were stopped before 100 My, so less orbits end their evolution in the Main belt, see Fig. 1. These ones are the missing percentage from the results, a part still happen to be as NEAs, a part reach our maximum tolerance value for eccentricity (0.95) and another small fraction has again impacts during the backward integration.

CURRICULUM VITAE

Anna Izabela Losiak

Department of Lithospheric Research, University of Vienna
 Althanstrasse 14, 1090 Vienna, Austria
anna.losiak@gmail.com

EDUCATION AND RESEARCH

PhD, Department of Lithospheric Research, University of Vienna (03.2010-06.2013)

Dissertation topic: Impact processes within Bosumtwi impact crater, GPA: 1.1 (out of 1.0)

- Participated in the MARS2013 mission by Austrian Space Forum (managed a group responsible for preparation of maps of the analog research area and participated in the traverse planning) (2012-2013).
- Participated in the "Geochronology Summer School" (09.2012).
- Participated in the field trips to South Africa (Vredefort and Tswaing craters 2010), Germany (Ries and Steinheim craters 2010), Tajikistan (Kara-Kul crater 2011), Hawaii (Big Island 2012) and Australia (Gosses Bluff, Boxhole, Kelly West and Amelia Creek craters 2012).
- Participated in the "Accelerator Mass Spectrometry short class" (2011).
- Participated in the "Nanobeams PhD School" (2011-2012).
- Participated in the "Field Training and Research Program at Meteor Crater" (2010).

MS, Geological Sciences, Michigan State University (09.2007-05.2009)

Dissertation topic: The development of evaporite minerals during weathering of Antarctic meteorites, GPA: 4.0 (out of 4.0)

- Received several scholarships, prizes and small research grants.
- Actively took part in research projects not directly related to the topic of MS thesis (e.g. weathering of dunites, apical angles of weathered pyroboles, rates of weathering of the plagioclases from Hawaii).
- Took part in the Lunar Exploration Summer Intern Program at LPI (2008).

MA (no dissertation), Spatial Management, Warsaw University, Faculty of Geography and Regional Studies (10.2004-07.2007)

GPA: 4.5 (out of 5.0)

- Research focus: distribution of services in a post-communistic city district.
- Inspired, managed and gained funding for a large student research project concerning the development of tourism in Pultusk, Poland.

MS, Geomorphology and Sedimentology, Warsaw University, Faculty of Geography and Regional Studies (10.2004-07.2006)

Dissertation topic: Changes of environment during accumulation of sediments from a borehole Leszczydol 1 (Miedzyrzecze Lomzynskie), GPA: 4.95 (out of 5.0)

- Collaborated on the fellowship in the research grant of Barbara Woronko on "Aeolization of sediments, as a stratigraphic indicator of Quaternary".

BS (with dissertation), Geography, Warsaw University, Faculty of Geography and Regional Studies (10.2001-06.2004)

Dissertation topic: Climatic changes in Southern Egypt during Quaternary, GPA: 4.78 (out of 5.0)

- Developed BA research project and gained money for project.

TEACHING AND RESEARCH EXPERIENCE

Teacher, International School of Hanna Buskiewicz-Piskorska (09.2009-02.2010)

- Taught courses: Geography (International Baccalaureate program)

Teaching Assistant, Michigan State University, Department of Geological Sciences (08.2008-05.2009)

- Taught courses: ISP 203L: Geology and the Human Environment.
- Taught and graded assignments for three sections of course (~ 70 students).

Intern, Lunar and Planetary Institute (05.2008-08.2008)

- Selected the best landing sites for establishing a precise absolute chronology of the lunar surface.
- Prepared the largest available lunar crater database with age of craters.
- Presented a poster on the Lunar Science Conference (as a part of the team).

Research Assistant, Michigan State University, Department of Geological Sciences (01.2008-05.2008)

- Prepared and analyzed samples (XRF, ICP-MS) for the study of M.A. Velbel on the weathering of dunites.

Teacher Assistant, Warsaw University, Faculty of Geography and Regional Studies (10.2006-06.2007)

- Taught courses: Geomorphology, Sedimentology for Archeologists.
- Developed the teaching program for both classes.
- Organized field trip for the course Sedimentology for Archeologists.

Teacher Assistant, Carleton University (Ottawa, Canada) (08.2005-12.2005)

- Assisted with management, preparation and running labs.
- Developed educational themes for term project to promote critical thinking.

PROFESSIONAL EXPERIENCE

Geologist, Geotech Sp. z o.o., Rzeszow

- Prepared geologic documentation for highways in Poland.
- Supervised on site investigations (drilling boreholes).

Translator, Swiat Nauki (Polish edition of Scientific American)

- Translated several articles about geology and/or planetary sciences.

Intern, Deloitte & Touche company

- Prepared part of a purchasing strategy for a big petroleum company.

Project manager, Wolska&Jefremienko s.c. company

- Prepared strategies of development for municipalities in Poland.
- Developed and designed a new method of evaluation of strategy implementation.

Project manager, Wolska&Jefremienko s.c. company

- Prepared company marketing strategy.

Intern, Warsaw City Hall, Department of Strategy and Development

- Worked on the preparation of the Warsaw Development Strategy (to the year 2020).

HONORS AND GRANTS

- MetSoc travel award (2011 and 2012).
- EGU Outstanding student poster award (2011).
- Student Research Grant Award of the Clay Minerals Society (2009).
- LPI Career Development Award (2009).
- Joint Annual Meeting of LEAG-ICEUM-SRR travel grant (2008).
- Neal Endowed Scholarship (2007-2008).
- GSA graduate students research grant (2008).
- Lucile Drake Pringle and Gordon H. Pringle Endowed Fellowship (2007-2008).
- Fulbright's Graduate Student Award (2007-2008).
- M.A degree with honors (2006).
- Scholarship of Ministry of National Education and Sport for the best Polish students (2004 and 2005).
- Scholarship from Carleton University (2005).
- Bachelor degree with honors (2004).
- Scholarship for the best students of University of Warsaw funded by PZU ZYCIE S.A (2003).
- Annually the best student on a year and won scholarships for very good grades (2001-2006).
- Finalist of National Geographic Contest (The Geographic Olympics) (2001).
- Scholarship of the Prime Minister of Poland for the best students of high schools (2000).
- Finalist of National Biologic Contest (The Geographic Olympics) (1997).

SKILLS

Language: Polish (mother tongue), English (fluent), Russian (intermediate), German (basic).
 Geological skills: SEM, TEM, XRF, ICP-MS, light microscopy, ^{10}Be system.

SCIENTIFIC OUTREACH AND COMMUNITY SERVICE

Journal Reviewer and Community Service

Reviewer for the journal Meteoritics and Planetary Science (2012).

Initiated the "How to become a planetary scientist?" program at Planetary Science Division EGU:
<http://www.egu.eu/ps/how-become-planetary-scientist/>

Workshops

Workshop for university students titled "Planetary Geology" (2010) Institute of Geology, Adam Mickiewicz University.

Cycle of workshops titled "Planetary Geology" for high-schools students in Warsaw (2008).

One week science-teaching program for pupils from a small village school in Wolka Czepowa, Poland (2002).

One year program of supplementary science classes for pupils with special needs or with problems with learning from primary school in Brodno, Warsaw, Poland (2002-2003).

Lectures

Presentation during the European Space Expo in Warsaw titled: "Making maps for astronauts during MARS2013 Analog Field Simulation" (2013).

Lecture at the Kuffner-Observatory titled "Impact craters: importance, formation recognition" (2013).

Lecture at the Naturhistorisches Museum Wien for the students of the Polish University of the Third Age in Vienna titled: "Meteorites and the Solar System" (2012).

Popular science articles

“Mars 2013 – kosmiczne manewry” – The MARS2013 – space maneuvers (05.03.2013): Tygodnik Powszechny.

“Zagrożenie z kosmosu” – The Danger from the Sky (25.02.2013): Przegląd.

“Prawdziwy koniec świata” – The real end of the world (01.12. 2012): Polonika.

„Dlaczego badamy Marsa?” – Why should we study Mars? (01.09.2012): AstroNautilus.

„Metryka Ukryta w Kraterze” – Dating planetary surfaces (01.05.2012): Wiedza i Życie.

Movies

“Le secret du lac Karakul” – The secret of lake Karakul – movie from the field research in Tajikistan (26 minutes) – cooperated on the creation of the movie, served as a translator (Russian) and gave an interview on scientific issues related to the Karakul crater. Introductory clip is available at: <http://www.youtube.com/watch?v=sG-LUPA9RSg>

Other

Translated a witness account from Russian to English for the “Meteorite Russe Les Lecons de Limpact Celeste” in the Ciel&Espace April 2013.

Contributed to the article: “Śmierć i zmartwychwstanie Marsa” (The death and the resurrection of Mars) written by the Wojciech Brzeziński, (14.04.2013): Tygodnik Powszechny.

PUBLICATIONS AND PRESENTATIONS

PEER-REVIEWED PAPERS

Galiazzo M.A., Bazso A., Huber M.S., Losiak A., Dvorak R., Koeberl C. (2013) A statistical dynamical study of meteorite impactors: a case study based on parameters derived from the Bosumtwi impact event, *Astronomische Nachrichten*. Accepted.

Huber M.S., Ferrière L., Losiak A., Koeberl C. (2011) ANIE: A mathematical algorithm for automated indexing of planar deformation features in quartz grains, *Meteoritics and Planetary Science* 46: 1418–1424.

Losiak A., Velbel M.A. (2011) Evaporite Formation during the Weathering of Antarctic Meteorites – a Weathering Census Analysis Based on the ANSMET Database, *Meteoritics and Planetary Science* 46: 443–458.

Velbel M.A., Losiak A. (2010) Corrosion morphologies of naturally weathered chain silicate minerals: implications for preliminary results from the Mars Phoenix Lander MECA (Microscopy, Electrochemistry and Conductivity Analyzed) Atomic Force Microscope, *Journal of Sedimentary Research* 80: 771-780.

Velbel M.A., Losiak A. (2008) Influence of surface-area estimation on rates of plagioclase weathering determined from naturally weathered 3400 y old Hawaiian basalt, *Mineralogical Magazine* 72: 91-94.

In review:

Losiak A., Schulz T., Buchwaldt R., Koeberl C. (2013?) Characteristics of granitic intrusions from the vicinity of the Bosumtwi impact crater, Ghana, *Lithos*.

Losiak A., Golebiowska I., Wojciechowski J., Ferrière L., Huber M., Koeberl C. (2013?) Spatial Analysis of Planar Deformation Features from Bosumtwi impact crater, Ghana. *Meteoritics and Planetary Science*.

Losiak A., Wild E.M., Michlmayr L., Koeberl C. (2013?) ^{10}Be Content in suevite breccia from the Bosumtwi impact crater, Ghana. *Meteoritics and Planetary Science*.

Kring D. A., Balcerski J., Blair D.M., Chojnacki M., Donohue P.H., Drummond S.A., Garber J.M., Hopkins M., Huber M.S., Jaret S.J., Losiak A., Maier A., Mitchell J., Ong L., Ostrach L.R., O'Sullivan K.M., Potter R.W.K., Robbins S., Shankar B., Shea E.K., Singer K.N., Sori M., Sturm S., Willmes M., Zanetti M., Wittmann A. (2013?) Fold Hinge in Overturned Coconino Sandstone and its Structural Displacement During the Formation of Barringer Meteorite Crater (a.k.a Meteor Crater), Meteoritics and Planetary Science.

In preparation:

Czechowski L., Losiak A. (2013?) Differentiation, mineralogy and melting of Rhea.

Losiak A., Czechowski L., Masse M., Velbel M. (2013?) Contemporary weathering on the Martian northern polar cap.

Losiak A., Hamers M., Habler G., Ivanov B., Koeberl C. (2013?) High pressure points within the shock metamorphosed quartz.

Groemer G. et al. (including Losiak A.) (2013?) Morocco 2013 Mars Analog Field Simulation.

CONFERENCE CONTRIBUTIONS AND PRESENTATIONS

SEMINARS AND INVITED TALKS

Geology of the Moon (October 2008) Department of Geological Sciences, Michigan State University.

Granites from the vicinity of the Bosumtwi crater (January 2012) Museum für Naturkunde, Berlin.

Limitations on information retrievable from Antarctic meteorites due to influence of terrestrial weathering (2012) Meteorites: insights into planet composition 19th Meeting of the Petrology Group of the Mineralogical Society of Poland Orlowicz.

CONFERENCE PRESENTATIONS**First author:**

¹⁰Be Content in suevite breccia from the Bosumtwi Impact Crater. (2013) Losiak A., Wild E.M., Michlmayr L., Koeberl C., EGU General Assembly, Vienna, Austria, Abstract #6381. Poster

The Role of the Photogeologic Mapping in the Morocco 2013 Mars Analog Field Simulation (Austrian Space Forum) (2013) Losiak A. et al. EGU General Assembly, Vienna, Austria, Abstract #11556. Poster.

Relation of the Shock Field Heterogeneity to Shock Pressure Estimations based on PDFs Characteristics. (2013) Losiak A. Koeberl C., 44th Lunar and Planetary Science Conference, Houston, USA, Abstract #1667. Poster

Antarctica as a Mars analogue: evaporites on ice and meteorites. (2013) Losiak A. The Martian Cryosphere 21-23.01.2013, Wrocław, Poland. Talk.

Limitations on information retrievable from Antarctic meteorites due to influence of terrestrial weathering. (2012) Losiak A., Velbel M.A. Meteorites: insights into planet composition 19th Meeting of the Petrology Group of the Mineralogical Society of Poland, Obrzycko, Polska. Mineralogia – Special Papers 40: 39-41. Invited talk.

¹⁰Be Content in Suevite Breccia Clasts from the Bosumtwi Crater Fill as a Proxy for the Content of Surface Components (2012) Losiak A., Wild E., Michlmayr L., Koeberl C. 75th Annual Meteoritical Society Meeting, Carnis, Australia, Abstract #5118. Talk.

Impact cratering processes in the Bosumtwi crater (2012) A. Losiak, C. Koeberl, Workshop on Mars – Connecting Planetary Scientists in Europe 05-07 June 2012, Budapest, Hungary. Poster

Zircon U-Pb and Hf-Nd isotopic constraints on the genesis of granites from the vicinity of Bosumtwi crater, (2012) A. Losiak, T. Schulz, C. Koeberl, EGU General Assembly, Vienna, Austria, Abstract #6574. Poster

Spatial Analysis of Planar Deformation Features (2011) Losiak A., Golebiowska I., Koeberl C., 74th Annual Meteoritical Society Meeting, London, UK, Abstract #5056. Talk.

Specific combinations of planar deformation feature orientations in shocked quartz grains from The Bosumtwi impact crater as a signature of β -quartz (2011) A. Losiak, L. Ferrière, C. Koeberl, EGU General Assembly, Vienna, Austria, Abstract #4243. Poster.

What is the Role of Alpha-Quartz in Impact Shock Metamorphism? Angles Between Pole Orientations of Planar Deformation Features as a Proxy for the Shock-Induced Temperature Change (2011) A. Losiak, L. Ferrière, C. Koeberl, 42nd Lunar and Planetary Science Conference, Houston, USA, Abstract #1284. Poster.

A Web-Based Program for Indexing Planar Deformation Features in Quartz (2011) A. Losiak, J. Wojciechowski, L. Ferrière, M. Huber, C. Koeberl, 42nd Lunar and Planetary Science Conference, Houston, USA, Abstract #1286. Poster.

Geographic Influences on Evaporite Formation During Weathering of Antarctic Meteorites (2009) A. Losiak, M. A. Velbel, 40th Lunar and Planetary Science Conference, Houston, USA, Abstract #1394. Poster.

A New Lunar Impact Crater Database (2009) A. Losiak, D. E. Wilhelms, C. J. Byrne, K. G. Thaisen, S. Z. Weider, T. Kohout, K. O'Sullivan, D. A. Kring, 40th Lunar and Planetary Science Conference, Houston, USA, Abstract #1532. Poster.

Establishing a Precise Absolute Chronology of the Moon — A Need for Robotic Missions (2008) A. Losiak, T. Kohout, K. O'Sullivan, K. Thaisen, S. Weider, D. Kring, Joint Annual Meeting of LEAG-ICEUM-SRR, Cape Canaveral, USA, Abstract #4072. Poster.

King Crater (Moon) as a potential landing site for the manned mission (2008) A. Losiak, Michigan Space Grant Consortium Conference, Ann Arbor, US. Talk.

Estimating crystal shape to estimate plagioclase weathering rates in naturally weathered basalt from Hawaii (2008) A. Losiak, GSA North-Central Section - 42nd Annual Meeting, Evansville, USA. Poster.

Contributing author:

Micromorphology of quartz grains as a tool in recognition of fluvial deposits based on field and experimental study (2013), Woronko B., Girit D., Losiak A., 10th International Conference on Fluvial Sedimentology, Leeds, UK.

Differentiation, mineralogy and melting of Rhea. (2013) Czechowski L., Losiak A., EGU General Assembly, Vienna, Austria, Abstract #9122.

Differentiation, Mineralogy and Melting of Rhea. (2013) Czechowski L., Losiak A., 44th Lunar and Planetary Science Conference, Houston, USA, Abstract #2558.

A statistical dynamical study of meteorite impactors: case study from Bosumtwi. (2012) Galiazzo M.A., Bazso A., Huber M., Losiak A. Joint Meeting „Paneth Kolloquium“, „SPP 1385: The First 10 Million Years of the Solar System“ and MEMIN, Nördlingen, Germany.

Karakul Depression, Tadjikistan — A Young Impact Crater? (2012) Baratoux D., Bouley S., Baratoux L., Colas F., Dauvergne J.L., Vaubaillon J., Chennaoui-Aoudjehane H., Jambon A., Gattacceca J., Losiak A., Bourdeille C., Jullien A., Ibadinov K. Asteroids, Comets, Meteors 2012, Proceedings of the conference LPI Contribution No. 1667, id.6037, Niigata, Japan.

Karakul: a young complex impact crater in the Pamir, Tajikistan (2011) Bouley S., Baratoux D., Baratoux L., Colas F., Dauvergne J., Losiak A., Vaubaillon J., Bourdeille C., Jullien A., Ibadinov K., American Geophysical Union, Fall Meeting 2011, San Francisco, USA, Abstract #P31A-1701.

ANIE: A Mathematical Algorithm for Automated Indexing of Planar Deformation Features in Shocked Quartz (2011) M. S. Huber, L. Ferrière, A. Losiak, C. Koeberl, 42nd Lunar and Planetary Science Conference, Houston, USA, Abstract #1200.

Fold Hinge in Overturned Coconino Sandstone and its Structural Displacement During the Formation of Barringer Meteorite Crater (a.k.a Meteor Crater) (2011) D. A. Kring, J. Balcerski, D. M. Blair, M. Chojnacki, P. H. Donohue, S. A. Drummond, J. M. Garber, M. Hopkins, M. S. Huber, S. J. Jaret, A. Losiak, A. Maier, J. Mitchell, L. Ong, L. R.

Ostrach, K. M. O'Sullivan, R. W. K. Potter, S. Robbins, B. Shankar, E. K. Shea, K. N. Singer, M. Sori, S. Sturm, M. Willmes, M. Zanetti, A. Wittmann, 42nd Lunar and Planetary Science Conference, Houston, USA, Abstract #1740.

Asymmetrical Distribution of Impact Ejected Lithologies at Barringer Meteorite Crater (a.k.a Meteor Crater) (2011) D. A. Kring, J. Balcerski, D. M. Blair, M. Chojnacki, P. H. Donohue, S. A. Drummond, J. M. Garber, M. Hopkins, M. S. Huber, S. J. Jaret, A. Losiak, A. Maier, J. Mitchell, L. Ong, L. R. Ostrach, K. M. O'Sullivan, R. W. K. Potter, S. Robbins, B. Shankar, E. K. Shea, K. N. Singer, M. Sori, S. Sturm, M. Willmes, M. Zanetti, A. Wittmann, 42nd Lunar and Planetary Science Conference, Houston, USA, Abstract #1746.

Denticles on Chain Silicate Grain Surfaces and Their Utility as Indicators of Weathering Conditions on Earth and Mars, (2010) M. A. Velbel, A. I. Losiak, First International Conference on Mars Sedimentology and Stratigraphy, El Paso, USA, Abstract #6056.

Corrosion Morphologies of Naturally Weathered Terrestrial Pyroxene: Implications for Preliminary Results from the Mars Phoenix Lander Atomic Force Microscope (2009) M. A. Velbel, A. I. Losiak, Workshop on the Microstructure of the Martian Surface, Copenhagen, Denmark, Abstract #9011.

Scientific Opportunities for Human Exploration of the Moon's Schrödinger Basin (2009) T. Kohout, K. O'Sullivan, A. Losiak, K. G. Thaisen, S. Weider, D. A. Kring, 40th Lunar and Planetary Science Conference, Houston, USA, Abstract #1572.

Geographic Information Systems: An Enabling Tool for Lunar Exploration (2008) K. G. Thaisen, A. Losiak, T. Kohout, K. O'Sullivan, S. Weider, D. Kring, Joint Annual Meeting of LEAG-ICEUM-SRR, Cape Canaveral, USA, Abstract #4098.

Robotic and Human Exploration of the Schrödinger Basin (2008) T. Kohout, K. O'Sullivan, A. Losiak, D. Kring, K. Thaisen, S. Weider, Joint Annual Meeting of LEAG-ICEUM-SRR, Cape Canaveral, USA, Abstract #4078.

Schrödinger Basin: a Geologically Diverse Landing Area (2008) K. O'Sullivan, T. Kohout, A. Losiak, D. Kring, K. Thaisen S. Weider, Joint Annual Meeting of LEAG-ICEUM-SRR, Cape Canaveral, USA, Abstract #4081.

Schrodinger basin – a prospective landing site (2008) K. O'Sullivan, T. Kohout, , A. Losiak, K. Thaisen, S. Weider, D. Kring, Lunar Science Conference at NASA Ames Research Center, Moffett Field, USA.

Findings of the LPI's 2008 Lunar Exploration Summer Intern Program (2008) Weider, S., Kohout, T., Losiak, A., O'Sullivan, K., Thasien, K. and Kring, D., UK Planetary Forum Early Career Scientists' Annual Meeting, London, UK.